Infrared Observations of Jupiter's Ionosphere

Rosie Eleanor Johnson

Radio and Space Plasma Physics Group

Department of Physics and Astronomy

University of Leicester

A thesis submitted for the degree of

Doctor of Philosophy

March 2018

Abstract

Rosie Eleanor Johnson
Infrared Observations of Gas Giant Aurora

In this thesis I have used infrared observations of Jupiter to investigate the flows of ions in the ionosphere and how they are coupled to the ionospheric heating in the auroral regions, determining the drivers of the heating and how they are related to the thermosphere and the magnetosphere.

I investigated the H_3^+ line-of-sight velocity in the mid-to-low latitude region, derived from the Doppler shift of the Q(1,0$^-$) emission line taken by IRTF-CSHELL. No evidence of flows in the region of the H Ly-α bulge predicted by a global circulation model were measured, and the H_3^+ ions in the mid-to-low latitude region were found to be corotating.

Using observations taken by VLT-CRIRES, polar projections of the intensity and line-of-sight velocity of the H_3^+ ions in Jupiter's northern auroral region were created. This revealed the ionospheric flows and how they relate to different morphological regions of the northern aurora. These flows vary from extremely sub-rotational to super-rotational, and the drivers of the flows range from the solar wind and magnetospheric interaction to a potential thermospheric driver.

The same set of VLT-CRIRES observations are then used to derive the rotational temperature, column density, and total emission of the H_3^+ ions in the northern auroral regions. These properties were mapped onto polar projections, which revealed changes in temperature during the observations (over a short period of ~80 minutes). The changes in temperature could be caused by local time changes in particle precipitation energy, or they could be caused by the thermospheric response to a transient enhancement of solar wind dynamic pressure, as predicted by models. By comparing all of the H_3^+ properties, the complex interplay between heating by impact from particle precipitation and Joule heating, as well as cooling by the H_3^+ thermostat effect was revealed.

Declaration

The research presented in this thesis is the work of the author. Information which has been taken from external sources has been appropriately reference. The following scientific works have been published based on the studies presented in this thesis:

Johnson, Rosie E., T. S. Stallard, H. Melin, S. Miller, and J. D. Nichols. 2016. Measurements of the Rotation Rate of the Jovian Mid-to-Low Latitude Ionosphere. *Icarus* 280. Elsevier Inc.: 249–54. doi:10.1016/j.icarus.2016.06.026.

Johnson, Rosie E., T. S. Stallard, H. Melin, J. D. Nichols, and S. W. H. Cowley. 2017. Jupiter's Polar Ionospheric Flows: High Resolution Mapping of Spectral Intensity and Line-of-Sight Velocity of H_3^+ ions. *Journal of Geophysical Research: Space Physics* 122 (7): 7599–7618. doi:10.1002/2017JA024176.

Acknowledgements

First of all, I'd like to thank my supervisors for all their guidance during my PhD. Tom, thank you for passing down your observing knowledge and helping me get a handle on all things H_3^+. Jonny, thank you for patiently answering my many questions about the jovian system.

I'd like to thank those who I met at conferences (especially the remainder of team H_3^+ across the pond!), and also the telescope operators and support astronomers at IRTF for all the useful discussions. Thank you to members of my department who helped me out despite not being in my field of research. There probably isn't a member of RSPP who I haven't asked a question to and I extend my thanks to you all for answering so diligently and also helping me navigate through the academic world.

Overall, RSPP has been a fantastically supportive research group: thank you for all the pub trips and weekly instalments of cake. A special mention goes to my BFF, Katie: thank you for being there through it all. A big thank you goes to Henrik for kindly grading any manuscript draft I handed to him and for helping me understand that H_3^+ temperatures can be just as fun as their velocities.

During my PhD I have volunteered at After18, which is a charity that supports young unaccompanied asylum seekers and refugees. I'd like to thank my tutees for keeping my writing on track and always checking in on my progress. To all my friends and family: thank you for all the encouragement. Mum, Dad and David: thank you for believing in me and keeping me motivated. Joe: thank you for lifting me up and making me strong.

As a kayaker, I'm the kind of person who enjoys retrospective fun, and parts of this PhD definitely slot into that category! That said, I've also had some pretty amazing opportunities, met some awesome and inspirational people, and I'm actually pretty proud of this thesis!

Contents

List of Tables

List of Figures

Chapter 1 Background Theory

The subject of this thesis is the ionosphere of Jupiter and how it is coupled to the magnetosphere. I investigate the ionosphere of Jupiter at the mid-infrared wavelengths, using observations of H_3^+ emission taken with spectrometers. Therefore, in this section I will cover the background theory regarding planetary plasma physics and H_3^+ spectroscopy. For further information on space plasma physics please refer to Baumjohnann and Treumann (1997). Greater detail about molecular spectroscopy and H_3^+ ions is given by Banwell and McCash (1994) and McCall (2001).

1.1 Planetary Plasma Physics

The space plasma studied in this thesis is created through the ionisation of a gas by photoionization or energetic particle impacts. Space plasmas have an equal number of positive and negative components and appear electrically quasi-neutral on a large scale.

1.1.1 Collisionless Space Plasmas

When a charged particle is travelling through magnetic (**B**) and electric (**E**) fields, the particle will experience the Lorentz force (**F**),

$$\mathbf{F} = \mathrm{q}(\mathbf{E} + \mathbf{v} \times \mathbf{B}) \qquad \textbf{1.1}$$

where q is the charge of the particle and **v** is the initial velocity of the particle.

If a particle is travelling in a uniform **B** field, where there is no **E** field present, the particle will gyrate about the magnetic field line of field strength B with an angular frequency given by Equation 1.2, where Ω is the gyrofrequency of particle with mass m and charge q; opposite charges gyrate in the opposite sense. If a particle has a non-zero component of velocity parallel to the **B** field, then it will gyrate in a helical path along the field line.

$$\Omega = \frac{\mathrm{qB}}{\mathrm{m}} \qquad \textbf{1.2}$$

In collisionless plasmas, where a component of the **E** field is perpendicular to the **B** field, the particles will drift in a direction perpendicular to both fields. This drift of particles is known as **E** x **B** drift and the drift speed (v_{drift}) is given by Equation 1.3. The

electric field is frame dependent, which means that if you transform into the frame of the moving particles, the electric field is zero.

$$v_{drift} = \frac{\mathbf{E} \times \mathbf{B}}{B^2} \quad \textbf{1.3}$$

where B =|**B**|.

1.1.2 Frozen-In Theorem

Temporal changes in the magnetic field are described by,

$$\frac{\partial B}{\partial t} = \nabla \times (\mathbf{v} \times \mathbf{B}) + \frac{1}{\sigma \mu_0} \nabla^2 \mathbf{B} \quad \textbf{1.4}$$

where σ is the conductivity of the plasma. Equation 1.4 is derived by combining Ohm's law for an ideal magnetohydrodynamic (MHD) plasma, Faraday's law, and Ampère's law. The first term on the right hand side is the convective term and the second term on the right hand side is the diffusive term.

If a plasma is highly conductive and collisionless, then the convective term dominates and the field is "frozen-in" to the motions of the plasma and vice versa. This is known as the frozen-in theorem or Alfvén's theorem (Alfven, 1976). When the frozen-in condition applies, Ohm's law becomes,

$$\mathbf{E} + \mathbf{V} \times \mathbf{B} = 0 \quad \textbf{1.5}$$

since in collisionless plasmas there is no friction so σ tends to infinity, and because an infinite current cannot exist, then **j**/σ = 0.

The magnetic Reynolds number is a dimensionless quantity used to understand which term in Equation 1.4 dominates and is given by Equation 1.6.

$$R_m = \frac{|\nabla \times (\mathbf{V} \times \mathbf{B})|}{|\nabla^2 \mathbf{B}/\mu_0 \sigma|} \approx \frac{VB/L}{B/\mu_0 \sigma L^2} = \mu_0 \sigma V L \quad \textbf{1.6}$$

If R_m >> 1, which occurs for collisionless space plasmas, where σ → ∞ and the characteristic length of the field variation (L) is large, the diffusion term can be neglected and the field is frozen into the flow. If R_m < 1 the diffusion term becomes important, the frozen-in condition breaks down and the plasma can diffuse through the field. This can occur in the ionosphere where there are high collision frequencies. Alternatively, the diffusion term can dominate in a process known as reconnection,

where oppositely directed field lines come in close proximity of each other, break apart and reconnect with each other, changing the magnetic field topology.

1.1.3 The Solar Wind

The Sun's atmosphere is known as the solar corona and reaches temperatures of over ~1.5 x 10^6 K. Owing to this large temperature in the solar corona, there is a large pressure gradient between it and interplanetary space that is sufficient to overcome the gravitational forces, leading to an outflow of plasma from the Sun, known as the solar wind. When the solar wind leaves the Sun it is sub-magnetosonic, however, it quickly accelerates to super-magnetosonic speeds within a few solar radii. The solar wind density, n, decreases with the relationship $n \propto 1/r^2$ as it expands through the interplanetary space.

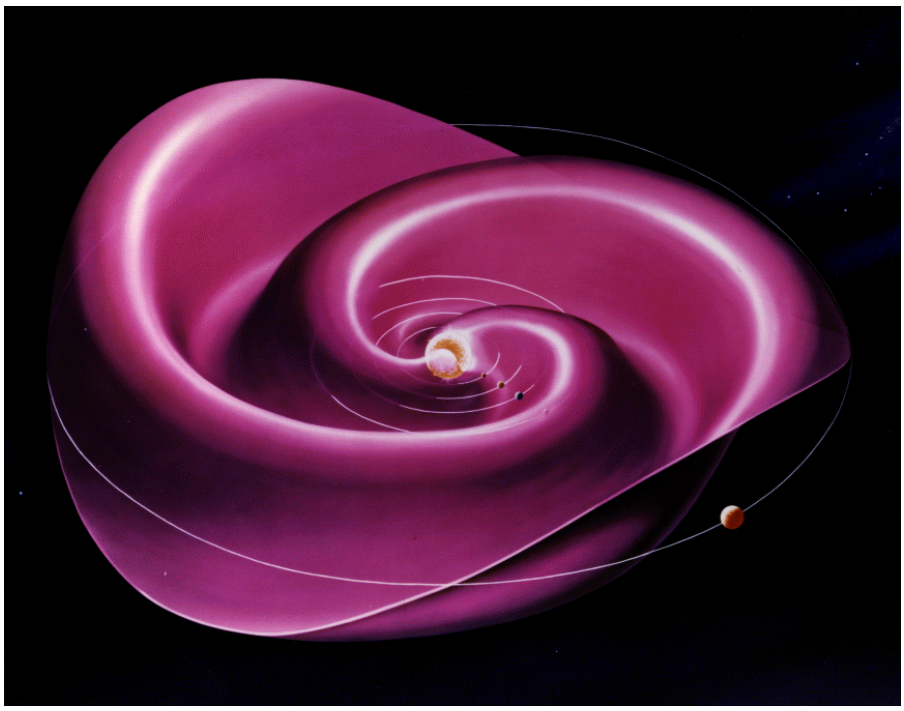

Figure 1-1: A schematic of the heliosphere current sheet which results from the influence of the Parker spiral structure of the solar wind. Image credit: Wikipedia[1].

The magnetic field of the Sun is embedded in the radially outward flowing solar wind, due to the frozen-in theorem, and is known as the interplanetary magnetic field (IMF). This forms a spiral structure in interplanetary space known as the Parker spiral

[1] Wikipedia. 2017. *Heliospheric current sheet*. [ONLINE] Available at: https://en.wikipedia.org/wiki/Heliospheric_current_sheet. [Accessed 17 April 2018].

(Parker 1958), which is shown in Figure 1-1. At the distance of Jupiter's orbit, the angle between the radial direction and the spiral arms of the solar wind is ~82° (measured during the declining phase of solar cycle 23 by Ulysess, Ebert et al. 2014). Different regions of solar magnetic field configurations produce different solar wind speeds. Slow solar wind (~400 km s^{-1}) emerges from regions of closed field, for example near the equator, however, fast solar wind (~800 km s^{-1}) emerges from open field regions, known as coronal holes.

1.1.4 Magnetosphere-Ionosphere Coupling

Figure 1-2 shows the vertical structure of Jupiter's atmosphere, which includes a troposphere, stratosphere, and thermosphere. Jupiter's atmosphere is about 90% hydrogen and 10% helium by mass, with trace amounts of carbon, oxygen, nitrogen and sulphur, which react and form more complex compounds. This thesis focuses on the upper atmosphere; for more information on the lower atmosphere please refer to Taylor et al. (2004), West et al. (2004), Ingersoll et al. (2004), and Moses et al. (2004). Coincident with the thermosphere is the ionosphere which is a charged layer of a planetary atmosphere. The ionosphere absorbs extreme ultraviolet (EUV) radiation from the Sun and energetic charged particles from the magnetosphere, creating ions. Ionospheres are quasi-neutral with the negative charges balancing the positive charges. For greater detail on ionospheres in general, please refer to Schunk and Nagy (2000); the specifics of Jupiter's ionosphere will be given in Section 2.1.

The region surrounding a planet that is dominated by the planetary magnetic field is known as the magnetosphere. The configuration of the Jovian magnetosphere is shown in Figure 1-3. The magnetosphere is an obstacle to the supersonic flow of the solar wind, forcing the flow to slow to sub-sonic speeds by forming a shock upstream of the planet, known as a bow shock. In between the bow shock and the magnetosphere is a region of shocked solar wind, known as the magnetosheath, which is heated and experiences a largely disordered magnetic field. To a first approximation the IMF and solar wind cannot mix with the planetary field and plasma due to the Frozen-in theorem. The boundary which divides these two regimes is known as the magnetopause. However, under certain conditions reconnection can take place along this boundary along what is known as an X-line (Speiser 1965a; Speiser 1965b; Speiser

1967). The dayside magnetosphere is compressed by the flow of the solar wind; however, downstream the magnetosphere becomes elongated and is known as the magnetotail.

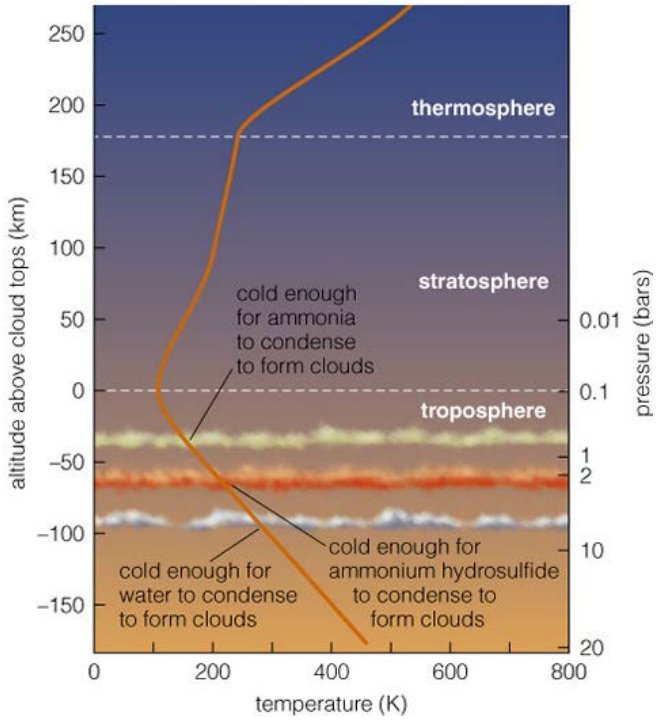

Figure 1-2: The vertical temperature profile of Jupiter atmosphere, with atmospheric layers and cloud tops labelled. Image credit: Pearson Education Inc.

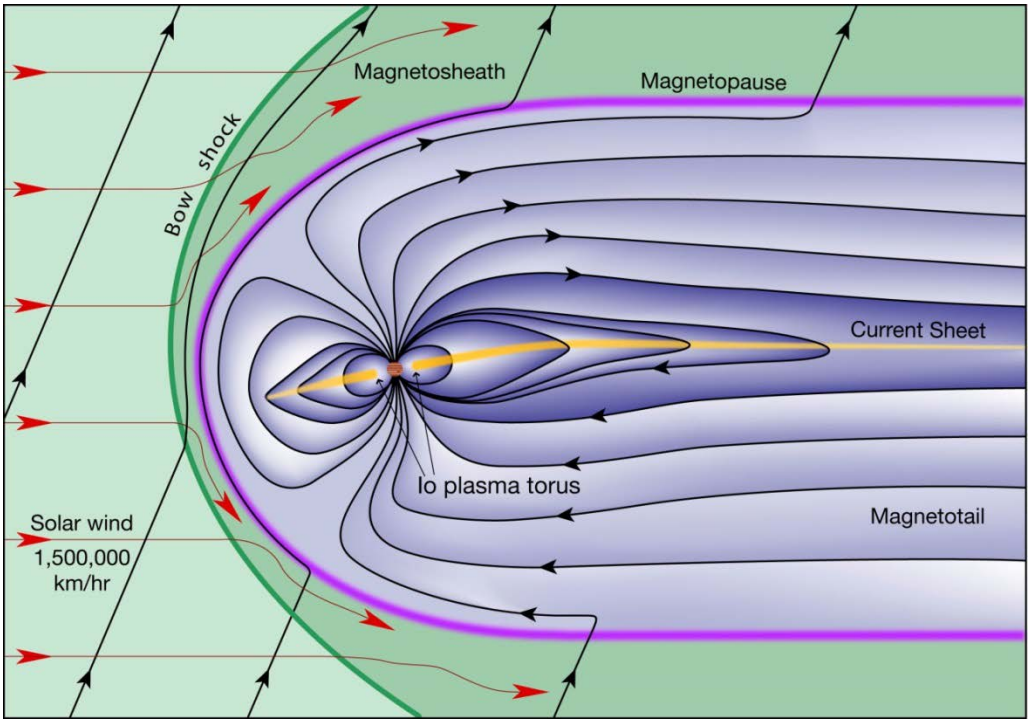

Figure 1-3: The configuration of Jupiter's magnetosphere. Image credit: F. Bagenal & S. Bartlett.

At the Earth, reconnection preferentially takes place at the dayside magnetopause when the IMF has a southward orientation. The newly reconnected field lines, which are now open to the solar wind, convect over the poles, reconnect in the magnetotail and rotate round to the dayside at lower latitudes as closed field lines; this is known as the Dungey cycle (Dungey 1961). At Jupiter, reconnection would preferentially take place when there is northward IMF due to the opposite orientation of Jupiter's magnetic field relative to the Earth's magnetic field. However, no global Dungey cycle is thought to exist at Jupiter (e.g.: Cowley et al. 2003; Delamere and Bagenal 2010), and the coupling of the outer magnetosphere to the solar wind is highly debated, as discussed in Section 2.3.3.

Currents occur in the magnetosphere due to the spatial gradients in the magnetic field, as shown by Ampere's law,

$$\nabla \times \mathbf{B} = \mu_0 \mathbf{j} \qquad \textbf{1.7}$$

where μ_0 is the permeability of free space ($4\pi \times 10^{-7}$ H m^{-1}) and **j** is the current generated by the curl in the **B** field. At Earth the currents are generated by the stresses that the solar wind imposes on the magnetosphere. However, at Jupiter the stresses are imposed on the magnetosphere due to the fast rotation rate. The result is two main currents flowing in Jupiter's equatorial plain: an outwardly directed radial current and an azimuthal current, which are both discussed in greater detail in Section 2.3.2. These currents couple to other currents in the ionosphere via field-aligned currents (FAC), which are also known as Birkeland currents, named after the Norwegian physicist who first proposed them during an arctic expedition 1902-1903 (Birkeland 1908; Iijima and Potemra 1976). Where current diverges, it must flow away from the shear in the flow, along the magnetic field lines. FACs are mainly carried by the more mobile electrons.

Where frequent collisions occur between the charged and neutral components of the ionosphere, the ions and electrons can no longer **E** x **B** drift. These collisions cause the motions of the ions and electrons to diverge, which is shown in Figure 1-4, where the neutral atoms and molecules are represented by the purple circles. At lower altitudes, ions collide with neutrals more frequently than the electrons, and therefore their drift is slower than the electron drift, and the divergence of their motions creates

a current. This process heats up the ionosphere via collisions, which is acting as a resistive load, and is discussed in Section 1.1.5.

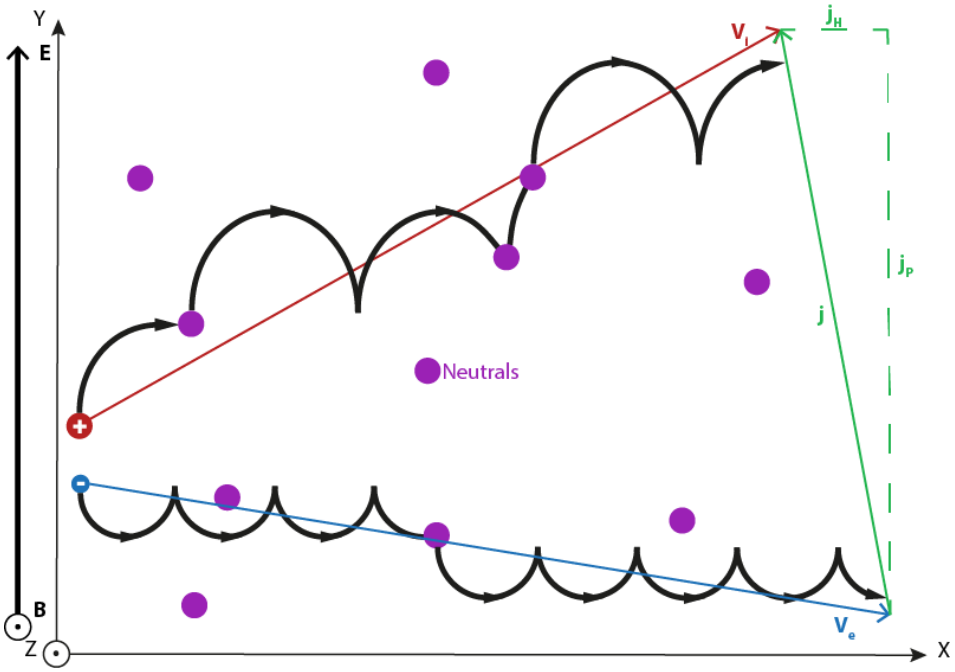

Figure 1-4: A schematic of the charged particle drift at altitudes where collisions with neutral atoms and molecules are frequent. The larger ions collide with the neutrals more frequently than the more mobile electrons, and so their drift speed ($\underline{v}_i$) is slower than the electron drift speed ($\underline{v}_e$) and there is a divergence of the charges. This sets up a current ($\underline{j}$), which has a component parallel to the $\underline{E}$ field known as the Pedersen current ($\underline{j}_P$) and a perpendicular component known as the Hall current ($\underline{j}_H$), represented by the dashed green lines.

The component of the current which is parallel to the **E** field is the Pedersen current ($\mathbf{j_P}$) and the component perpendicular to the **E** field is the Hall current ($\mathbf{j_H}$). The Pedersen current is carried by ions and the Hall current is carried by electrons. These currents are labelled in Figure 1-4 by the dashed green lines. The conductivity depends on the relationship between the gyrofrequency (Equation 1.2) and the neutral collision frequency (ν_{in}). The Pedersen conductivity peaks approximately where the ion gyrofrequency and ion-neutral collision frequency are equal. The Hall conductivity peaks at lower altitudes where the ion-neutral collision frequency is high and the ions mobility is very low.

Figure 1-5 shows a schematic of the magnetosphere-ionosphere coupling system at Earth. The Pedersen and Hall currents, which flow in the ionosphere, are labelled in the schematic, as well as the FACs, which couple to the currents flowing in the magnetosphere. As mentioned above, a magnetosphere-ionosphere coupling system

exists at Jupiter, although it manifests itself differently and is generated by different drivers to the Earth system, which is covered in Section 2.3.2.

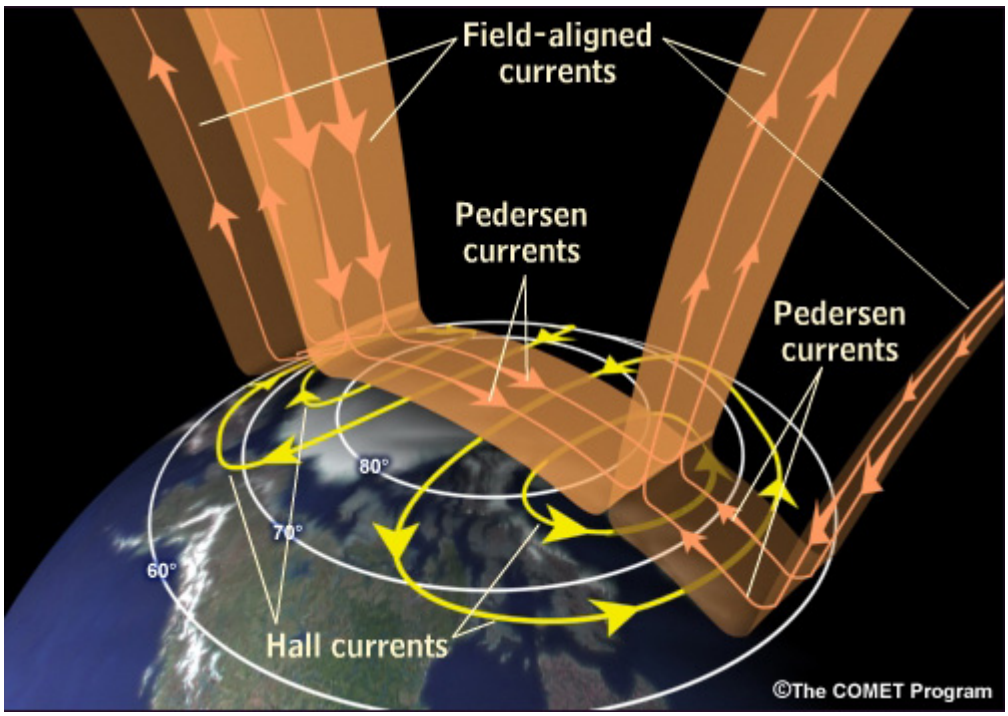

Figure 1-5: A schematic of the ionosphere-magnetosphere coupling currents present at the Earth, where the Hall, Pedersen, and Field-aligned currents are labelled. Image credit: The COMET Program.

1.1.5 Joule heating

The mechanical energy from the magnetosphere is converted into electromagnetic energy and transferred to the ionosphere down the magnetic field lines as Poynting flux, which is given by Equation 1.8. In the ionosphere this energy is dissipated as Joule heating, which is **j·E** in the ionospheric rest frame. The heat produced through Joule heating therefore depends on the magnitude of the ionospheric flows in the ionosphere rather than the number of precipitating particles and particle impact is a separate driver of heat.

Hall currents do not contribute to Joule heating as only currents flowing parallel to the electric field contributes to Joule heating, i.e.: the Pedersen currents. If the Hall conductivity is greater than the Pedersen conductivity then the currents are non-dissipative and there is no Joule heating. Typically, this occurs deeper down in the atmosphere, where only the highest energy particles can penetrate. If the Pedersen conductivity is greater than the Hall conductivity then Joule heating can occur as the currents are dispersive, which usually this takes place in at higher altitudes. The Joule

heating rate (Q_J) in the rest frame of the ionosphere is given by Equation 1.9, where σ_P is the Pedersen conductivity and $\mathbf{v}_n$ is the velocity of the neutrals.

$$S = \frac{1}{\mu_0}\mathbf{E} \times \mathbf{B} \qquad \textbf{1.8}$$

$$Q_J = \sigma_p(\mathbf{E} + \mathbf{v}_n \times \mathbf{B}) \qquad \textbf{1.9}$$

1.2 H_3^+ Spectroscopy

The discovery of the molecular ion H_3^+ was made by J. J. Thomson in 1912 during his experiments on "rays of positive electricity" (Thomson 1911). Having no electron transitions, and no (allowed) rotational spectrum, H_3^+ emits in the infrared (IR) through ro-vibrational transitions. As technology developed, it was possible to study the infrared spectrum of H_3^+ in laboratory work and was first measured by Oka (1980). The first astronomical detection of the infrared spectrum of H_3^+ was made by Drossart et al. (1989) in the upper atmosphere of Jupiter. H_3^+ was discovered at Saturn and Uranus by Geballe et al. (1993) and Trafton et al. (1993) respectively, however, there has been no detection of H_3^+ at Neptune to date (Melin et al. 2018).

H_3^+ is the simplest polyatomic molecule, consisting of three hydrogen nuclei in an equilateral triangle configuration (as shown in Figure 1-6), with two electrons forming an electron deficient covalent bond. In a hydrogen-rich atmosphere, abundant in molecular hydrogen, H_3^+ is produced through a fast chain reaction, which starts with ionisation. The production and destruction of H_3^+ in Jupiter's upper atmosphere is discussed in Section 2.1.1.

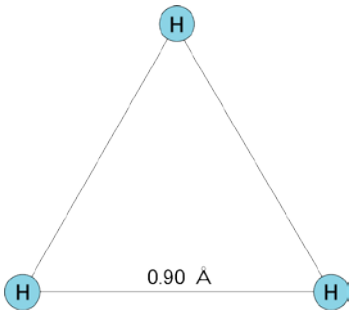

Figure 1-6: The geometry of H_3^+: three hydrogen atoms with an inter-nuclear separation of 0.90 Å, in an electron deficient covalent bond. Image credit: Wikipedia[2].

[2] Wikipedia. 2017. *Trihydogen Cation*. [ONLINE] Available at: https://en.wikipedia.org/wiki/Trihydrogen_cation. [Accessed 01 January 2018].

Most molecules experience electronic transitions that produce emission in the UV and optical wavelengths, but H_3^+ has no stable excited electronic states. Molecules have quantised vibrational and rotational transitional states that produce emission in the infrared. Since H_3^+ is a symmetrical molecule, it has no allowed rotational spectrum and produces emission through a forbidden ro-vibrational spectrum.

Rotational spectra are caused by a quantised change in angular momentum. If the molecule has an uneven charge distribution, then this can result in a torque being applied to the molecule, which causes the molecule to rotate. Although H_3^+ has D_{3h} symmetry, as the molecule rotates, centrifugal forces distort the equilateral triangle configuration of the molecule, which causes the electrostatic forces to become imbalanced and create vibrational states. This shifts the molecule away from its equilibrium state and into a state where the length of the molecular bonds periodically increase and decrease.

The total number of degrees of freedom for a polyatomic molecule of N atoms is 3N. The translational movement and the rotation of the molecules both require 3 of the 3N degrees of freedom, leaving the molecule with 3N-6 degrees of freedom. The only other motion a molecule will experience is vibration and therefore the molecule has 3N-6 fundamental vibrations. There are N-1 bonds, N-1 of the vibrations are bond stretching, while 2N-5 are the vibrations are bending motions (for a non-linear polyatomic molecule). From above, it can be determined that H_3^+ has 3 allowed vibrational modes, which are shown in Figure 1-7.

The symmetric 'breathing' mode ν_1 is IR-inactive, where the bonds expand and contract equally at the same rate and hence there is no change in the dipole moment. However, the asymmetric vibrational modes ν_{2a} and ν_{2b} causes a change in dipole moment due to the stretching and bending of the molecule, allowing the molecule to become infrared active. The ν_{2a} and ν_{2b} vibrational modes are degenerate and hence have the same frequency, therefore throughout this thesis they are referred to collectively as ν_2.

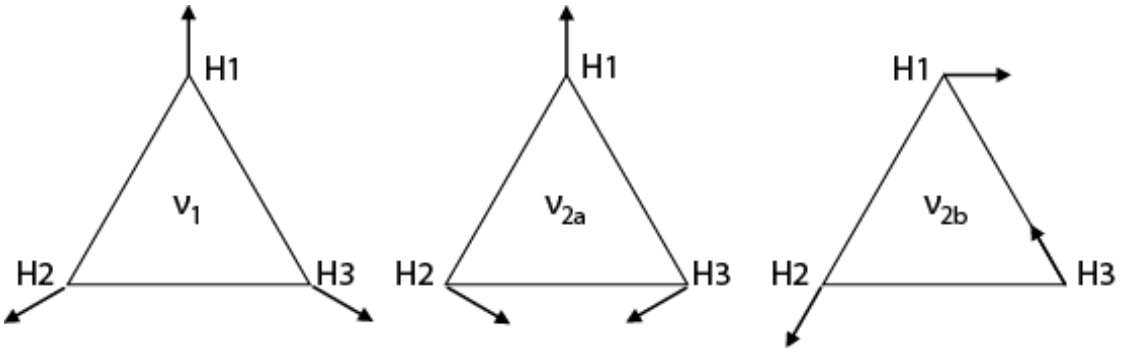

Figure 1-7: The three vibrational modes of H_3^+: the symmetric mode ν_1, which is IR-inactive and the asymmetric modes ν_{2a} and ν_{2b} which are IR-active. Reproduced from Johnsen and Guberman (2010).

The H_3^+ ro-vibrational spectrum is forbidden because H_3^+ is a molecule with a non-ideal symmetry and does not follow the selection rules of quantum mechanics, which assume ideal symmetry. The selection rules for the forbidden transitions are $\Delta J = 0, \pm 1$ and $\Delta K = \pm 3$, where J is the rotational angular momentum and K is the projection of the angular momentum onto the molecule's spin axis. The spectral branches P, Q and R, shown in Figure 1-8 correspond to $\Delta J = -1, 0, +1$ respectively. Transitions in the Q branch exhibit only changes in vibrational energy. However, in the R branch the rotational angular momentum energy is added to the vibrational energy in the transition, where as in the P branch the rotational energy is subtracted.

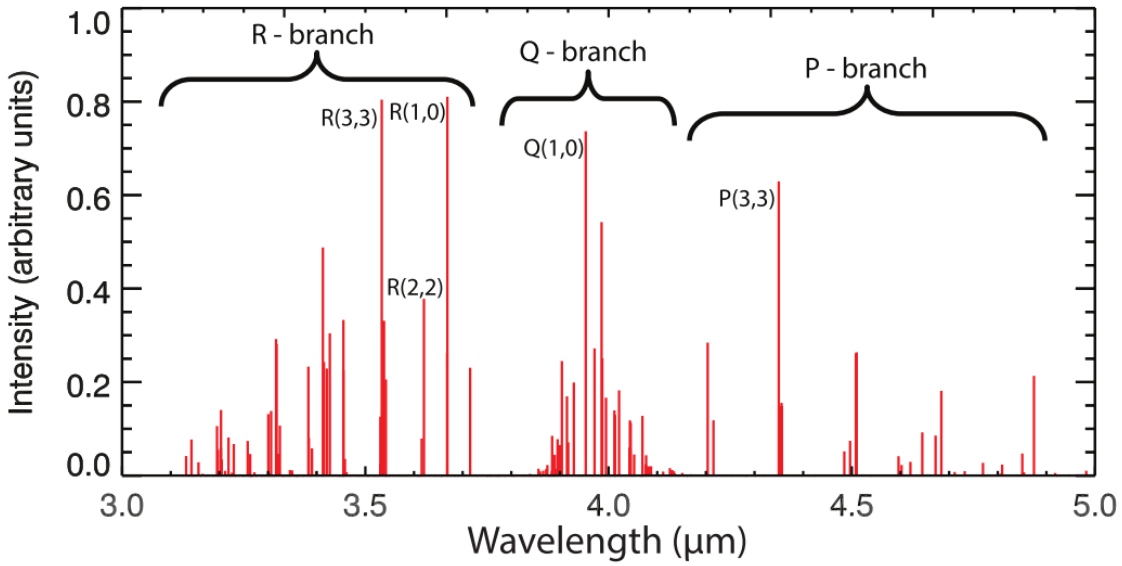

Figure 1-8: A model spectrum of H_3^+, at temperature of 550 K. The intensity of discrete spectral lines of H_3^+ emission versus wavelength. The branches Q, R and P are shown where the numbers in the brackets are values of the quantum number J and K respectively. Reproduced from O'Donoghue (2014).

Several transitions arise in each spectral branch and the transitions that are discussed in this thesis are shown in Figure 1-9. The fundamental transitions $v_2 \rightarrow 0$ produce the most intense emission, and are transitions from the first excited vibrational energy level to the ground state. This emission is the strongest because the first excited vibrational energy level is always the first to be populated. Hot band transitions produce emission through transitions from the second excited vibration energy level $v_2 \rightarrow 1$ to the first vibrational level. As this energy level is only populated once the first energy level is full, this emission is therefore weaker than emission from the fundamental. This band of spectral lines is known as 'hot' because temperatures greater than room temperature are required to populate them. Overtone emissions are produced by transitions from the second excited vibration energy level and above, $v_2 \geq 2$. These are progressively weaker as the transitions involve energy levels which are less and less likely to be populated. As the fundamental is the strongest band of lines, these ro-vibrational transitions are the easiest to detect when observing astronomical object.

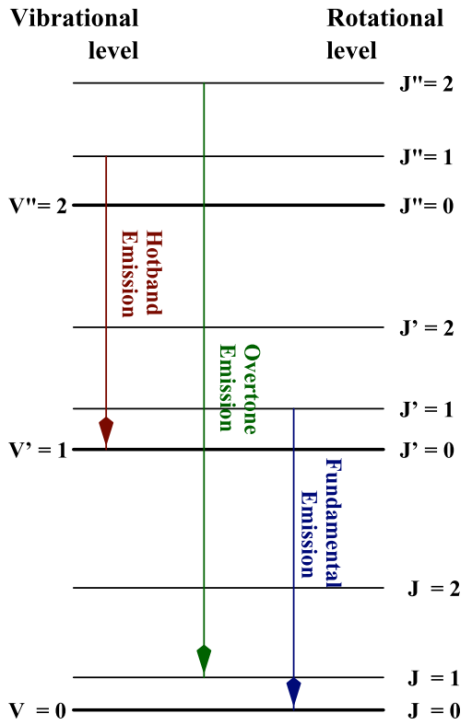

Figure 1-9: The rotational and vibrational energy levels of H_3^+. Reproduced from Stallard (2001).

Chapter 2 The Jovian System

In this chapter I will outline the jovian system and hence it is useful at this stage to define some planetary parameters. Since Jupiter is a gas giant and has no solid surface, a reference surface is commonly used and is defined as the one bar pressure level (100,000 Pa). The rapid rotation of the planet transforms Jupiter into an oblate spheroid, with equatorial radius of ~71,492 km and polar radius of ~66,854 km (Lindal et al. 1985).

The calculations of Jupiter's rotation period are based on ground-based radio observations. The spin period of Jupiter was found to be ~9 hours 55 minutes and the coordinate system based on this spin period is known as System III (1965) (Seidelmann and Divine 1977). In System III, the prime meridian, where the longitude $\lambda_{III} = 0°$, is defined as the central meridian longitude on a specific date in 1965. In the left hand system, which is used in this thesis, the longitude (λ_{III}) observed from Earth increases with time as Jupiter rotates. The latitude (θ_{III}) in System III is defined from the equator where $\theta_{III} = 0°$. This configuration is shown in Figure 2-1, where Z is the spin axis of Jupiter, X is longitude which is zero at the Prime Meridian and Y is the latitude, which completes the left handed orthogonal system.

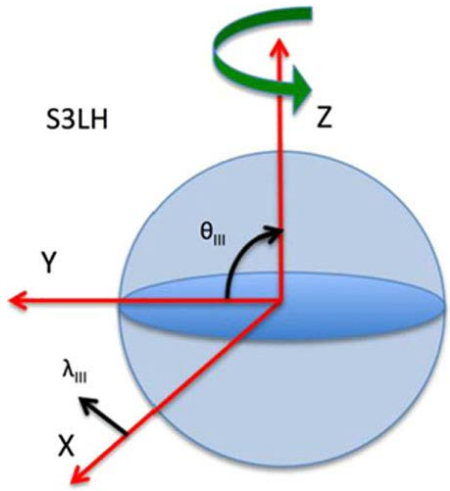

Figure 2-1: The left handed System III (1965) coordinate system. Z is the spin axis, x is the longitude and y is the latitude. Reproduced from Bagenal et al. (2014).

2.1 The Ionosphere

Jupiter's ionosphere was first detected through radio occultation taken by Pioneer 10 during its 1974 flyby (Kliore et al. 1974), and begins approximately 240 km above the 1 bar level. The following section gives an overview of Jupiter's ionosphere, for further detail please refer to Yelle and Miller (2004).

In the lower atmosphere, gases are mixed by turbulent diffusion and their abundances controlled by chemistry in a region called the homosphere. At higher altitudes, the mean free path of gas molecules becomes large and molecular diffusion dominates in a region known as the heterosphere. The homopause separates the homosphere and the heterosphere, and is located in Jupiter's lower thermosphere.

In the heterosphere different species of gas separate out according to their individual scale height, creating a vertical distribution where heavier gases dominate at low altitudes and light gases dominate at higher altitudes. The scale height, H, is given by Equation 2.1 where T is temperature, m is the mean mass of the gas, g is the gravitational field strength and k_B is the Boltzmann constant (~1.38 x 10^{-23} J K^{-1}). As the different species become separated in the heterosphere, the chemistry of the upper atmosphere becomes relatively simple, with the heavier constituent confined to low altitudes, at about 0.1-1 μbar.

$$H = \frac{k_B T}{mg} \qquad \textbf{2.1}$$

2.1.1 Ion Production and Populations

At low latitudes, the neutral constituents of Jupiter's atmosphere are ionised by EUV radiation, whereas at higher latitudes the ionisation is additionally caused by energetic particle impact. At Earth, the Chapman theory calculates the production of ionised particles in the ionosphere by considering the exponential decrease of the ionising radiation as it penetrates the Earth's atmosphere and the exponential decrease of the atmosphere's density with increasing height. Figure 2-2 shows the intensity and density functions as a function of altitude. It can be seen that the peak in the ionisation rate occurs at the crossover point of the intensity and density functions. A similar relation between radiation intensity and neutral density exists at Jupiter.

Ionization makes direct products and electrons; these secondary electrons can go on to cause further ionisation. The ions and secondary electrons react with other ambient species in Jupiter's ionosphere to create new ions or neutrals. A model of the vertical profile of Jupiter's ion density is shown in Figure 2-3a, reproduced from Tao et al. (2011). This figure shows the primary ions H^+, H_2^+, and H_3^+, and a thin layer of hydrocarbon ions around 300 km above the 1 bar level, which is created through photoionization (Kim and Fox 1994).

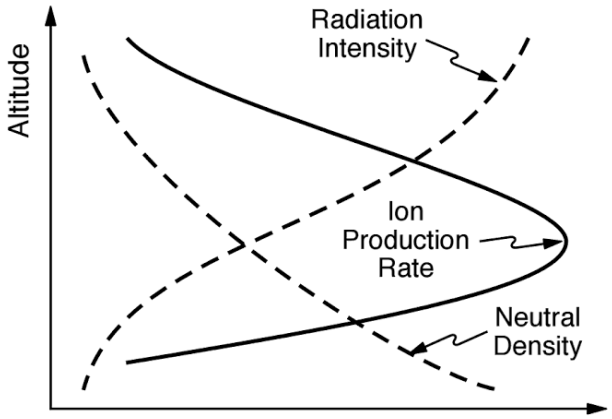

Figure 2-2: The profiles of radiation intensity and neutral density in the Earth's atmosphere. A Chapman ionisation layer is formed in the Earth's upper atmosphere due to the interplay of increasing absorption and decreasing radiation intensity with altitude creates a peak in ion production rate at the altitude where the two profile cross. Reproduced from Baumjohnann and Treumann (1997).

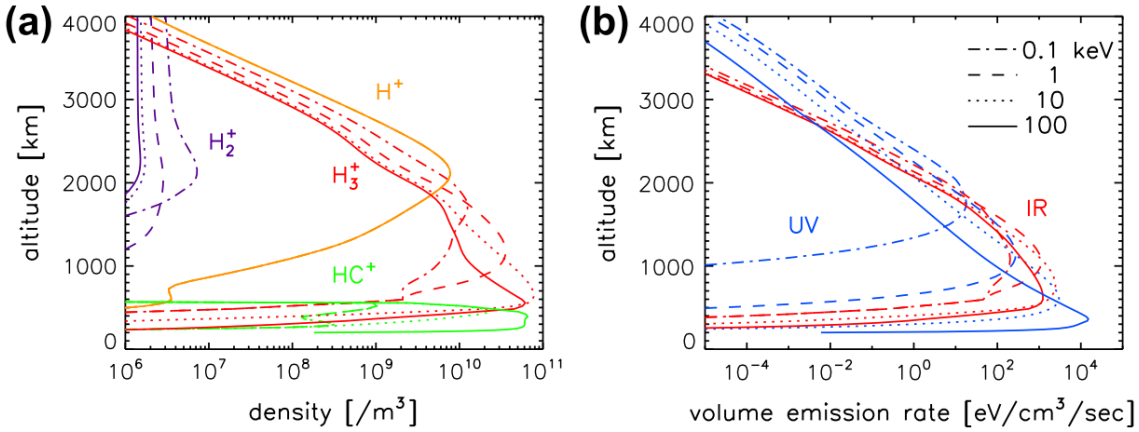

Figure 2-3: The vertical profile of (a) the ion density in Jupiter's ionosphere and (b) the vertical profile of the volume emission rate for precipitating electrons with initial energy 0.1 (dot-dashed), 1 (dashed), 10 (dotted), and 100 keV (solid), reproduced from Tao et al. (2011). (a) The ion densities for hydrocarbons (green line), H_2^+ (purple line), H_3^+ (red line), and H^+ (yellow line). (b) The blue lines represent UV emission in the 117-174 nm wavelength range and the red lines represent the infrared emission of the H_3^+ Q(1,0$^-$) line. The altitudes are relative to 1 bar level in Jupiter atmosphere.

Ionisation can occur through photon (hν) or electron (e^-) impact, shown by the following equations,

$$H_2 + h\upsilon\ [\text{or } e^-] \rightarrow H + H + e^-[+e^-] \quad \textbf{2.2}$$

$$H_2 + h\upsilon\ [\text{or } e^-] \rightarrow H_2^+ + e^-\ [+e^-] \quad \textbf{2.3}$$

$$H_2 + h\nu\ [\text{or } e^-] \rightarrow H^+ + H + e^-\ [+e^-] \quad \textbf{2.4}$$

where the resulting neutral atomic hydrogen atoms can go on to be ionised,

$$H + h\nu\ [\text{or } e^-] \rightarrow H^+ + e^-\ [+e^-]. \quad \textbf{2.5}$$

H^+ dominates at high altitudes, above 2000 km above the 1 bar level, as shown in Figure 2-3a. Here, H^+ can recombine directly via radiative recombination, which is a very slow process. Alternatively, a charge exchange between H^+ and H_2, which is in an excited vibrational state of $\nu \geq 4$, could take place, as shown by Equation 2.6 (McElroy 1973).

$$H^+ + H_2\ (\nu \geq 4) \rightarrow H + H_2^+ \quad \textbf{2.6}$$

The density of H_2^+ is low, as shown in Figure 2-3a, because it reacts with H_2 to produce H_3^+, as shown by Equation 2.7 (Hogness and Lunn, 1925). This reaction is very rapid and exothermic, with a Langevin rate coefficient of 2 x 10^{-15} m^{-3} s^{-1} (McCall 2001).

$$H_2^+ + H_2 \rightarrow H_3^+ + H \quad \textbf{2.7}$$

The destruction of H_3^+ is either through dissociative recombination with a free electron (Equation 2.8 and 2.9) or through proton exchange with a neutral species (Equation 2.10, where X is a neutral species). At low altitudes, close to the homopause, most H_3^+ ions are destroyed by neutral hydrocarbons. Above the homopause, the time life of H_3^+ is a function of electron density, as the main loss process is through electron recombination.

$$H_3^+ + e^- \rightarrow H_2 + H \quad \textbf{2.8}$$

$$H_3^+ + e^- \rightarrow 3H \quad \textbf{2.9}$$

$$H_3^+ + X \rightarrow HX^+ + H_2 \quad \textbf{2.10}$$

At the mid-to-low latitudes, Melin and Stallard (2016) calculated that the H_3^+ lifetime was 1.6 ± 0.4 hours. This value is similar to those predicted by Achilleos et al. (1998), using the Jovian Ionospheric Model (JIM) which estimated a lifetime of ~1.05 hours. The minimum life time of the auroral H_3^+ is predicted to by ~10 s by JIM,

although this could be longer in different regions of the aurora depending on the electron density.

Jupiter's ionosphere is dominated by H_3^+ in the 500-1500 km altitude region, with the peak density altitude varying with the energy of the precipitating electrons Figure 2-3a; above this altitude the H_3^+ density slowly decreases. The small local maximum of H_3^+ density at about 1600 km above the one bar level, is caused by ionisation by solar EUV radiation. At altitudes of 2200 km, where H^+ densities peak, there is a small local minimum of H_3^+ density caused by the enhanced electron densities at this altitude which destroy H_3^+.

From observations taken with the Keck-NIRSPEC of the H_3^+ emission in Jupiter's auroral regions, Lystrup et al. (2008) derived a vertical ion density profile, shown in Figure 2-4 as the solid line alongside modelled profiles. The dashed line is the vertical ion density profile of H_3^+ produced by the model of Grodent et al. (2001), which is a self-consistent 1D model developed from the in-situ Galileo measurements (Seiff et al. 1998) to constrain the neutral density profile. The dotted line is the vertical ion density profile from Melin et al. (2005) who adapted the model by Grodent et al. (2001) to include non-local thermal equilibrium effects, which can occur at high altitudes and are discussed in Section 2.1.3. From Figure 2-4 it can be seen that the derived H_3^+ densities compare well with the model by Melin et al. (2005) up to ~1800 km, beyond which the measured density is higher than the model.

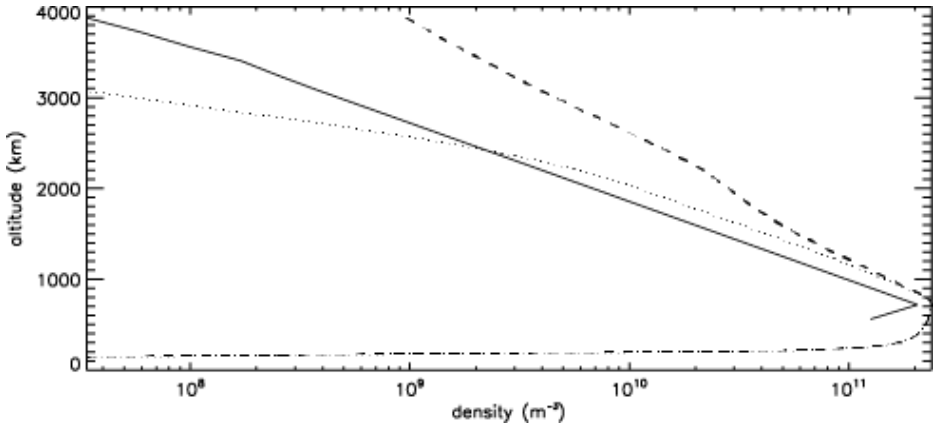

Figure 2-4: A comparison of measured and convolved modelled vertical H_3^+ density profile, produced from Lystrup et al. (2008). The derived H_3^+ density from the data is given by the solid line. The dashed line represents the profile predicted by the convolved model from Grodent et al. (2001). The dotted line represents the profile predicted by the convolved model from Melin et al. (2005). The altitudes are relative to 1 bar level in Jupiter's atmosphere.

Figure 2-3b, reproduced from Tao et al. (2011), shows the modelled vertical profile of the UV and IR emission. It can be seen that for both UV and IR emission, as the energy of the incident electron increases, the peak altitude of the maximum emission decreases because the high energy electrons can penetrate deep into the atmosphere. At higher altitudes, the H_3^+ emission falls off quicker than the UV emission, as the populations of the excited vibrational levels depart from local thermal equilibrium, which is discussed in greater detail in Section 2.1.3.

Although Figure 2-3b shows that the peak emission altitude of the H_3^+ Q(1,0$^-$) line differs depending on energy of the precipitating electrons, a model by Melin et al. (2005) places the peak emission altitude of H_3^+ at ~550 km. Different H_3^+ emission lines originate from different altitudes in Jupiter's ionosphere. Uno et al. (2014) determined the vertical emissivity profile of the H_3^+ overtone and hot overtone emission lines. The peak altitude of the overtone and hot overtone were ~700-900 km and ~680-950 km respectively, placing them at a higher altitude than the fundamental emission. However, in this thesis the investigations are based on properties derived from fundamental H_3^+ emission lines, therefore, I will assume that the H_3^+ originates from an altitude of ~550 km.

2.1.2 Conductivity

The degree to which the magnetosphere is coupled to the upper atmosphere is determined by the electrical conductivity of the ionosphere. There are two conducting layers which are associated with the different currents that flow in Jupiter's ionosphere, the Pedersen and the Hall layer, introduced in Section 1.1.4.

The H_3^+ ions are responsible for producing ~90% of the height-integrated Pedersen conductivities in the auroral regions of Jupiter (Millward et al. 2002). Since the height integrated current densities depend on the density of Jupiter's upper atmosphere, as the H_3^+ production increases, so does the conductivity. Millward et al. (2002) found that if the precipitating particles have energy of ~60 keV then they will deposit their energy at an altitude where H_3^+ density is maximised (~550 km), as shown by Figure 2-5, where the solid line is the Pedersen conductivity and the dashed line is the Hall conductivity. This altitude is coincident with a region of the ionosphere where

the values of ion-neutral collision frequency and the ion gyrofrequency are such that the Pedersen conductivity is maximised.

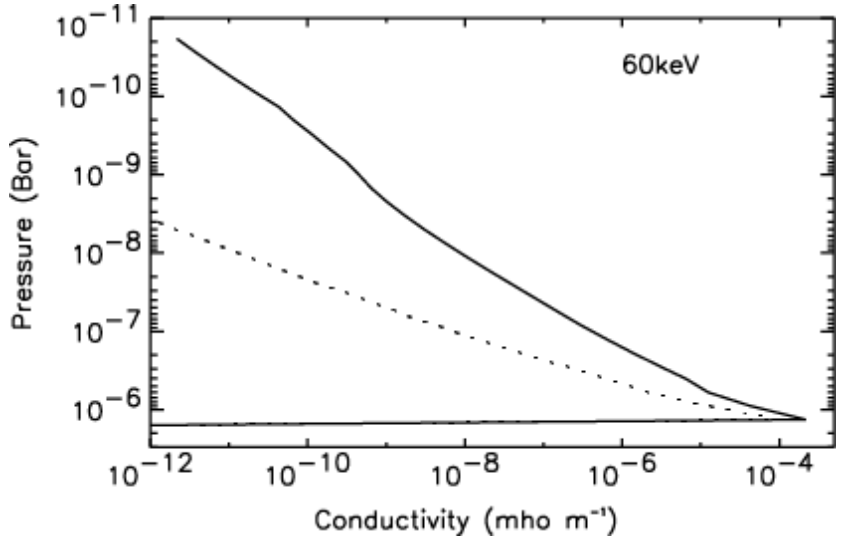

Figure 2-5: The predicted Pedersen (solid line) and Hall (dotted line) conductivities generated by incident electrons with a constant number flux of 6.25×10^{12} cm^{-2} s^{-1} and initial electron energy of 60 keV respectively. Reproduced from Millward et al. (2002).

2.1.3 Local Thermal Equilibrium

As H_3^+ is a polyatomic molecule it experiences rotational and vibrational motions as well as translational kinetic motions, and therefore the rotational and vibrational temperatures of H_3^+, as well as kinetic temperatures, can be derived. The kinetic temperature of the H_3^+ ions can be derived from the width of the spectral emission lines. The rotational temperature of the H_3^+ ions can be derived from the ratio of the intensity of different rotational lines within the same vibrational manifold. The vibrational temperature of the H_3^+ ions can be derived from the ratio of the intensity of emission lines from different vibrational manifolds.

In order to derive the temperature, column density, and total emission from the H_3^+ spectra, an assumption used in the past was that the ionosphere is in local thermal equilibrium (LTE). LTE means that the energy levels of H_3^+ are populated in a Boltzmann distribution. If LTE holds in Jupiter's upper atmosphere then the rotational, vibrational and kinetic temperatures measured from H_3^+ emission lines, which were measured simultaneously, would reveal identical temperatures (Geiner et al. 2001). Miller et al. (1990) derived a vibrational temperature of 1100 ± 100 K, which was in agreement with the rotational temperature of 1100 ± 100 K derived by Drossart et al.

(1989), implying that the LTE assumption held; therefore, the derived temperature was representative of the temperature of the thermosphere as well as the ionosphere.

However, studies such as Kim et al. (1992) dismissed the LTE assumption, and discuss how non-LTE affects the population of excited vibrational levels. Through near-resonant transfer with H_2, Kim et al. (1992) suggested that the $\nu_2 = 2$ level population was selectively increased. However, Stallard et al. (2002) found no evidence for this over population and proposed that the upper vibrational excited level are populated by a proton-hopping collision mechanism. The collisional excitation of the vibrational level n, with energy E_n, is inversely proportional to $\exp[E_n/kT]$, showing that to achieve highly excited H_3^+ vibrational levels, harder collisions are required. The proton-hopping collision mechanism requires high temperatures of ~1500 K at the altitude of H_3^+ production. However, these temperature may be realistic for the $2\nu_2$ and $3\nu_2 - \nu_2$ levels, as shown by Melin et al. (2005).

Through comparison of spectra measured in the atmospheric windows K (Raynaud et al. 2004) and L (Stallard et al. 2002), Melin et al. (2005) showed that LTE is not a valid assumption over the whole altitude range of the ionosphere. They found that only a non-LTE model could produce the H_3^+ line intensities which matched the observations. Figure 2-6, reproduced from Tao et al. (2011), shows the altitude profile of the LTE fraction for different H_3^+ excited states. The LTE fraction, $\eta(z)$, is calculated using the following equation,

$$\eta(z) = \frac{n(H_3^+)_{\mathrm{nonLTE}}}{n(H_3^+)_{\mathrm{LTE}}} \qquad \textbf{2.11}$$

where $n(H_3^+)_{\mathrm{nonLTE}}$ is the population density including non-LTE effects and $N(H_3^+)_{\mathrm{LTE}}$ is the population density calculated under LTE conditions. From Figure 2-6 it can be seen that the LTE fraction decreases with altitude except for the ground state (dashed grey line), which becomes over populated relative to the other states. Departure from LTE is most significant between 1000 and 2000 km above the one bar level for all vibrational states, which is in agreement with the study by Melin et al. (2005). Below an altitude of 500 km, the model by Melin et al. (2005) found no noticeable departure from LTE distribution. Above this altitude, the first vibrational state ($\nu_2 \rightarrow 1$) starts to become under populated and by 800 km the departure from LTE is measureable in all vibrational manifolds.

The population of vibrational states of H_3^+ is determined by a balance between the collisional excitation and de-excitation, and the radiation transition which produces the IR radiation. At high altitudes, there is a reduction of the excited population from LTE due to the radiative de-excitation and a decrease in H_2 density. Where H_2 density decreases, collisional excitation will also decrease. If the radiative de-excitation occurs over a time scale which is faster than the collisional excitation rate then populations of certain vibrational excited states with higher A_{if} values will be lower than those in the LTE case. The under population of these levels causes a reduction in H_3^+ emission intensity, which was found to be significant at Jupiter by Melin et al. (2005). As temperature increases (i.e.: efficiency of IR emission increases) and/or the H_2 density decreases (i.e.: the collisional excitation rate decreases), the intensity reduces further because the non-LTE effect has become larger. By assuming LTE, it is possible that the temperature may be underestimated, as H_3^+ is mainly under populated at higher altitudes, where it is hotter (Melin et al. 2013).

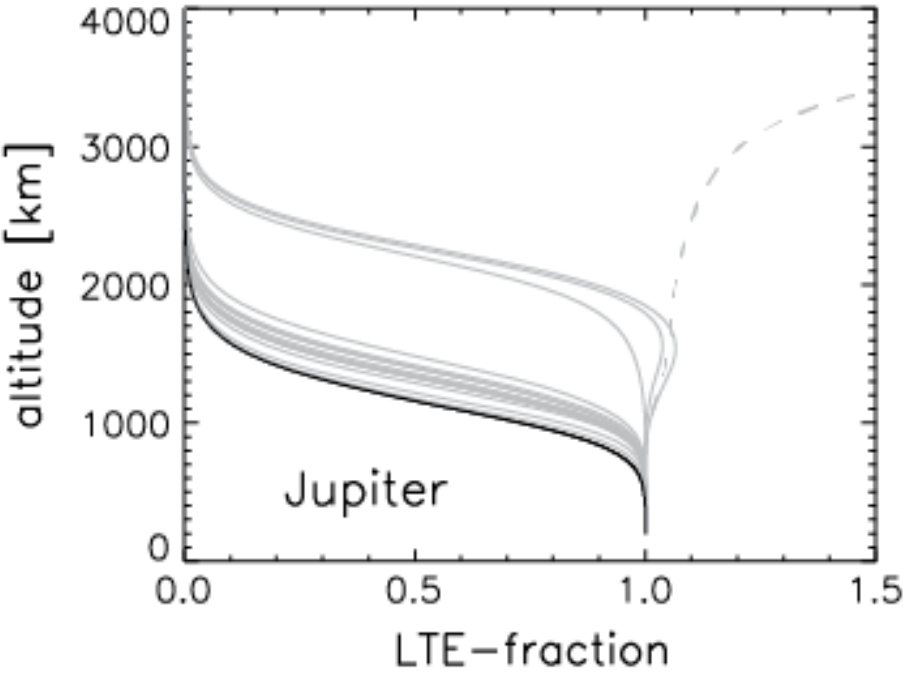

Figure 2-6: The altitude profile of the LTE-fraction of different vibrational states of H_3^+ in Jupiter's upper atmosphere (grey-lines), reproduced from Tao et al. (2011). The dashed grey line represents the ground state and the black line represents the v_2 vibrational states.

However, the fundamental $v_2 \rightarrow 0$ emission is the least effected by non-LTE effects. Figure 2-7, reproduced from Melin et al. (2005), shows the intensity of this line under LTE (solid line) and non-LTE (dashed line) conditions. It can be seen that these

two intensities do not vary significantly at the H_3^+ peak emission altitude (~550 km). Studies such as Stallard et al. (2002) use an assumption known as quasi-LTE (q-LTE) where it is acknowledged that some departures from LTE may exist but LTE is still a valid assumption for the calculations. Therefore, it is possible to use the q-LTE assumption to calculate the temperature from the line ratios and subsequently calculate the density, especially when deriving these properties from the fundamental emission lines.

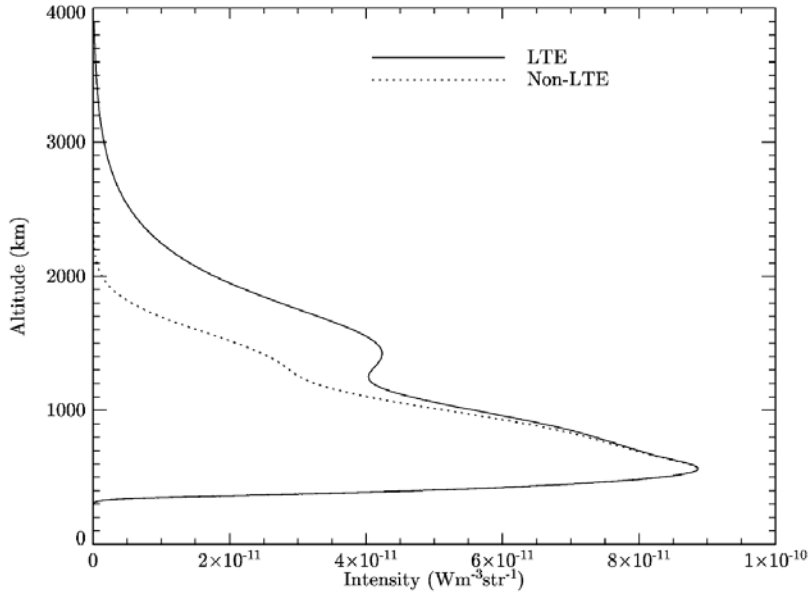

Figure 2-7: The emission altitude profile of the emission intensity of the fundamental H_3^+ $\nu_2 \rightarrow 0$ Q(1, 0^-) line, reproduced from Melin et al. (2005). The solid lines shows the intensity under LTE conditions and the dashed line shows the intensity accounting for the non-LTE effects.

Giles et al. (2016) detected H_3^+ lines in Jupiter's auroral regions in the 5 micron window and were the first study to measure all three temperatures simultaneously. They obtained a kinetic temperature of 1390 ± 160 K, a rotational temperature of 960 ± 40 K, and a vibrational temperature of 925 ± 25 K. These three temperature values are not in agreement with each other, suggesting a departure from LTE. Considering these studies, a fully rigorous study of the kinetic, rotational, and vibrational temperature of H_3^+ would perhaps not be able to use the assumption of q-LTE. The investigation in Chapter 6 is of the rotational temperature of H_3^+, derived from the ratio of intensities of the $\nu_2 \rightarrow 0$ Q(1, 0^-) and $\nu_2 \rightarrow 0$ Q(3, 0^-) H_3^+ emission lines. These are fundamental emission lines and are least affected by non-LTE effect (as outlined above), therefore, it is reasonable to assume q-LTE for this investigation. Assuming q-

LTE means that the temperatures derived are representative of the co-located ionospheric and thermospheric temperatures, and this assumption is used throughout this thesis.

2.2 Non-auroral Emissions

Jupiter's aurora extends to latitudes of ~50° in North and ~60° in the South, however, ionospheric emission also occurs equatorward of these latitudes. The sub-auroral emission of H_3^+ is defined as the diffuse region of emission directly adjacent to and surrounding the auroral regions, which gradually reduces in brightness as latitude decreases. Miller et al. (1997) postulated that this emission was caused by the transport of H_3^+ ions from the auroral regions. Since H_3^+ can have a relatively long lifetime, the H_3^+ produced in the auroral regions could be transported to lower latitudes by neutral winds. However, models such as JIM (Achilleos et al. 1998) have not shown neutral winds capable of transporting H_3^+ to the lower latitudes. Morioka et al. (2004) found that the region of sub-auroral emission varied in size with Jovian auroral activity. They discuss how the emission could be caused by precipitation from the inner magnetosphere, caused by pitch angle scattering through wave-particle interactions (Abel and Thorne, 2003). Studies such as Mauk et al. (2002) have demonstrated that the dynamics of the inner magnetosphere are correlated with auroral emissions. However, the origin of the sub-auroral emission still remains unclear.

Lam et al. (1997) is the only study to date to map the H_3^+ emission across all latitudes and longitudes using observations taken with the UKIRT CGS4 spectrometer. Over the course of the observation the planet rotated under the slit, covering all longitudes and latitudes. Lam et al. (1997) noted a gradual reduction in H_3^+ emission brightness from pole to equator. Studies by Rego et al. (2000), Morioka et al. (2004), and Stallard et al. (2012) also showed that the H_3^+ auroral emission gradually reduces to a minimum at the equator. However, using Cassini-VIMS observations of the nightside of Jupiter, Stallard et al. (2015) did not observe any significant non-auroral emission. At the Io magnetic footprint, the emission was ~1 mWm^{-2} μm^{-1} sr^{-1}, however by 40° latitude the intensity was ~0.25 mWm^{-2} μm^{-1} sr^{-1}, which dropped to zero by 30°

latitude. This suggests that all non-auroral H_3^+ is generated through the reaction that begins with ionization by solar EUV.

Outside of the auroral regions the H_3^+ emission is not uniform and some regions experience variations in H_3^+ brightness caused by localised temperature changes. Stallard et al. (2017) observed a dark region centred on 55° N and 300° W, which they called the Great Cold Spot (GCS) and is thought to be linked to thermospheric dynamics. O'Donoghue et al. (2016) observed enhanced H_3^+ brightness in a location above the Great Red Spot (GRS) and suggest that the heating in this region is caused by acoustic waves propagating up from the GRS below. These localised regions of heating and cooling are discussed further in Section 2.6.1.

Compared to the dramatic temporal and spatial variations in intensity in the auroral regions, the equatorial H_3^+ emission has very little variation. However, equatorial observations of the far ultraviolet (FUV) wavelengths have revealed a region of enhanced brightness at 60°-120° in System III in the equatorial region. Atomic hydrogen Lyman-α (H Ly-α) emission occurs at ~121.6 nm in the FUV. During early observations of Jupiter, two independent studies by Clarke et al. (1980) and Sandel et al. (1980), using data taken by Voyager 1 and 2, observed the enhanced brightness in the hydrogen Lyman-α emission, known as the H Ly-α bulge. Dessler et al. (1981) found that the bulge was fixed in System III but does not follow the jovigraphic equator and instead follows the magnetic drift equator. Clarke et al. (1991) observed evidence of broadening of the H Ly-α line profile for measurements taken at the location of the bulge. This may suggest that the bulge is produced by a broadening of the H Ly-α line profile rather than an increased H density. Emerich et al. (1996) suggested that the broadening may be due to turbulent flows.

On the dayside, Melin and Stallard (2016) found a correlation between bulge brightness and solar H Ly-α brightness, and Skinner et al. (1988) found that for the descending phase of the solar cycle 21 (1979 – 1986) the peak bulge brightness correlated with the solar H Ly-α flux. Both of these studies provide evidence that solar resonance scattering is the dominant mechanism creating the bulge on the dayside. McConnell et al. (1980) found the bulge was persistent on the nightside, where Melin and Stallard (2016) found that it was only ~6% of the dayside brightness. Modelling by McConnell et al. (1980) and Shemansky et al. (1985) showed that resonant scatter of

interplanetary or interstellar emission is not sufficient to explain the brightness of the bulge on the nightside. Melin and Stallard (2016) proposed that the H Ly-α emission in the bulge is being produced via the dissociative recombination of H_3^+. On the dayside, Lam et al. (1997) observed that H_3^+ is dimmer at the position of the bulge, therefore, where H_3^+ is lost, H is produced, leading to enhanced H Ly-α emission. Melin and Stallard (2016) did not unambiguously conclude that the bulge follows the magnetic drift equator; however, they still suggest that the bulge is associated with magnetospheric mechanisms. To create the bulge through dissociation electron recombination of H_3^+ requires an enhancement of flux of soft electrons. Melin and Stallard (2016) proposed that this is driven by **E** x **B** drift which vertically merges the dense layers of H_3^+ and electrons.

2.3 The Magnetosphere

Jupiter's magnetosphere is the largest planetary magnetosphere in the solar system, with an equatorial magnetic field strength of ~0.4 x 10^{-3} T. Jupiter has a 9.6° tilt between the magnetic dipole axis and the planetary rotation axis. Jupiter's volcanic moon, Io, is a powerful internal plasma source, which, combined with the strong magnetic field and fast rotation, creates a unique environment surrounding Jupiter. The majority of the magnetospheric dynamics are thought to be controlled by these parameters (e.g.: Khurana et al. 2004 and Clarke et al. 2004).

A rough estimation of magnetopause sub-solar standoff distance for Earth is given by equating the balance between the solar wind dynamic pressure and magnetic pressure of the terrestrial magnetosphere. However, this estimation is insufficient at Jupiter because the magnetosphere contains a substantial plasma source, which adds a significant contribution to the overall magnetospheric pressure. From various spacecraft flybys, Jupiter's magnetopause has been found to vary between ~45 and 100 R_J at the sub-solar point. The outer region of Jupiter's dayside magnetosphere is known as the cushion region as it can be easily compressed by changes in the solar wind conditions. For example, if the solar wind dynamic pressure increase by a factor of 10, the dayside magnetopause can move planetward by a factor of ~2 (Bagenal et al. 2014). The magnetic field lines in the magnetotail are extremely elongated by more than ~7000 R_J.

The Jovian magnetosphere is rotationally driven, which can be investigated by determining the stagnation point. The stagnation point occurs where the rotational flow opposes the flows controlled by the Dungey cycle (Section 1.1.4) that are imposed by the solar wind. Figure 2-8 shows the equipotential of stream line flows for Earth and Jupiter. At the Earth the stagnation point distance is less than the magnetopause distance and so the stagnation point lies within the Earth's magnetosphere. This means that close to the Earth there are corotational flows, however, the main flow is dominated by the solar wind coupling through the Dungey cycle (as discussed in Section 1.1.3). At Jupiter the stagnation point distance is much greater than the magnetopause distance and so this point would lie outside the magnetosphere. Therefore, the corotational flows dominate in Jupiter's magnetosphere. In reality there are limitations imposed on the corotational flow, which will be discussed in further detail in the following sections.

a) b)

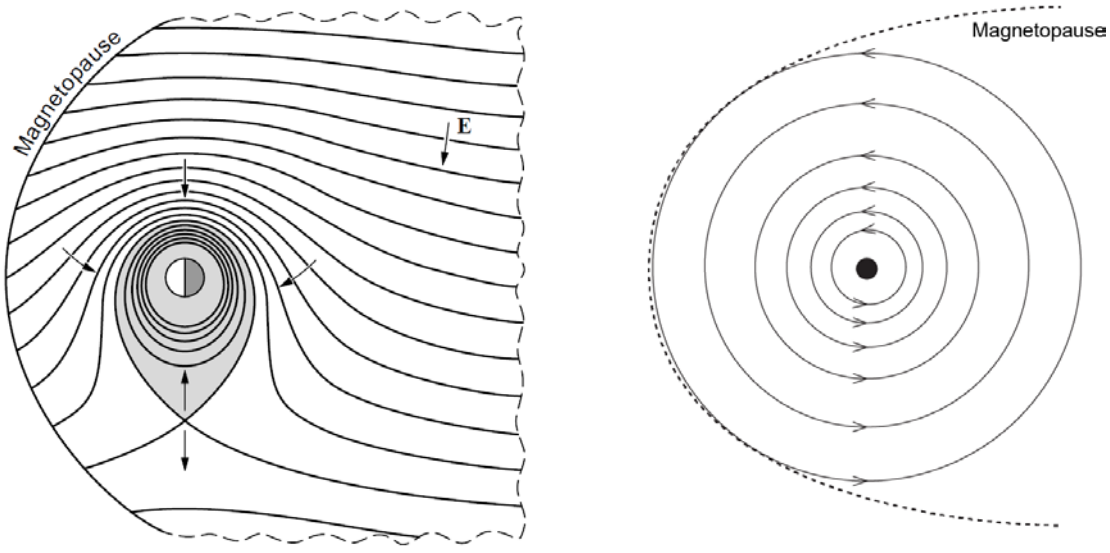

Figure 2-8: (a) A schematic of the electric equipotentials contours in the equatorial plane of the Earth's magnetosphere, reproduced from Baumjohnann and Treumann (1997), where the sun is to the left of the diagram. The direction of the E field is given by the arrows. Close to the planet the plasma is corotational; however, moving away from the planet the stagnation point can be seen in the dusk sector of the magnetosphere. (b) At Jupiter the stagnation point lies outside of the magnetosphere, and so this schematic shows that corotational flow dominates in Jupiter's magnetosphere. Again the sun is to the left of the diagram. Image credit: S. Milan.

2.3.1 Inner Magnetosphere

The inner magnetosphere is often defined as the region planetward of ~10R_J, where plasma production takes place. The magnetic field in the inner magnetosphere can be approximated as a dipole due to the corotation of the plasma within this region. Jupiter's radiation belts are located ~1.2-1.7 R_J and are a powerful source of pulsed radiation. The energetic electrons, trapped in the radiation belts have energies of ~1-30 MeV and emit Bremsstrahlung radiation (Santos-Costa et al. 2014).

Jupiter's ionosphere, the solar wind, and the surface and atmosphere of the moons all contribute to the plasma production in Jupiter's magnetosphere. The ionosphere and solar wind contribute a few tens of kg s^{-1} (Hill et al. 1983). The icy moon Europa, at ~9.4 R_J is a minor source of neutral oxygen, contributing ~50 kg s^{-1} of ions (Ip et al. 1998). However, Io is the dominant mass production plasma source, producing ~1000-3000 kg s^{-1} of plasma in the Io torus, which originates from the moon's volcanic activity (Broadfoot et al. 1981; Brown 1994; Bagenal et al. 1997; Delamere and Bagenal 2003). The sulphur and oxygen neutrals from Io form a torus along Io's orbit, which has a keplerian velocity of ~17 km s^{-1} (Schreier et al. 1998). Khurana et al. (2004) found that the bulk velocity of the plasma in the Io torus to be ~75 km s^{-1}, which is a value close to corotation. Torque sourced from Jupiter's deep interior is transferred through ion-neutral collisions to the magnetic field which is frozen-in to the plasma in the inner magnetosphere. Therefore, once the neutrals in the Io torus are ionised through electron impacts, they are then influenced by electromagnetic forces and are accelerated up to corotation, as well as beginning to gyrate around the magnetic field lines.

2.3.2 Middle Magnetosphere

After the neutrals in the Io torus are ionised, the flux tubes which thread the torus become mass loaded. These flux tubes become centrifugally unstable, diffuse radially outwards and are replaced by mass depleted flux tubes in a process known as flux interchange. Plasma is thought to be removed from the magnetosphere through the pinching off of plasmoids in the outer magnetosphere, discussed in greater detail in Section 2.3.3. The mass depleted field lines then move back inwards causing compression and heating, which was observed by Voyager (Mauk et al. 1996), Ulysses

(Lanzerotti et al. 1993), and Galileo (Mauk et al. 1999). This creates a low density hot population of plasma, which contributes significantly to the overall magnetosphere plasma pressure (Caudal 1986). The centrifugal forces from the planet's rapid rotation confine the plasma populations in the middle magnetosphere to the equatorial plane; however, the plasma pressure resists this compression, keeping the plasma sheet at a width of ~5 R_J. Since Jupiter has a 9.6° tilt between the magnetic dipole axis and the planetary rotation axis, the plasma sheet wobbles up and down with respect to the jovigraphic equator as Jupiter rotates.

As the iogenic plasma diffuses radially outward from the planet, its angular velocity falls below that of the planet, in order to conserve angular momentum. Since the magnetic field is frozen into the plasma, the magnetic field lines also begin to slow. However, these field lines close in the ionosphere, where there are collisions between ions and neutrals. These collisions work towards spinning the field and plasma back up to corotation. Angular momentum from Jupiter's deep interior is transferred through the atmosphere, via the ionosphere, to the magnetosphere through a field aligned current system (Hill, 1979). Figure 2-9 illustrates the ionosphere-magnetosphere coupling circuit: the circuit flows out of the ionosphere as a field aligned current, then flows radially out away from the planet in the plasma sheet, returning back to the ionosphere at higher latitudes along the magnetic field lines and finally closes in the ionosphere through equatorward Pedersen currents.

The radially outward-directed currents, which are flowing through the plasma sheet, are sufficient to accelerate the plasma back towards corotation through the **J** x **B** force. If this torque was not being provided by these so called corotational reinforcement currents, then the angular momentum would fall off with the usual inverse square law relation. However the radial currents can only sustain near-rigid corotation until an equatorial radial distance of ~10 R_J. After this point corotation breakdown occurs and the ionosphere can no longer provide sufficient angular moment to keep equatorial plasma at near rigid corotation. It is at ~20 R_J that the main auroral emission is thought to map to, with the upward field aligned current generating this aurora (Cowley and Bunce 2001; Hill 2001).

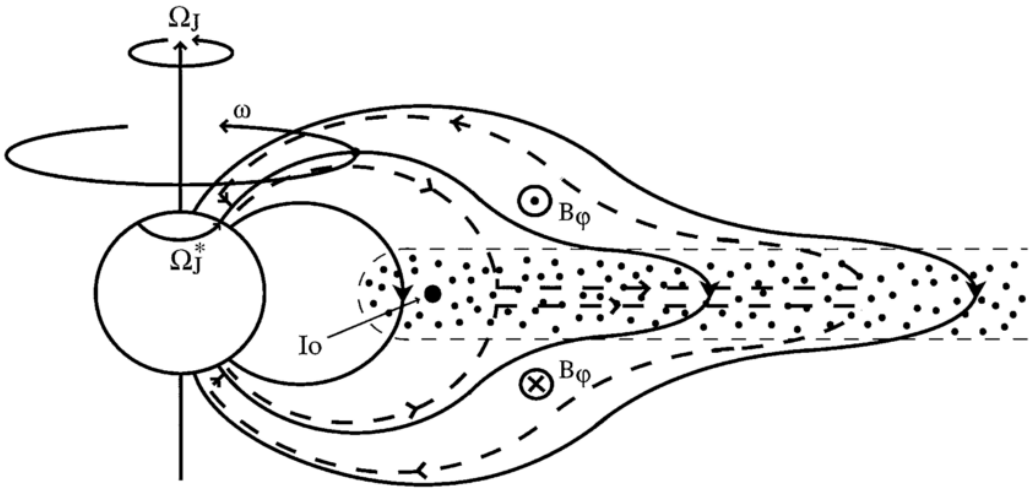

Figure 2-9: A sketch of Jupiter's magnetosphere in the meridian plane. Solid arrows represent field lines. Dashed arrows represent the ionosphere-magnetosphere coupling circuit. The dotted region represents the the Io torus and plasma sheet. There are three angular velocites shown in the sketch: the angular velocity of the planet Ω_J, the angular velocity of a particular shell of field lines ω, and the angular velocity of the neutral upper atomsphere in the Pedersen conducting layer Ω_J*. It is expected that Ω_J* will lie between ω and Ω_J. In the case of sub-corotation $\omega \leq \Omega_J$. Reproduced from Cowley and Bunce (2001).

In-situ measurements of the angular velocity of the magnetospheric plasma were taken with spacecraft during flybys through Jupiter's magnetosphere. From the pre-noon inbound passes of Voyager 1 and 2, the middle magnetosphere was found to have a ratio of angular velocity of the plasma to Jupiter's deep interior angular velocity of ~0.8 at 10-20 R_J and ~0.5 at 40 R_J (Belcher 1983; Sands and McNutt 1988). By modelling Galileo data, Bagenal et al. (2016) showed that within ~5-20 R_J the plasma flow is dominated by azimuthal flow at 80-100% of corotation. Their study showed that the plasma flow is slightly more corotational in the dawn-side magnetosphere than the dusk, this dawn-dusk asymmetry has previously been reported by Krupp et al. (2001) and Woch et al. (2002).

The lagging configuration can be seen in Figure 2-10, where the low latitude mapping field lines are bent back out of the meridian. The slowing field line imposes a change in angular velocity in this region of the ionosphere, causing this region to sub-rotate. As this occurs at high latitudes, here the magnetic field lines can be approximated as normal to the planetary surface and the angular velocity can be approximated to be azimuthal, hence the resulting electric field is equatorward. Assuming a constant Pedersen conductivity, the variation in the electric field causes a variation in current. As there is a meridional change, the electrons travel azimuthally or

vertically due to Kirchoff's law. The system is axisymmetric to first approximation; hence the electrons must travel up the field lines creating an upward field aligned current, which creates the main auroral emission.

However, there is a limit to the upward current density which can be carried by unaccelerated precipitating hot magnetospheric electrons, beyond which downward acceleration by upward-directed field-aligned electric fields is required, as described by the kinetic theory of Knight (1973). Estimates for Jupiter's corotation enforcement currents suggest current densities peaking at values more than an order of magnitude larger than the limiting value, such that the magnetospheric electrons must be accelerated downwards to energies of ~100 keV, thereby producing the bright emissions of the main auroral oval (e.g., Cowley et al. 2008).

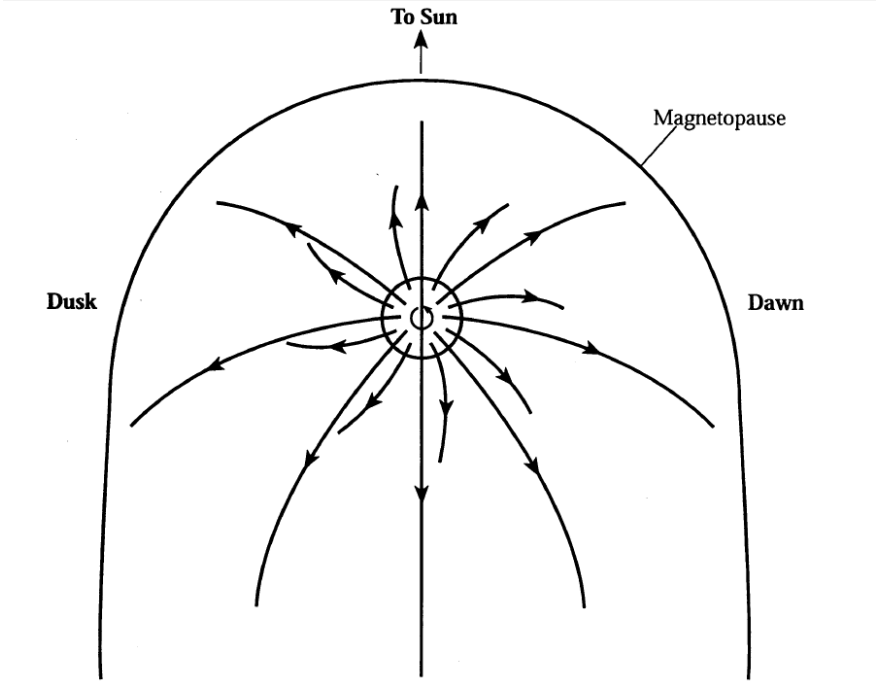

Figure 2-10: A sketch of Jovian field lines in the equatorial plane replicated from Cowley and Bunce (2001). The lower-latitude field lines, mapping to the middle magnetosphere, are bent out of the magnetic meridians into a lagging configuration due to a magnetosphere-ionosphere coupling circuit. The higher-latitude field lines, mapping to the outer magnetosphere are bent away from noon by the interaction with the solar wind.

2.3.3 Outer Magnetosphere

In the outer magnetosphere the plasma and magnetic field lines are significantly sub-rotational. On the dayside, the magnetosphere is confined by the solar wind, but on the nightside the magnetotail is extremely extended by several thousand R_J down tail. The magnetotail is cylindrical with a diameter of 300-400 R_J and has two lobes

separated by a thin current sheet, only a few R_J thick. Since the current sheet has become very thin, mass loss can take place via the release of plasmoids. Figure 2-11 shows the plasmoid mechanism suggested by Vasyliunas (1983), where plasmoids may escape down the magnetotail. This process begins at ~60-80 R_J and the release of plasmoids has a periodicity of ~2-3 days (e.g.: Woch et al. 1998). As the magnetic field lines rotate round the dusk sector they are radially extended as they are no longer constricted by the solar wind pressure. The magnetic field lines extend downstream and reconnect where they are oppositely orientated and in close proximity, ejecting plasmoids down the magnetotail. The newly reconnected field lines then rotate around the dawn sector to begin the process again. This is known as the Vasyliunas cycle.

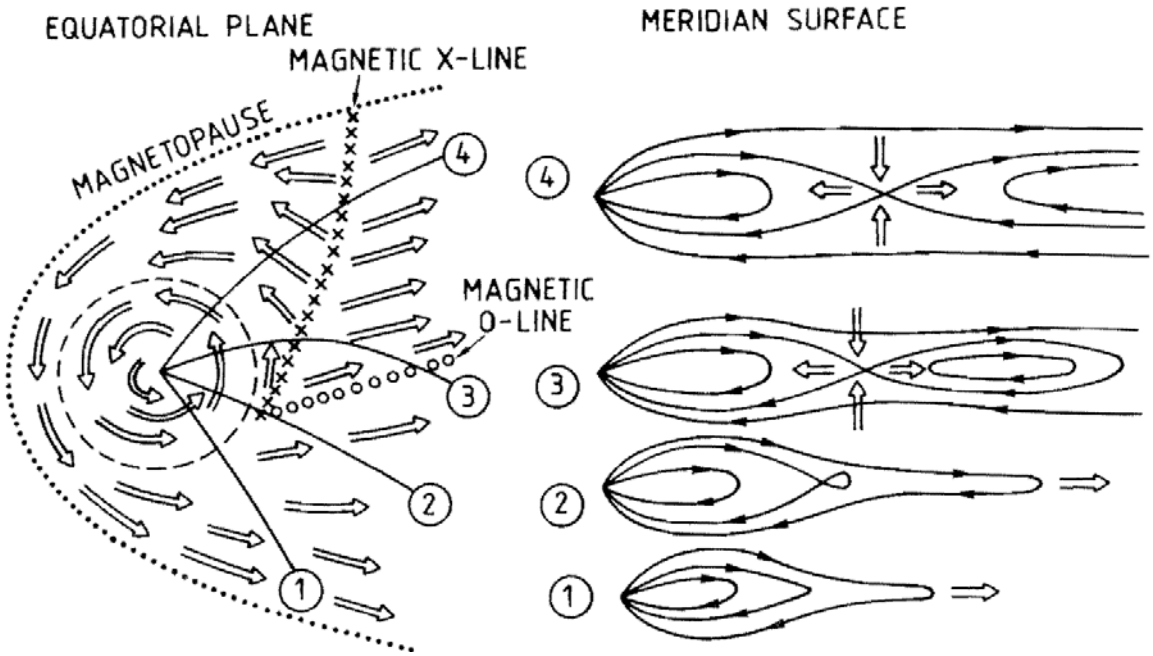

Figure 2-11: A sketch of flows in the Jovian equatorial plane (left) and meridian surface (right) showing the plasmoid mechanism proposed by Vasyliunas (1983). Dotted line represents the magnetopause. Arrows represent plasma flows. Dashed line presents the boundary between rigidly corotating and sub-corotating flows. Bold lines represent Jupiter's magnetic field lines.

Figure 2-10 shows that there is an influence of solar wind on the magnetosphere as the field lines bend away from noon on the dayside and beyond 60 R_J the plasma sheet is parallel to the flow of the solar wind. Cowley et al. (2003) suggested that part of the outer magnetosphere is coupled to a Dungey cycle process, confined to the dawn sector by the Vasyliunas cycle, as shown in Figure 2-12. Magnetic flux is opened

on the dayside through reconnection with the IMF, transported across the pole to close in the magnetotail, and finally returned in the restricted dawn region. Cowley et al. (2003) based their arguments for an open magnetosphere on plasma angular measurements from Ulysses observations (Cowley et al. 1996) and the ionospheric flow measurements from Stallard et al. (2001; 2003).

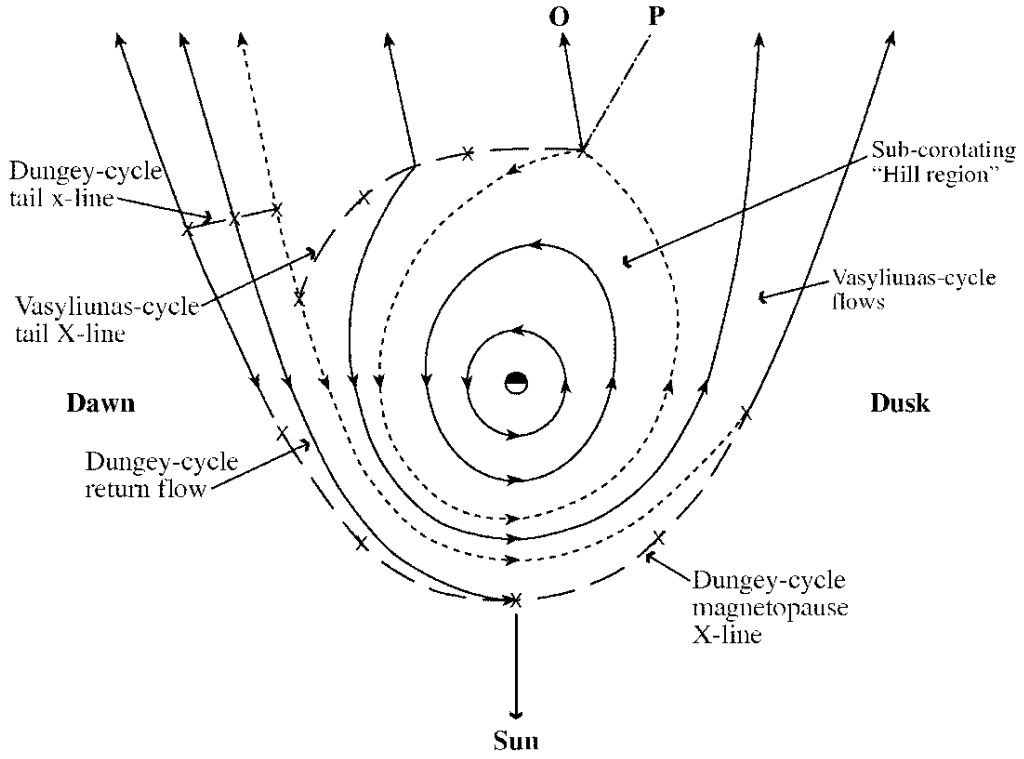

Figure 2-12: A sketch of the flows in Jupiter's magnetosphere in the equatorial plane reproduced from Cowley et al. (2003). Plasma flow lines are represented by bold and dashed arrows. Reconnection lines are represented by long dashed lines.

However, McComas and Bagenal (2007) suggested that due to the vast scale of the jovian magnetosphere, the time scales involved in a Dungey-style global cycle of reconnection are improbable. Instead, they proposed that flux is opened on the dayside and then closed through dual lobe reconnection, which leaves Jupiter's magnetosphere mainly closed. However, Cowley et al. (2008) refuted this as they argued that unless the reconnection rate in both lobes was equal, the mechanisms put forward by McComas and Bagenal (2007) would not hold true, and the magnetosphere would not stay mainly closed. The debate continued, with McComas and Bagenal (2008) stating that their new concept is consistent with observations by New Horizons (McComas et al. 2007), which implied that the magnetotail is largely filled with detached blobs of iogenic plasma. Ultimately, McComas and Bagenal (2008) called for

more measurements of Jupiter's ionosphere and magnetosphere to further investigate these issues.

Delamere and Bagenal (2010) proposed that the outer magnetosphere was connected intermittently to the IMF through viscous interaction along the dawn flank of the magnetopause. They based their model on Axford and Hines (1961) and described how Kelvin-Helmholtz instabilities moderate the viscous interaction of the magnetopause and IMF. They postulated that the ionospheric wind measurements of Stallard et al. (2001; 2003) are explainable in a regime of a closed magnetosphere, where the stationary velocities of the H_3^+ ions could be associated with the solar-wind driven viscous drag. These ionospheric flows will be discussed further in Section 2.5.

2.4 The Aurora

Jupiter's aurora is the most powerful in the solar system and is hundreds of times more energetic than the Earth's aurora, and over 10 times brighter. Jupiter's aurora has been observed at radio, IR, visible, UV and X-ray wavelengths, using both ground based and space based telescopes as well as spacecraft visiting Jupiter (see review by Bhardwaj and Gladstone 2000). The fact that Jupiter's aurora produces emission at many different wavelengths implies that there is a variety of mechanisms driving the Jovian aurora. In this thesis I study the IR aurora of Jupiter using observation of the H_3^+ emission at a wavelength of ~ 4 μm.

Jupiter's UV aurora was first observed by Broadfoot et al. (1979) using data taken by Voyager 1 during its 1979 flyby. Since then it has been observed by Galileo (e.g.: Mauk et al. 2002), Cassini (e.g.: Pryor et al. 2005), the Hubble space Telescope (e.g.: Nichols et al. 2009), Hisaki (e.g.: Kimura et al. 2015) and Juno (e.g.: Bonfond et al. 2017), and an overview of the UV aurora is given by Grodent (2015). Jupiter's UV aurora is generated by inelastic collision between atomic or molecular hydrogen and energetic electrons which precipitate down the magnetic field lines into the auroral regions and excite the hydrogen. When the hydrogen de-excites to the ground-state, UV photons are emitted predominantly from H Lyman-α and H_2 Lyman and Werner bands.

Jupiter's UV emission is relatively instantaneous compared to H_3^+ emission, which can last over longer time scales (as discussed in Section 2.1.1). Variation within

timescales of ~100 s cannot be distinguished in H_3^+ emission because this is comparable to the lifetime of H_3^+ (Stallard et al. 2016). H_3^+ is subject to transport during its lifetime; therefore it creates a diffuse view of precipitation, which is a life time average map of the particle precipitation morphology whereas H_2 emission is an instantaneous view of the injected energy.

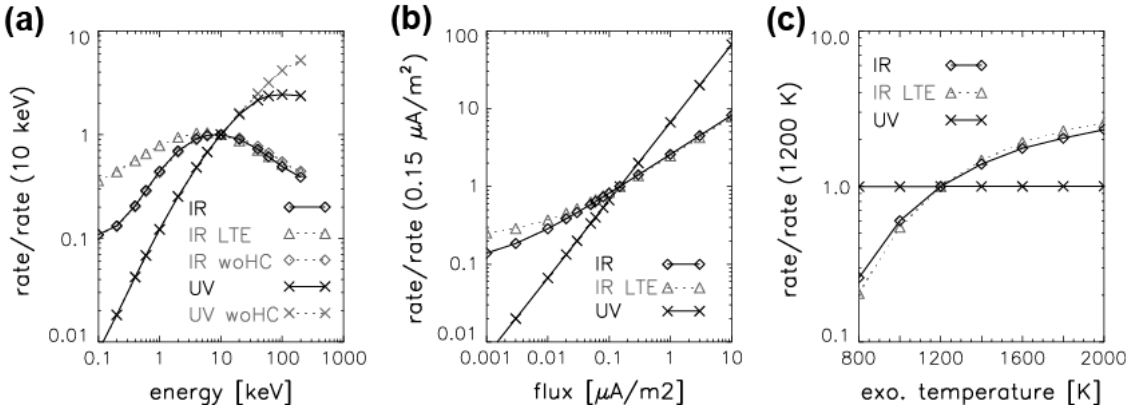

Figure 2-13: IR and UV emission rates versus (a) the energy, (b) number flux of the precipitating electrons, and (c) exospheric temperature, reproduced from Tao et al. (2011). For the IR emission rates, the non-LTE and LETC cases are shown by the black diamonds and grey triangle respectively. The IR emission rates excluding the hydrocarbons are shown by the grey diamonds. The UV emission rates are shown by the black crosses and the UV emission rates excluding the hydrocarbons are shown by the grey crosses.

As discussed in Section 2.1.1, the model created by Tao et al. (2011) shows that the peak altitude of the maximum emission becomes lower as the energy of the incident electron increases, at both UV and IR wavelengths. Figure 2-13a, reproduced from Tao et al. (2011), shows the IR and UV dependence of the emission rates on energy of the precipitating electron. The UV emission rate increases with incident electron energy, however, the IR emission rate increases more slowly in the electron energy range 0.5-10 KeV and decreases for electron energy above ~ 20 KeV. This is because electrons with energies above 20 KeV can penetrate to low altitudes where IR excitation efficiency is low due to the lower temperatures at lower altitudes, as shown by Figure 2-13c. The grey triangles show the emission accounting for the non-LTE effects of H_3^+. Figure 2-13a shows that for low energy electrons the non-LTE effect reduces the H_3^+ emission rate by about 10%. When hydrocarbons are taken into account, at high energies, the emission rates for UV and IR are reduced. This is due to hydrocarbon absorption of the UV emission at low altitudes and losses of H_3^+ through dissociative recombination with hydrocarbons. Figure 2-13b shows the emission rate

dependence on the precipitating electron flux. Tao et al. (2011) conclude that the UV emission rate is proportional to the electron flux, whereas the H_3^+ intensity is proportional to the square root of the incident electron flux due to the time-scale in the ion chemistry.

In general, when observed in the UV or IR, Jupiter's aurora consists of at least three distinct regions of emission which are labelled in Figure 2-14.

1. The main auroral emission which forms an irregular oval surrounding the magnetic pole.
2. The polar aurora, consisting of all auroras poleward of the main auroral emission including the dark, swirl and active regions. This region is highly variable and dynamic over short time scales.
3. The auroral signatures of the Galilean moons, equatorward of the main auroral emission, which create spots and trailing arcs about the magnetic footprints of the moons.

The following sections will give an overview of the aurora at Jupiter, for greater detail please refer to Clarke et al. (2004).

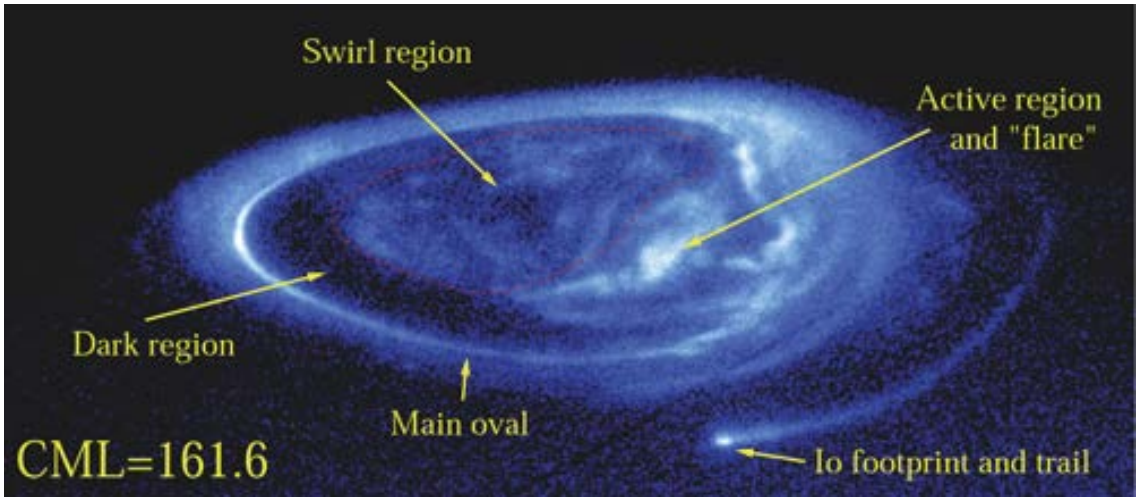

Figure 2-14: Raw image taken on 14 December 2000 by the Space Telescope Imaging Spectrograph on the Hubble Space Telescope, reproduced from Grodent et al. (2003). The image was taken of the northern aurora when the central meridian line (CML) was 161.6°. The recurrent auroral features are labelled: the main auroral emission (or main oval), the Io footprint and trail, and the polar aurora (dark, swirl and active regions).

2.4.1 Satellite Footprint Aurora

Through interactions with Jupiter's magnetosphere the Galilean moons Io, Ganymede and Europa created footprint aurora in Jupiter's ionosphere. When observed in the UV, the footprints of the Galilean moons all appear equatorward of the main auroral emission except Calisto's footprint, which has not yet been detected due its proximity to the main auroral emission. The Io auroral footprint was first discovered in the IR by Connerney et al. (1993), and has proved very useful as a constraint for modelling the Jovian magnetic field. Using the locations of the ionospheric footprint of the field lines which map from Io's orbital radial distance, information on the magnetic field in a region of the magnetosphere close to the planet, which until Juno arrived at Jupiter, had not been sampled before. The auroral footprint in can present as multiple spots and has a trailing arc which maps to the orbit of Io (Bonfond 2012). The Io footprint aurora is created through interactions between the magnetospheric plasma and Io via Alfvén waves (reviewed by Kivelson et al. 2004).

2.4.2 Main Auroral emission

The northern magnetic pole is tilted further towards the equator than in the south, allowing the northern aurora to be observed more easily from Earth. Therefore, many studies, like this thesis, focus on the northern aurora. The bulk of the morphology of the main auroral emission is fixed in System III longitude (Grodent et al. 2003). Although the main emission in the southern hemisphere is oval in shape (Figure 2-15), the main emission in the northern hemisphere creates a kidney shape, which is believed to be due to a magnetic anomaly (Grodent et al. 2008). The main emission of the northern aurora is narrow and defined on the dawn side, when observed on the dayside. On the dusk side, the main emission is broad and diffuse, exhibiting narrow arcs, discontinuities and diffuse patches of emission, which can be seen in Figure 2-14. The typical width of the main auroral emission is ~1500 km (~1°) in latitude however this does vary.

The location of the UV and IR main auroral emissions have been found in approximately the same positions by studies such as Clarke et al. (2004) and Radioti et al. (2013). Extreme brightening of the UV aurora can occur, fixed in local time near dawn and known as Dawn Storms (Gustin et al. 2006). The Dawn Storms happen over a

time scale of about an hour, which could suggest association with the solar wind however no mechanism has been put forward. These dawn storms have not been observed in the IR aurora to date.

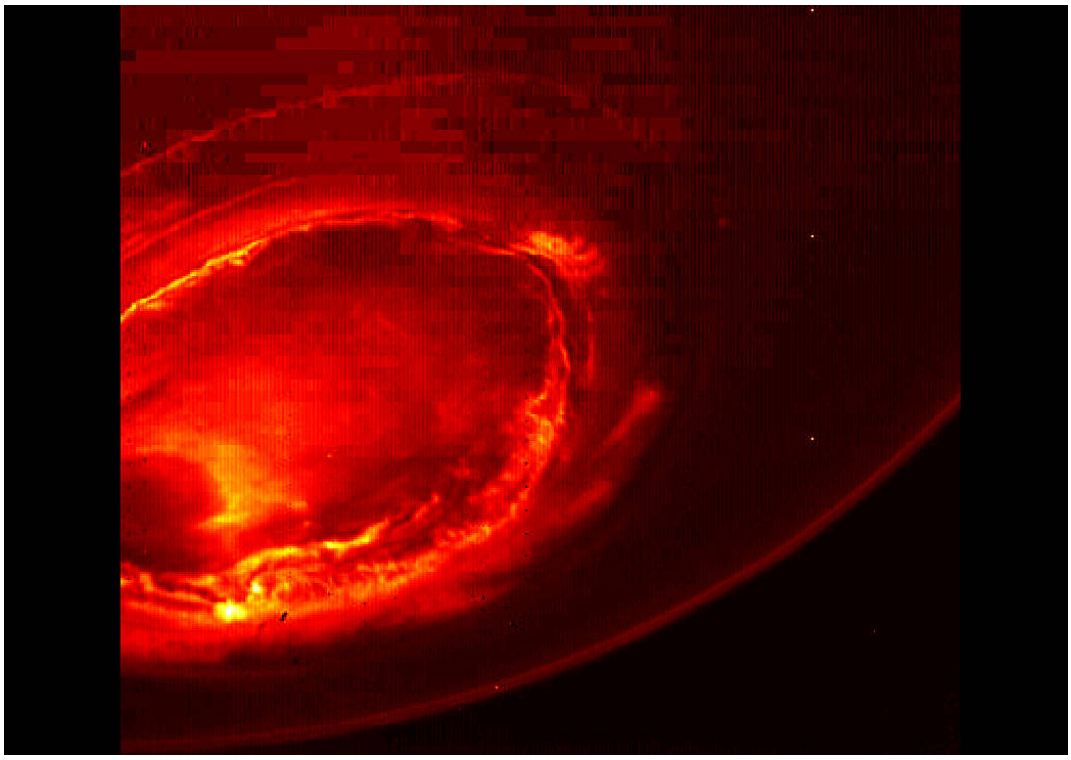

Figure 2-15: Jupiter's southern aurora as observed by Juno-JIRAM during perijove 1. Image credit: NASA/JPL-Caltech/SwRI/ASI/INAF/JIRAM.

The origin of the main emission has been linked to the magnetosphere-ionosphere coupling by a number of studies (e.g.: Cowley and Bunce 2001; Southwood and Kivelson 2001), as discussed in Section 2.3.2. Recent in-situ observations taken by Juno have further begun to explore the origins of Jupiter's main auroral emission. Using the Jupiter Energetic Particle Detector Instrument (JEDI, Mauk et al. 2017a), the acceleration process of the electrons which generate the main emission have been investigated. It was thought that discrete auroral processes would be observed at Jupiter due to the powerful nature of the planet's aurora. Mauk et al. (2017b) describe how the 'inverted V' signatures in the electron energy, which implies discrete acceleration processes (analogous to the terrestrial system), were detected, however, they were embedded in other ongoing stochastic processes. They conclude that it is possible that Jupiter's aurora is generated by discrete broadening through stochastic processes leading to a complicated acceleration process.

2.4.3 Polar Aurora

The aurora poleward of the main aurora emission consists of diffuse emission. This aurora consists of a variety of structures including multiple arcs and broad diffuse emission, and experiences strong local time effects. The UV polar aurora is usually grouped into three broad regions: the swirl, active, and dark regions (Grodent et al. 2003). Prangé et al. (1998) observed transpolar emission and Pallier and Prangé (2001) additionally observed arcs in the northern auroral regions, however, no arcs were observed in the southern polar aurora, only diffuse emission around noon. When observed over short time scales, the morphology of the UV polar aurora is usually more complex than three simple and distinct regions. However, over moderate time scales, Stallard et al. (2016) showed that the morphology of the UV aurora was similar to the IR aurora.

The origin of Jupiter's polar aurora is not clear. Gustin et al. (2004) showed that there is no clear correlation between the energy flux and the energy of the precipitating electrons in the polar aurora, suggesting that the mechanisms here involve different processes to those which generate the main auroral emission. Spectral observations of the northern and southern X-ray aurora have shown that the precipitating particles of highly charged oxygen, sulphur and/or carbon relate to downward current regions (Bunce et al. 2004; Cravens et al. 2003). Using a model by Vogt et al. (2011), the northern and southern X-ray auroral spots were mapped to regions in the magnetosphere beyond 60 R_J (Dunn et al. 2017). Both open and closed field lines have been theorised to understand this region of emission.

Auroral signatures linking the polar aurora to the magnetotail have been observed by Grodent et al. (2003; 2004) and Radioti et al. (2008; 2010; 2011). These studies have suggested that small bursts of polar emission on the dusk and nightside are associated with plasmoids disconnecting from the plasma sheet and moving down tail. There is some auroral evidence of a connection to the solar wind observed in Jupiter's polar aurora. Pallier and Prangé (2001; 2004) found an arc of aurora surrounding a dark region, which they suggested could be the open closed field line boundary at Jupiter. They, and other studies (e.g.: Waite et al. 2001 and Bonfond et al. 2011), have observed bright spot around noon, that could potentially be an auroral signature of the cusp. Coincident with the bright spots in the UV is a X-ray hot spot,

which is also been suggested to be a signature of Jupiter's northern cusp (Elsner et al. 2005; Branduardi-Raymont et al. 2008; Dunn et al. 2016). Even if this region is not a cusp analogous to the terrestrial system, the coincidence of bright spots in UV and X-ray, as well as stratospheric hot spot mid-infrared (Flasar et al. 2004) suggests that pulses of precipitation of high-energy ions are persistent in this region.

2.4.4 Influences of the Solar Wind on the Jovian Aurora

Theoretical and numerical models have suggested that the solar wind dynamic pressure and auroral brightness should be anti-correlated (e.g.: Southwood and Kivelson 2001; Cowley et al. 2007; Yates et al. 2014). When the magnetosphere contracts, due to a solar wind pressure increase, the magnetic field lines will move inwards and their angular velocity will increase due to the conservation of momentum. This has the effect of weakening the corotating reinforcement currents and hence weakening the aurora.

However, a number of observations of Jupiter's aurora have shown that auroral brightness is positively correlated to solar wind dynamic pressure. This was first shown using ground based IR observations of H_3^+ and solar wind properties measured by Ulysses (Baron et al. 1996). A positive correlation was also seen at the UV wavelength by Waite et al. (2000), Nichols et al. (2007; 2009) and Clarke et al. (2009). Kita et al. (2016) used the 1D MHD model by Tao et al. (2005) to show a statistical relation between total power and solar wind dynamic pressure, in a long-term Hisaki/EXCEED study. Nichols et al. (2017) took advantage of Juno's close proximity to the planet in order to measure the solar wind properties near to the planet while HST was observing the aurora. They observed the aurora through the arrival of rarefactions and compressions, which revealed that Jupiter's auroral response is much more complex than previously though.

Using a model by Vogt et al. (2011) showed that the swirl region contains flux tubes which are mapping to the solar wind. At Earth, it takes several minutes to propagate from the bowshock to the planet, but it has been estimated that this would take hours at Jupiter. These timescales do not match the rapid variation observed in the polar aurora by Nichols et al. (2017) using HST-STIS, however, the exact mapping in

the polar regions of Jupiter's aurora remain uncertain, and it could be the case that the swirl region does not contain open field lines.

Increases in Io's volcanic acitivity have also been shown to produce a positive correlation with Jupiter's auroral brightness (Yoneda et al. 2010; Bonfond et al. 2012). Some studies have begun to disentangle the internal effects on the aurora from Io and the influence of the solar wind. Kimura et al. (2015) showed that a sudden brightening of the aurora during a significant rarefaction in the solar wind, which they attribute to a change in particle precipitation provided by the output of Io's volcanoes. Moore et al. (2017) also measured a brightening of the aurora during a period where the solar wind was quiescent, suggesting that the brightening was caused by internal magentospheric processes.

2.5 Ionospheric Flows

In this section I will outline the ionospheric flows in both the auroral and non-auroral regions, including the flows derived from observations as well as global circulation models. Several reference frames are used in the existing literature and in this thesis to study the ionospheric flows. The first is the planetary reference frame, which was used by studies such as Stallard et al. (2001) and Chaufray et al. (2011). This reference frame is fixed in System III, helping us to understand the atmospheric drivers of the ionospheric flows. The second reference frame is the magnetic pole reference frame, which was used by Stallard et al. (2003). In this reference frame the magnetic pole of Jupiter is set to zero, helping us to understand the magnetospheric drivers of the ionospheric flows. The magnetic pole reference frame has been modified slightly hereto use the auroral centre defined by Grodent et al. (2008) rather than using the dipole from Connerney et al. (1998) as this was not appropriate for the study in this thesis. Further details are given about the reference frames in Section 3.5.2, which outlines how the line-of-sight (LOS) velocity of the H_3^+ ions is derived.

2.5.1 Mid-to-Low Latitude Ionospheric Flows

As discussed in Section 2.2, Clarke et al. (1991) and Emerich et al. (1996) suggested that the Doppler broadening of the H Ly-α bulge spectra was caused by turbulent flows. Sommeria et al. (1995) created a global model which attempted to model the circulation needed to create the turbulence at the location of the H Ly-α bulge. Figure

2-16 shows a schematic of the flows, adapted from Sommeria et al. (1995), where the red bold and dashed arrows represent the flow pattern and are overlaid on a map of H Ly-α brightness measured by Voyager 1. The model initiates in the polar regions at 20 km s^{-1} at ~1000 km above the 1 bar level. This velocity is significantly larger than the measured velocity in the auroral regions of ~ 4 – 8 km s^{-1} at ~1500 km above the 1 bar level by Chaufray et al. (2010) from HST-STIS observations of H Ly-α emission. The modelled flows suggest that these two jets travel equatorward from the auroral regions, and collide in the equatorial region at the location of the bulge. This generates the turbulence that causes the observed broadening of the H Ly-α line profiles at the location of the bulge (Emerich et al. 1996). It can be seen from Figure 2-16 that eastward and westward jets are produced after the auroral jets collide at the position of the bulge, with initial velocities of 9.3 km s^{-1} and 7.9 km s^{-1} respectively.

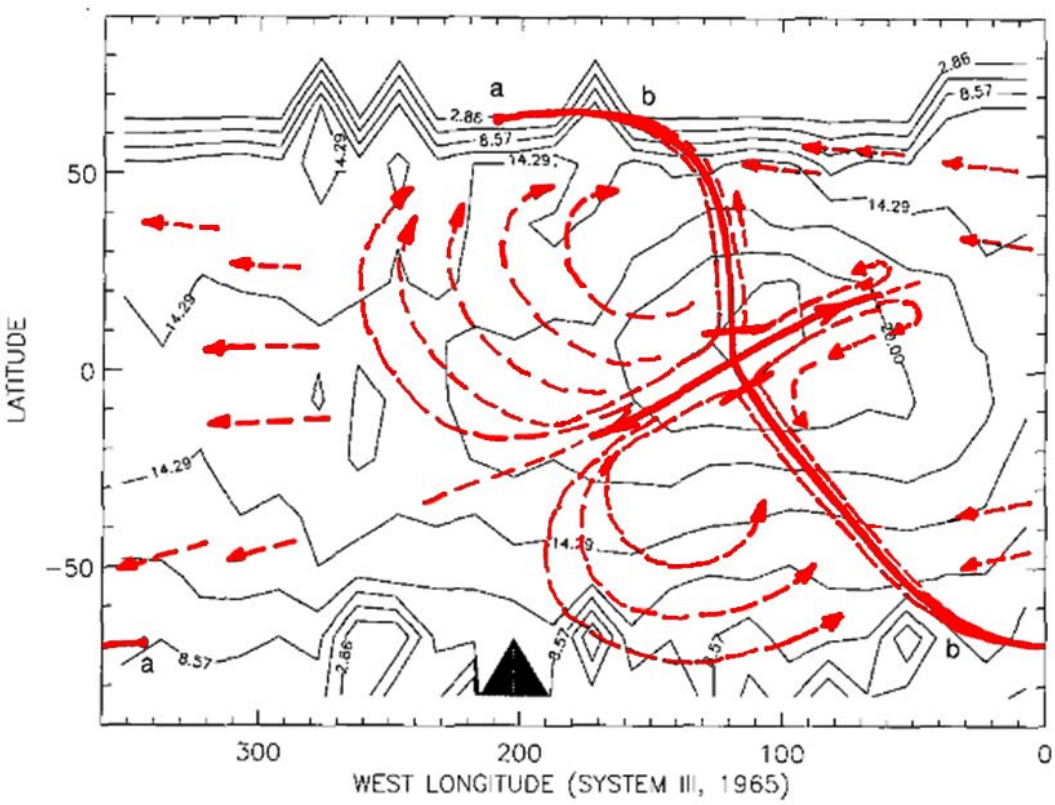

Figure 2-16: A schematic showing the circulatory pattern suggested by the model of Sommeria et al. (1995), adapted from Sommeria et al. (1995). The red bold and dashed arrows represents the H Ly-α winds and are overlaid on a map of H Lyman-α brightness measured by Voyager 1.

Measurements of the neutral velocity are very limited. The only two measurements of neutral winds were taken in the auroral region by Chaufray et al.

(2010; 2011). Using observations of the H Ly-α line profile taken with HST-STIS of the northern auroral region, Chaufray et al. (2010) calculated a velocity of ~4-8 km s^{-1} at ~1500 km. Through IR observations using the Fourier Transform Spectrometer (FTS/BEAR) instrument at the Canada-France Hawaii Telescope (CFHT), Chaufray et al. (2011) derived an upper limit on the LOS velocity of <1.0 km s^{-1} for the H_2, at altitude ~560-690 km above the one bar level (Uno et al. 2014). However, the velocity of the neutral winds remains unknown at lower latitudes.

Majeed et al. (2016) showed that neutral flows are easily produced by ionospheric flows, and it could be the case that neutral winds can drive ion flows. This could present an issue as auroral models (e.g.: Cowley and Bunce 2001) require the mid-to-low latitude ionosphere to be corotating. Before the work published in this thesis, which is discussed in Chapter 4, no literature had reported on the H_3^+ LOS velocities in the mid-to-low latitude region of Jupiter's ionosphere.

2.5.2 Auroral Ionospheric Flows

Huang and Hill (1989) discuss how the collisions between ions, which are magnetically connected to the sub-rotational regions of the magnetosphere, and the neutrals in the thermosphere produces a "rotational slippage" of the upper atmosphere. During modelling of the ionosphere-magnetosphere coupling Cowley and Bunce (2001) introduced a constant k to account for this slippage,

$$\mathrm{k} = \frac{\Omega_\mathrm{J} - \Omega_\mathrm{n}}{\Omega_\mathrm{J} - \Omega_\mathrm{i}} \qquad \textbf{2.12}$$

where Ω_J is the rotation rate of Jupiter's deep interior (1.76 x 10^{-4} rad s^{-1} or 870.536° per Earth day), Ω_n is the rotation rate of the neutrals in the thermosphere and Ω_i is the rotational rate of the ionosphere (which maps to the sub-rotational plasma sheet in the mid-magnetosphere). In steady state it is expected that the angular velocities are arranged in the following order: $\Omega_J > \Omega_n > \Omega_i$. Through a modelling study conducted by Millward et al. (2005), the value k was calculated to be ~ 0.5 at the ion production peak in the jovian ionosphere. It is worth noting that $\Omega_n < \Omega_i$ could be possible under certain conditions in some regions of Jupiter's ionosphere, however, very few studies have measured the rotation rate of the neutral thermosphere, as discussed below, and hence it is often assumed to be corotating.

A number of studies have taken advantage of the thermosphere-ionosphere-magnetosphere coupling to indirectly measure the angular velocity of the magnetosphere by calculating the LOS velocity of the coupled region of the ionosphere from H_3^+ observations. Rego et al. (1999) measured significant flows in the northern auroral regions using the long-slit Echelle Spectrometer CSHELL (Greene et al. 1993) previously available at the NASA Infrared Telescope Facility (IRTF) at the Mauna Kea Observatories, Hawaii. They measured a maximum LOS velocity of -3.3 ± 0.4 km s^{-1} at CML ~ 264° and an average LOS velocity over the observations of -2.7 ± 0.3 km s^{-1}, relative to the rotation of the planet. Further measurements using IRTF-CSHELL by Stallard et al. (2001) measured LOS velocities of ~-1.5 km s^{-1} in the region of the main auroral emission, taken from discrete slit positions in the CML range 132°-229°, at a variety of auroral latitudes. Additionally, Lystrup et al. (2007) measured the LOS of H_3^+ as ~-2 – 0 km s^{-1} in the southern auroral regions using IRTF-CSHELL measurements. Using the Fourier Transform Spectrometer (FTS/BEAR) instrument available at the Canada-France Hawaii Telescope (CFHT) at the Mauna Kea Observatories, Hawaii, Chaufray et al. (2011) measured an average LOS velocity of -3.1 ± 0.4 km s^{-1} in the northern auroral region for CML ~179°.

The strong sub-rotational H_3^+ flows measured by Rego et al. (1999) were attributed to an auroral electrojet. The Hall drift drives the electrons and ions along the main auroral emission in a clockwise direction, as viewed from the rotational norther pole. This is motion opposes corotation and therefore the ionosphere collides with the neutral thermosphere, with the electrons being collisionally decelerated much less than the ions. Measurements by Stallard et al. (2001) also show ionospheric flows in the main emission dominated by the electrojet. They measure the electrojet over several jovian rotations, recording velocities of 0.5-1.5 km s^{-1}. The detection of this electrojet is in agreement with the prediction of the Hill (1979) model for enforcing plasma corotation. Achilleos et al. (2001) developed a dynamical model for ion, electron, and neutral velocities, which produces an electrojet within the region of the auroral oval in response to magnetosphere forcing. The model shows, as do the measurements of Stallard et al. (2001), and Chaufray et al. (2011), that the H_3^+ ions flow around the auroral oval and are controlled by the Hall drift associated with the model ionospheric electric field. Achilleos et al. (2001) showed that the neutrals are

strongly coupled to the ions and a circumpolar neutral jet develops with a velocity of up to ~60% of the ion velocity in the electrojet.

Flows poleward of the main emission were found to be varied. Stallard et al. (2001) measured stronger flows of ~3 km s^{-1} in a dark region of Jupiter's IR polar aurora. Rego et al. (1999), Stallard et al. (2001), and Chaufray et al. (2011) analysed the LOS velocity of the H_3^+ ions in a reference frame which is fixed in System III, and thus rotates with the planet. However, Stallard et al. (2003) transformed the velocities derived by Stallard et al. (2001) into the magnetic pole reference frame, where the LOS component of the velocity of the magnetic pole is set to zero. They discovered that part of the IR dark polar region, coincident with the swirl region of the UV aurora, was stationary in this inertial frame, which they defined as the fixed dark polar region (f-DPR). The remainder of the dark polar region, approximately coincident with the dark region of the UV aurora, was found to be corotational and was defined as the rotating dark polar region (r-DPR) as this region rotated with the planet. These regions are shown schematically in Figure 2-17.

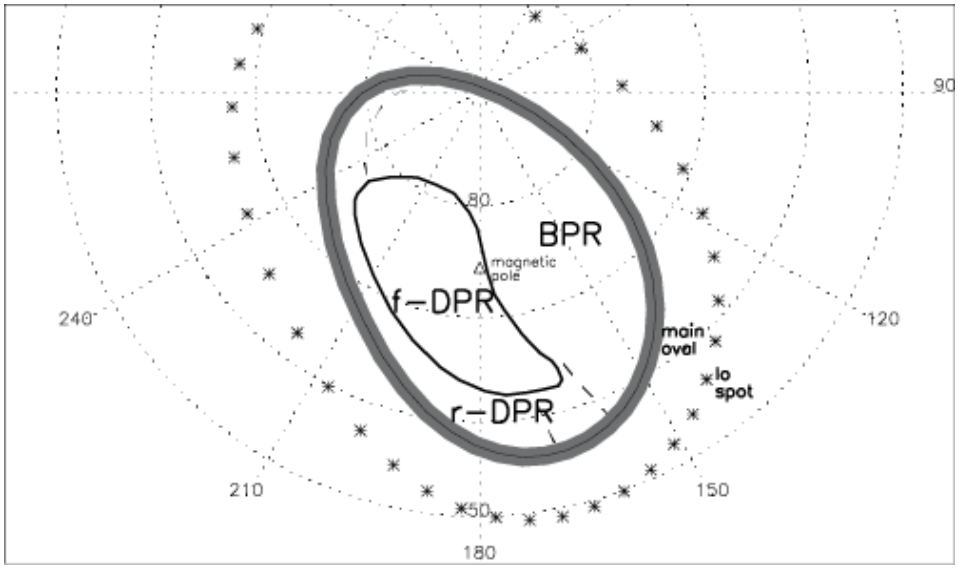

Figure 2-17: A schematic of the regions of flows in Jupiter polar ionosphere, reproduced from Stallard et al. (2003).

Stallard et al. (2003) postulated that the stationary f-DPR was coupled to the solar wind. Owing to the large distances involved in Jupiter's magnetosphere, it would take a very long time for the solar wind flow to move the magnetic field lines, which were coupled to the solar wind, from the dayside magnetopause (where reconnection between jovian field lines and the solar wind takes place) over the polar region to the

magnetotail. Therefore, in a reference frame that is stationary relative to the magnetic pole, the field lines coupled to the solar wind appear stationary relative to the closed field lines that have some velocity, although sub-rotational. Cowley et al. (2003) described how this coupling is governed by Dungey cycle flows in Jupiter's magnetosphere. Due to the asymmetry imposed by the Vasyliunas cycle, the Dungey cycle at Jupiter would be confined to a single-cell ionospheric pattern in the dawn region, as shown in Figure 2-18, where the open flux is shown as the hatched region.

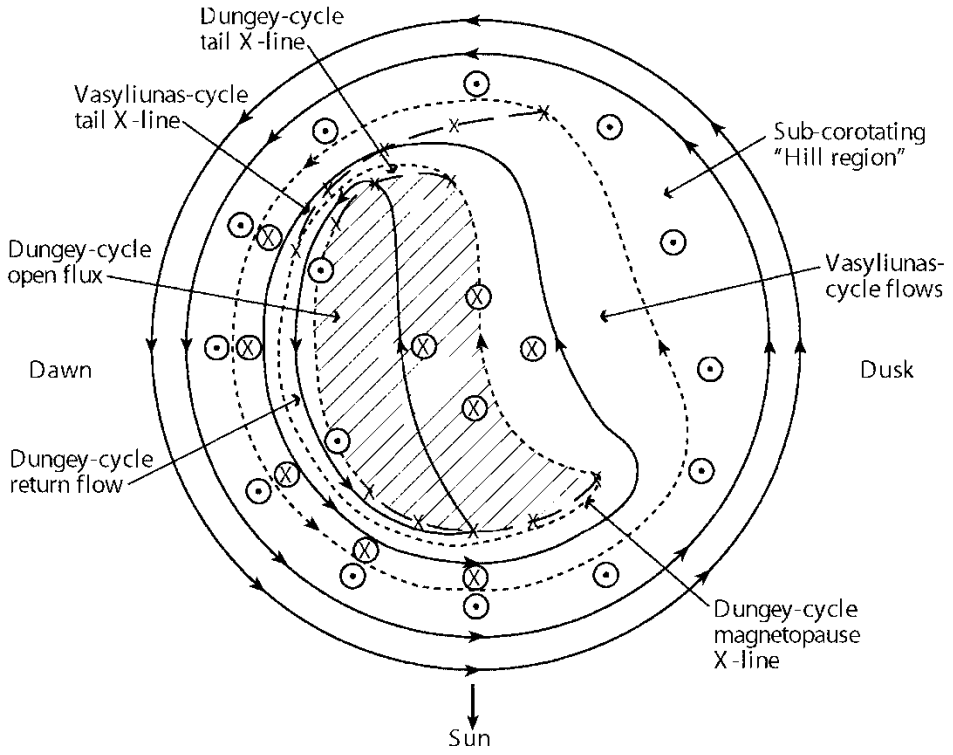

Figure 2-18: A sketch of the ionospheric flows in Jupiter northern auroral region, reproduced from Cowley et al. (2003). The upward FACs are labelled with the cross in the centre of the circle and the downward FACs are labelled with the dot in the centre of the circle. The different regions representing the Dungey-cycle and Vayliunas-cycle are labelled. The Sun is to the bottom of the diagram.

Super-rotational flows have also been measured in Jupiter's auroral regions. Rego et al. (1999) measured super-rotational flow of ~ 1 km s^{-1} in the PRF at a CML of 270°,and was attributed to coupling with radial currents in Jupiter's magnetosphere ~0.2 R_J inside Io's orbit, which also caused auroral hiss measured by Voyager and discussed by Morgan et al. (1994).

Although the magnetosphere-ionosphere-thermosphere (MIT) coupling system tends to drive sub-rotational flows, super-rotational flows are predicted in the thermosphere by models such as Smith and Aylward (2009) and Yates et al. (2012),

and through collisions with the neutral atmosphere, it may be plausible the H_3^+ ions can also super-rotate. Smith and Aylward (2009) concluded that meridional advection rather than vertical viscous transport is the main way which angular momentum is distributed in Jupiter's thermosphere, with momentum transferred by winds that blow along or across fixed pressure surfaces. In regions where Joule heating and ion drag do not balance the Coriolis force, a significant advection term arises to restore the thermosphere to equilibrium. When ion drag becomes negligible, gas can upwell which expands and cool adiabatically creating a pressure gradient. Meridional advection can now take place and drive poleward flows along this pressure gradient at altitudes ~600 km above the 1 bar level. The ion drag force creates sub-rotational ionospheric flows, whereas, the Coriolis forces works to keep the thermosphere corotating, and unhindered it can accelerate the thermosphere into regions of super-rotation. Smith and Aylward (2009) calculated an angular velocity of the thermosphere as a factor of 1.05 to that of the angular velocity of the deep interior of Jupiter at latitudes of ~65° – 73°. The latitudes map to a region of the middle magnetosphere where the ions would be sub-rotating, therefore, these models show the importance of including the coupling to the thermosphere as well as the magnetosphere-ionosphere coupling in global circulation models.

Observations measuring the velocity of the neutrals in the thermosphere are very limited. Chaufray et al. (2011) were able to simultaneously measure H_3^+ and H_2 IR emissions at 2 μm. They derived a LOS velocity of -3.1 ± 0.4 km s^{-1} for H_3^+ and an upper limit on the LOS velocity of <1.0 km s^{-1} for the H_2. Yates et al. (2012) predict a range of velocities for the neutrals of <1 – 2.5 km s^{-1}, however, this model is axisymmetric and uses strong magnetosphere-ionosphere coupling forcing the neutral velocity to almost match the ion velocity in places, which may not be realistic. The measurements by Chaufray et al. (2011) only constrain the altitudes in which they were measured, that is at an altitude range of ~560 – 690 km for the H_2 emission (Uno et al. 2014). Until further simultaneous measurements of taken of both the neutral and charged components, to further constrain the models of the thermosphere, it is assumed that the neutrals in the thermosphere are corotating. The investigations in this thesis regarding the line-of-sight velocity of the H_3^+ ions in the auroral regions are discussed in Chapter 5.

2.6 Ionospheric Heating and Energy Balance

2.6.1 H_3^+ Temperature Measurements in Jupiter's ionosphere

The temperature of Jupiter's ionosphere has been investigated since H_3^+ was detected by Drossart et al. (1989). Table 2-1 shows the rotational (T_{rot}), vibrational (T_{vib}), and kinetic (T_{kin}) temperatures measured in Jupiter's ionosphere by various studies (note this list is not exhaustive). Some studies show rotational and vibrational temperatures in agreement of each other. However, Giles et al. (2016) simultaneously measured the kinetic (1390 ± 160 K), vibrational (925 ± 25 K) and rotational (960 ± 40 K) temperatures of H_3^+ in Jupiter's northern auroral region. The disagreement of these three temperature values shows that there is potentially a departure from LTE. For a full discussion on the LTE assumption, please refer to Section 2.1.3.

Table 2-1: A table showing a summary of the rotational, vibrational and kinetic temperatures of H_3^+ measured by several studies.

Study	T_{rot} (K)	T_{vib} (K)	T_{kin} (K)
Drossart et al. (1989)	1099 ± 100		
Drossart et al. (1993)			1150 ± 60
Oka and Geballe (1990)	~ 670		
Miller et al. (1990)	1100 ± 100		
Maillard et al. (1990)	835 ± 50 (North) 1000 ± 40 K (South)		
Lam et al. (1997)	700 - 1000		
Stallard et al. (2002)		900 – 1250	
Raynaud et al. (2004)	1170 ± 75	960 ± 50	
Giles et al. (2016)	960 ± 40	925 ± 25	1390 ± 160
Moore et al. (2017)		600 – 1000	

The early measurements of H_3^+ temperatures were taken from single slit positions; however, later studies acquired greater spatial information. By using a series of discrete slit positions, Stallard et al. (2002) measured the vibrational temperature in the northern auroral region in the range of ~900 – 1250 K. A study by Lam et al. (1997) mapped the H_3^+ temperature globally. The largest temperatures were measured in the auroral regions, typically 800-950 K, although poleward of the main auroral emission in the south had temperature of ~750 K. Some temperature variation was measured in the mid-to-low latitudes, with temperatures <700 – 950 K, although the heating by solar radiation is thought to be uniform. As well as deriving vertical density profiles (discussed in Section 2.1.1), Lystrup et al. (2008) also derived a vertical temperature profiles from the H_3^+ measurements. They measured an average exospheric temperature of 1450 K, which is 150 K higher than the predicted vertical temperature model from Grodent et al. (2001), which could suggest that the auroral temperatures are highly variable.

Raynaud et al. (2004) identified a northern hot spot which was ~250 K hotter than the surrounding auroral temperatures. This hot spot was coincident with the thermal infrared hot spot observed at 5-15 μm (Flasar et al. 2004), which is at the location of bright spots observed in FUV associated with the cusp (Pallier and Prangé 2004). Additionally, this region experiences a bright spot observed at the X-ray wavelengths (Gladstone et al. 2002), clearly showing complex processes, involving very energetic particle precipitation, which produce emission at several wavelengths.

The Jovian InfraRed Auroral Mapper (JIRAM, Adriani et al. 2008) is an infrared imager and spectrometer on-board Juno, which takes H_3^+ and methane measurement at 2-4 μm. Dinelli et al. (2017) report on the temperatures and column densities measured in the northern auroral region during perijove 1, covering a full jovian day (~10 Earth hours), shown in Figure 2-19. They found that a 90° - 170° longitude the temperature is high equatorward of the main auroral emission, and the column density is also high. However, at 200° - 210° longitude the column density is high poleward of the main auroral emission, but the high temperatures remain equatorward of the main emission. Overall, the column densities of the northern aurora were within the range of 1.8 – 2.8 x 10^{12} cm^{-2} and the temperatures were between 800 and 900 K.

Adriani et al. (2017) show that the temperature of the southern aurora is higher than the northern aurora, which agrees with previous studies (e.g.: Maillard et al. 1990) and models. During perijove 1, JIRAM only sampled the dayside southern aurora, measuring column densities in the range of 0.2 – 4 x 10^{12} cm^{-2} and temperatures between 600 and 1400 K, as shown in Figure 2-19. Adriani et al. (2017) found that the high column densities were coincident with the main emission. However, the temperature didn't exactly correlate with the main emission: at 270° - 360° longitude it was hotter equatorward of the main emission, but at 0° - 90° longitude the elevated temperatures were coincident with the main emission as well as equatorward. It was found that there were diurnal variations in the southern aurora temperature: the ionosphere was hottest in the morning and then remained constant for the rest of the day.

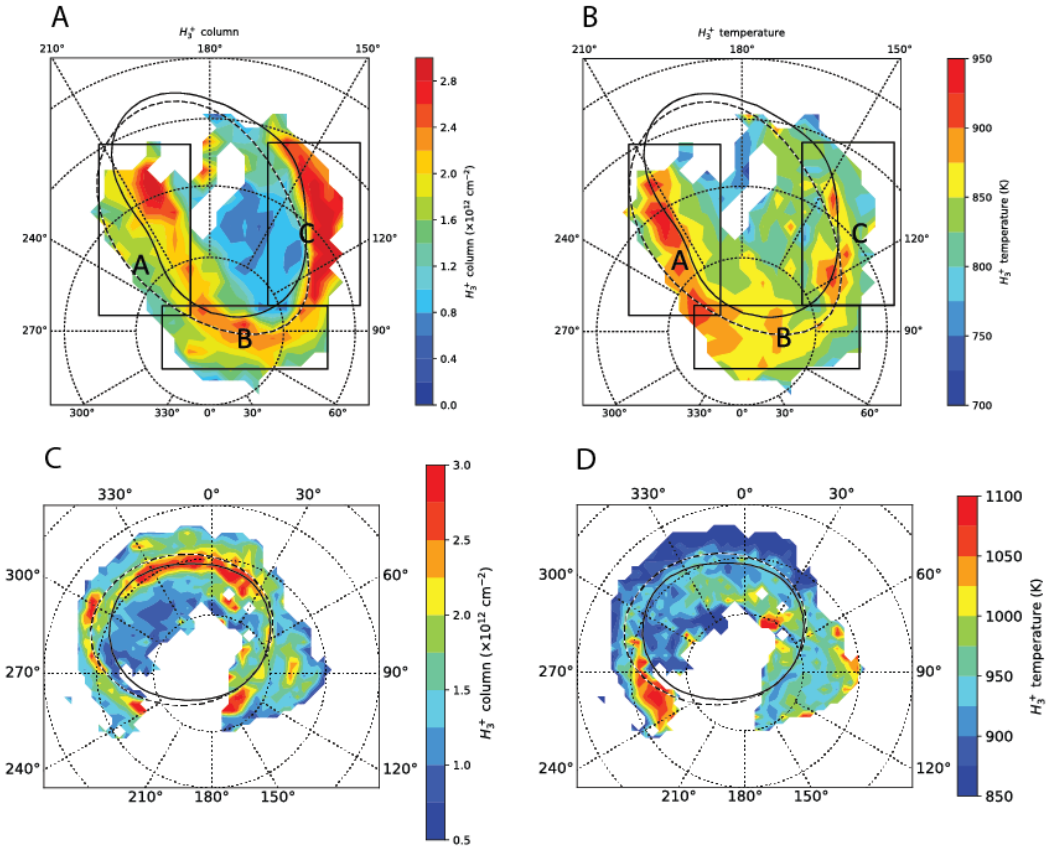

Figure 2-19: The effective temperature and column density of Jupiter's northern (top panels, produced from Dinelli et al. 2017) and southern aurora (bottom pannels, reproduced from Adriani et al. 2017), measured by Juno-JIRAM during perijove 1. The column densities are shown in (a) and (b), and the effective temeprature is shown in (b) and (d). The statisical position of the main auroral emission is given by the solid black line and and the modelled position is given by the dashed black line.

Several studies have tried to determine the drivers of heating events in Jupiter's ionosphere. Stallard et al. (2002) observed a heating event over 3 Earth days (~7.3 jovian days), where temperature rose by ~125 K in Jupiter's northern auroral region. They suggested that the heating was driven by an expansion of the magnetosphere caused by a decrease in the solar wind dynamic pressure. Melin et al. (2006) calculated that the heating event caused the combined ion drag energy and Joule heating rates to increase from 67 to 277 mWm^{-2}. Moore et al. (2017) observed a cooling event in Jupiter's auroral ionosphere was using Keck-NIRSPEC, where the mean temperature decreased by 60 K, as shown in Figure 2-20. As Juno was in the solar wind, upstream IMF data was acquired by the Juno-MAG instrument and other solar wind properties were calculated using MHD propagation models (Tao et al. 2005; Zieger et al. 2015). They found that a solar wind shock arrived at Jupiter leading up to the cooling event, after which the solar wind was quiescent. Moore et al. (2017) suggest that the cooling event was caused by shock recovery processes, similar to those modelled by Yates et al. (2014).

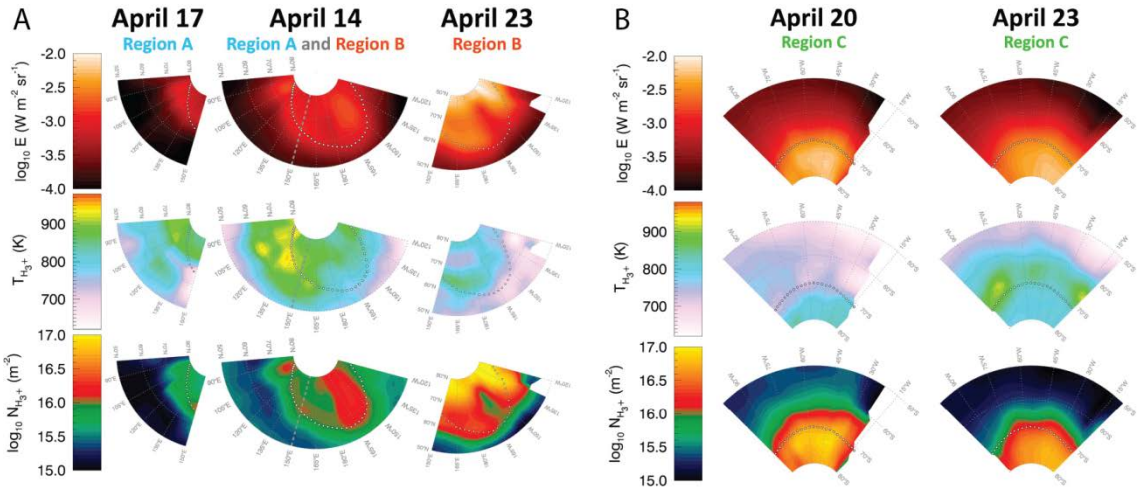

Figure 2-20: The derived H_3^+ properties in regions of Jupiter's (a) northern and (b) southern aurora, reproduced from Moore et al. (2017). The top row is the radiance, the middle row is the temperature, and the bottom row is the column density for observation taken on the 17 (left panel), 14 (middle panel) and 23 (right panel) April. The dashed grey line in 14 April plots divides regions A and B. The white does represent the statistical location of the main auroral emission from Connerney et al. (1998).

As well as auroral heating and cooling events, more localised heating and cooling has been observed in non-auroral regions. O'Donoghue et al. (2016) found elevated temperatures of 1600 K above the Great Red Spot (GRS), which is hundreds of degrees hotter than temperatures measured anywhere else on the planet. This suggests a

localised heating process which the authors attribute to heating from upward propagating acoustic or gravity waves, originating from the lower atmosphere. A region of reduced temperatures has been observed by Stallard et al. (2017) in Jupiter's sub-auroral thermosphere, suggesting a region of localised cooling. Temperatures inside the 'Great Cold Spot' were on the order of ~200 K colder than the surrounding regions. Previously, it had been thought that there would be a gentle gradient of heat flowing away from the auroral regions. However, the great cold spot shows that the heat distribution is not uniform, perhaps unsurprisingly as the temperature morphology in the auroral regions is complex. Stallard et al. (2017) postulated that the localised cooling was driven by thermospheric dynamics. Both studies by O'Donoghue et al. (2016) and Stallard et al. (2017) show that the distribution of heating in Jupiter's thermosphere is very complex.

2.6.2 The H_3^+ Thermostat

There are several ways through which the upper atmosphere of Jupiter is cooled. Yelle and Miller (2004) and Melin et al. (2006) discuss how conduction to lower altitudes is very inefficient in the thermosphere. Alternatively, cooling could be achieved through radiation to space. H_2 infrared emission has been observed by Trafton et al. (1989), however, this emission, and the energy it re-radiates to space, is weak compared to the emission and heat re-radiation of H_3^+. In the L band atmospheric window, Wien's displacement law shows that when the temperature is around 1000 K the maximum wavelength is ~3 μm (Miller et al. 2006), where maximum wavelength is the wavelength at which the maximum emission is produced for a black body. H_3^+ emits at around this value of maximum wavelength and therefore is an efficient coolant of Jupiter's upper atmosphere.

Owing to its ability to reradiate heat into space and control the temperature of the upper atmosphere, H_3^+ has been described as a thermospheric thermostat. The amount of energy radiated to space was studied by Lam et al. (1997) using the total emission, which is the total emission emitted by all of the H_3^+ emission lines. They found that in the equatorial region the total emission was 2 or 3 times greater than the solar EUV absorbed locally by the thermosphere, suggesting an additional heat source. However, in the auroral regions Rego et al. (2000), showed that the total emission was

comparable to the energy supplied by particle precipitation. Melin et al. (2006) used a 1D self-consistent model by Grodent et al. (2001) to analysis a heating even observed by Stallard et al. (2001). They showed that the H_3^+ emission in the auroral regions can compensate for any increased particle precipitation. H_3^+ is a more efficient coolant at high temperatures; however, it is less efficient at high altitudes where non-LTE effects can be strong.

2.7 Summary and Outline

In this thesis, H_3^+ is used to probe the upper atmosphere of Jupiter. By studying the near-infrared emission from Jupiter's ionosphere, the line-of-sight velocity, temperature, density and total emission of the H_3^+ molecule is derived. Discussion in this thesis shows how these properties can be used to further our understanding of the dynamic processes occurring in Jupiter's ionosphere and of the coupling with Jupiter's magnetosphere.

To place the work of this thesis in a broader context, an outline of the relevant plasma physics (Chapter 1) and the jovian system (Chapter 2) was given. Chapter 3 gives an overview of the instruments used in this thesis as well as how they are used to observe Jupiter. The data reduction and data analysis used to extract the H_3^+ properties is also given in Chapter 3. The ionospheric flows of H_3^+ are the focus of Chapter 4 and Chapter 5. Chapter 4 deals with the line-of-sight velocity of the H_3^+ at the mid-to-low latitudes, where predicted flows related to the H Ly-α bulge are investigated and the rotation rate of the ionosphere is determined. The auroral ionospheric flows of H_3^+ are discussed in Chapter 5, where flows, which range from sub-rotational to super-rotational, are mapped onto polar projections and their drivers are discussed. Chapter 6 focuses on the temperature, column density and total emission of the H_3^+ in Jupiter northern auroral region. Temperature changes are identified which could be to a local time change in particle precipitation energy, or thermospheric response to a transient solar wind compression. Finally, Chapter 7 brings the three data chapters together in a summary discussing how the work has contributed to our knowledge of the jovian system, as well as outlining future work.

Chapter 3 Instrumentation, Observations and Data methods

In this chapter I will describe the instruments used in this thesis and outline how they are used at their respective telescopes to take the observations. I will give an overview of the data sets, the data reduction processes and the data analysis methods, showing how the H_3^+ line-of-sight velocity, temperature, column density, and total emission are extracted from the infrared observations of Jupiter.

3.1 Instruments

In this thesis two instruments were used: the CSHELL instrument previously available at the NASA Infrared Telescope Facility (IRTF) and the CRIRES instrument previously available The Very Large Telescope (VLT), a telescope facility operated by the European Southern Observatory (ESO). The optical layouts of the instruments are shown in Figure 3-3 and Figure 3-4 for CRIRES and CSHELL respectively, and specific differences are highlighted in Table 3-1. The following gives an overview of the instruments; however, the precise technical information on design and performance is beyond the remit of this thesis. Further information for CSHELL can be found in Greene et al. (1993), Tokunaga et al. (1990), and in the CSHELL user manual[3]. Further information for CRIRES can be found in Kaufl et al. (2004) and in the CRIRES user manual[4].

The CSHELL instrument was one of the first high-resolution long-slit spectrometers, available at the IRTF until August 2016 when it was replaced by the new instrument, iSHELL. The IRTF has a primary mirror with a diameter of 3 m and is located at the Mauna Kea Observatories, Hawai'i, at an elevation of ~4200 m. The observatory is situated on an island and benefits from exceptionally stable air since there is no major surrounding land mass to cause undesirable air currents, which could distort the signal observed from Jupiter. A tropical inversion cloud layer ~600 m thick isolates the summit from the lower moist maritime air, therefore, the summit skies are

[3] NASA Infrared Telescope Facility. 2010. *CSHELL.* [ONLINE] Available at: http://irtfweb.ifa.hawaii.edu/~cshell/ [Accessed 31 January 2018].
[4] European Southern Observatory. 2017. *CRIRES Documentation.* [ONLINE] Available at: http://www.eso.org/sci/facilities/paranal/instruments/crires/doc.html [Accessed 31 January 2018].

dry and free from atmospheric pollutants. This reduces the amount of absorption of the infrared signal by water vapour and atmospheric pollutants.

The CRIRES instrument was available at the VLT until July 2014 when it was removed due to an instrument upgrade, however, the new instrument CRIRES+ will not be available until late 2018. The VLT has a primary mirror with a diameter of 8.2 m and is located on Cerro Paranal in the Atacama Desert of northern Chile at an elevation of 2635 m. Due to the elevation and location in a desert, the summit skies at the VLT are very dry, which reduces the absorption of the infrared signal.

Although the two instruments have different spectral resolutions, the light path and components which interact with the light in both instruments are very similar, with differences outlined in Table 3-1. The light enters the instrument directly from either the telescope or the calibration unit, which is within the instrument. The calibration unit contains spectral and continuum lamps, which are used to take calibration data required for the data reduction processes and discussed further in Section 3.3.

When light enters from the telescope, it first encounters a dichroic, which is an interference filter. After the light is re-imaged, it passes through an order sorter which is needed to isolate a single order, chosen by the observer. If there were no order sorter component then all the spectral orders would be overlaid on top of each other. Figure 3-1 shows a schematic of the light path in the CRIRES instrument and how the light passes through the slit to a pre-disperser and intermediate slit, which limits the wavelength range that is passed onto the Echelle spectrometer.

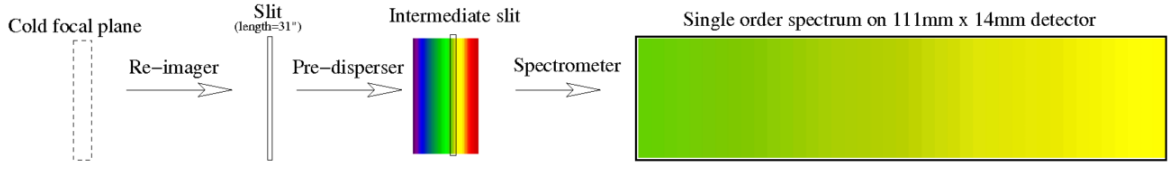

Figure 3-1 A schematic of the simplified light path of the CRIRES instrument. Adapted from Oliva et al. (2014).

The light then reaches the Echelle grating, which has the same set up for both CSHELL and CRIRES, as shown in Table 3-1. A general description of Echelle spectrometers is given in Section 3.1.1. Prior to the Echelle grating, the light was

culminated as the Echelle gratings require parallel rays. Finally, the light is recorded on infrared detectors, which are housed in a cold box to reduce the detector noise.

3.1.1 Echelle Spectrometers

Echelle spectrometers have a grating which is a reflective surface with grooves cut into it. These grooves reflect the incoming radiation and through constructive and destructive interference, spectra are created, involving the same principles as those first studied in the laboratory by Thomas Young in 1801. If the path difference between the light from adjacent grooves is equal to an integer multiple of the wavelength then there will be constructive interference, which creates the spectral orders.

When observing astronomical bodies such as Jupiter, the radiation will be polychromatic, a schematic for which is shown in Figure 3-2. As the light is diffracted, a rainbow of dispersed wavelengths will occur on the surface of the detector. To separate the wavelengths, so the orders do not overlap, Echelle gratings have grooves with a small separation and a large focal length. This set up causes a reduction in light intensity; therefore, a large blaze angle is used to concentrate the radiation to the higher orders. Due to the large blaze angle, the angles incidence and reflection are approximately equal for the Echelle grating configuration. The diffraction equation for an Echelle grating is,

$$n\lambda = d\sin(\beta) \qquad \textbf{3.1}$$

where β represents the angle of incidence or the angle of reflection.

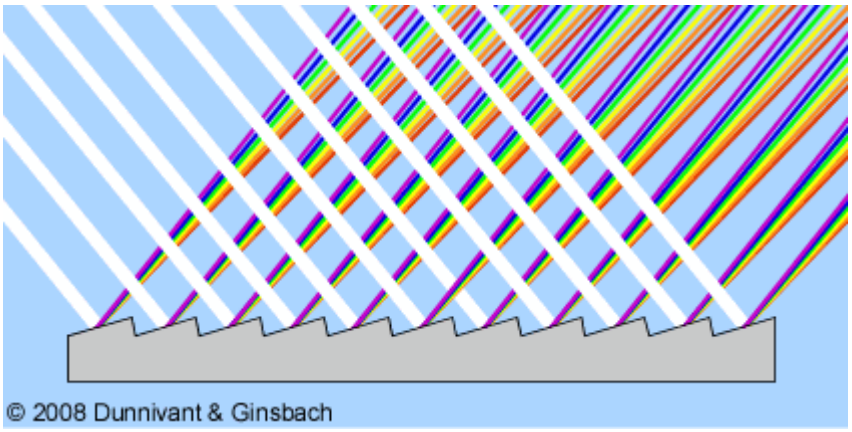

Figure 3-2: A schematic of polychromatic radiation incident on a diffraction grating, reproduced from Dunnivant and Ginsbach (2009).

Table 3-1: The instrument parameters for CSHELL and CRIRES.

	CSHELL	CRIRES
Wavelength range	1.08-5.6 µm	0.95-5.38 µm
Spectral resolution (for smallest slit width)	~43,000	~100,000
Slit widths	0.5'', 1'', 1.5'', 2.0'' and 4''	0.2''-1''
Slit orientation adjustment	To orientate the slit, the instrument had to be manually rotated by the telescope operator.	The orientation of the slit could be adjusted internally.
Slit length	30''	40''
Adaptive optics	N/A	MACOA system (60 actuator deformable mirror) – not used in the studies in this thesis.
Calibration system	3 spectral lamps (argon and krypton) and 1 continuum lamp.	2 blackbodies, 2 spectral lamps, gas cells.
Vacuum vessel temperature	~65 K	~77 K
Spectral order sorter	Circular Variable Filter (CVF) wheels, which are interference filters and isolate a single order (orders 11 – 56).	The light is pre-dispersed with a ZnSe prism spectrometer and then exits through an intermediate slit, which isolates a single order (orders 11 – 58).
Light culmination	Off-axis collimator	3 mirror anastigmat (TMA)
Echelle grating	31.6 lines per mm, 63.5° blaze	31.6 lines per mm, 63.5° blaze
Infrared detector array	256 spectral by 256 spatial pixels using a SBRC InSb detector, cooled to ~30 K.	4096 spectral by 512 spatial pixels, with a 283 pixels inter-detector gap, using 4 InSb Aladdin III detectors, cooled to ~ 25 K.
Pixel plate scale	0.2''	0.089''

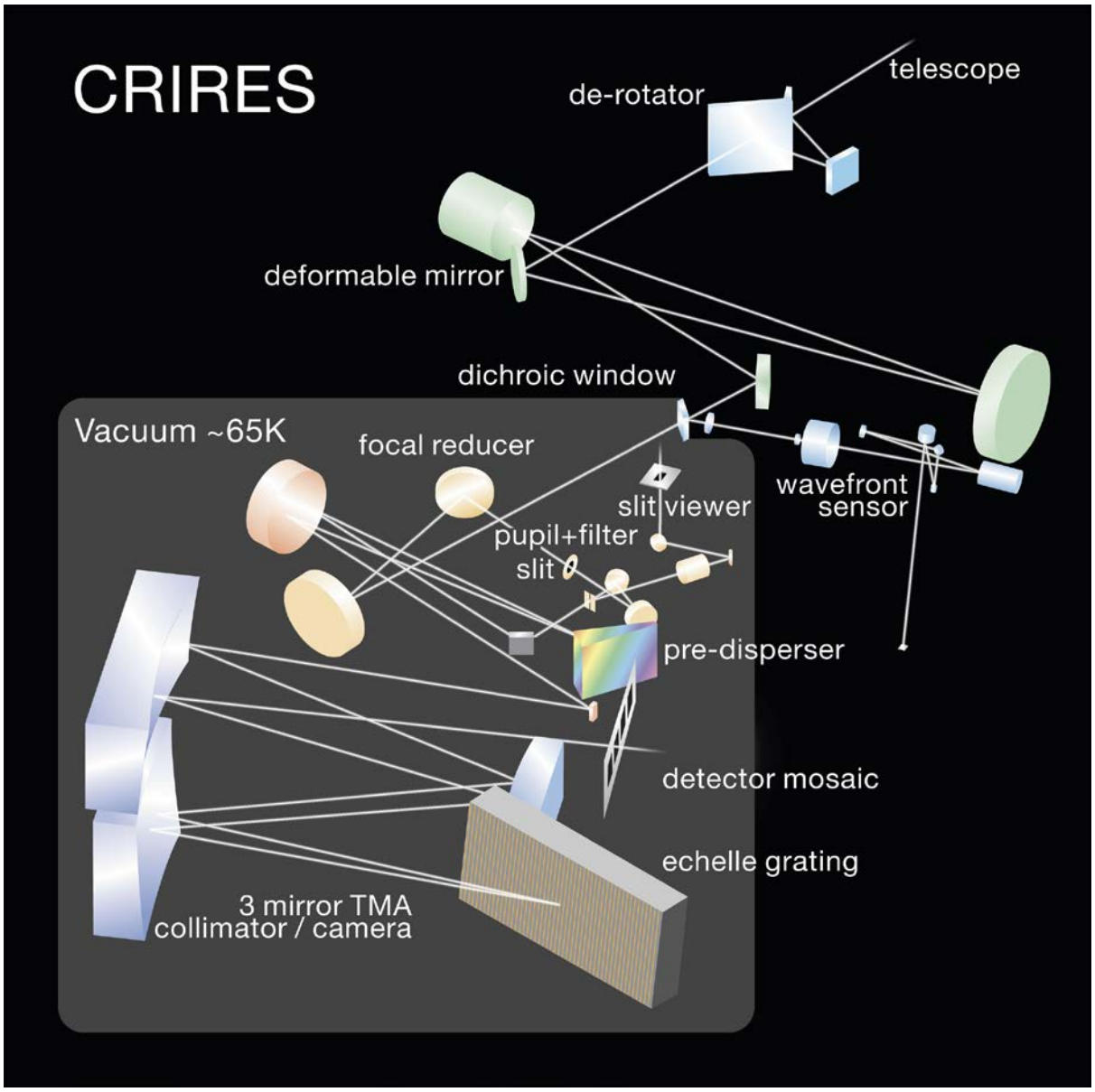

Figure 3-3: A schematic of the optical arrangement of CRIRES-VLT. Reproduced from the CRIRES manual.

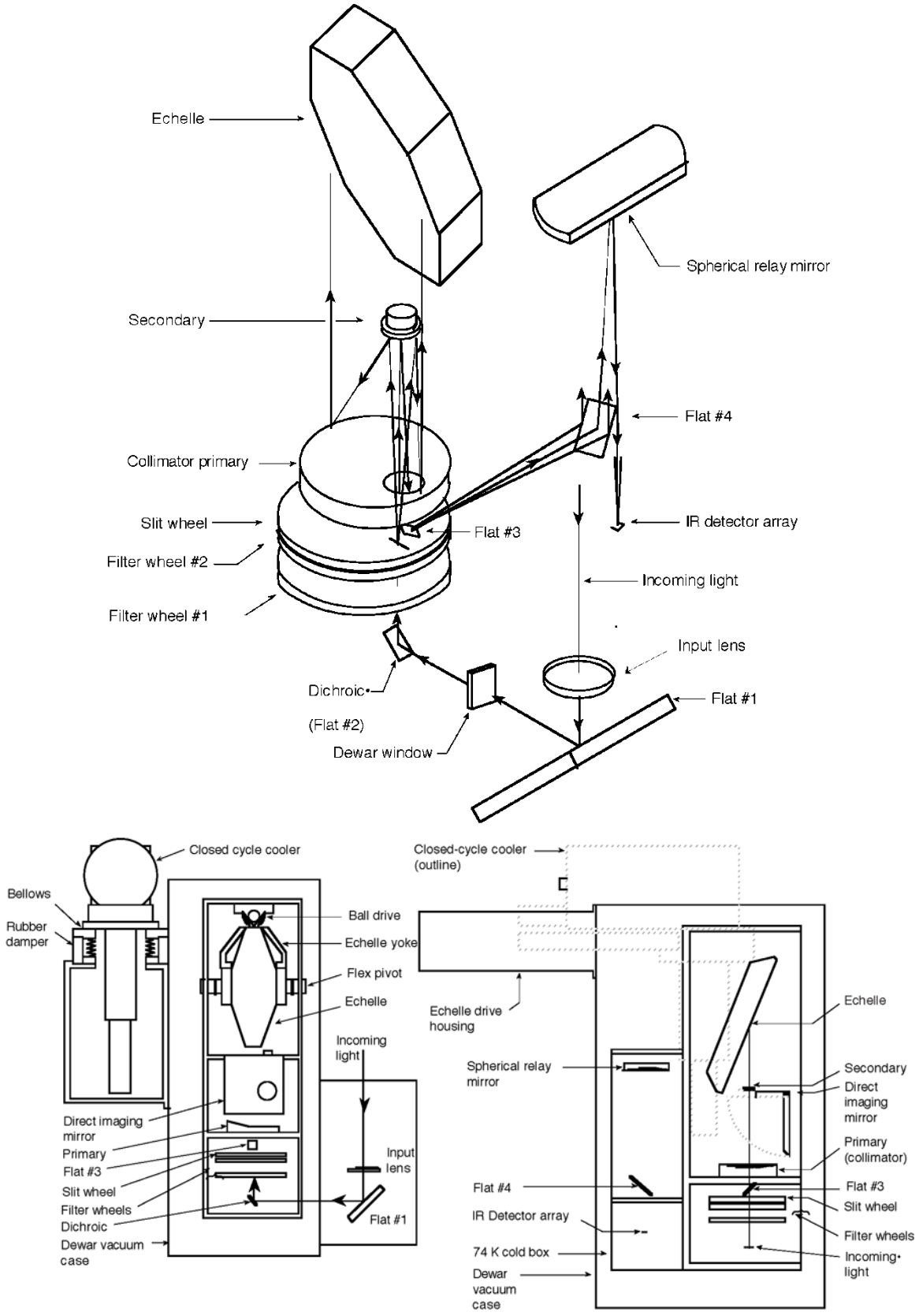

Figure 3-4: A schematic of the CSHELL-IRTF. The top panel shows the optical arrangement of the instrument and the bottom panel shows the instrument setup from and side and top down view. Reproduced from the CSHELL manual.

3.2 Observing Jupiter

Molecules in the Earth's atmosphere absorb a variety of different wavelengths which restrict Earth based observations. However, there is an atmospheric window which coincides with the highest intensity of H_3^+ spectral lines of the Q and R branches between 3.1 and 4.1 µm, as shown in Figure 3-5. This atmospheric window is referred to as the L-band window and lacks excessive absorption by the Earth's atmosphere. Note that the L' band is at wavelengths with the least absorption by the Earth's atmosphere, and this coincides with the Q branch, which is reported upon in this thesis. The L-band window also coincides with the wavelength at which solar radiation at Jupiter is strongly absorbed by methane in the Jovian atmosphere, therefore less sunlight is reflected. However, when observing at lower latitudes a larger amount of reflected sunlight is measured.

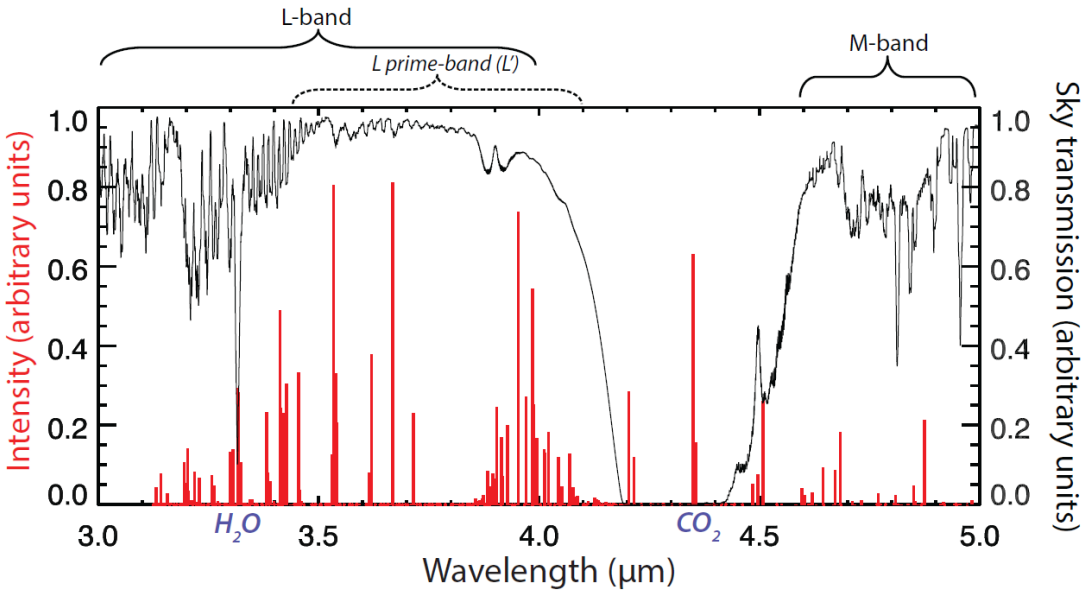

Figure 3-5: The red lines show the same H_3^+ emission lines as in Figure 1-8, and the black line shows the normalised sky transmissions, which represents how much the light is absorbed by the Earth's atmosphere. Water and carbon dioxide are labelled in purple, and these molecules are responsible for preventing sky transmission, as shown by the black line which reaches a minimum at these wavelength regions. The infrared spectrum of the atmospheric emission was generated using the ATRAN modelling software (Lord 1992), accessed via the Gemini Observatory[5]. This figure is replicated from O'Donoghue (2014).

[5] Gemini Observatory. 2012. *IR Transmission Spectra*. [ONLINE] Available at: http://www.gemini.edu/sciops/telescopes-and-sites/observing-condition-constraints/ir-transmission-spectra [Accessed 31 January 2018].

When observing, it is important to take the air mass of Jupiter into consideration. Air mass, z, is a measure of the amount of the Earth's atmosphere that the light you observe must pass through and is approximated using the following equation,

$$z = \sec(ZA) \quad \textbf{3.2}$$

where ZA is the zenith angle, which represents the angle between the zenith (the point on the sky directly above the observer) and the object that you are observing in the sky, as shown in Figure 3-6. Therefore, the lowest air mass is achieved when the object is directly above the observer and the approximation sec(ZA) increases to infinity as the object sets below the horizon. Observations of objects with air masses beyond 2 are of poor quality and therefore the observations used in this thesis of Jupiter are at air masses less than 2.

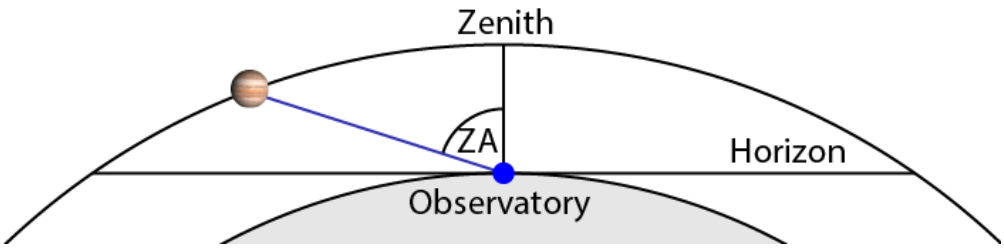

Figure 3-6: A schematic showing the geometry of observing Jupiter through the Earth's atmosphere and the air mass associated with this. ZA is the zenith angle.

In addition to air mass, poor telluric seeing can also reduce the quality of the data taken during an observation. The seeing is a measure of how much the Earth's atmosphere perturbs the emission coming from the object you are observing. If the seeing is high, due to bad weather, the images and spectra will appear blurry and the data quality will be poor. To measure the seeing the full width at half maximum of a star is taken. Fortuitously, the location of the VLT and IRTF allows for many nights of clear skies and excellent observing conditions.

For the majority of the observations, the slit of the instrument was aligned perpendicular to the rotation axis of Jupiter, with a small number of spectra taken when the slit was parallel to the rotation axis. The slit in the perpendicular orientation can be seen in Figure 3-7, where the slit is the black line cutting across at high latitudes and the image of Jupiter was taken using the K filter with the CRIRES slit viewer. At both telescopes off axis-guiding could be used to guide the telescope. If there were no

star bright enough in the field of view, tracking rates at which Jupiter appears to move across the sky, taken from HORIZONS Web-Interface[6], could be used.

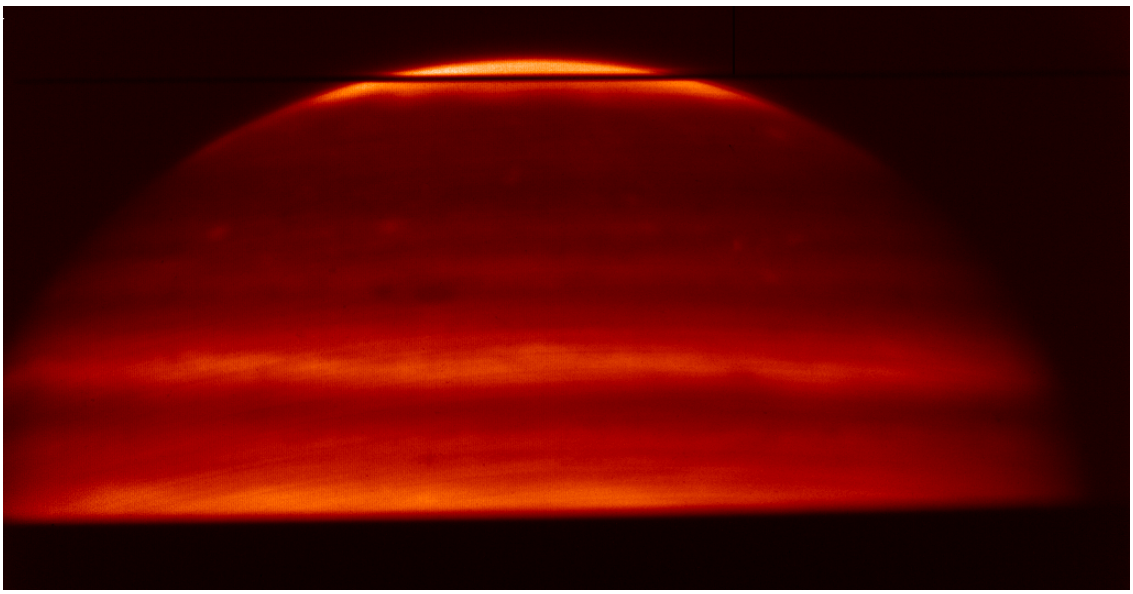

Figure 3-7: K band image of Jupiter's northern hemisphere taken with the CRIRES slit viewer. The slit can be seen at the black line cutting through the planet at high latitudes. Image credit: T. Stallard, ESO.

The observing procedure at both telescopes is similar. In general the observations involve taking jovian spectra, terrestrial emission spectra, star spectra, and calibration spectra. The star spectra and calibration spectra were either taken at the start or the end of the observing run depending on strategy used on that night. The star used changed in each observing run and was chosen to acquire spectrum of a representative air mass of the observations. The calibration macros, which were available at CSHELL and CRIRES, took spectra of emission from a series of spectral lamps, as well as taking dark frames and flat frames. These spectra and their uses in the data reduction processes will be discussed further in the following section.

3.3 Data reduction

3.3.1 Infrared Detector Array Calibrations

Detector arrays are not perfect and there are two notable effects which must be removed from the data. The first instrumental effect is signal caused by thermal or

[6] NASA | Jet Propulsion Laboratory | California Institute of Technology. 2018. *HORIZONS Web-Interface*. [ONLINE] Available at: http://ssd.jpl.nasa.gov/horizons.cgi. [Accessed 21 January 2018].

dark currents. CSHELL and CRIRES both have liquid nitrogen cooling systems to prevent charge accumulating in the detector pixels due to thermal excitation during long integrations, however, some thermal currents still remain. Additionally, all exposures include a dark current contribution caused by the physical processes within the detector itself. This effect can be removed using dark frames, which are exposures taken when all the light into the instrument is blocked. Figure 3-8 shows a dark frame taken by CSHELL, and any signal in this dark frame is an instrumental effect. (Note that similar dark frames were taken by CRIRES). Before subtraction the dark files must be scaled to the data files by multiplying by the ratio of the exposures of the dark frame and the spectral frame. Then the dark image is subtracted from the data array, removing any false signal due to thermal excitation in the detector.

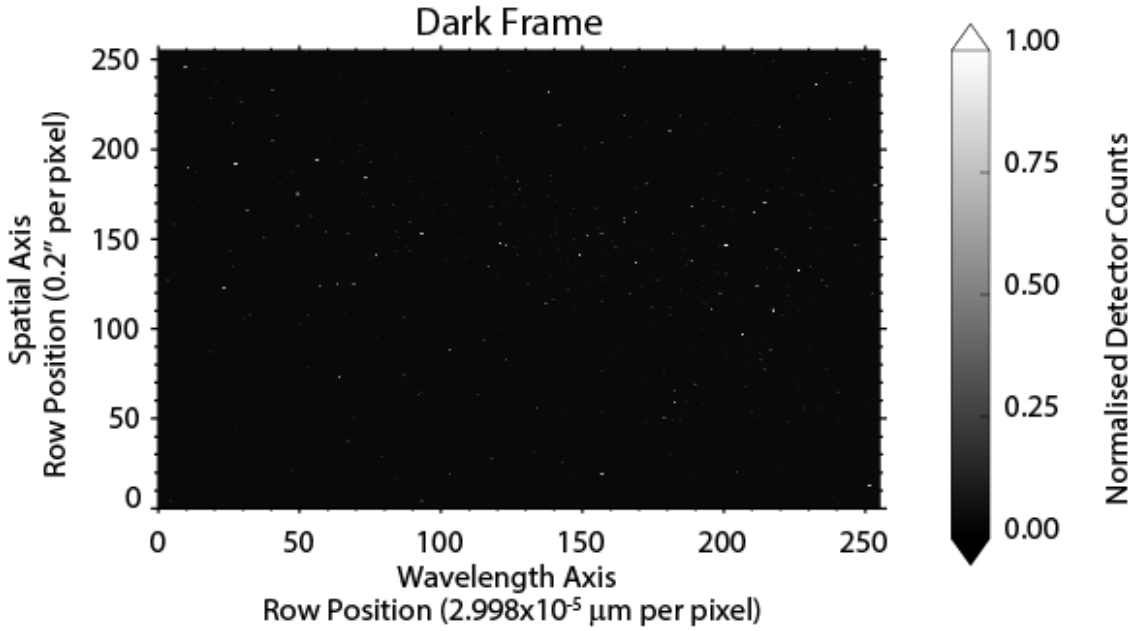

Figure 3-8: The dark frame captured by CSHELL during the observations taken in September 1998.

The second instrumental effect is the variation in pixel sensitivity caused by imperfections across the infrared detector. To correct for this, flat fields are used, where an exposure is taken of an evenly illuminated field of view, which is equal across all wavelengths and spatial direction, generated by the continuum lamp. If the detector was perfect, all pixels would detect the same signal, however, due to the imperfections some are more sensitive than other. To remove the asymmetries in the light gathering capabilities, each spectral frame is divided by the normalised flat field. The normalised flat frame is created by scaling the exposure times of the flat and dark

frame and then the dark frame is removed from the flat frame, which eliminates the false signal due to thermal excitation in the detector. An example of a normalised flat frame, created from data taken by CSHELL, is shown in Figure 3-9. (Note that similar dark frames were taken by CRIRES).

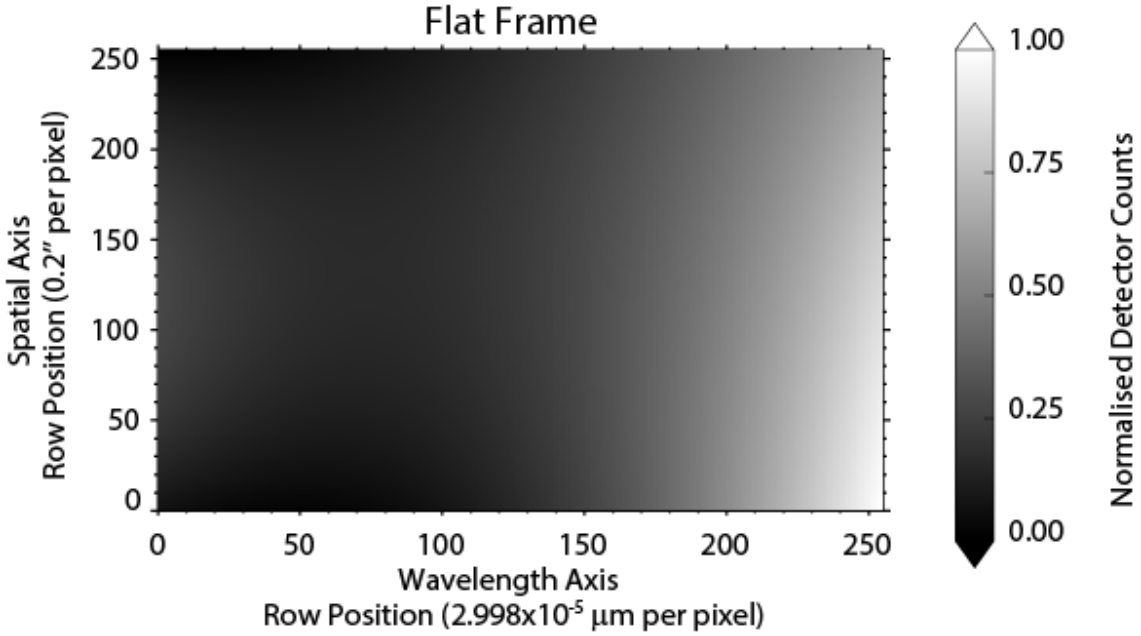

Figure 3-9: The flat frame captured by CSHELL during the observations taken in September 1998.

3.3.2 Sky Subtraction

The terrestrial emission can be removed from the jovian spectra by using a process known as 'sky subtraction' and is illustrated by Figure 3-10, which shows spectra taken by CSHELL. Spectra taken of Jupiter are known as 'A frames' and terrestrial emission spectra are known as 'B frames' and are collected by 'nodding' the telescope. A 'nod' of the telescope involves the telescope moving from the target object to a position where there is no emission from any other astronomical body. When observing Jupiter, this is typically 60'' north or south of the planet depending on which latitudes are being observed. Both terrestrial and jovian emission lines can be seen in the A frame in Figure 3-10a. Only terrestrial emission lines can be seen in Figure 3-10b as the spectrum was taken when the slit was positioned off the planet so no jovian emission lines can be recorded. Figure 3-10c shows the spectra after the A-B subtraction is performed, and it can be seen that only one jovian emission line remains.

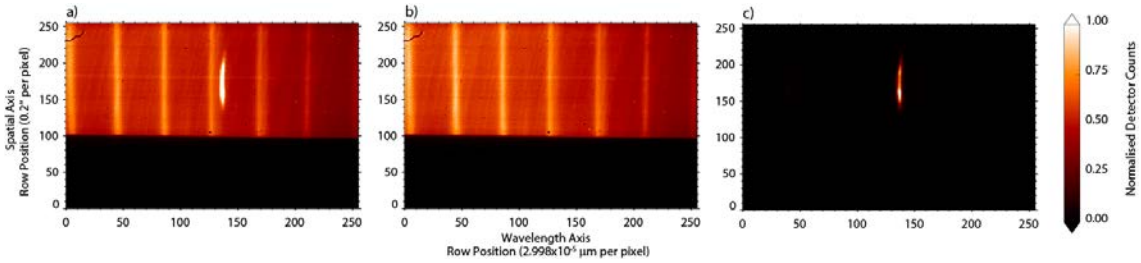

Figure 3-10: The sky-subtraction process illustrated by spectra taken with CSHELL. a) The A frame is taken when the slit is on the planet and shows a H_3^+ emission line as well as the skylines. b) The B frame is taken when the slit is postioned off the planet and only skylines are measured. c) The A-B frame is the remaining spectra after the B frame is subtracted from the A frame.

Note that both the A and B frame in Figure 3-10 have had the dark frame subtracted and been divided by the flat frame. The slit of CSHELL is 30'' or ~150 pixels on the infrared detector. Therefore, the data is recorded on the row positions in the range of ~105 – 255 on the spatial axis (y-axis Figure 3-10) and the pixels below ~105 can be disregarded as they contain no data, which is apparent in Figure 3-10. A similar situation arises for CRIRES, as the slit is 40'', which is ~450 pixels on the infrared detector, and since the detector is 512 pixels in the spatial direction, again a small part of the bottom of the array contains no data and is disregarded. At the IR wavelengths of these observations, the Earth's atmosphere does not vary significantly over a timescale of minutes, and therefore it is assumed that there is no variation over the timescales of the exposure lengths of the spectral frames used in this thesis.

3.3.3 Fitting a Gaussian Profile

In order to complete the data reduction and analysis, Gaussian profiles must be fitted to the various spectra used in this thesis. The following equation of a Gaussian profile superposed on a slowly-varying quadratic background, f(x), is used throughout this thesis to fit to spectral emission lines,

$$f(x) = A_0 e^{-z^2/2} + A_3 + A_4 x + A_5 x^2 \qquad \textbf{3.3}$$

where $z = \frac{x - A_1}{A_2}$, A_0 is the height of the Gaussian, A_1 is the pixel position of the peak of the Gaussian, and A_2 is the width of the Gaussian. The additional terms A_3, A_4 and A_5 are included to acquire a suitable fit to the background, where A_3 is the constant term, A_4 is the linear term and A_5 is the quadratic term. The variable x is the row position in

the wavelength axis of the detector array. The Gaussian profile is fitted to the data using the IDL function *gaussfit.*

Figure 3-11a shows an example of an H_3^+ emission line measured by CSHELL. The Gaussian profile has been fitted to the data at the position of the dashed white line. Figure 3-11b shows the Gaussian profile as the red line, which was fitted to the counts measured by the infrared detector of CSHELL (the black crosses). Note that similar fits were produced for the CRIRES data set.

The coefficients of the function, A_0 and A_1, are labelled in Figure 3-11 and represented by the blue arrows. Figure 3-11b shows the full width half maximum (FWHM) of the Gaussian profile, represented by the blue line. This is calculated using the width of the Gaussian, A_2, as shown by Equation 3.4.

$$\mathrm{FWHM} = A_2 \times \sqrt{2 \times \ln(2)} \times 2 \qquad \textbf{3.4}$$

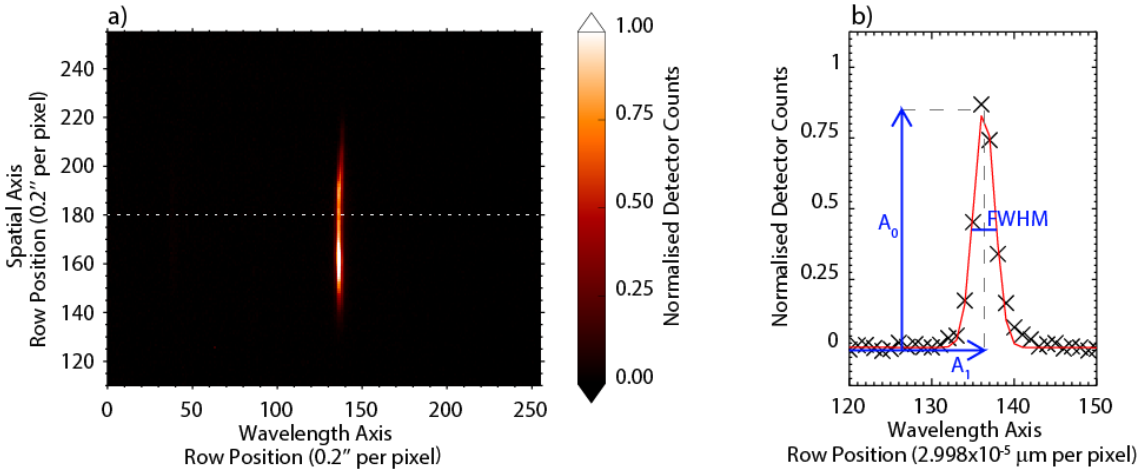

Figure 3-11: a) The Q(1,0$^-$) emission line, measured by CSHELL on 7th September 1998. The x-axis is the wavelength axis (2.998x10^{-5} µm per pixel) and the y-axis is the spatial axis (0.2'' per pixel). The emission line shows a slice through Jupiter's northern aurora. b) Shows the Gaussian profile (red line), as describe in Equation 3.3, which was fitted to the spectral data (black crosses) at the position of the dashed white line in a). The spectral data is given by the crosses and the Gaussian profile is the red line. The height of the Gaussian profile (A_0), the position of peak of the Gaussian profile (A_1) and the full width at half maximum (calculated from the width of the Gaussian profile, A_2), are labelled in b), with the blue lines showing the qualities they represent.

The following data reduction methods introduce errors into the parameters derived from the H_3^+ emission lines, in addition to the instrumentation error. Using *gaussfit*, errors are propagated to a final error at each spatial position along the slit, which is applied to the derived H_3^+ properties as discussed in the appropriate chapter.

3.3.4 Spectral Dispersion

The optics of CSHELL and CRIRES both introduce a degree of non-linearity to the dispersion on the data array. This dispersion is in both the spectral and spatial directions and must be corrected before the wavelength calibration can be performed. Additionally, it is important to remove this distortion so that it is not falsely interpreted as Doppler shifts caused by ionospheric flows. The methods used to correct the distortion of the data array are different for CSHELL and CRIRES.

At CSHELL the spectral distortion was removed using arc lines, which are emission lines produced by the spectral calibration lamps, and are shown in Figure 3-12. The arc lamp is mounted inside the instrument, moving at zero velocity relative to the instrument and therefore should produce a non-Doppler shifted emission line. Utilising the knowledge that the arc line should be completely straight, the distortion of the data array can be deduced.

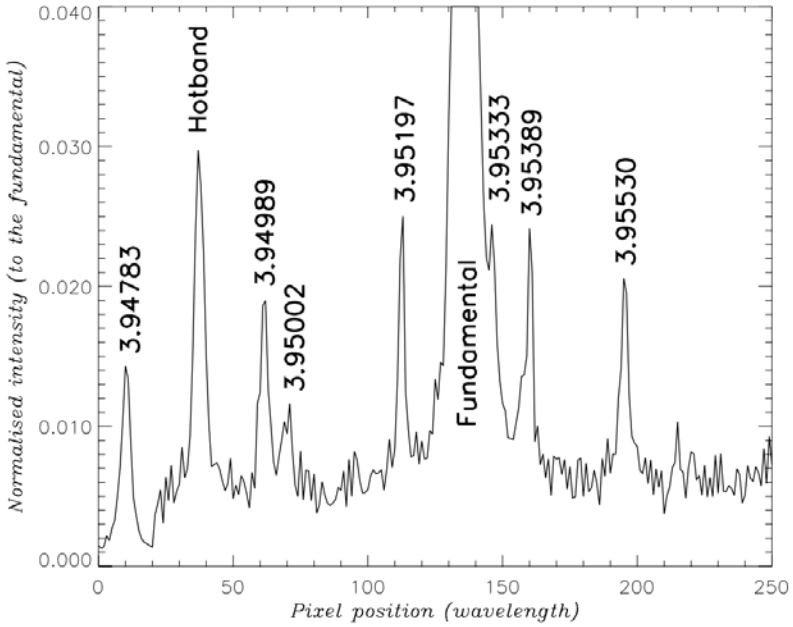

Figure 3-12: The arc lines measured by CSHELL, which are used to calibrate the spectral data array. The fundatmental Q(1,0$^-$) and the hotband emission lines are also labelled in the plot. Reproduced from Stallard (2001).

One of the closest arc line to the Q(1,0$^-$) fundamental H_3^+ emission line is at a wavelength of 3.95389 μm and is shown in Figure 3-13. Through comparison to the vertical red dashed line in this figure, it can be seen that the arc line in Figure 3-13a is distorted. A Gaussian profile (Equation 3.3) was fitted to every position in the spatial direction along the arc line (along the y-axis in Figure 3-13). The shift in position from

the first position was determined and a second order polynomial was fitted to this shift in the arc line using the IDL function *poly_fit*. Assuming a linear relationship between each arc line, the distortion across the whole array can be interpolated. Once the distortion across the whole array is known, the distortion at the position of the H_3^+ line can be removed from the spectral array.

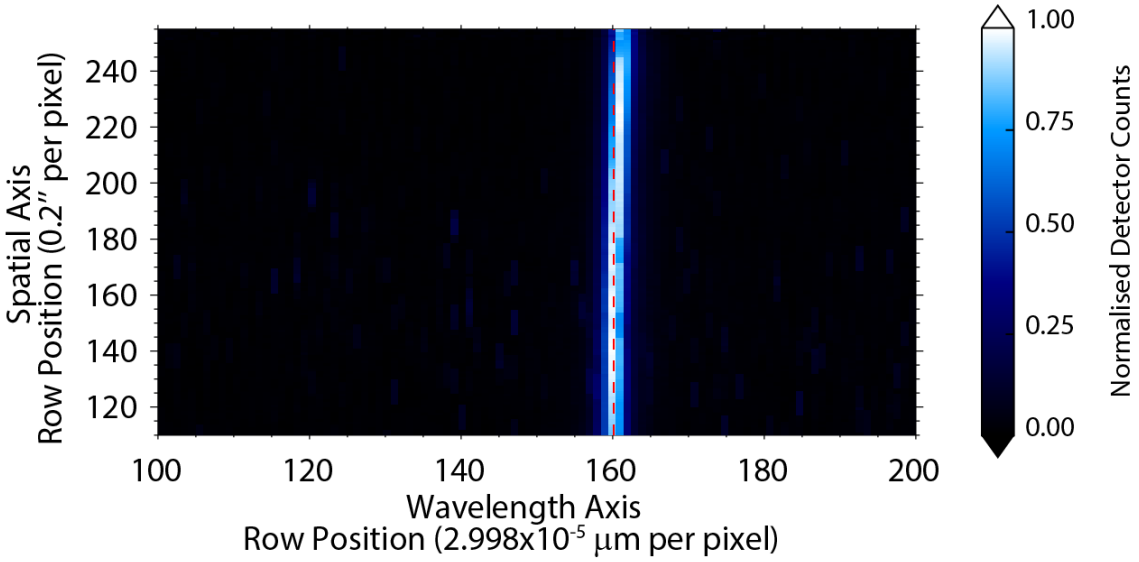

Figure 3-13: Arc lamp emission line at 3.95389 μm taken with CSHELL. The red vertical line can be used to guide the eye and shows the spectral distortion of the arc line.

It was not possible to use this method for the CRIRES data arrays as the available spectral emission lamps did not fall in the required wavelength range. Therefore, the terrestrial emission lines, known as sky lines, were used to correct the spectral dispersion across the array. This is not a viable method for the CSHELL data set as the spectral resolution is insufficient; however, it is an appropriate substitution for the CRIRES data set due to the high spectral resolution of CRIRES. Figure 3-14a shows the skylines across the 4 detectors of CRIRES. By fitting a surface to the position of the telluric emission lines across each array, the spectral dispersion across each array, in both the wavelength (x-axis) and spatial (y-axis) direction was determined, which can then be removed from the data array.

3.3.5 Spatial Distortion

For the CRIRES data set there is a discrepancy in the alignment of the 4 detector arrays in the spatial direction. It is important that the emission lines are precisely aligned because if not then the offset will cause false temperatures to be derived as the ratios

between emission lines will not be correct. By using the stellar spectra, the 4 detector arrays can be aligned in the spatial direction.

Figure 3-15 shows the spectra of the A0 star HR1578, which was used to calibrate the CRIRES data set. During the observations the star was kept on the slit, so that it was measured in both the A and B beams, hence the positive and negative spectra visible in Figure 3-15Figure 3-15. Using the horizontal yellow dashed line, it can be seen that as the wavelength increases along the x-axis, the stellar spectra appears at lower values of row position on the y-axis. To determine the position of the stellar spectra in each detector array, the sum of the stellar spectra was taken in the wavelength direction and a Gaussian was fitted to this for each array. Using the first array as a reference, the subsequent arrays were shifted to align them. The relevant shift for each detector array was subsequently applied to the jovian spectra.

3.3.6 Wavelength Calibration

The wavelength calibration is important as it aids H_3^+ line identification and flux calibration. For the CSHELL data arrays, the arc lines were fitted with a Gaussian profile and through determining the exact pixel separation between the arc lines, the wavelength scale could be established. Since CRIRES has a high spectral resolution, the skylines can be used to perform the wavelength calibration. It is possible to identify the wavelength of these skylines because of the large number of well characterised telluric emission lines.

The infrared spectrum of the atmospheric transmission was generated using the ATRAN modelling software (Lord, 1992). Figure 3-16 shows the skylines for each detector array of CRIRES, as the black lines. The grey dotted line shows the infrared spectra of atmospheric transmission, this gives the proportion of the infrared signal that is transmitted through the Earth's atmosphere. Within the region of the skylines, the transmission of infrared signal from external sources (i.e.: Jupiter) are reduced significantly. Each prominent skyline in each detector array was fitted with a Gaussian, and by using the infrared spectra of atmospheric transmission, the wavelength at each pixel position of the skylines could be determined and hence complete the wavelength calibration of the detector arrays.

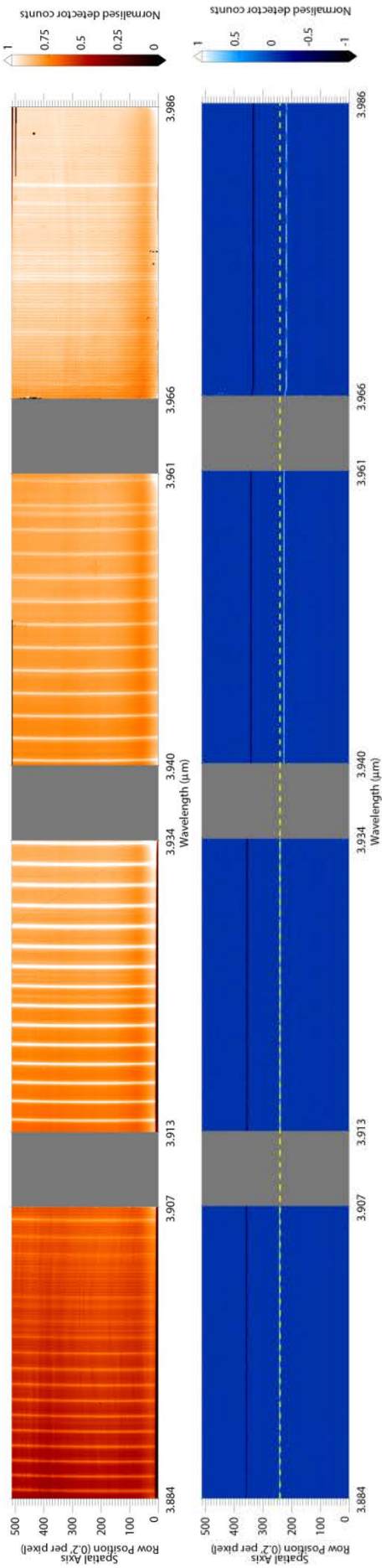

Figure 3-14: The skylines measured by CRIRES across the four detector arrays before the spectral dispersion correction is performed. Although these arrays have been reduced they still contain some data artefacts. The detector counts have been normalised.

Figure 3-15: The stellar spectra measured by CRIRES across the four detector arrays. The horizontal dashed yellow line shows the difference in position of the spectra in each detector array. The detector counts have been normalised.

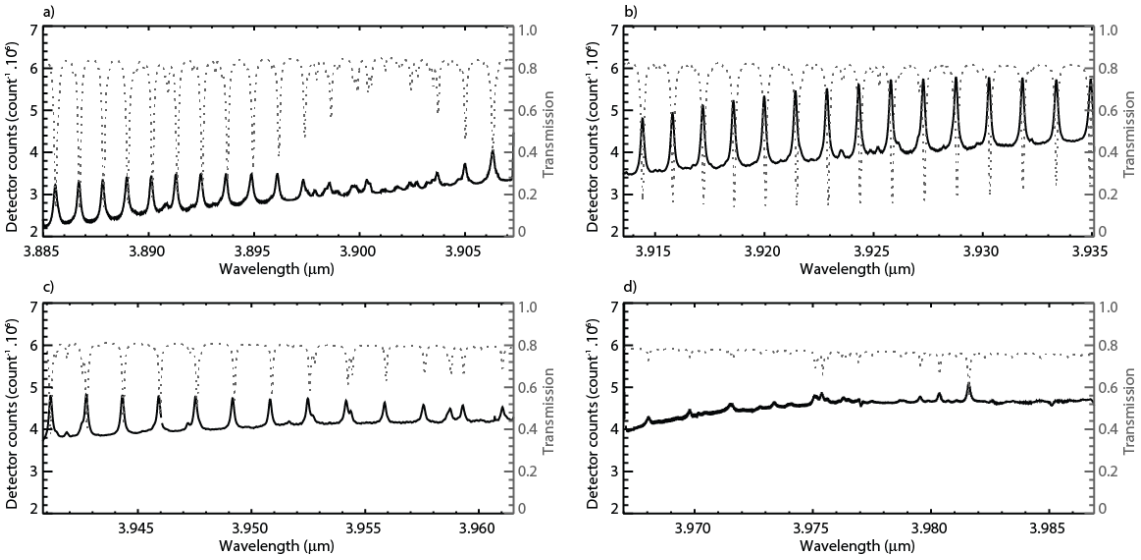

Figure 3-16: Four plots showing the skyline lines measured by CRIRES (black lines) over the 4 detector, with the units count^{-1}. The model skylines are represented by the dotted grey line and are taken from the ATRAN modelling software (Lord, 1992).

3.3.7 Flux Calibration

The flux calibration process converts the jovian spectra from counts per second to flux. Additionally, any terrestrial absorption is accounted for by performing the flux calibration. During each observing run spectra are taken of a standard star and the stars used to calibrate the observations in this thesis are shown in Table 3-2. The star selected must be at an air mass that is representative of the majority of the observations. The star must be an A0 main sequence star as this star emits as an almost perfect black-body in the infrared, with very few emission lines. A flux calibration spectrum is used to calibrate the jovian spectra and is determined by dividing the theoretical flux from a perfect black-body emitter by the flux observed from a standard star.

Table 3-2: The stars used to calibrate the CSHELL and CRIRES data sets

Instrument	Observations	Star
CSHELL	7 – 11 September 1998	BS8647
	2, 3 June, 2, 3, 4 March 2007	BS5384
	25 February 2007	BS3492
	19, 22, 21 April 2013	HR4781
CRIRES	31 December 2012	HR1578

The modelled black body spectrum of the star, $F_{bb}(\lambda)$, is given by the following equation,

$$F_{bb}(\lambda) = F_{A0}(\lambda) \times \left(\frac{\lambda_{AW}}{\lambda}\right)^5 \times \left(\frac{\exp\left[\frac{hc/k_B}{\lambda_{AW} \times T}\right]}{\exp\left[\frac{hc/k_B}{\lambda \times T}\right]}\right) \quad \textbf{3.5}$$

where λ_{AW} is the wavelength of the atmospheric window, the constant 14,388 μm K is from the product of h is the Planck constant (~6.63 x 10^{-34} J s), c is speed of light (~2.99 x 10^{8} m s^{-1}), k_B is the Boltzmann constant (~1.38 x 10^{-23} J K^{-1}), and $F_{A0}(\lambda)$ is the flux of the A0 star in the particular atmospheric window it was observed in. The black body curve depends on the temperature of the star and the magnitude at a certain wavelength. Since an A0 star is used, it can be assumed that the temperature is T ~ 10,000 K and this determines the shape of the black body curve. $F_{A0}(\lambda)$ is given by the following equation,

$$F_{A0}(\lambda) = F_{\alpha\ Lyrae} \times 10^{-0.4 m_\lambda} \quad \textbf{3.6}$$

where m_λ is the magnitude of the star at the wavelength of the atmospheric window, -0.4 is a constant, and $F_{\alpha\ Lyrae}$ is the flux of α Lyrae (Vega) in this atmospheric window. The apparent magnitude of a star is the measure of the flux it produces at given wavelength. The magnitude of every star is measured relative to α Lyrae, which has been assigned an apparent visual magnitude of zero. Blackwell et al. (1983) made measurements of α Lyrae intensities in each atmospheric window.

The observed flux can be derived from the star spectrum, such as the one shown in Figure 3-15Figure 3-15 for HR1578. First, the star spectrum in Figure 3-15 was divided by the exposure time to convert the data array into counts per second, and then a Gaussian profile was fitted to the star spectra at every spectral position (along the x-axis in Figure 3-15). Using the height of the Gaussian profile (A_0) and the FWHM, the observed flux ($F_{observed}$ [$count^{-1}$]) of the star can be derived, as shown by the following equation,

$$F_{observed} = A_0 \times FWHM \quad \textbf{3.7}$$

where FWHM is calculated using Equation 3.4. To account for any light emitted from the star that was not collected by the slit, observed flux of the star must be multiplied by a factor which takes this light into account. The area of the slit is divided by the full

width at half maximum and then the observed flux is then multiplied by this factor, which now includes the light from the wings of the Gaussian that were not previously captured by the observation.

Figure 3-17 shows the observed flux of HR1578 as the black line and the modelled black body spectrum is given by the grey line. There is a lot of variation in the observed flux of HR1578 due to the Earth's atmosphere absorbing different amounts of radiation at different wavelengths. Similar models were created for the calibration star spectra used in the CSHELL investigation.

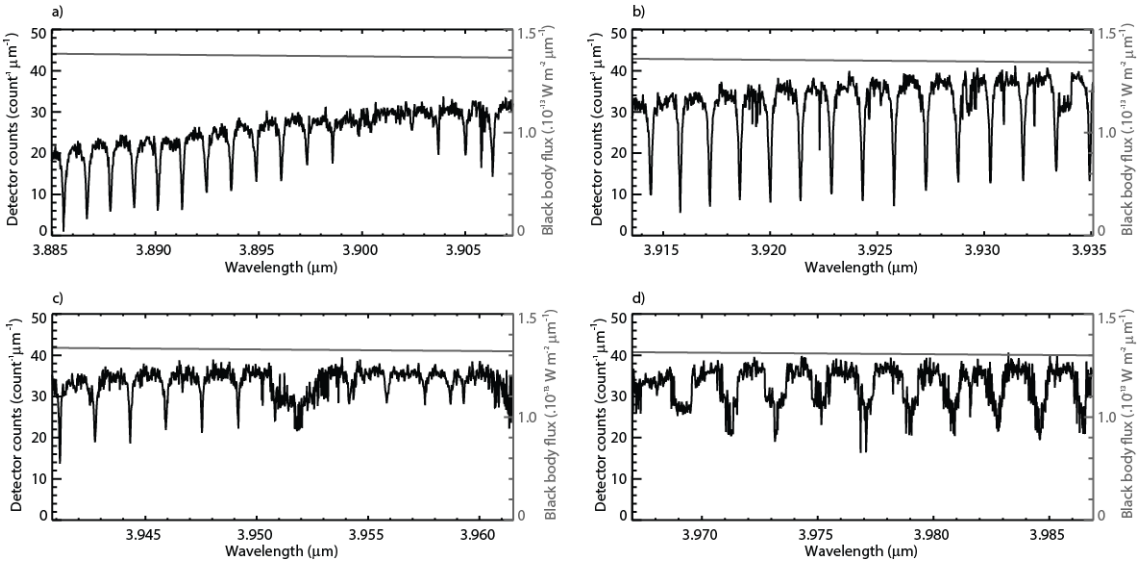

Figure 3-17: The spectrum of HR1578, taken by CRIRES on 31 December 2012 and recorded across the 4 spectral arrays. The detector counts as a function of wavelength is given by the black line. The modelled theoretical flux from a perfect black-body emitter for this star is given by the grey line.

The calibration spectrum (F_C) can now be calculated using Equation 3.8, where the model black body spectrum of the star $F_{bb}(\lambda)$ is divided by the observed flux from the star $F_{observed}$.

$$F_C = \frac{F_{bb}(\lambda)}{F_{observed}} \qquad \textbf{3.8}$$

The calibration spectrum for the CRIRES data is shown in Figure 3-18. Similar calibration spectra were made for CSHELL. This calibration spectrum is multiplied by the jovian spectra (F_J) to create a flux calibrated jovian spectra (F_{JC}). This process is achieved using Equation 3.9, which also has additional constants to calibrate the units: The number of arc seconds squared in a steradian (~4.2545 x 10^{10}) and the area of each pixel in arc seconds, A. The latter can be calculated through the product of the

number of arc seconds per pixel and the slit width in arc seconds. Therefore, the final units of the flux calibrated spectra are W m^{-2} sr^{-1} μm^{-1} and is more commonly referred to in astronomy as the spectral radiance, which is the flux emitted per unit of solid angle per unit wavelength.

$$F_{JC} = F_J \times F_C \times \frac{4.2535 \times 10^{10}}{\mathrm{A}} \qquad \textbf{3.9}$$

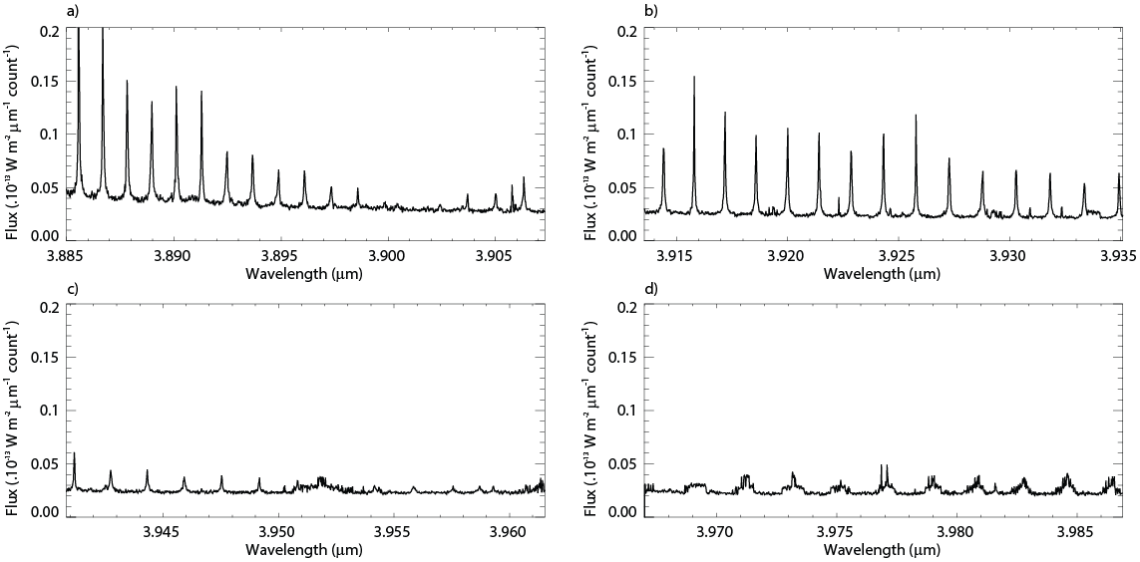

Figure 3-18: The calibration spectrum for the CRIRES data set of the 31 December 2012, shown across the four detector arrays.

3.4 Data sets

3.4.1 CSHELL Data set

Chapter 4 investigates the line-of-sight velocity of the H_3^+ ions in the mid-to-low latitude ionosphere of Jupiter. The latitudinal range used in this study is specified in Chapter 4. The data used in this investigation were from several nights of observations using CHSELL taken in 1998, 2007 and 2013: 5 nights in 1998 (7 – 11 September), 2 nights in 2007 (2, 3 June) and 3 nights in 2013 (19, 21, 22 April). As Jupiter and the Earth are moving relative to each other, the angular width of Jupiter's equatorial diameter changes over the years observed: over the three separate observations it was ~49.7'', 45.8'' and 34.2''. The observer sub-latitude was ~2.5°, -3.3° and 2.9° for 1998, 2007 and 2013 respectively, which defines the latitude of the centre of Jupiter's disk as seen at the specific location of the observer. A wide range of observer sub-

longitudes were observed as Jupiter's rotation rate is small (period ~9.7 hours) relative to the length of the observations.

In 1998, scans of the northern and southern auroral regions were carried out using an observing methodology described in detail by Stallard et al. (2001) and the observations in 2007 were made in a similar way. The slit was aligned East-West on Jupiter, perpendicular to the rotational axis. During a scan the telescope is positioned so that the slit of CSHELL is at the Northern or Southern polar limb of Jupiter and then the telescope is moved equatorward to discrete positions over the auroral region. Additionally, the 1998 and 2007 observing procedure included a jump to the equatorial regions and it is these measurements that are reported upon in Chapter 4. No auroral data was taken in 2013 as the telescope was at a fixed equatorial position; hence all the measurements taken in this year were used in the investigation discussed in Chapter 4.

Across these observations, the weather varied significantly, and therefore certain spectra could not be used in the final data analysis as discussed in Chapter 4. During bad weather the beam pattern was ABBA, however, if the skies were clear the most common beam pattern was ABAAAABA. The exposure time used for all CSHELL A and B frames was 50 seconds. Dark and flat frames were taken, as well as spectra of a standard stars, which are shown for each observation in Table 3-2.

3.4.2 CRIRES Data set

Chapter 5 and Chapter 6 investigate the LOS velocities, rotational temperatures, column densities and total emission of H_3^+ in the northern auroral region of Jupiter. The observer sub-latitude of Jupiter was +3.4°, therefore, the northern aurora was favourably displayed. The data used for these investigations was taken with CRIRES on the 31 December 2012. During the observations Jupiter was setting, causing the air mass to increase from 1.4 to 1.6 atmospheres, which decreased the signal-to-noise. The weather was clear and stable, with the seeing at ~0.5'', causing minimal smearing of the spectra. In additional to dark and flat frames, and stellar spectra, six individual spectra were taken with the slit of CRIRES in a North-South orientation with the slit aligned along the CML. As Jupiter's equatorial diameter subtended 46.9'' on the sky on

the 31 December 2012, the 40'' slit of CRIRES encompassed the northern aurora and the mid-to-low latitude region of Jupiter's ionosphere.

During the observations, the auroral region was repeatedly scanned with the slit aligned West-East on Jupiter, perpendicular to the rotational axis. The scan involved positioning the slit at the polar limb with the centre of the slit aligned on the centre of the planet, and then incrementally adjusting the telescope so that the slit is stepped equatorward through the auroral region, with step sizes equivalent to the slit width of 0.2''. The scans cover a region from the polar limb of the planet through to ~45° latitude which takes 35 steps. The exposure time for each spectrum was 25 seconds. As the weather during the observation was good, B frames were taken at the start and end of the scans. For this investigation six scans taken from 02:13 to 04:15 UT on 31 December 2012 are used as these provide the most complete view of Jupiter's northern H_3^+ aurora.

3.5 Extracting the H_3^+ Properties

3.5.1 Intensity

The intensity (I [W m^{-2} sr^{-1}]) of the H_3^+ emission lines can be calculated with the following equation,

$$I = A_0 \times \mathrm{FWHM} \qquad \textbf{3.10}$$

where A_0 [W m^{-2} sr^{-1} μm^{-1}] is the spectral radiance (Section 3.3.7), and FWHM is derived using Equation 3.4. Figure 3-19b shows the intensity profile derived from an average H_3^+ emission line taken by CRIRES, which is shown in Figure 3-19a. The H_3^+ emission lines used in this average are discussed in Chapter 5.

A two-dimensional intensity map (or spectral image) can be built by sequentially plotting the intensity derived at each slit position in the scan, and an example of which, taken by CRIRES is shown in Figure 3-20. To lower the contrast, and allow different features in Jupiter's aurora to be easily identified, a gamma correction of 0.4 was applied to the spectral image in Figure 3-20. The gamma correction (γ) is applied to the intensity using the following equation,

$$I_{out} = I^{\gamma} \qquad \textbf{3.11}$$

where I is the linearly scaled intensity and I_{out} is the non-linear corrected intensity.

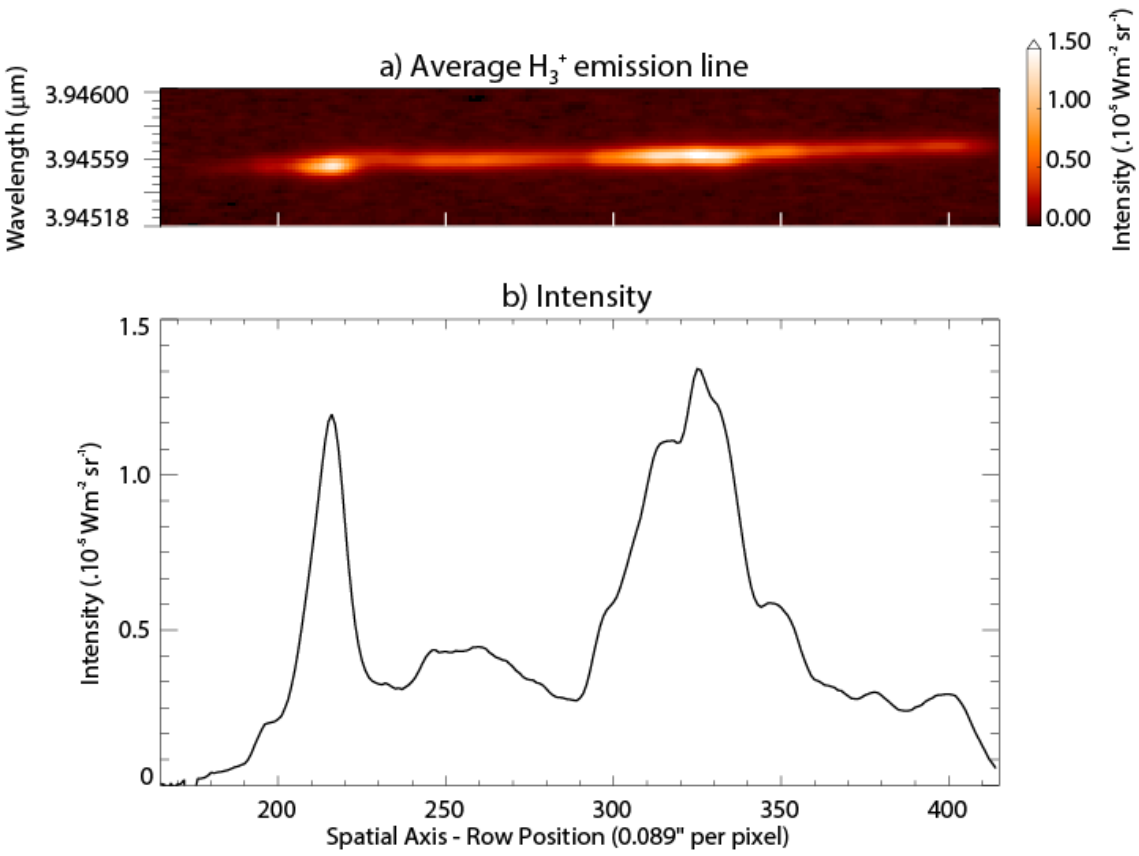

Figure 3-19: a) An average H_3^+ emission line taken when the centre of the slit was positioned at CML ~173° and latitude ~66°. b) The intensity profile derived by fitting a Gaussian to every spatial position along the average H_3^+ emission line in a). The x-axis in both a) and b) is the spatial axis (0.089'' per pixel) and the centre of the rotational axis is assumed to be at the centre of the slit.

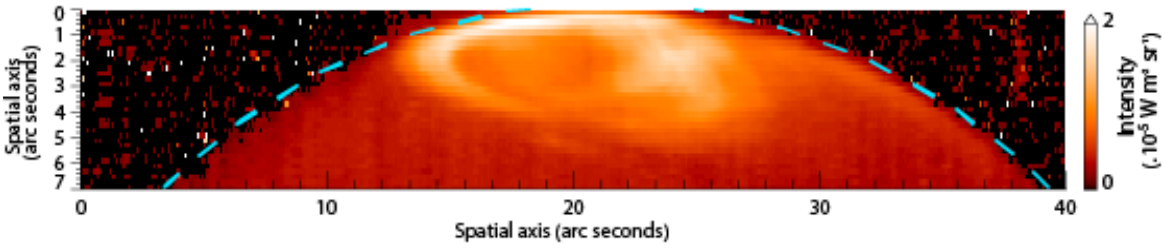

Figure 3-20: A spectral image covering a CML range of 180° - 193°, taken by CRIRES on 31 December 2012. The 2D intensity map is created by sequentially plotting the intensity profiles. The white arrow shows the direction of the scan. The spectral image is overlaid with a calculated planetary limb (blue dashed line) which was manually fitted to the planetary disk. A gamma correction of 0.2 was applied to the spectral image. The x-axis corresponds to the slit width (40'') and the y-axis corresponds to the scan length. Each step in the scan is equivalent to one slit width (0.2'') and the total scan length is ~7'' which was 35 steps (note that Jupiter's equatorial width during the observations was ~47'').

3.5.2 Mapping

3.5.2.1 Pixel assignment of latitude and longitude

For the investigations in Chapter 5 and Chapter 6, it was important to assign the pixels in the spectral image (and other 2D maps of data products) with a latitude and longitude. To locate the limbs, the spectral image was overlaid with a calculated planetary limb, accounting for Jupiter's polar flattening, the sub-Earth latitude, and the plate scale of CRIRES. This calculated planetary limb is shown in Figure 3-20, and is an oblate spheroid which has a semi-major axis of Jupiter's equatorial radius and a semi-minor axis of Jupiter's polar radius at the 1 bar level, both radii with an additional 550 km altitude to approximate the peak emission height of H_3^+ (Melin et al. 2005).

The H_3^+ emission observed on the dawn limb is weaker than the emission observed on the dusk limb because of low production rates. Stallard et al. (2015) showed an absence of non-auroral H_3^+ emission on the nightside, but once the nightside ionosphere rotates through dawn the H_3^+ production can begin, which starts with ionisation of H_2 by EUV. This generation of H_3^+ isn't instantaneous and the dawn limb is not fully illuminated, so the production rates of H_3^+ are lower at the dawn limb than the dusk. Therefore, the position of the calculated planetary limb (blue dashed line in Figure 3-20) was manually fitted to the dusk limb of the planet. It was assumed that there was no drifting of the telescope during a scan and the guiding was completely accurate. This is a reasonable assumption due to the reliable off-axis guiding provided by the VLT.

Once the location of the limb in each spectrum was known the latitude and longitude could be assigned to the corner of each pixel. Using the row position of each pixel, and taking into account the polar flattening of Jupiter, the distance from the centre of the planet in pixels (r) can be determined using Equation 3.12, where x and y are positions along the x- and y-axis of Figure 3-20, which both have units of pixels.

$$r = \sqrt{x^2 + y^2} \qquad \textbf{3.12}$$

The angular distance from the centre (θ) is then calculated using Equation 3.13, where R is the equational radius of Jupiter in pixels (R ~ 273 pixels).

$$\theta = \sin^{-1}\left(\frac{r}{R}\right) \qquad \textbf{3.13}$$

The longitude (λ) and latitude (ϕ) can be calculated using equations 3.14 and 3.15, where SEL is the sub-earth latitude of the telescope and CML is the central meridian longitude.

$$\lambda = \mathrm{CML} - \tan^{-1}\left(\frac{\mathrm{x} \times \sin(\theta)}{\mathrm{r} \times \cos(\mathrm{SEL}) \times \cos(\theta) - \mathrm{y} \times \sin(\mathrm{SEL}) \times \sin(\theta)}\right) \quad \textbf{3.14}$$

$$\phi = \sin^{-1}\left(\cos(\theta) \times \sin(\mathrm{SEL}) + \frac{\mathrm{y} \times \sin(\theta) \times \cos(\mathrm{SEL})}{\mathrm{r}}\right) \quad \textbf{3.15}$$

3.5.2.2 Line-of-sight Intensity Correction

When an image or spectrum is taken of Jupiter at near-IR wavelengths, limb brightening is observed. The limbs appear brighter than the centre of the planet due to an effect caused by the observer's line-of-sight intercepting more H_3^+ emission towards the limb of Jupiter. Once the LOS intensity correction has been performed, the intensity value will appear as viewed normal to the planetary surface.

The LOS intensity correction is performed by calculating the limb brightening and removing this from the 2D intensity maps. Since the latitude and longitude have been assigned to each pixel, the pathway from the centre of the planet to each pixel ($r_{pathway}$) can be determined. The LOS intensity correction value (LOS_c) is determined using a cosine function of the pathway ($r_{pathway}$) and the planetary radius ($r_{planetary\_radius}$) at the particular latitude of the pixel.

$$\mathrm{LOS_c} = \cos\left(\frac{\mathrm{r_{pathway}}}{\mathrm{r_{planetary\_radius}}}\right) \quad \textbf{3.16}$$

Figure 3-21 shows the intensity for an individual emission line before the LOS intensity correction as the black dotted line. The LOS intensity correction is shown by the dashed red line. The LOS intensity correction is performed through multiplication of the LOS intensity correction values and the uncorrected intensity values, as shown in Equation 3.17.

$$I_{LOS_c} = I \times LOS_c \quad \textbf{3.17}$$

The correction reduces the intensity across the whole region (as the entire auroral region is located close to the limb), with the limb brightening effect strongest at the ends of the slit. After correction, the LOS corrected intensity ($\mathrm{I_{LOS_c}}$) is significantly lower, as shown by the black line in Figure 3-21.

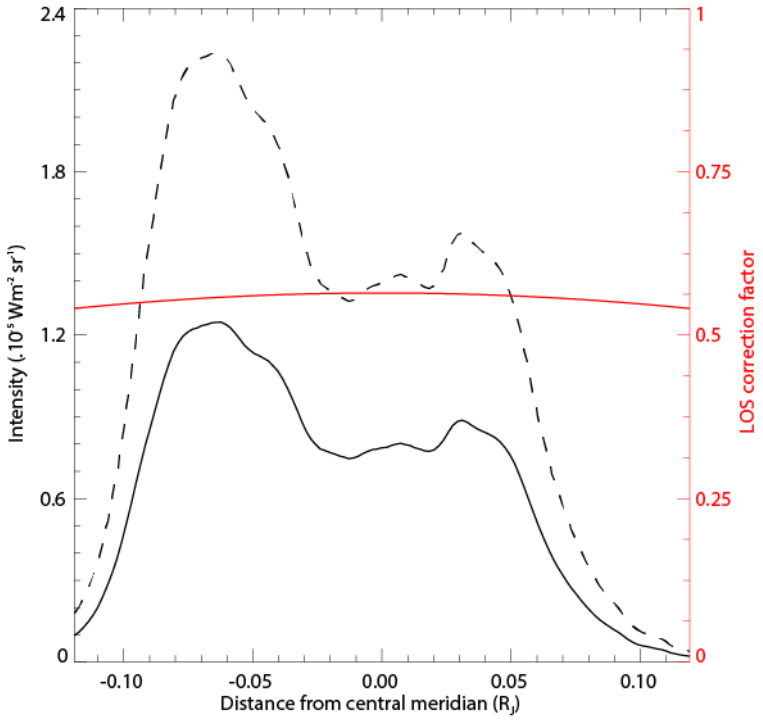

Figure 3-21: Intensity calculated from CRIRES data taken at CML ~170° and latitude of ~82°. The x-axis represents the distance from the central meridian line and is in R_J, where R_J ~71,492 km plus the peak emission height of H_3^+, which is ~550 km. The dashed red line represents the LOS intensity correction factor that is applied to the reduced data. The black dashed line represents the intensity derived prior to LOS intensity corrections. The black line represents the intensity after the LOS intensity correction is performed.

3.5.3 Line-of-sight Velocity

The LOS velocity of the H_3^+ ions can be derived from the Doppler shift of the average H_3^+ emission line. Through interpretation in different reference frames and observing the aurora as it rotates through different CMLs, a near complete picture of the flows in Jupiter's ionosphere can be attained.

By relating the spectral resolution ($R = \lambda/\Delta\lambda$) to the Doppler shift of the H_3^+ emission line, which is taken as the position of the peak of the Gaussian (A_1), the measured LOS velocity (v_m) can be derived using the following equation,

$$v_m(y) = A_1(y) \times \frac{1}{R} \times c \qquad \textbf{3.18}$$

where c is the speed of light and y is the spatial position along the H_3^+ emission line. A positive v_m implies the H_3^+ ions are moving towards the observer (blue-shifted) and a negative v_m implies moving away (red-shifted).

3.5.3.1 The Observers Reference Frame

The measured LOS velocity (v_m) includes the relative velocity of the observer and Jupiter hence a zero point velocity (v_0) must be subtracted from v_m. The zero point velocity is specific to each investigation in this thesis, and is discussed in the relevant chapter. The first reference frame used in both the CSHELL and CRIRES studies is the observers reference frame (ORF). To transform into this reference frame, Equation 3.19 is used to derive LOS velocities in the ORF, $v_{ORF}(y)$.

$$v_{ORF}(y) = v_m(y) - v_0 \quad \textbf{3.19}$$

An example of the LOS velocities in the ORF is shown in Figure 3-22 as the red line. This data was taken by CSHELL on 7 September 1998 and it was used in the investigation in Chapter 4. The orientation of the slit was perpendicular to the rotational axis when the slit was at the mid-to-low latitudes (further information will be given on the location of slit on Jupiter in Chapter 4). Since the slit of CSHELL was centred on the planet's rotation axis, in this reference frame the centre of the planet is set to zero velocity relative to the observer. The centre of the slit is at approximately row position 180, and the positive values of LOS velocity at row positions less than 180 represent the region of Jupiter's ionosphere which is rotating towards the observer, and the negative values of LOS velocity at row positions greater than 180 represent the region of Jupiter's ionosphere which is rotating away from the observer.

3.5.3.2 The Planetary Reference Frame

The thermosphere is strongly coupled to the ionosphere at Jupiter, as discussed in Section 2.5, and so it is useful to derive a reference frame in which flows are relative to the planet. As in Stallard et al. (2001), the LOS velocities can be transformed into the planetary reference frame (PRF), which rotates with System III. The LOS component of Jupiter's rotation varies linearly across the disk of the planet, as described by Stallard et al. (2001),

$$v_r(y) = \frac{v_{r_0} y'}{R_{pixels}} \quad \textbf{3.20}$$

where v_{r_0} is the LOS velocity at the equatorial limb, y' is the distance in pixels from the centre of the planet and R_{pixels} is the equatorial radius in pixels. In Figure 3-22, $v_r(y)$ is represented as the dashed red line, which is the corotational velocity in the ORF.

To transform into the PRF, Equation 3.21 is used to derive LOS velocities in the PRF, $v_{PRF}(y)$.

$$v_{PRF}(y) = v_{ORF}(y) - v_r(y) \quad \textbf{3.21}$$

The LOS velocities in the PRF, calculated from CSHELL data, are shown in Figure 3-22 by the black line. If the ions are corotating in this reference frame then they will have zero velocity, and hence, the line of corotation is shown by the dashed black line. The small variations from corotation seen in Figure 3-22 are discussed in Chapter 4.

3.5.3.3 Magnetic Pole Reference Frame

The ionosphere is also strongly coupled to the magnetosphere; hence it is useful to derive a reference frame in which the LOS component of the angular velocity of the magnetic pole is set to zero. This reference frame is known as the magnetic pole reference frame (MPRF) and was defined by Stallard et al. (2003). For the investigation in Chapter 5 the auroral centre defined by Grodent et al. (2004) is used as a proxy for the northern magnetic pole as the dipole location was not suitable for this study.

The magnetic pole correction velocity for each slit position (v_{MP}) calculated by the following equation,

$$v_{MP} = 3.41 \times \sin(185 - CML) \times \cos(SEL) \quad \textbf{3.22}$$

where 185° is the longitudinal position of the auroral centre and the calculated velocity of the magnetic pole (~3.41 km s^{-1}), and given by Equation 3.22.

To transform into the MPRF, Equation 3.23 is used to derive LOS velocities in the MPRF, $v_{MPRF}(y)$.

$$v_{MPRF}(y) = v_{ORF}(y) - v_{MP} \quad 3.23$$

Figure 3-23a is an average H_3^+ emission line, which is discussed further in Chapter 5. From this average H_3^+ emission line the LOS velocity in each reference frame can be derived, as shown in Figure 3-23b. The LOS velocities in the PRF are represented by the black line, with the dashed black line showing the corotational velocity in that reference frame. The LOS velocities in the ORF are represented by the red line, with the dashed red line showing the rotation rate of the planet, which is the corotational velocity in this reference frame. The LOS velocities in the MPRF are represented by the blue line, and the corotation in this reference frame is shown as the blue dashed line.

By comparing the LOS velocities in the ORF and MPRF, it can be seen that the zero point has been shifted from the centre of the planet to a position where the LOS component of the angular velocity of the magnetic pole has been set to zero. The large scatter of values of LOS velocity at row positions less than 180 are generated by noise measured in the dawn sector of Jupiter's ionosphere. More detail on the ionospheric flows shown in Figure 3-23 will be given in Chapter 5.

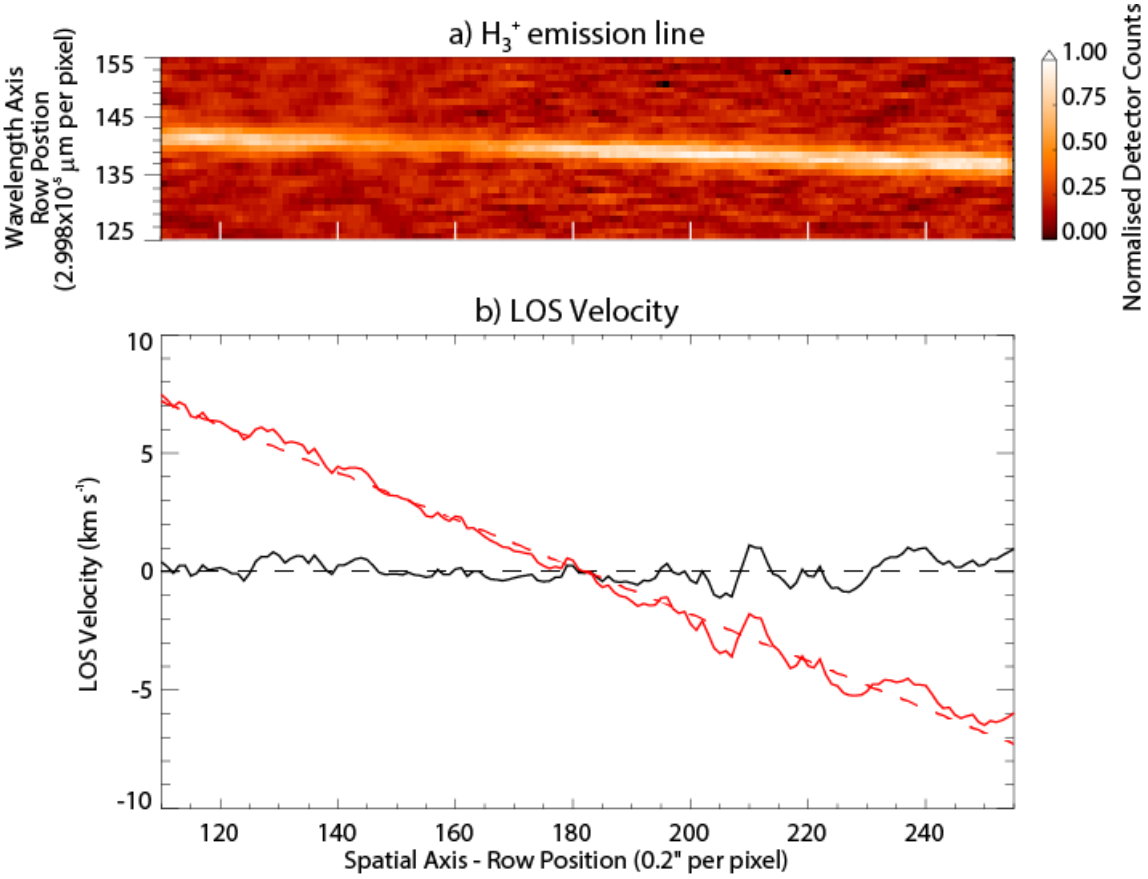

Figure 3-22: a) The H_3^+ emission line taken by CSHELL on 7th September 1998 when the centre of the slit was positioned at CML ~90° in the mid-to-low latitude region. b) Two mid-to-low latitude LOS velocity profiles, derived by fitting a Gaussian to every spatial position along the average H_3^+ emission line in a). The LOS velocity in the observer reference frame (ORF) is indicated by the red line. This reference frame includes the LOS component of Jupiter's rotation, which is represented by the dashed red line. The LOS velocity in the planetary reference frame (PRF) is indicated by the black line. In this reference frame the LOS component of Jupiter's rotation has been removed and the H_3^+ ions that are corotating will have a velocity of zero, represented by the dashed black line. The x-axis in both a) and b) is the spatial axis (0.2'' per pixel) and the centre of the rotational axis is assumed to be at the centre of the slit.

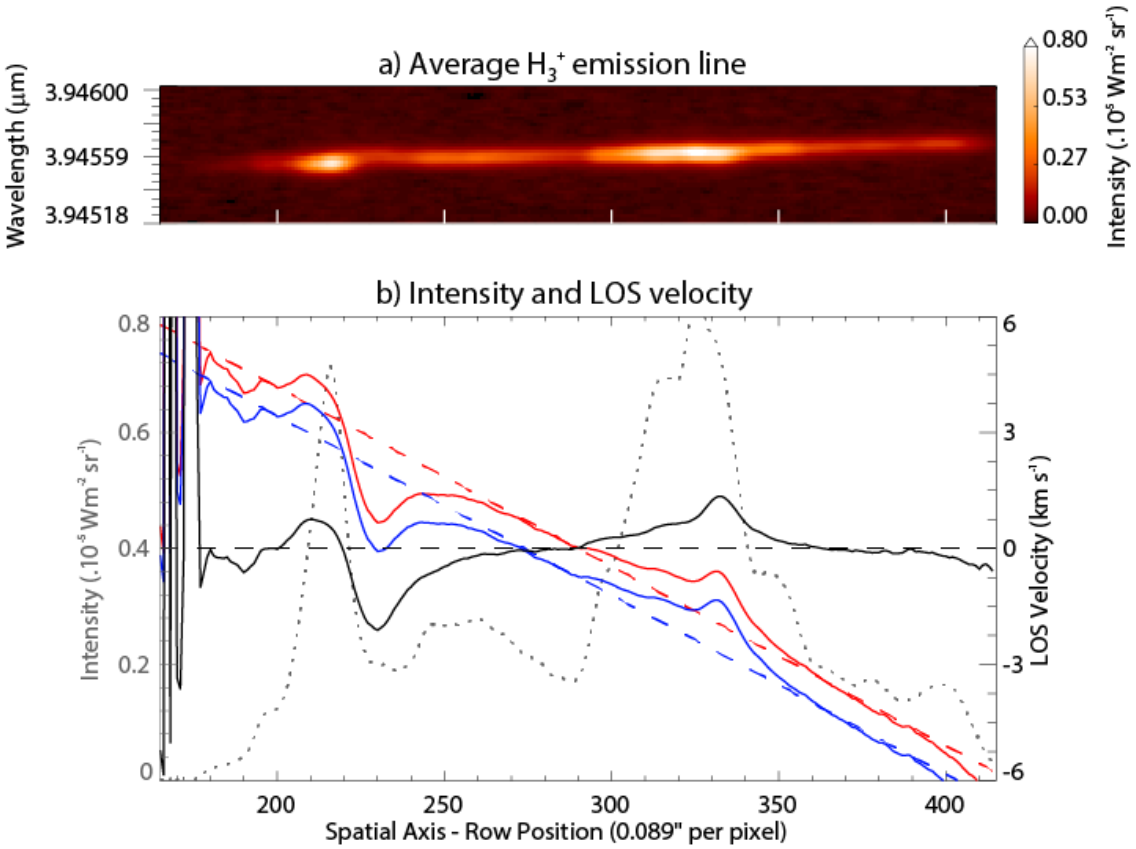

Figure 3-23: (a) An average H_3^+ emission line taken when the centre of the slit was positioned at CML ~173° and latitude ~66°. A gamma correction of 0.6 was applied to the average H_3^+ emission line. (b) Intensity and line-of-sight (LOS) velocity derived from the average H_3^+ emission line. The grey dotted line is the LOS corrected intensity of the average H_3^+ emission line. The red line is the LOS velocities of the H_3^+ ions in the observers reference frame (ORF), and the red dashed line represents corotation in this reference frame. The blue line is the LOS velocities of the H_3^+ ions in the magnetic pole reference frame (MPRF), and the blue dashed line represents corotation in this reference frame. The black line is the LOS velocities of the H_3^+ ions in the planetary reference frame (PRF), and the black dashed line represents corotation in this reference frame. The x-axis in both a) and b) is the spatial axis (0.2'' per pixel) and the centre of the rotational axis is assumed to be at the centre of the slit.

3.5.3.4 LOS velocity spatial correction

The variation in Jupiter's aurora cause uneven illumination across the slit leading to false Doppler shifts in the apparent line position of those generated by the motion of the H_3^+ ions. A correction must be applied, in all reference frames, to remove the LOS spatial anisotropy velocities which arise from these false Doppler shifts. This effect can be disregarded when observing lower latitudes, where the slit is evenly illuminated; however, it must be taken into account when observing the auroral latitudes. Therefore, in the following section, I will discuss the LOS velocity spatial correction which was performed on the CRIRES data set, which is discussed further in Chapter 5.

The slit width of CRIRES is 0.2'', which represents ~ 610 km of the disk of Jupiter at the equator for that observation, a distance over which the aurora is known to vary and create intensity anisotropy across the slit (Stallard et al. 2001). By using near-simultaneous images of the H_3^+ emission, Stallard et al. (2001) could determine the variation of intensity inside the slit for each pixel. There are no H_3^+ images available for the CRIRES data set, and therefore the intensity variation inside the slit must be approximated by interpolating between slit positions.

Figure 3-24 shows a schematic of intensity anisotropies that can occur inside the slit of CRIRES. A pixel of interest is chosen on the limb of the planet, which is bound by the blue box. The intensity at three positions inside the slit (P_1, P_2 and P_3) are determined by interpolating across the three slit positions (S_1, S_2 and S_3) shown in Figure 3-24. Inside the pixel of interest in Figure 3-24, it can be seen that the intensity variation across the slit is not constant. When fitting a Gaussian to the intensity inside this pixel of interest the peak is be shifted towards P_1, which causes additional wavelength shifts on top of any existing Doppler shift due to the motion of the H_3^+ ions. The intensity variation ΔI(x, y) in the pixel of interest can be modelled using the following equation,

$$\mathrm{I}(\mathrm{x},\mathrm{y}) = \frac{\mathrm{p}_3 - \mathrm{p}_1}{\mathrm{p}_3 + \mathrm{p}_1} \qquad \textbf{3.24}$$

where p_1 is the pixel at the bottom of the slit and p_3 is the pixel at the top of the slit, as shown in Figure 3-24.

The intensity variation is related to the spatial anisotropy velocity Δv_s through the following linear relationship,

$$\Delta \mathrm{v}_\mathrm{s}(\mathrm{y}) = \mathrm{b}\Delta\mathrm{I}(\mathrm{x},\mathrm{y}). \qquad \textbf{3.25}$$

where b is a constant. Stallard et al. (2001) determined the constant b value theoretically and empirically. The theoretical velocity resolution of the 0.5'' slit of the IRTF instrument, CSHELL, is 7 km s^{-1}. Through testing this value against others, Stallard et al. (2001) empirically determined the b value to be 10 km s^{-1}, by using simulated illumination calculated from the H_3^+ images. The theoretical velocity resolution for the 0.2'' CRIRES slit is 3 km s^{-1}, and this value was tested empirically on the CRIRES data and was found to be a suitable value for the constant b. It should be noted that since the emission line spreads across several pixels, by using a Gaussian to fit the emission

line to sub-pixel accuracy, LOS velocity values smaller than the theoretical velocity resolution may be derived. Stallard et al. (2001) estimated a Gaussian could be fitted to the position of the emission line to an accuracy of 0.1 pixels, suggesting the Gaussian fitting accuracy in this thesis is ~300 m s^{-1}.

Once the spatial anisotropy velocity, Δv_s, was determined for each pixel this value could be removed from the derived LOS velocity in the appropriate reference frame, as shown by the Equations 3.26 and 3.27.

$$v_{MPRF\_SC}(y) = v_{MPRF}(y) - \Delta v_s(y) \quad \textbf{3.26}$$

$$v_{PRF\_SC}(y) = v_{PRF}(y) - \Delta v_s(y) \quad \textbf{3.27}$$

A full discussion on the LOS spatial anisotropy velocities and how they affect the CRIRES data set is given in Chapter 5.

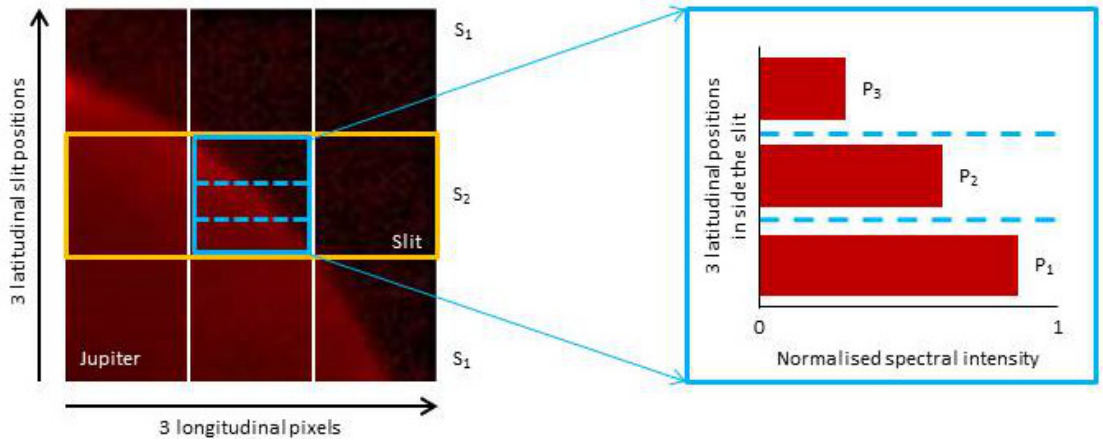

Figure 3-24: A schematic showing the intensity anisotropies which occur inside the slit. The slit width is exaggerated to emphasize the anisotropies inside the slit. The blue box bounds the pixel of interest, and the intensity values inside the pixel were determined through interpolation of the intensity inside the slit across three slit positions (S_1, S_2 and S_3). Once the intensity inside the slit is known the intensity variation inside the slit can be determined, from which the spatial anisotropy velocity can be derived.

3.5.4 Rotational Temperature, Column Density and Total Emission

3.5.4.1 H_3^+ Transition Intensity

The intensity of a single spectral line produced by the H_3^+ in Jupiter's ionosphere, I(λ, T), is given by Equation 3.28 (Stallard et al. 2002). The subscript i denotes the initial value and the superscript f denotes the final value in the transition which produces the emission at wavelength, λ. In this equation, ω is the transition frequency (or wavenumber of the emission produced by the transition), g is the nuclear spin

degeneracy, J is the rotational quantum number, E is the energy, A is the Einstein A-coefficient, and Q(T) is the partition function. The constants in this equation are the Planck constant (h~6.63 x 10^{-34} m^2 kg s^{-1}), the speed of light (c~2.99 x 10^8 m s^{-1}), and the Boltzmann constant (k_B~1.38 × 10^{-23} m^2 kg s^{-2} K^{-1}). The factor 100hc is needed in equation 3.28 to convert the wavelength to SI units. The factor of 1/4π normalises the equation to include units of per steradian.

$$I(\lambda, T) = \frac{n(H_3^+)\, g_{if}\, J'_{if}\, \omega_{if}\, A_{if} \times 100hc}{4\pi\, Q(T)} \times \exp\left[-\frac{E'_{if} \times 100hc}{k_B T(x,y)}\right] \quad \textbf{3.28}$$

Equation 3.28 uses the H_3^+ partition function, which describes a statistical ensemble. The partition function used in this thesis is taken from Miller et al. (2013) and is shown in Figure 3-25, for a temperature range of T~100-1800 K. The partition function can be calculated using Equation 3.29, where the constants A_n are the Einstein coefficients, which give the probability per unit time that an atom or molecule will spontaneously emit a photon and move the atom or molecule into a lower energy state. The values for the Einstein coefficients are shown in Table 3-3.

$$Q(T) = A_0 + A_1 T + A_2 T^2 + A_3 T^3 + A_4 T^4 + A_5 T^5 + A_6 T^6 \quad \textbf{3.29}$$

Table 3-3: A table of the Einstein coefficients used in the partition function (Miller et al. 2013).

Coefficient	Value (s^{-1})
A_0	1.11391
A_1	0.0581076
A_2	0.00030297
A_3	2.837240 x 10^{-7}
A_4	2.31119 x 10^{-10}
A_5	7.15895 x 10^{-14}
A_6	1.00150 x 10^{-17}

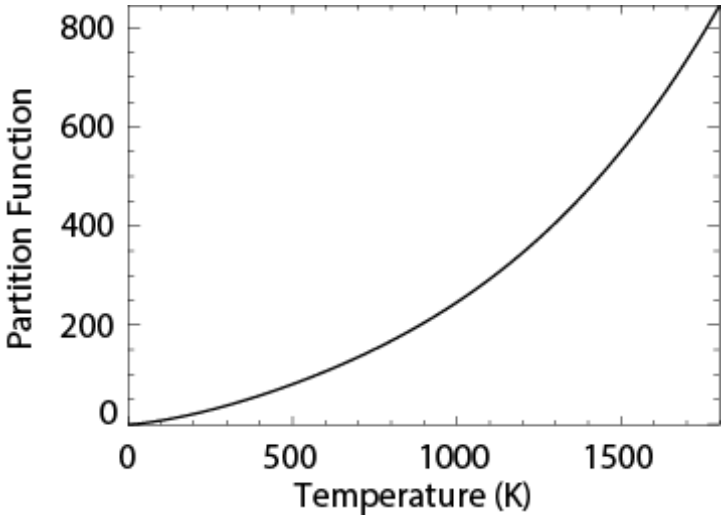

Figure 3-25: The partition function, Q(T), of H_3^+ as a function of temperature.

3.5.4.2 Rotational Temperature

In this thesis, the assumption that the upper atmosphere of Jupiter is in q-LTE is used, as described in Section 2.1.3. This assumption means that temperatures derived from H_3^+ are representative of the region of atmosphere where the H_3^+ emission was measured (Miller et al. 1990). The rotational temperature is determined from the relative spectral radiance of two lines which are in the same vibrational manifold, but in different rotational manifolds, as discussed in Section 2.6. In this thesis, the Q(1,0$^-$) and Q(3,0$^-$) emission lines are used and represent transitions from the first excited vibrational energy level to the ground state, $v_2 \rightarrow 0$, which is a fundamental transition (McCall 2001).

The ratio of the spectral radiances of the Q(1,0$^-$) and Q(3,0$^-$) fundamental lines is given by the following equation, where the subscripts Q1 and Q3 refer to Q(1,0$^-$) and Q(3,0$^-$) respectively,

$$\frac{I_{Q_1}}{I_{Q_3}} = \gamma \exp\left[\frac{(E_{Q_3} - E_{Q_1})}{k_B T}\right] \qquad \textbf{3.30}$$

where

$$\gamma = \frac{g_{Q_1} \times (2J'_{Q_1} + 1) \times hc\omega_{Q_1} \times A_{Q_1}}{g_{Q_3} \times (2J'_{Q_3} + 1) \times hc\omega_{Q_3} \times A_{Q_3}} \qquad \textbf{3.31}$$

and the parameters are given by Table 3-4, which are taken from the theoretical spectroscopic line list of Neale et al. (1996).

Table 3-4: Parameters required for deriving the physical properties of H_3^+.

Parameters (taken from Neale et al., 1996)	Q(1,0$^-$)	Q(3,0$^-$)
Energy of the upper state, E'	2552.57 cm^{-1}	2961.84 cm^{-1}
Einstein A-coefficient, A	128.7 s^{-1}	123.2 s^{-1}
Nuclear spin degeneracy, g	4	4
Rotational quantum number of the upper state, J'	3	9
Transition frequency, ω	2529.73 cm^{-1}	2509.08 cm^{-1}
Partition function, Q(T)	Taken from Miller et al. (2013)	

Figure 3-26 shows an example of the spectral radiance of the Q(1,0$^-$) (black line) and Q(3,0$^-$) (dotted black line) emission lines, which is derived from the CRIRES data set through the methods outlined in Section 3.5.1. The ratio of the spectral radiance of the two lines is given by the blue line in Figure 3-26. The ratio shows that Q(3,0$^-$) is generally more intense than Q(1,0$^-$) in the auroral region, and changes depending on the location. Outside the auroral region, the Q(1,0$^-$) emission can be more intense than the Q(3,0$^-$) emission, however, these regions coincide with poor signal-to noise.

Equation 3.30 can be rearranged to solve for temperature as shown by Equation 3.32, which can be used to convert the ratio of Q(1,0$^-$) and Q(3,0$^-$) to the rotational temperature of H_3^+.

$$T = \frac{[E'_{Q_1} - E'_{Q_3}] \times 100 \times {}^{hc}/_{k_B}}{\ln(\gamma) - \ln\left(\frac{I(\omega_{Q_1})}{I(\omega_{Q_3})}\right)} \qquad \textbf{3.32}$$

Figure 3-27 shows the temperature profile (red line) as well as the spectral radiance profiles of Q(1,0$^-$) and Q(3,0$^-$) (solid and dashed black lines respectively). The temperature variation seen in Figure 3-27 and across the whole auroral regions will be discussed in Chapter 6.

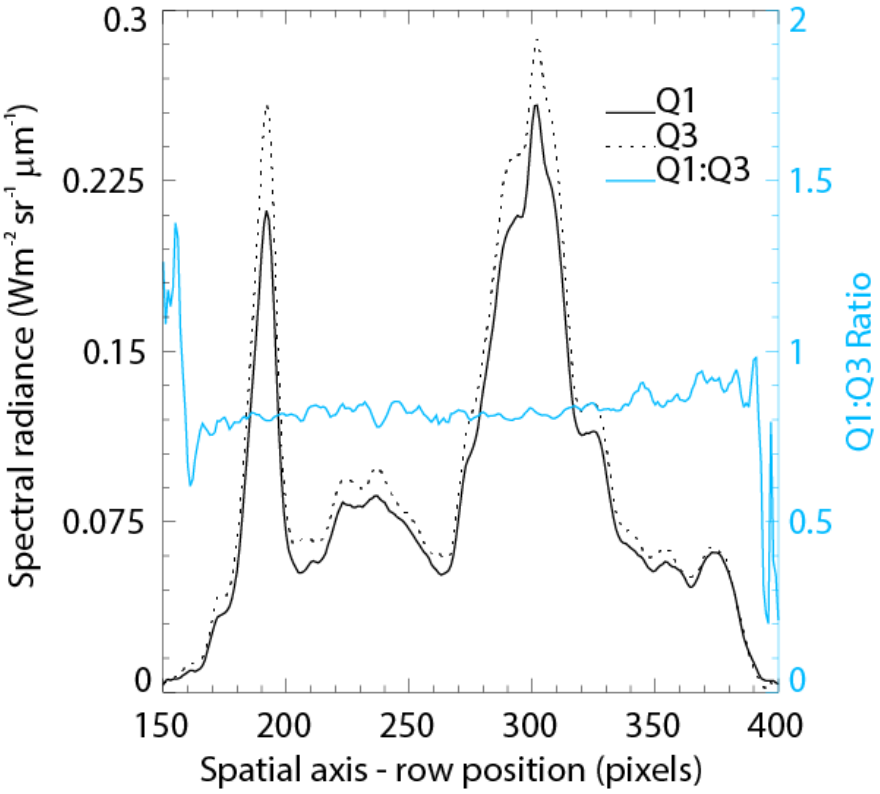

Figure 3-26: The ratio (blue line) of the spectral radiances of Q(1,0$^-$) and Q(3,0$^-$) (solid and dashed black lines respectively). Data taken by CRIRES on 31 December 2012.

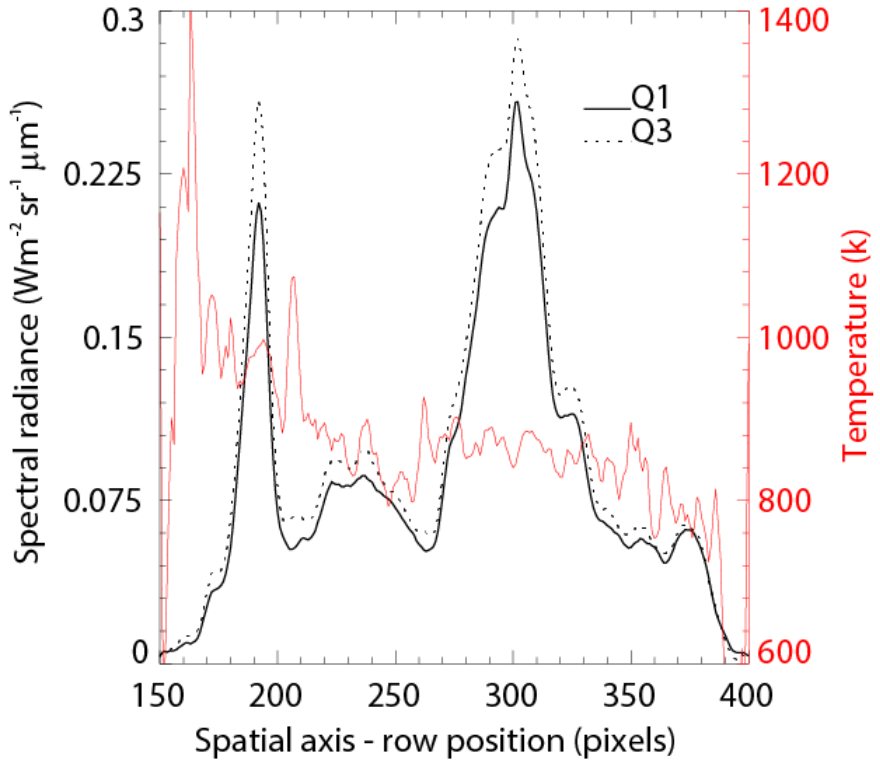

Figure 3-27: The temperature profile (red line) derived from the ratio of the spectral radiances of Q(1,0$^-$) and Q(3,0$^-$) (solid and dashed black lines respectively). Data taken by CRIRES on 31 December 2012.

3.5.4.3 Column Density

The column density, $N(H_3^+)$, is the density of a column of the planet's atmosphere perpendicular to the planet's surface. It is calculated by dividing the measured intensity from the emission line (I_{obs}) by the theoretical emission per molecule from that particular line (I_{model}), shown by Equation 3.33.

$$N(H_3^+) = \frac{I_{obs}(\lambda)}{I_{model}(\lambda, T)} \quad \textbf{3.33}$$

Section 3.5.1 outlines how the intensity (I_{obs} [W m^{-2} sr^{-1}]) is derived. The theoretical emission produced by one molecule wavelength of the transition ($I_{model}(\lambda, T)$ [W sr^{-1}]) can be calculated using Equation 3.34. Figure 3-28 shows the theoretical intensity produced by the Q(1,0$^-$) emission line, where the parameters used to calculate I_{model}(Q1, T) are given in Table 3-4, and the temperatures used are the rotational temperatures as calculated above.

$$I_{model}(\lambda, T) = \frac{g_{if}\ J'_{if}\ \omega_{if}\ A_{if} hc \times 100}{4\pi\ Q(T)} \times \exp\left[-\frac{hc\ E'_{if} \times 100}{kT(x,y)}\right] \quad \textbf{3.34}$$

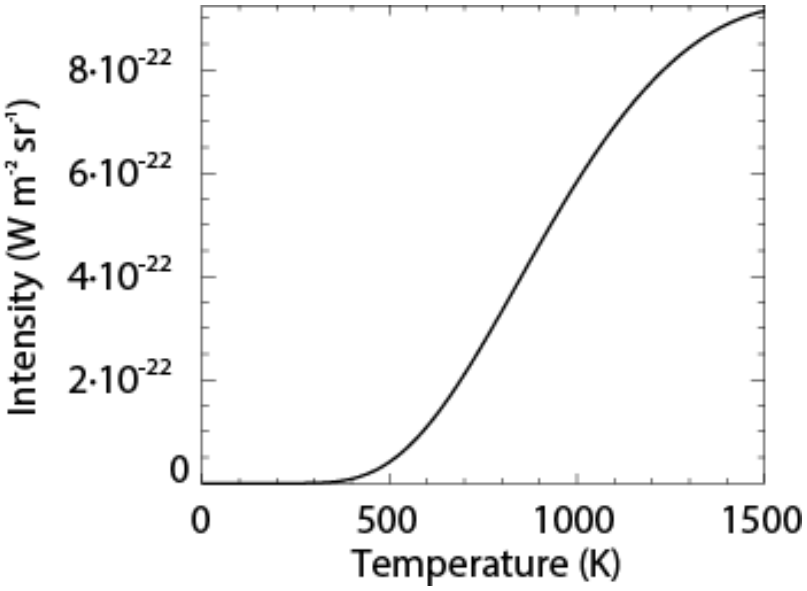

Figure 3-28: The theoretical intensity produced by the Q(1,0$^-$) H_3^+ emission line as a function of temperature.

3.5.4.4 Total Emission

The total emission, $E(H_3^+)$, is the total emission from the H_3^+ population across all possible energy transitions at a given temperature and was first introduced by Lam et al. (1997), and it represents the amount of energy lost to space by the ionosphere through radiative cooling. It is calculated by multiplying the theoretical emission from

all emission lines produced by one molecule ($E(\lambda, T)$) by the column density ($N(H_3^+)$), as shown by the following equation,

$$E(H_3^+) = E(\lambda, T) \times N(H_3^+) \times 2\pi \quad \textbf{3.35}$$

where a hemispheric emission factor of 2π steradian is needed to produce the total energy escaping the planet, and the values for column density are as calculated above.

$E(\lambda, T)$ is calculated by taking the exponential of the cooling function as defined by Miller et al. (2013). The coefficients of the cooling function are given in Table 3-5 and the cooling function can be calculated using Equation 3.36. Then by taking the exponential of the cooling function, $E_{H_3^+}(\lambda, T)$ can be determined and is plotted in Figure 3-29.

$$Q(T) = C_0 + C_1 T + C_2 T^2 + C_3 T^3 + C_4 T^4 + C_5 T^5 + C_6 T^6 \quad \textbf{3.36}$$

Table 3-5: The coefficients of the cooling function by Miller et al. (2013).

Coefficient	$T \sim 300 - 800$ K	$T \sim 801 - 1800$ K
C_0	-92.2048	-62.701
C_1	0.298920	0.0526104
C_2	-0.000962580	-7.22431e-5
C_3	1.82712e-6	5.93118e-8
C_4	-2.04420e-9	-2.83755e-11
C_5	1.24970e-12	7.35415e-15
C_6	-3.22212e-16	-8.01994e-19

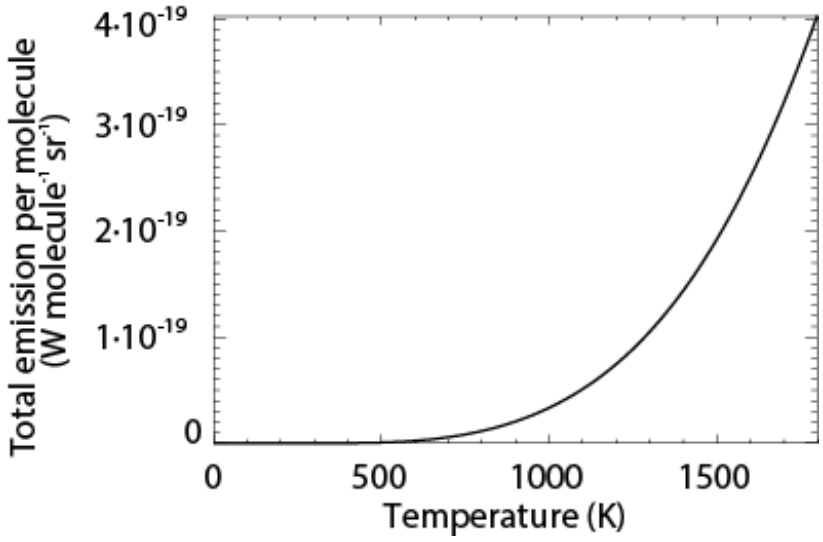

Figure 3-29: The total emission per molecule as a function of temperature.

Chapter 4 Measurements of the Rotation Rate of the Jovian Mid-to-Low Latitude Ionosphere

4.1 Introduction

In this chapter, I investigate the line-of-sight (LOS) velocity of the H_3^+ ions in Jupiter's mid-to-low latitude ionosphere, reporting on the study by Johnson et al. (2016). As discussed in Section 2.3.2, our current understanding of Jupiter's main auroral emission comes from models which couple the main auroral emission to corotation breakdown in the middle magnetosphere. These models include the specific assumption that the non-auroral ionosphere is corotating. Therefore, it is important to validate this assumption by measuring the LOS velocity of the H_3^+ ions.

The mid-to-low latitude ionosphere maps to Jupiter's inner magnetosphere, which near rigidly corotates (Khurana et al. 2004). Therefore, it is expected that the ionosphere in the mid-to-low latitude region is also corotating, and there should not be any auroral currents present at these latitudes. In the absence of electron precipitation, electron excited H and H_2 emissions are expected to be limited in this region. However, past observations have shown that the H Ly-α emission at mid-to-low latitudes is not uniform: there is a region of enhanced brightness, fixed in System III at 60-120° longitude, known as the H Ly-α bulge, which is described in greater detail in Section 2.2.

In order to explain the H Ly-α bulge, Sommeria et al. (1995) created a circulatory model, which is described in Section 2.5.1. Sommeria et al. (1995) models two jets, which originate from the auroral regions, colliding in the region of the H Ly-α bulge and generating strong eastward and westward jets. It could be the case that the strong neutral flows are driving ionospheric flows, which would oppose the assumption that the mid-to-low latitude ionosphere is corotating. Until the study by Johnson et al. (2016), which is reported on in this chapter, previous studies had not measured the H_3^+ LOS velocities in this region. These flows of H_3^+ are investigated to determine whether they are influenced by the predicted circulatory pattern suggested by Sommeria et al. (1995), or corotating as required by the auroral models.

4.2 Data Analysis

The data used in this investigation were taken from several nights of observations in 1998, 2007 and 2013 with IRTF-CSHELL. The smallest slit width, 0.5'' was used in order to provide the highest spectral resolution (R~36,000). Greater detail on the observing procedure and data set are given in Section 3.2 and 3.4.1 respectively. The data was reduced as described in Section 3.3.

At high latitudes, where the limbs of the planet are visible inside the 30'' slit, it is possible to determine the latitude using the length of the chord of emission. However, at lower latitudes where the body of the planet entirely fills the slit, it is difficult to identify the exact latitude position of the measurement. Figure 4-1 shows three schematics of Jupiter, as viewed by the observer from Earth, for observations in 1998, 2007 and 2013. The equatorial position of the slit is shown by the dark grey line and the latitude ranges of the data have been approximated and are shown by the shaded regions.

The maximum range of observed latitudes of the mid-to-low latitude data, due to uncertainties in positing the slit, was calculated by relating Jupiter's apparent equatorial diameter to CSHELL's slit length of 30''. As Jupiter and the Earth are moving relative to each other, Jupiter's angular equatorial diameter changes over the years observed: over the three separate observations it was ~49.65'', 45.75'' and 34.19''. As the angular diameter decreases, the maximum latitude range also decreases, which can be seen in Figure 4-1. The light grey region in Figure 4-1 represents the maximum range of latitudes which includes data equatorward of ~ 48.3°, ~ 43.3° and ~ 15.0° latitude in both hemispheres over the three separate observations.

The maximum range is a broad range which accounts for drift of the telescope, which may occur, for example, if the guide star is lost, and accounts for human error in correcting for this drift. This range was refined by using the change in declination caused by the telescope moving from the equatorial measurement back to the polar limb, effectively providing the expected latitude range given perfect observing conditions. This reduced the latitude range in 1998 and 2007 to ~ 25.8° and ~ 27.1° colatitude and is represented by the dark grey region in Figure 4-1. The latitude range could not be refined in this way for 2013 as the position of the telescope was fixed at Jupiter's equator, and so no offset information was available.

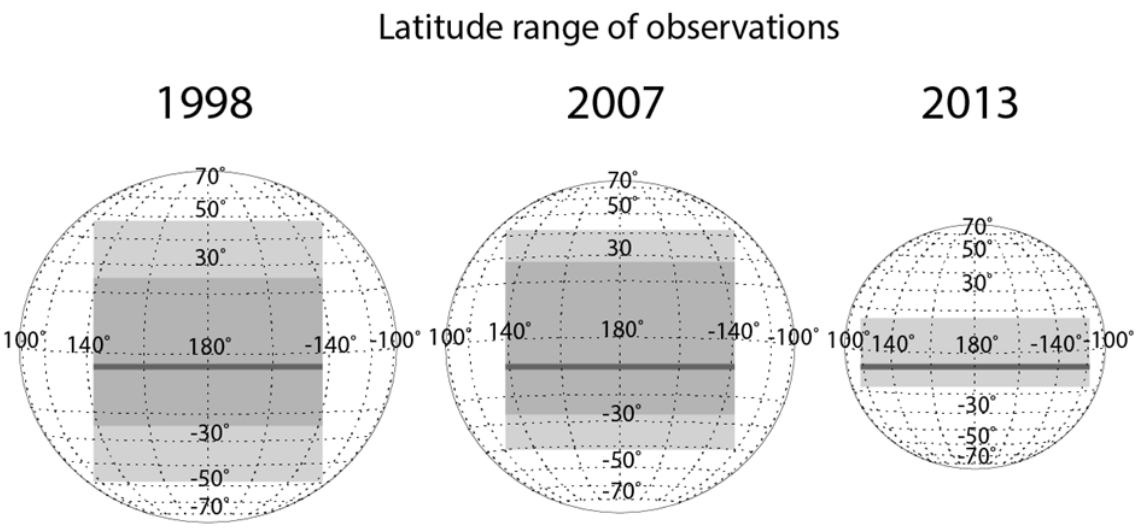

Figure 4-1: A schematic of the latitude ranges of the collated mid-to-low latitude H_3^+ emission data taken in 1998, 2007 and 2013. The light grey region is the maximum range of latitudes of the data: ~ 48.3°, ~ 43.3° and ~ 15.0° colatitudes respectively. The dark grey region represents the refined latitude range: ~ 25.8° and ~ 27.1° colatitudes for 1998 and 2007 respectively. This schematic is to scale except for the slit width. The sub-Earth latitude of the observer and the flattening of Jupiter have been taken into account.

Velocity profiles derived from single exposures are used in this study to investigate any longitudinal various in the H_3^+ LOS velocity. The emission efficiency of H_3^+ depends on temperature (as discussed in Section 2.4), and the emission of H_3^+ is weaker at the cooler equator than in the hotter auroral regions (Lam et al. 1997). In addition, at equatorial latitudes, the methane in Jupiter's atmosphere becomes less efficient at absorbing sunlight at the wavelength at which H_3^+ emission is observed because of the smaller column of absorbing methane in the line-of-sight in this region. As a result, the background emission can become bright relative to the H_3^+ emission lines.

To enhance the signal-to-noise, an average of the H_3^+ spectra across one year of observations were taken to study the average LOS velocity of H_3^+ in that particular year. Before taking the average, the line-of-sight component Jupiter's rotation must be removed. Since the apparent size of Jupiter in the sky varies across the 3 years of data (Figure 4-1), the change in rotational velocity per pixel across the slit also changes. Undertaking an average prior to removing the component of Jupiter's rotation would result in meaningless LOS velocities. As the slit is aligned perpendicular to the rotation axis, the change in velocity per pixel is independent of longitude or latitude. The velocity at the limbs of the planet can be calculated using the rotation rate and

circumference of Jupiter, as discussed in Section 3.5.3. By using the angular size of Jupiter and the pixel size, the change in velocity per pixel can be calculated. Figure 4-2 shows the spectra after Jupiter's rotation rate has been removed, and so by visual inspection the Q(1,0$^-$) emission line appears vertical and has no Doppler shift due to the rotation.

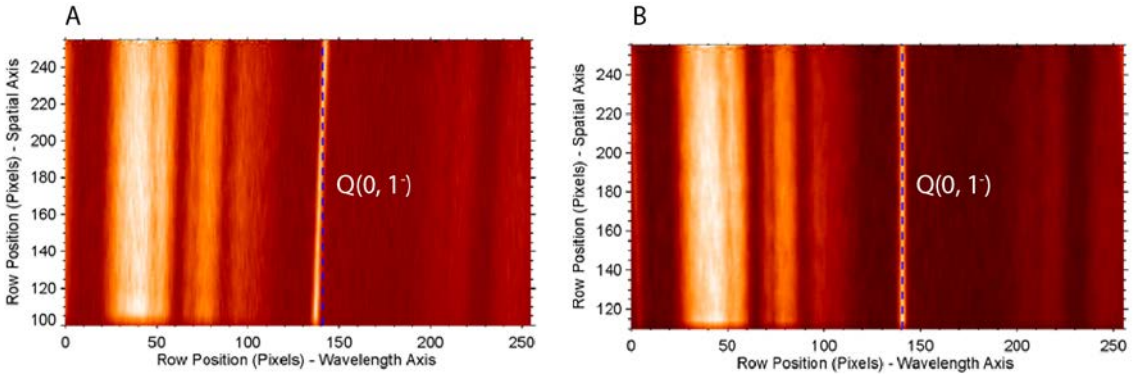

Figure 4-2: H_3^+ emission line taken with CSHELL on 7 Septemeber 1998, the Q(1, 0$^-$) emssion line is labelled and is at row position ~140 on the wavelength axis. The slit position is equatorial and therefore there is a large amout of reflected sunlight present in the array. (a) The H_3^+ spectra, prior to correction, including the planets rotation in the H_3^+ emission line and the spectral dispersion across the array. (b) The corrected spectra where Jupiter's rotation rate removed has been removed as well as correction for the spectral dispersion applied. The blue dashed line is a straight line to be used as a reference to the gradient of the emission line due to the rotation of Jupiter.

By fitting a Gaussian to every spatial pixel along the corrected Q(1, 0$^-$) emssion line (row position ~140 on the wavelength axis in Figure 4-2b), the LOS velocity can be derived using the methods outlined in Section 3.5.3. The zero point velocity (v_0) used in this study was taken as the median value of the LOS velocity. Ideally the LOS velocity at the central meridian longitude (CML) could be used as the zero point velocity; however, since the limbs of the planet are not visible in the slit the centre of the planet cannot be accurately identified. As the rotation rate of Jupiter has already been removed, the resulting LOS velocities are in the planetary reference frame (PRF). If the spatial anisotropies are present in the illumination across the slit, then a spatial correction must be performed on the LOS velocity to remove any false Doppler shifts, as discussed in Section 3.5.3. However, the spatial correction was excluded from the data analysis for this study as it is not required at mid-to-low latitudes since brightness variations in this region are on a spatial scale much larger than the slit (Lam et al. 1997). Through propagation of errors accumulated during the data reduction, a final

error at each spatial position along the slit was produced, and is indicated in the figures, where appropriate.

4.3 The Line-of-Sight Velocity of the H_3^+ Ions at Mid-to-Low Latitudes

An example of six mid-to-low latitude H_3^+ LOS velocity profiles from the 7th September 1998 is shown in Figure 4-3. The solid black line is the calculated LOS velocity of the H_3^+ ions in the PRF. The dashed black line is a linear fit to the LOS velocities. In the PRF, a LOS velocity of zero infers that the H_3^+ ions are corotating and is represented by the solid red line in Figure 4-3. Departures from corotation would be indicative of ionospheric flows. The linear fit has a gradient very close to zero in the 6 plots in Figure 4-3, showing that the bulk flow of the equatorial H_3^+ is corotating during these observations. The LOS velocity of the H_3^+ ions in Figure 4-3 does show some variability, which may indicate small scale flows in this region, but these velocities remain inside the ~ 0.5 km s^{-1} error.

Figure 4-3 is an example of six LOS velocity profiles from the 7th September 1998 observations; a total of 113 individual spectra of mid-to-low latitude H_3^+ emission lines were investigated across several observations taken in 1998, 2007 and 2013. Through visual inspection of the LOS velocity profiles derived from the 113 individual spectra, those with low signal-to-noise were discarded. The signal was found to be adequate to derive the LOS velocity in 95 of the spectra. Eight of the velocity profiles showed some small scale flows i.e.: exhibiting LOS velocity values greater than the corresponding error. Therefore, it can be said that most of the velocity profiles showed no small scale flows and overall no returning features were identified that may be associated with the H Ly-a bulge. If the gradient of the linear fit was less than 1, then the H_3^+ ions were considered to be approximately corotating. It was found that 82 velocity profiles were corotating during these observations within experimental errors.

To investigate the bulk flow of the H_3^+ ions, the average LOS velocity was calculated for each year and is shown in Figure 4-4. By taking an average, this prevents any evidence of longitudinal variability being observed, but allows a greater accuracy of measurement of the rotation rate of the mid-to-low latitude region. If the gradient of the linear fit to the average LOS velocities for each year deviates from zero, then this will imply a departure from corotation in the bulk flow of the H_3^+ ions. The

gradient of the linear fit is -0.0013 ± 1.4 x 10^{-4}, 6.8 x 10^{-5} ± 3.6 x 10^{-4}, and 0.0045 ± 3.0 x 10^{-4} for 1998, 2007 and 2013 respectively. Although the gradient of the linear fit for 1998 and 2013 shows slight departures from corotation, the maximum deviation of the linear fit from corotation for 1998, 2007 and 2013 is 0.091 ± 0.25 km s^{-1}, 0.0082 ± 0.30 km s^{-1} and 0.31 ± 0.51 km s^{-1} respectively. These are not significant deviations from corotation and therefore the bulk flow of the H_3^+ ions is corotational within the bound of our experimental errors.

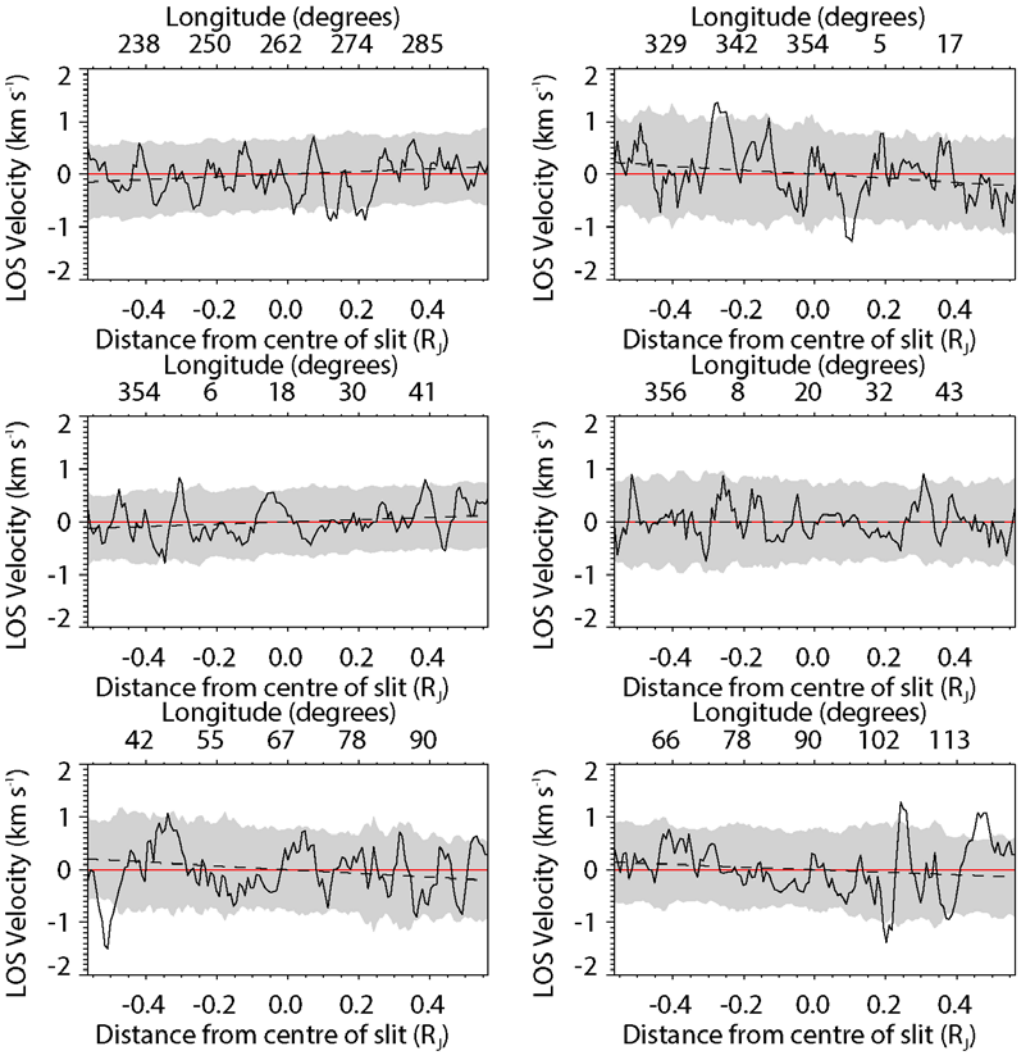

Figure 4-3: Mid-to-low latitude LOS velocity profiles in the planetary reference frame, derived from mid-to-low-latitude H_3^+ emission CSHELL data, taken on 7th September 1998. The x-axis represents the distance from the centre of slit, and is given in R_J (where R_J ~71,492 plus the peak emission height of H_3^+, which is ~550 km). The data covers a wide range of longitudes, which is also shown by the x-axis. The solid black line is the derived LOS velocity of the H_3^+ ions. The dashed black line is a linear fit to the LOS velocity values. In this reference frame, a zero velocity implies corotation and is represented by the solid red line. The grey shaded region represents the propagated errors.

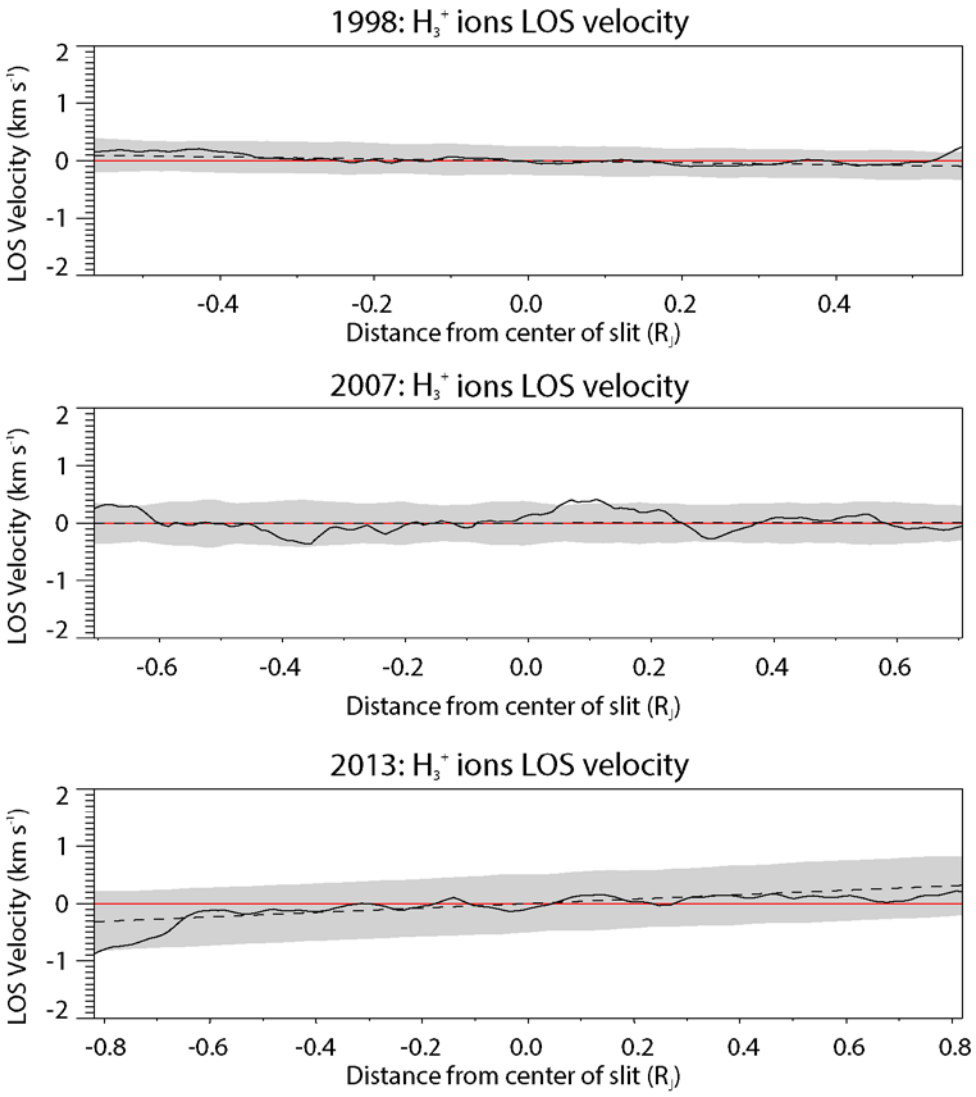

Figure 4-4: The average LOS velocity of the mid-to-low-latitude H_3^+ ions for the 1998, 2007 and 2013 observations. The solid black line is the average LOS velocity of the H_3^+ ions for each year. The dashed black line is a linear fit to the derived LOS velocity values. In this reference frame, a zero velocity implies corotation and is represented by the solid red line. The grey shaded region represents the errors.

4.4 Discussion

Emerich et al. (1996) measured turbulent velocity of ± 7 km s^{-1} at the location of the H Ly-α bulge from the spectral line width of the H Ly-α emission. They thought this turbulence could be caused by the collision of supersonic jets as described by Sommeria et al. (1995). As well as broadening due to turbulence, CSHELL introduces broadening into the measured emission line width. Using the arc lamps, situated inside CSHELL, the line spread function was calculated from the half width at full maximum. For 1998, 2007 and 2013 the standard deviation of the half width at half maximum was found to be ~ 1.59 pixels. This means that CSHELL can only detect turbulence greater

than ± 5 km s^{-1} and the relatively low signal-to-noise signal of H_3^+ at the equator increases this error further. As such, this data cannot be used to measure the spectral broadening caused by turbulence within the H Ly-α region, and so this study concentrates on bulk flows.

The thermosphere and ionosphere of Jupiter are coincident with each other, with the neutral and charged components of the atmosphere coexisting here. The neutrals and ions interact through collisions, and depending on the relative number of ions and neutrals and the forces which they impart on each other: sometimes the ions velocity drives neutral winds or the neutral velocity drives ionospheric flows. This interaction between neutrals and ions is observed at Earth in a phenomena is known as the flywheel effect (e.g.: Förster et al. 2011). The ionospheric convection drives neutral twin cell flows, which continue even after ionospheric convection stops (e.g.: due to northward turn in IMF B_z). In regions where the neutral density dominates, through collisional forcing, the neutral winds will drive the ions, forcing them to continue to flow in the ionospheric convection pattern. Modelling by Achilleos et al. (2001) has shown that an auroral electrojet at Jupiter could drive neutral flows. Rego et al. (1999) and Stallard et al. (2001) observed the H_3^+ ions flows around the main auroral emission in a clockwise direction, as viewed from the North Pole, with LOS velocity of ~3 km s^{-1} and 0.5-1.5 km s^{-1} respectively. Achilleos et al. (2001) showed that the neutral winds were aligned with the electrojet, and had a velocity of up to ~60% of the H_3^+ velocity. It is possible that at Jupiter, like the Earth, that under certain conditions, the neutrals can drive ionospheric flows at Jupiter.

There is no observational evidence of neutrals driving the ions at Jupiter as measurements of neutral winds are very limited. As previously discussed in Sections 2.3 and 5.1, it is assumed that both the neutrals and ions, which coexist in the thermosphere, are corotating at low latitudes. From simulations using the 3D Jupiter Thermospheric Global Circulation Model (3D-JTGCM), an increase in the neutral thermosphere wind velocity by a factor of 2 was shown in the northern auroral region between 550 – 3600 km (Bougher et al. 2005 and Majeed et al. 2005; 2009). H Ly-α emission occurs over a wide range of altitudes (200 km to 2200 km above the 1 bar level, Chaufray et al. 2010); however, the core of the line emission will correspond to high altitudes because there will be a significant amount of scattering in the column of

atmosphere. The H_3^+ emission from the fundamental line peaks lower down in the atmosphere at ~550km above the 1 bar level (Melin et al. 2005). From the studies by Chaufray et al. (2010) and Stallard et al. (2001), the H Ly-α velocity is higher than the H_3^+ velocity, which is consistent with an increase in velocity with altitude. However, the velocities produced by 3D-JTGCM were a factor of 2-3 times less than measured by Chaufray et al. (2010). Therefore, Chaufray et al. (2010) conclude that the model under-estimate the velocity gradient of the upper thermosphere in the auroral regions.

The H Ly-α is Doppler broadened by the turbulence suggested by Emerich et al. (1996), with the wings being subject to less scattering as they are optically thinner than the core. Therefore, the emission from the wings of the Gaussian is likely to originate from low altitudes (Jaffel et al. 2007), and the emission from the broadened component of H and H_3^+ could be produced at similar altitudes. From K band observations of overtone and hot overtone H_3^+ emission and H_2 IR emission, Chaufray et al. (2011) measured a lower velocity for H_2 winds (~<1 km s^{-1}) than the H_3^+ winds (-3.1 ± 0.4 km s^{-1}). They suggested that the H_2 emission originated from lower altitudes than the overtone and hot overtone H_3^+ emission due to the differences in velocity and the observed morphology of the emission. However, Uno et al. (2014) created vertical density profiles from Subaru data, and showed that the H_3^+ overtone and hot overtone and H_2 IR emission originate from the similar altitudes, although they do not offer an explanation for the differences in velocities.

It could be the case that the flows predicted by the Sommeria et al. (1995) model exist at a higher altitude to the H_3^+ flows. If the velocity of the neutrals increases with altitude, then this implies that the H_3^+ velocity at a lower altitude would be at a lower velocity the neutral flows in the Sommeria et al. (1995) model. Since the winds predicted by Sommeria et al. (1995) are large, it would be expected that there may be sub- or super- rotational H_3^+ flows depending on the location of the measurements. Alternatively, the flows of H_3^+ and Sommeria et al. (1995) model may exist at the same altitude but the neutrals and ions could have different velocities. It is expected that through collisions, the flows predicted by Sommeria et al. (1995) would have a measureable effect on the H_3^+ because of the strong velocities suggested by the model.

Investigations by Tao et al. (2014) have shown that the maximum thermospheric neutral wind velocity, generated by solar EUV flux at latitudes less than 30° is 6.54 m s^{-1} in the PRF. These winds are very weak, and even if they do drive H_3^+ flows the flows would be below the sensitivity of CSHELL (>100 m s^{-1}). Therefore, no deviations from corotation due to winds caused by solar EUV flux are expected to be measured in the CSHELL data. Although I have tried to consider all possible thermospheric flows which may influence the H_3^+ flows in the low latitude region, it is worth noting that further complexity in the dynamics of the thermospheric winds may exist, which has not yet been captured by models.

Flows in the circulatory pattern described by Sommeria et al. (1995) would appear in the LOS velocity profiles as deviations from corotation at fixed longitudes. Since the H Ly-α bulge is fixed in magnetic System III longitude, as Jupiter rotates the localised deviation from corotation would appear to move along the slit. Figure 4-3 shows the LOS velocity profiles for a range of longitudes, covering approximately half a Jovian rotation and explores the longitude location of the H Ly-α bulge, which is fixed at ~100° longitude. If the localised deviations from corotation predicted by Sommeria et al. (1995) exist, then they would be observed as a prominent returning feature in Figure 4-3, with the strongest flows expected in the centre of the H Ly-α bulge which would be observed in the top two panels. There is no evidence of returning features associated with the H Ly-α bulge outside the mean error of ± 0.51 km s^{-1} and any observed variation in the LOS velocity are likely to be the result of noise.

The modelled circulatory patterns from Sommeria et al. (1995) include an eastward and westward jet, emerging from the position of the bulge. The eastward jet dominates the westward jet, and therefore if the circulatory pattern from Sommeria et al. (1995) exists it would be seen in the average H_3^+ velocity in a year (Figure 4-4) as a general sub-rotational trend due to the main flows in the model being against rotation. If the flows modelled by Sommeria et al. (1995) are influencing the H_3^+ flows, then a LOS velocity deviation from corotation by several km s^{-1} is expected due to the dominating eastward jet. However, as shown in Section 4.3, no general sub-rotation was found and the average velocity of the H_3^+ ions, across all three year in which it was observed, was near-corotational.

Since the H_3^+ ions in Jupiter's mid-to-low latitude ionosphere are assumed to be corotating with the neutrals, there will be no Joule heating or ion drag in this region. This is because the velocity of the neutrals approximately matches that of the H_3^+ ions, and therefore collisions between them will be severely limited. The remaining energy inputs in the equatorial region are heating by atmospheric waves from lower altitudes (Tao, et al. 2009 and O'Donoghue et al. 2016), redistribution of polar auroral energy (Bougher et al. 2005 and Majeed et al. 2005; 2009), and a small contribution to heating by solar photons. Energy losses will be due to downward conduction and H_3^+ radiation to space (Yelle and Miller 2004). It remains unclear if and how this limited set of energy terms can produce the observed high thermospheric temperatures at the equator. There is also disagreement over the mechanisms through which the energy is transported in the Jovian ionosphere. Through meridional advection, the model by Smith and Aylward (2009) describes poleward flow of heat raising the temperature of the polar region and cooling the mid-to-low latitudes. However, the models by Bougher et al. (2005) and Majeed et al. (2005; 2009) discuss how heat transported from the auroral regions through meridional advection heats the mid-to-low latitude region. I hope that the LOS velocity measurements in this study will go some way to constraining the equatorial conditions and hence work towards a unified model.

4.5 Conclusions

The study by Johnson et al. (2016), which is reported on in this chapter, is the first to measure the LOS velocity of the H_3^+ ions in Jupiter's mid-to-low latitude ionosphere. The LOS velocity derived from the Doppler shifted H_3^+ emission line shows that the H_3^+ ions in Jupiter's ionosphere are corotating. No evidence that the H_3^+ ions are sub- or super-rotational has been found in this data. This confirms that the ionosphere near-rigidly corotates at mid-to-low latitudes, such that the departures from corotation are confined to the polar region and are therefore likely to be due to magnetosphere-ionosphere coupling at those latitudes, as is often asserted.

No returning features were observed in the individual H_3^+ velocity profiles taken over a wide range of CML, and no general trends were identified in the average H_3^+ velocity. Therefore, there is no evidence of strong flows at the mid-to-low latitude region, which the circulation pattern in the model by Sommeria et al. (1995) implies.

This lack of evidence suggests that the H Ly-α bulge is produced through a different process than that modelled by Sommeria et al. (1995). However, neutral winds in this region cannot be ruled out as Uno et al. (2014) showed that two velocity regimes from neutral and ions can coexist at the same altitudes. Although, if the neutral winds do exist it is likely that they will be slower than those suggested by Sommeria et al. (1995) as only velocities <10 km s^{-1} have been measured in Jupiter's thermosphere so far (Chaufray et al. 2010).

The spectral resolution of CSHELL is insufficient to test whether the thermosphere corotates as a result of vertical viscous transport, which could result in up to a 0.1 km s^{-1} super rotation at the equator due to Jupiter's tropospheric jets, or meridional advection which would smooth thermospheric flows globally. In future work it will be important to test whether the angular momentum is transferred by meridional advection as suggested by Smith and Aylward (2009), Bougher et al. (2005) and Majeed et al. (2005; 2009), or by vertical transport similar to the coupling of the altitudes in the auroral regions discussed in Chaufray et al. (2010). The results presented here highlight the need for simultaneous measurements of both H_3^+ and H Ly-α emissions, as well as other thermospheric components in both the auroral region and at lower latitudes. Such measurements would allow us to better understand how this region couples to both the lower atmosphere and the surrounding magnetosphere.

Chapter 5 High Resolution Mapping of Intensity and Line-of-Sight Velocity of H_3^+ Ions

5.1 Introduction

In this chapter I report on the work published in Johnson et al. (2017). This study presents observations of the H_3^+ intensity and LOS velocity in Jupiter's northern auroral region, using data taken on 31 December 2012 with VLT-CRIRES.

Figure 5-1 shows the projected H_3^+ intensity of the northern auroral region taken from the data set used in this study. A thorough discussion of Jupiter's aurora is given in Section 2.4 and the main auroral morphological regions are labelled in Figure 5-1. The main auroral emission is labelled M_1 in the narrow bright section of the main auroral emission and M_2 in the more diffuse kink section. Although faint, Io's footprint aurora is also labelled and is located close to 180° longitude. The polar aurora has been separated into different morphological regions according to intensity. The bright polar region in the IR corresponds to the active region in the UV (A). The IR dark polar region has been split up further into 3 regions: a crescent shaped dark region confined close to the M_1 section of the main auroral emission that corresponds to the UV dark region (D), a brighter region that corresponds to the UV swirl region (S) and a second dark region located near to the magnetic pole (P), which does not appear in UV observations.

The mechanisms which govern the main auroral emission have been extensively modelled (e.g.: Pontius and Hill 1982; Huang and Hill 1989; Hill 2001; Cowley and Bunce 2001; Southwood and Kivelson 2001; Nichols and Cowley 2004; Nichols 2011; Ray et al. 2014, as discussed in Section 2.3.2.); however, the origin of the polar aurora is less clear. The endeavour to understand the mechanisms involved in generating Jupiter's polar aurora requires measurements of the dynamics in Jupiter's ionosphere and magnetosphere. To investigate the flows of ions in the upper atmosphere, and hence infer the motions of the coupled magnetic field lines, ionospheric flows are derived from observations of the Doppler shifted H_3^+ emission lines. For example, Stallard et al. (2001) measured the LOS velocity of the H_3^+ ions in the northern auroral region using IRTF-CSHELL. They measured an electrojet flowing clockwise (anti-

corotational) around the main auroral emission (when viewed from North Pole), with LOS velocity of 0.5 – 1.5 km s^{-1}. In the polar aurora they found that the dark polar region (which includes regions D, S and P from Figure 5-1) was dominated by strong subrotational flows of up to ~3 km s^{-1} (anti-corotational) and the bright polar region (region A in Figure 5-1) experienced very small flows, close to zero. Rego et al. (1999) measured the electrojet with a higher velocity of 3 km s^{-1}. Additionally they measured super-rotational flows slightly equatorward of the main auroral emission. From global circulation models (e.g.: Achilleos et al. 1998, Smith and Aylward 2009, and Majeed et al. 2016), thermospheric super-rotational flows were shown to be present in this region. A full discussion of the LOS velocity in the auroral regions is given in Section 2.5.2.

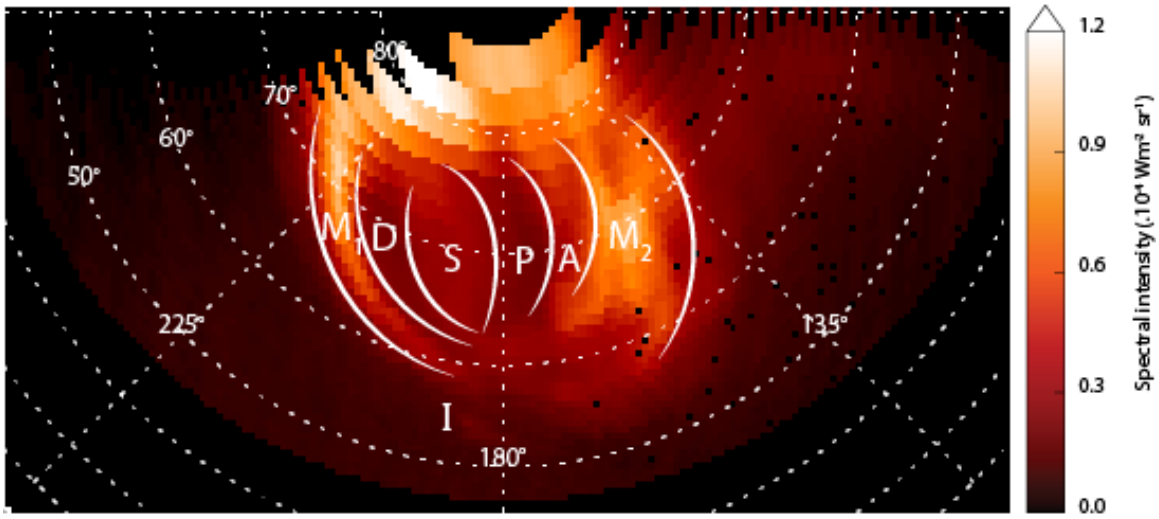

Figure 5-1: A polar projection of intensity of Jupiter's northern auroral region, created from data taken on the 31 December 2012 using VLT-CRIRES for central meridian line ~180°. The different regions of morphology are labelled on the polar projection as in Stallard et al. (2016): dawn sector of the main auroral emission, M_1; dusk sector of the main auroral emission, M_2; dark region of polar aurora, coincident with UV dark polar region, D; medium bright polar aurora, coincident with UV swirl region, S; a second dark region of the polar aurora, surrounding the magnetic north pole, P; bright polar aurora, coincident with the UV active region, A; Io footprint aurora, I. A gamma correction of 0.6 was applied to the polar projection.

One drawback of the ionospheric flow studies carried out by Stallard et al. (2001) and Rego et al. (1999) was the limited spatial resolution of the data sets. In this chapter, a new analysis of Jupiter's ionospheric flows using higher spatial and spectral resolution data taken with VLT-CRIRES is presented. Polar projections of the intensity (such as Figure 5-1) and LOS velocities of the H_3^+ ions over the entire northern auroral

region were created. Several regions of significant flows were identified in Jupiter's ionosphere and related to different regions of auroral morphology. These flows not only help us understand the motions of the ionosphere, but give us information about the dynamics of Jupiter's magnetosphere due to the coupling of the ionosphere and magnetosphere.

5.2 Data Analysis

The data used in this chapter were taken with VLT-CRIRES on 31 December 12 and is described in Section 3.4.2, with the observing procedure outline in Section 3.2. The data were reduced using the methods described in Section 3.3.

During the observations the slit was orientated West-East on the planet, with the slit centred on the rotational axis of the planet. Figure 5-2 shows an example of the spectra from the night, where (a) was taken in the auroral regions and (b) was taken at lower latitudes. It can also be noted that there are several more emission lines observed at auroral slit position, and these emission lines are stronger than the corresponding emission lines at sub-auroral latitudes. As the H_3^+ emission is a thermal emission, different ro-vibrational transitions are achieved at different temperatures. Therefore, different ratios of emission lines are observed in auroral and non-auroral regions due to changes in temperature of the ionosphere. The most intense H_3^+ emission lines are bound by the dashed white lines.

As well as taking spectra with the slit perpendicular to the rotational axis, six spectra were taken with the slit aligned with the rotational axis. Using an average of the six spectra taken when the slit of CRIRES was aligned along the CML in a North-South orientation, the brightest H_3^+ emission lines were identified and the observed wavelengths of these H_3^+ emission lines are shown in Table 5-1. It is possible to calculate the stationary wavelength of these emission lines using the average of the emission lines taken in the equatorial region due to two assumptions. The first assumption is there will be a minimal LOS component measured in this location as the slit is aligned at the centre of the planet, to an accuracy of ~ ±1'' in the longitudinal direction. The second assumption is that there was no Doppler shifts present in spectra measured in the equatorial region due to ionospheric flows. Johnson et al. (2016) showed that in Jupiter's mid-to-low latitude region the LOS velocity of the H_3^+ ions

were near-rigidly corotating. Therefore, the only Doppler shift of these emission lines will be due to the relative motion of Jupiter and the observer, a value for which is obtained from HORIZONS Web-Interface.

To identify the wavelength of the 5 bright emission lines, spectra taken near to the equatorial region are used. The H_3^+ emission will be weaker relative to the background here because at these latitudes methane is less efficient at absorbing the sunlight and the H_3^+ itself is weaker as there are cooler temperatures here. Therefore, to enhance signal-to-noise, the sum of the spectra in the spatial direction was taken for each of the 5 bright emission lines. The Doppler shifted wavelength was determined by fitting a Gaussian to the sum of each bright emission line, and this wavelength is shown in Table 5-1. Once the relative motion between Jupiter and the observer was removed, the measured rest wavelengths of the bright H_3^+ lines was found to be: $Q(3,3^+)$ at 3.90397 μm; $Q(2,2^+)$ at 3.91443 μm; $Q(1,0^-)$ at 3.95295 μm; $Q(2,1^-)$ at 3.97103 μm and $Q(3,0^-)$ at 3.98558 μm, as shown in Table 5-1. Table 5-1 also shows the *ab initio* values of the wavelength of these emission lines, taken from Neale et al. (1996). The calculated stationary wavelength matches well with the Neale et al. (1996) ab initio values, within the given errors as shown in Table 5-1.

Once the exact wavelength of these bright H_3^+ lines had been determined, the average of the 5 bright emission lines was taken for the spectra taken in the West-East orientation. In the auroral regions, methane is efficient at absorbing sunlight, meaning that the signal of the H_3^+ emission lines is bright relative to the background. As there are 5 bright lines observable in the spectra across the latitudes measured, the signal can be maximised by taking the average of these lines. The average emission line was smoothed using a box car average with a width of 5 pixels. After data reduction, the brightest portion of the main auroral emission had a maximum signal-to-noise of ~38, whereas in the non-auroral regions the maximum signal-to-noise was less than ~10.

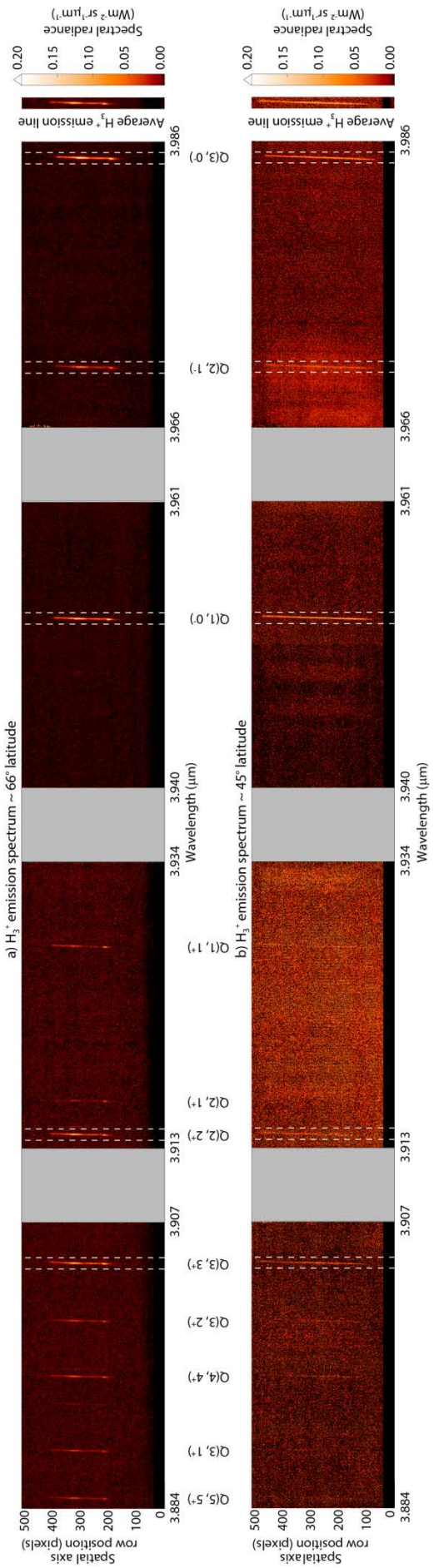

Figure 5-2: (a) The H_3^+ emission spectra measured across the 4 Aladdin detector arrays of CRIRES. The spectra were measured when the centre of the slit was at ~67° latitude. The white dashed lines bound the region which was used to create the average H_3^+ emission line which is shown next to the colour bar. (b) The H_3^+ emission spectra taken when the slit was in the most equatorial position in a scan at ~45° latitude. The same emission lines were used to create the average H_3^+ emission line, as in all slit positions. The grey regions represent the gap between the detector arrays. A gamma correction of 0.6 was applied to the H_3^+ emission spectra in both (a) and (b) and the x-axis represents spatial pixels and the y-axis represents spectral pixels over the four detector arrays.

Table 5-1: The measured Doppler shifted and rest wavelengths of the prominent H_3^+ lines bound by the white dashed lines in Figure 5-2, in a comparison with ab initio values (Neale et al. 1996).

Detector array	Line	Wavelength resolution (μm)	Ab initio (μm)	Measured Doppler shifted wavelength (μm)	Measured rest wavelength (μm)	Difference between ab initio values and measured rest wavelength (μm)
1	$Q(3,3^+)$	2.18147×10^{-5}	3.90396 ± 0.00007	3.90417 ± 0.0000103	3.90397 ± 0.0000103	1.0×10^{-5}
2	$Q(2,2^+)$	2.10620×10^{-5}	3.91440 ± 0.00007	3.91462 ± 0.0000140	3.91443 ± 0.0000140	3.0×10^{-5}
3	$Q(1,0^-)$	2.02413×10^{-5}	3.95299 ± 0.00007	3.95315 ± 0.00000804	3.95295 ± 0.00000804	4.0×10^{-5}
4	$Q(2,1^-)$	1.94608×10^{-5}	3.97106 ± 0.00007	3.97123 ± 0.00000909	3.97103 ± 0.00000909	3.0×10^{-5}
4	$Q(3,0^-)$	1.94608×10^{-5}	3.98552 ± 0.00007	3.98578 ± 0.00000915	3.98558 ± 0.00000915	6.0×10^{-5}

Using the methods outlined in Section 3.5.1, the intensity of the H_3^+ emission was derived. Polar projections of the H_3^+ intensity were created by assigning latitude and longitude to each pixel, as described in Section 3.5.2. The latitude and longitude information were used to map the pixel values, in an array 360° longitude and 180° latitude, onto a polar projection with 0.1° bins. Figure 5-3 shows six polar projections of the intensity created from the scans of Jupiter's northern auroral region. The white diamond marks the position of an auroral centre defined by Grodent et al. (2004) at 185° longitude and 74° latitude. The white dashed line is the magnetic footprint of Io, determined by the Grodent et al. (2008) model.

The polar projections of the intensity have been corrected for the limb brightening effect. Figure 5-4a shows the intensity at CML ~180° at constant latitude mapped onto a polar projection before LOS intensity correction, where the intensity shown is along the LOS of the observer. The LOS intensity correction transforms the intensity from a slanted LOS enhanced view to one that is a surface normal view. The full description of the LOS intensity correction and how it was applied to the data is presented in Section 3.5.2. Figure 5-4b shows the intensity at CML ~180° mapped onto

a polar projection after LOS intensity correction. When comparing the Figure 5-4a and Figure 5-4b, it can be seen that the intensity towards the limbs has been reduced.

To confirm that the longitudes and latitudes had been correctly assigned to the appropriate pixels, the UV statistical oval taken from Nichols et al. (2009) was overlaid on the polar projections, as shown in Figure 5-3 by the blue line. Studies such as Clarke et al. (2004) and Radioti et al. (2013) have shown that the UV main auroral emission can be used as a reasonable proxy for the position of the IR main auroral emission. It can be seen in Figure 5-3 that the UV statistical oval fits well with the IR main auroral emission, hence the assignment of longitudes and latitudes in the projections appear to be correct.

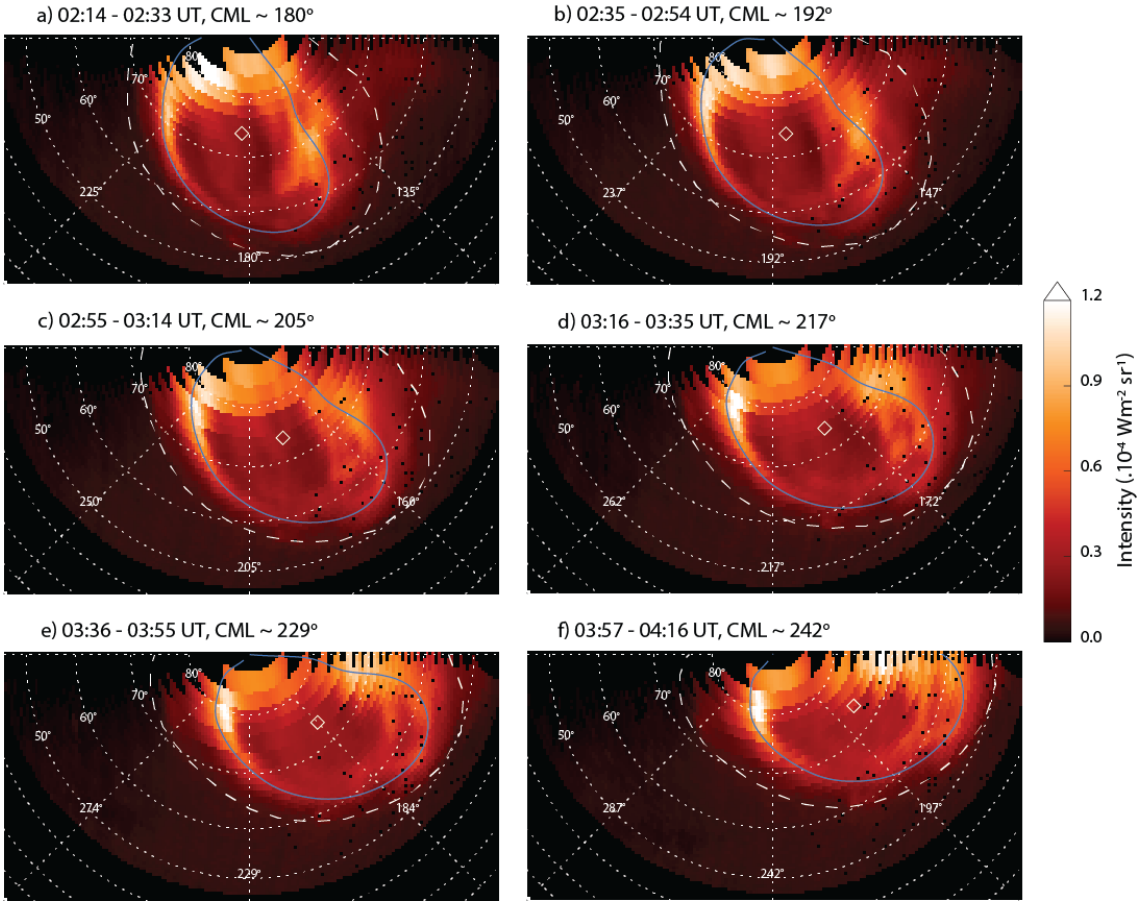

Figure 5-3: (a) – (f) Six polar projections of the intensity created from six scans of Jupiter's northern auroral. The blue line is the statistical UV oval (Nichols et al., 2009), overlaid on the polar projection. The diamond marks the position of an auroral centre defined by Grodent et al. (2003) at 185° longitude (System III) and 74° latitude. The white dashed line is the magnetic footprint of Io according to the Grodent et al. (2008) model. A gamma correction of 0.6 was applied to the polar projections. The LOS intensity correction has been performed on these polar projections. The longitudes are in System III, each scan is about ~13° CML apart, and the latitudes are planetocentric.

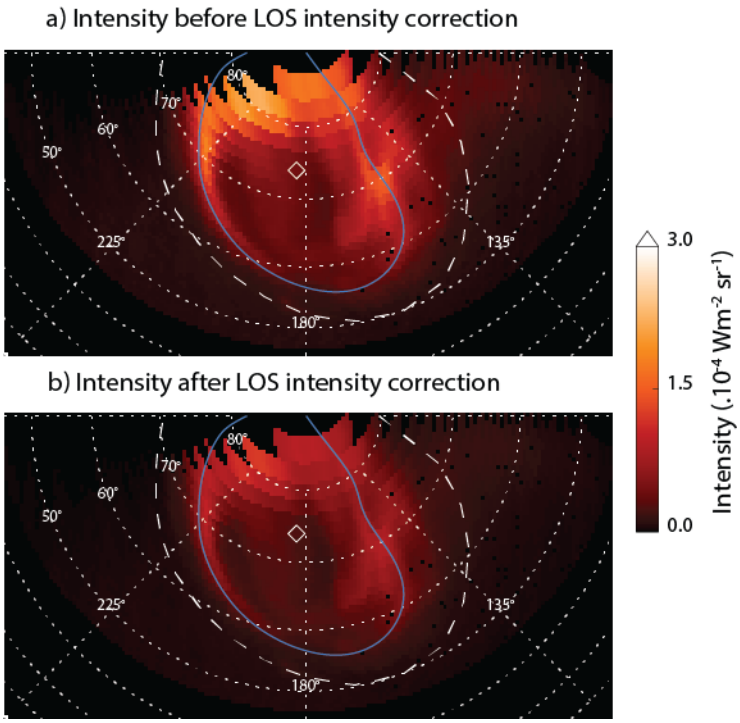

Figure 5-4: Polar projections of intensity (a) before and (b) after the line-of-sight (LOS) intensity correction was performed. A gamma correction of 0.6 was applied to the projected images in both (a) and (b).

The LOS velocity was derived using the methods described in Section 3.5.3. The average wavelength (λ ~ 3.94559 µm) and average change in wavelength per pixel ($\Delta\lambda$ ~2.06447 x 10^{-5} µm per pixel) were used in Equation 3.18. The value v_0 was determined using LOS velocity derived in the equatorial region at noon. The average was taken of the six spectra with a North-South orientation and the LOS velocity derived in the equatorial section of the average emission line. It is possible to use this LOS velocity as v_0 because Johnson et al. (2016) showed that the H_3^+ ions were corotating here and since the LOS velocity at the CML is being derived, there will be no component of the planet's rotation. It is assumed that meridional ionospheric flows are negligible as no significant flows were identified in Johnson et al. (2016) in the mid-to-low latitude ionosphere.

The LOS velocity spatial correction was applied to the velocities as described in Section 3.5.3. Figure 5-5 shows a H_3^+ intensity profile across the disk of Jupiter when the centre of the slit of CRIRES was positioned at ~74° latitude. Overlaid on the intensity (grey dotted line) is the LOS velocity in the PRF before (green crosses) and after LOS velocity spatial correction was applied (pink crosses). The spatial anisotropy velocities, derived from the intensity anisotropies, are represented in Figure 5-5 by the

black line. The spatial anisotropy velocity varies as the intensity varies; in particular large spatial anisotropy velocities are derived at the limb due to the significant intensity gradient here. The green crosses are the LOS velocity in the PRF before spatial correction is performed. It can be seen that the majority of the variation is independent of the spatial anisotropy velocities (black line). This implies that the LOS velocity in the PRF is derived from Doppler shifts caused by the H_3^+ motions, with only small additional Doppler shifts caused by the spatial effects. As CRIRES has a narrow slit of 0.2'' there is less spatial variation across the slit width than compared to previous studies which used the 0.5'' slit. Therefore by using a narrower slit, this reduces the LOS velocity spatial anisotropy effect compared to the study by Stallard et al. (2001).

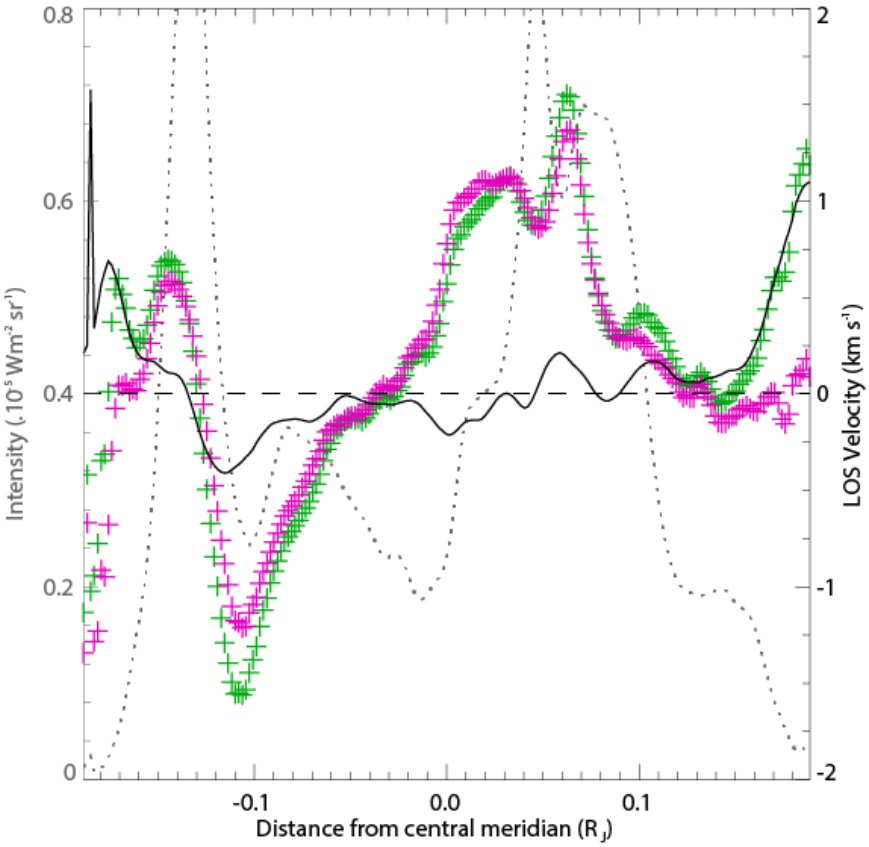

Figure 5-5: A comparison of the LOS velocity before and after spatial correction in the planetary reference frame (PRF), when the centre of the slit was positioned at CML ~171° and latitude ~74°. The intensity is represented by the grey dotted line. The spatial anisotropy velocities, calculated using Equation 3.25, are represented by the black line. The LOS velocity before correction, $v_{PRF}(y)$, is represented by the green crosses and the LOS velocity after correction, $v_{PRF\_SC}(y)$, is represented by the pink crosses. The black dashed line of zero gradient represents corotation in the PRF.

Towards the limb, beyond ~±0.16 R_J, however, the positive values in the LOS velocity (green dashed line) are caused by the spatial anisotropies creating additional blue-shifts in the spatial anisotropy velocity (black line). By removing the spatial anisotropy velocity as in 3.27, the blue-shift on the limb can be reduced. In this sub-auroral dusk region of Jupiter's ionosphere, it is expected that the ions are corotating and hence have a LOS velocity of ~0 km s^{-1} in the PRF. The pink crosses show the LOS velocities in the PRF after spatial correction. At ~0.16 R_J it can be seen that the blue-shifted velocities are significantly reduced to ~0 km s^{-1} after the LOS velocity spatial correction is performed. A similar reduction is also seen on the dawn limb at ~-0.16 R_J, however unreliable results are seen at distances larger than ~-0.16 R_J, due to the noise being relative large compared to weak signal on the dawn limb. This effect is not seen on the dusk limb as signal here is strong owing to this limb being fully illuminated. There is some variation in the spatial anisotropy velocities seen across the main auroral emission and polar aurora. However, the variation in the spatial anisotropy velocities here differs significantly from the derived LOS velocity in the PRF, therefore the LOS velocity spatial correction only alters the LOS velocity in the PRF slightly, as shown by the green and pink crosses.

5.2.1 Errors

Figure 5-6 shows the uncertainty in the LOS velocity which is applicable to the derived LOS velocities in all reference frames. This error consists of uncertainties due to:

- correcting the spectral dispersion across the detector array
- fitting a Gaussian to the H_3^+ emission spectra
- determining v_0
- correcting the LOS velocity spatial effect

and are discussed further in the sub-sections below.

Outside the auroral regions, where the H_3^+ signal is weaker, the error increases as can be seen in Figure 5-6. This investigation focuses on morphological features and H_3^+ flows which are poleward of the Io magnetic footprint, which is a region of relatively low uncertainties (typically <± 0.3 km s^{-1}). The uncertainty in the non-auroral regions can be seen to vary in a pattern which approximates curved stripes across the polar projection. This effect may be caused by the flat-fielding process of the data

reduction introducing systematic errors. This error is thought to be instrumental, potentially caused by temperature changes inside the instrument with the flat frames being taken at a separate time to the observations. It appears that this effect is prominent in regions of poor signal-to-noise, while inside the auroral regions the effect seems limited due to the higher H_3^+ intensities.

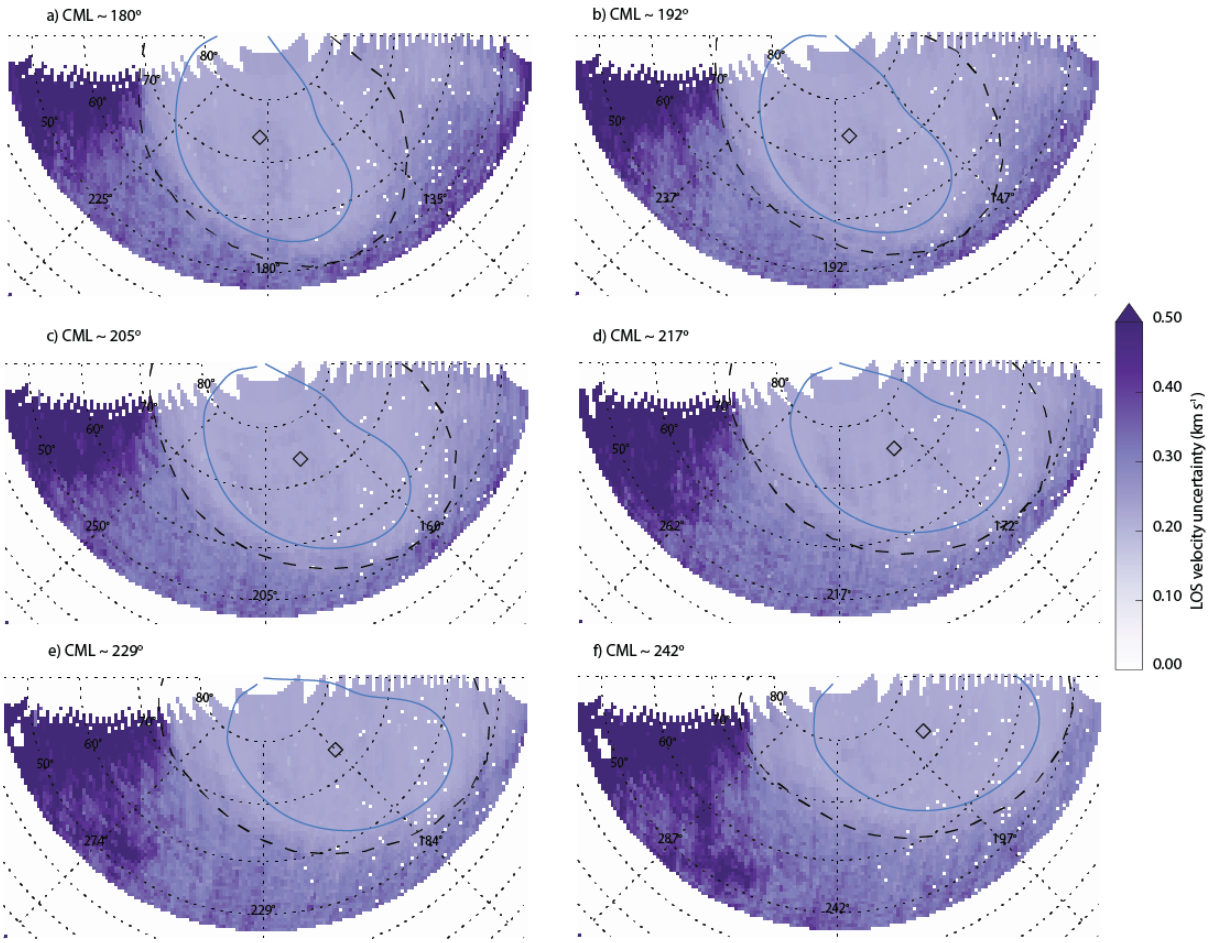

Figure 5-6: (a) – (f) Six polar projections of the individual uncertainties of the derived LOS velocity values. Similar format to Figure 5-3.

5.2.1.1 Projection

As with all projections, there are significant errors associated with the pixels that map toward the planetary limb. Pixels located at the limb will map to a larger range of latitudes and longitudes than pixels located at the centre of the disk of the planet. For example, at the most equatorial slit position (~45° latitude), a pixel at the limb covers a longitude range of ~2.2° and a latitude range of ~0.7°. However, at the most poleward slit position (~86° latitude), a pixel at the limb covers a longitude range of ~4.1° and a latitude range of ~2.6°.

The polar projections are created from a sequence of spectra, each integrated for 25 s. During this time Jupiter will rotate 0.26° causing a smearing of 0.504 pixels in the spectra in the spatial direction. However, this smearing is smaller than the seeing (~0.5'', which equates to ~5.6 pixels) and hence does not introduce a significant error.

Despite the errors in creating the projections, the precise mapping of the flows is not the main aim of this study. Although the errors must be noted, the positional discrepancies do not affect the main results of this investigation. By creating polar projections of the intensity and ion flows using the same method, the intensity morphology can still be directly compared with the flow regimes. However, if one were to consider how the flow regions in Jupiter's ionosphere map to the magnetosphere then it would be wise to use caution.

5.2.1.2 Spectral Dispersion

The wavelength variation across the detector array was determined using telluric emission lines, which was part of the data reduction. During this process the 1-sigma error estimate on the position and peak of the Gaussian fitted to every spatial position along the telluric emission line and the 1-sigma error estimate on the second order polynomial, which was fitted to the telluric emission line, were determined. The propagated error from correcting the spectral dispersion was 0.053 km s^{-1}.

5.2.1.3 Fitting a Gaussian

To derive the LOS velocities from the H_3^+ emission line the spectral position of the line must be measured so the relative Doppler shift can be related to the resolution of the instrument. By fitting a Gaussian to every spatial position along the average H_3^+ emission line, the position of the Gaussian was identified and hence the relative Doppler shift was determined. Therefore, each derived value of LOS velocity there is a 1-sigma error on fitting the position of this Gaussian.

5.2.1.4 Zero Point Velocity

The value v_0 was determined by fitting a Gaussian to the equatorial region of the average spectra taken in a North-South orientation. There is an uncertainty associated with the position of the peak of this Gaussian which is included in the v_0 uncertainty. The accuracy of aligning the slit with the centre of the planet was ~ ±1'' in the

longitudinal direction, which introduces a small LOS velocity values due to the rotation of the planet. Both of these uncertainties are taken into account and a final uncertainty of ± 0.15 km s^{-1} is applied to all measured LOS velocities values in all reference frames.

5.2.1.5 Line-of-Sight Velocity Spatial Correction

Performing the spatial correction on the LOS velocity values introduces uncertainties because no simultaneous H_3^+ images were available to determine the intensity variation inside the slit, and therefore the calculated spatial anisotropy velocities are an approximation. The 1-sigma error from fitting a 2D polynomial to the interpolated results is included in the total error for each derived value of LOS velocity.

5.3 Key Results

5.3.1 Intensity

The intensities for the six scans of Jupiter's northern aurora are shown in Figure 5-3. The average of these scans is shown in Figure 5-7. In addition to the UV statistical oval (Nichols et al. 2009), a white line is shown that represents the most intense part of the H_3^+ main auroral emission, which was identified manually from the peak brightness of the average intensity. The location of this overlay is almost coincident within the 4° region that Nichols et al. (2009) uses to define the main auroral emission.

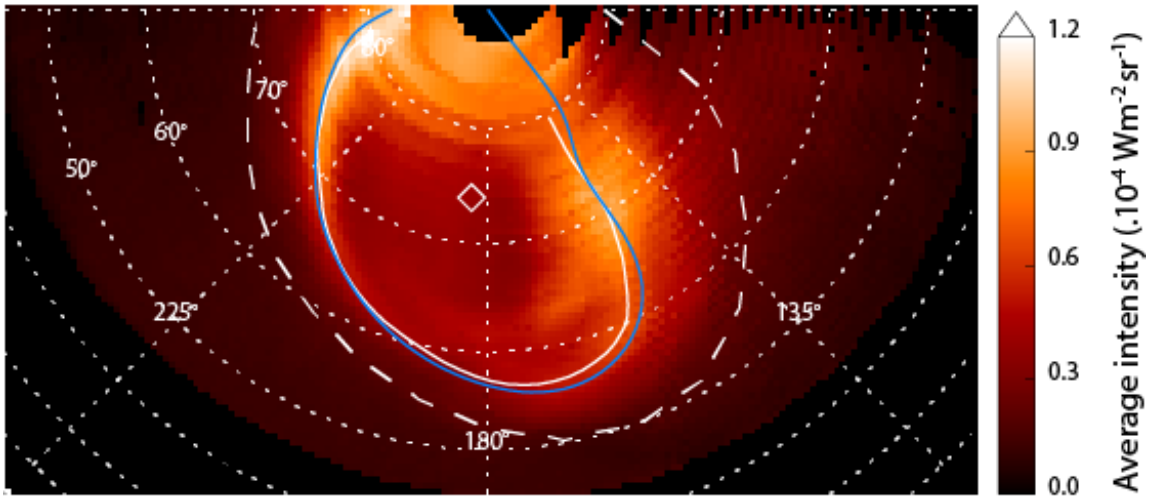

Figure 5-7: The average intensity derived from six scans. Similar format to Figure 5-3, with an additional white line which represents the most intense part of the average H_3^+ intensity. A gamma correction of 0.8 has been applied to the image.

The main auroral emission in the dawn sector (M_1) is narrow and bright. The intensity varies from ~1.2 x 10^{-4} Wm^{-2} sr^{-1} at ~ 250° longitude to ~0.3 x 10^{-4} Wm^{-2} sr^{-1} at ~180° longitude. At ~180° longitude the intensity of the main auroral emission is at its lowest magnitude, which is a region of low intensity also seen in the UV (Grodent, 2015).

The dusk sector of the main auroral emission (M_2) is more diffuse than emission in the M_1 region. The intensity of the M_2 region is ~0.3 –0.9 x 10^{-4} Wm^{-2} sr^{-1} and comes to a maximum near to the location of the kink in the shape of the main auroral emission, at the approximate location of the magnetic anomaly (Grodent et al. 2008). The dusk limb is brighter than the rest of the sub-auroral disk emission, with an intensity of ~<0.15 x 10^{-4} Wm^{-2} sr^{-1}, whereas the disk emission of H_3^+ is usually has an intensity of ~<0.1 x 10^{-4} Wm^{-2} sr^{-1}.

The two dark regions, D and P, have intensities of ~0.2 – 0.3 x 10^{-4} Wm^{-2} sr^{-1}. Region D is approximately coincident with the UV dark region. The dark region P is not so readily observed in the UV as this region sits between the UV swirl and active regions. The morphology of emission in the swirl and active regions can be dynamic, variable and bright in the UV. However, in the IR Stallard et al. (2016) observed that the polar regions appeared to remain consistently absent of variability. The polar region S has an intensity of ~0.25 – 0.35 x 10^{-4} Wm^{-2} sr^{-1} and is coincident with the UV swirl region. Polar region A has an intensity ~0.3 – 0.6 x 10^{-4} Wm^{-2} sr^{-1} and is coincident with the UV active region. There is an arc of H_3^+ emission which extends from the A region, below the P region, along the boundary between the D and S regions. Note that the different morphology regions of the polar aurora, observed at the UV wavelengths are labelled in Figure 2-14.

5.3.2 Line-of-Sight Velocity

At Earth, the ionosphere is very strongly coupled to the magnetosphere and therefore geomagnetic coordinates are usually used to present terrestrial ionospheric flows (Rishbeth, 1988). However at Jupiter, there is complex thermosphere-ionosphere-magnetosphere coupling, such that no single reference frame can used in isolation to study the H_3^+ flows in Jupiter's ionosphere. The degree to which the ionosphere is coupled to the magnetosphere and the thermosphere changes depending on the

location in the ionosphere. Away from the aurora, in the mid-to-low latitude regions, it is possible to work in the planetary reference frame (PRF) as Johnson et al. (2016) showed that the ionosphere rotated with System III. It is not possible to solely work in the PRF in the auroral regions due to currents induced by the strong coupling to the middle magnetosphere (e.g.: Cowley and Bunce, 2001), therefore, the magnetic pole reference frame (MPRF) must also be considered. The neutral atmosphere remains partially coupled to the ionosphere in the auroral regions and cannot be disregarded in favour of a purely magnetic reference frame. It is important to consider both reference frames when studying the dynamics of Jupiter's ionosphere, in particular when studying the polar aurora as the origin of this aurora is not very well understood. Through identification of different regions of morphology, the intensity can be associated with the flows measured in Jupiter's ionosphere. Hence, the notation established in Figure 5-1 will be used to describe the regions of different ionospheric H_3^+ flows.

When dealing with LOS velocity measurements it is important to consider the effect of the viewing geometry of the observer on the velocities. As the ionospheric flows become increasingly perpendicular to the line-of-sight of the observer, and hence become parallel to the slit, the LOS component of the velocity of the H_3^+ approaches zero. Therefore it is important to observe the aurora as it rotates across the dayside of the planet.

5.3.2.1 Line-of-Sight velocities in the Planetary Reference Frame

Using the method described in Section 5.2, polar projections of the LOS velocities in the PRF were created. Six LOS velocity projections in the PRF are shown in Figure 5-8 corresponding to the six scans. In the PRF the LOS component of the planet's rotation has been removed, so that a LOS velocity of zero is interpreted as the ions moving with rigid corotation. As discussed in Section 5.2, instrumental artefacts cause variations in signal-to-noise in the sub-auroral region, where the patterns in Figure 5-8 are associated with the errors shown in Figure 5-6. The large variation and large values of LOS velocities measured on the dawn limb are unreliable. They are due to the poor signal-to-noise in this region, and are reflected in the large uncertainties in this region in Figure 5-6.

As discussed in Chapter 4, it is assumed that the non-auroral ionosphere is corotating. Therefore, it is expected that the sub-auroral region would corotate due to a lack of auroral currents in those regions, and the majority of the sub-auroral region has been found to corotate within the bounds of experimental error. However, it can be seen from Figure 5-8 that this is not the case for the dusk limb of Jupiter where the H_3^+ flows on the dusk limb are moving away from the observer and exceed planetary rotation for reasons which are not clear. In this chapter I will focus on auroral ionospheric flows, leaving the study of sub-auroral ionospheric flows to future studies.

In the auroral region, several regimes of strong ionospheric flows can be observed. An ionospheric flow with a LOS velocity towards the observer, relative to the planet, is observed between 190° – 270° longitude and is interpreted as a super-rotational flow. This super-rotation is mainly located in the M_1 region. Rego et al. (1999) measured super-rotational flow of ~ 1 km s^{-1} at a CML of 270° and this study measures a flow of ~0.7 km s^{-1} at the same longitude as shown in Figure 5-8e and f. However, the super-rotational flow measured by Rego et al. (1999) were equatorward of those measured in this study, lying closer to the Io magnetic footprint than the main auroral emission. Stallard et al. (2001) measured a super-rotational flow at a similar position to this study. For example, when the East-West orientated slit was aligned on a CML of 155°, Stallard et al. (2001) measured a super-rotational flow of ~0.5 km s^{-1}.

A strong velocity shear is observed between 190° – 270° longitude, located near to the M_1 region. The peak of the velocity shear is located just poleward of the peak in the average intensity of the H_3^+ emission, as shown by the solid black line in Figure 5-8.

In the region coincident with the UV dark region (D) strong ionospheric flows with a LOS velocity away from the observer relative to the planet are observed between 180° – 225° longitude, with a maximum derived LOS velocity of ~-2.2 km s^{-1}, which implies a significant sub-rotation. In the region A, coincident with the UV active region, flows towards the observer relative to the planet are measured, implying sub-rotation. The sub-rotation in the region A extends through region M_2, with a maximum derived LOS velocity of ~1.5 km s^{-1}. Weaker flows are derived in the S and P regions with LOS velocities approximately within the range $-0.5 < v_{SC_{PRF}}(y) < 0.5$km s^{-1}. These results differ somewhat from those of Stallard et al. (2001): the strong sub-rotation is now measured in the region D and weaker flows are measured mainly in the S and P

regions, whereas Stallard et al. (2001) identified strong red-shifts in the region bounded by the black dot-dashed line in Figure 5-8, which overlaps parts of the S and P regions, and measured weaker flows in the region D.

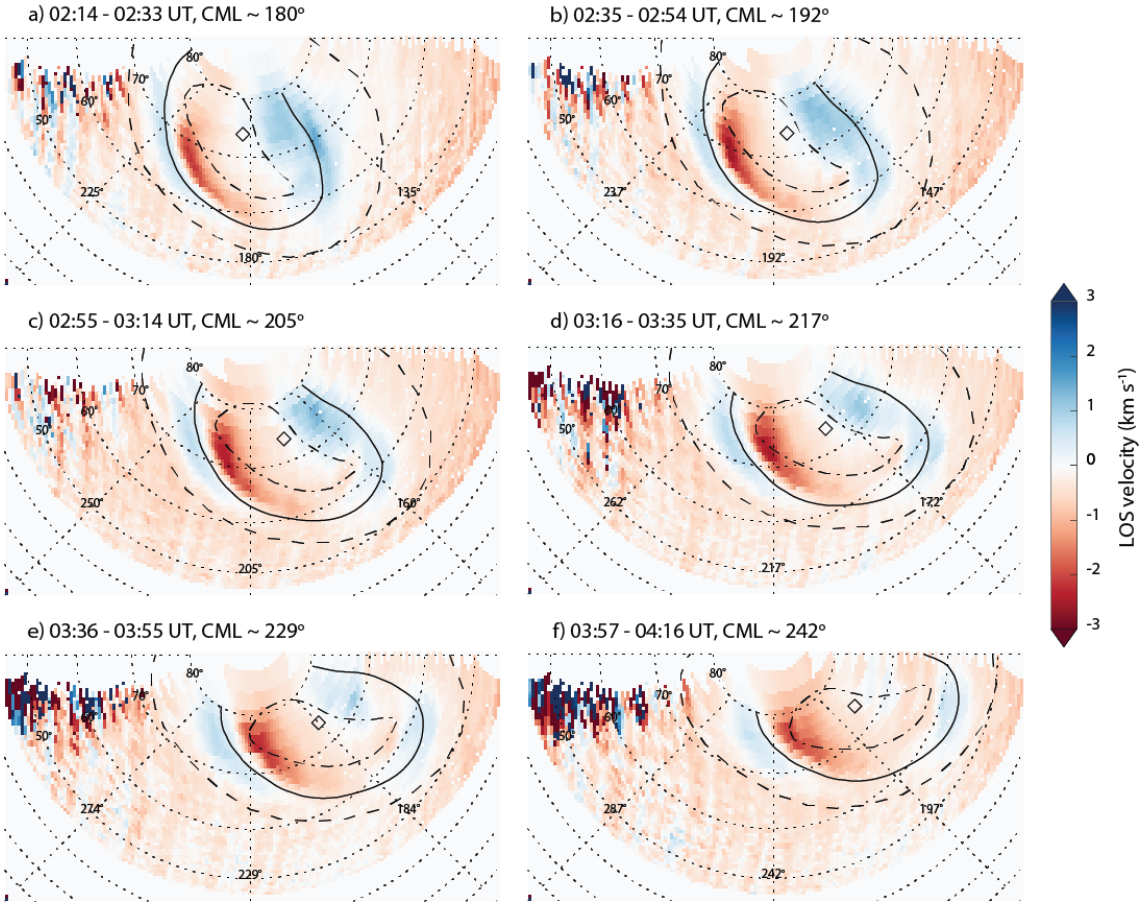

Figure 5-8: (a) – (f) Six LOS velocity polar projections in the planetary reference frame (PRF). The black line represents the most intense part of the average H_3^+ intensity. The diamond marks the position of an auroral centre defined by Grodent et al. (2003) at 185° longitude (System III) and 74° latitude. The black dashed line is the magnetic footprint of Io according to the Grodent et al. (2008) model. The black dot-dash line bounds the fixed dark polar region (f-DPR) as defined by Stallard et al. (2003).

5.3.2.2 Line-of-sight Velocities in the Magnetic Pole Reference Frame

Polar projections of the LOS velocities in the MPRF were created using the method described in Section 5.2, and are shown in Figure 5-9. In this reference frame, the LOS component of Jupiter's rotation is included; therefore, it is harder to decipher the small deviations from corotation. The values are saturated at ±4 km s^{-1} to aid identification of the different flows in the auroral region. The key result achieved by transforming into the MPRF is that the sub-rotating flow measured in the dark region (D) in the PRF is now observed as a stationary region of LOS velocity in the MPRF. This

suggests that the ions here are fixed with a zero velocity in the MPRF. Stallard et al. (2003) also identified a stationary region in Jupiter's polar ionosphere, however, in their study it was located in the region bounded by the black dot-dashed line in Figure 5-9. Exactly what causes the difference between the location of these flows in Stallard et al. (2001) and this study will be explored in Section 5.4.

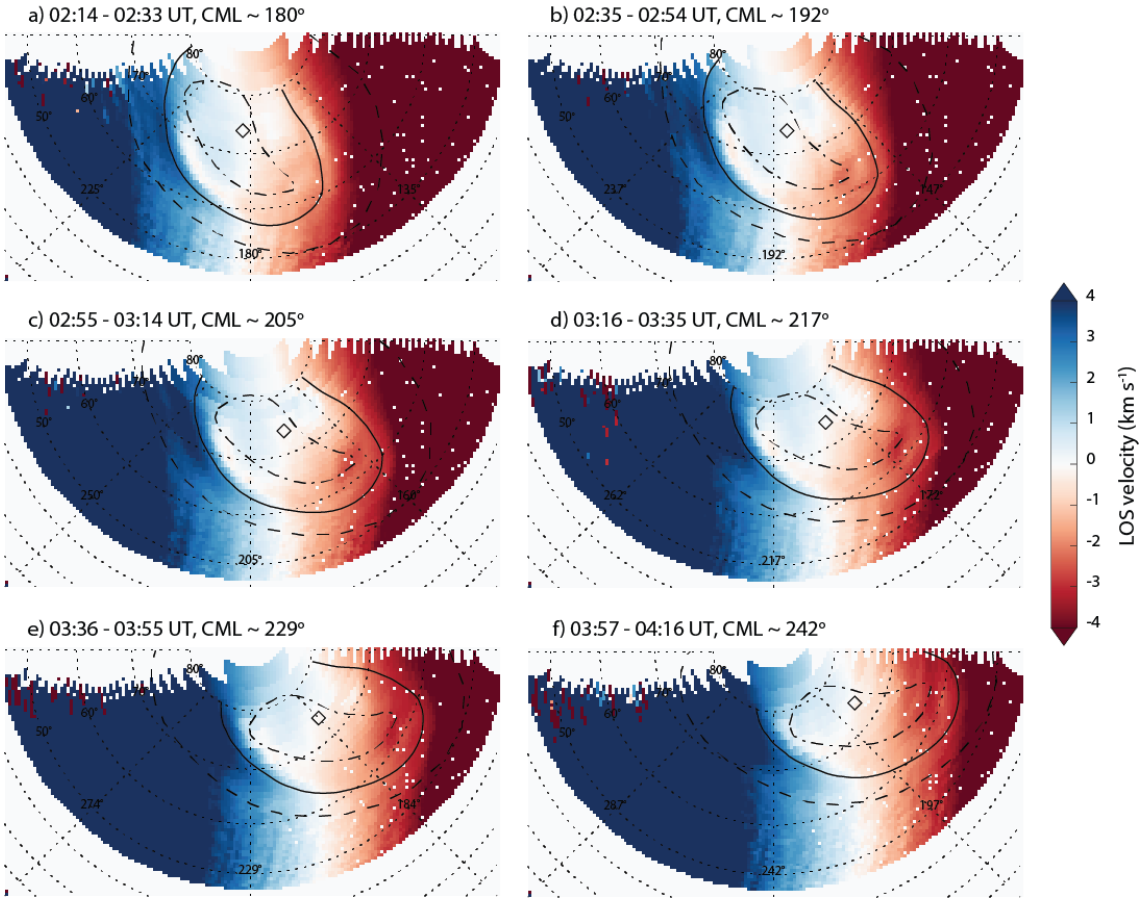

Figure 5-9: (a) – (f) Six LOS velocity polar projections in the magnetic pole reference frame (MPRF). Similar format to Figure 5-8.

5.4 Discussion

Several distinct regions of H_3^+ ionospheric flows have been identified in Jupiter's auroral region. Through comparison of the PRF (Figure 5-8) and MPRF (Figure 5-9), and with the aid of the average intensity polar projection (Figure 5-7), these ionospheric flows have been associated with the different morphological regions. The three main flows are illustrated in the schematic in Figure 5-10, where the black arrows approximate the ionospheric flow direction.

1. In the PRF and MPRF, the H_3^+ ions observed in the main auroral emission in the M_1 region (~180° - 270 ° longitude) have a LOS velocity which surpasses the

rate of planetary rotation, which means they are super-rotating (green shaded region in Figure 5-10).

2. In the PRF, the H_3^+ ions observed in the UV dark region (D) have a LOS velocity which is lagging behind the rate of planetary rotation, which means that they are sub-rotational. In the MPRF, near zero values are observed in this region, which implies this region is stationary relative to the magnetic pole (dark blue shaded region in Figure 5-10).
3. In the PRF and MPRF, the H_3^+ ions observed in the main auroral emission in the M_2 and A regions have a LOS velocity which is lagging behind the rate of planetary rotation, which means they are sub-rotating (light blue shaded region in Figure 5-10).

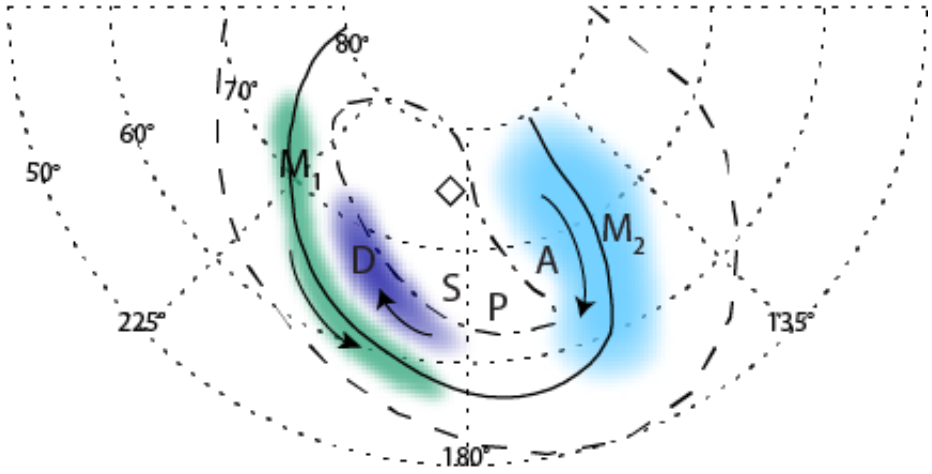

Figure 5-10: A schematic of the ionospheric flows measured in this study, presented in the PRF and viewed from above the north pole of Jupiter. The black arrows suggest the direction of the ionospheric flows (note the arrow length is arbitrary). The green shaded region represents super-rotating ionospheric flows and the blue regions represent sub-rotating ionospheric flows. The dark blue region has very strong sub-rotational flow and contains the stationary values of LOS velocity when transformed to the MPRF, whereas the light blue region has weaker sub-rotational flows. The format is similar to Figure 5-8 and the different regions of morphology observed in Jupiter's aurora are labelled, as identified in Figure 5-1.

The super-rotational flows measured by Rego et al. (1999) in the PRF were observed slightly equatorward to the super-rotational flows measured in this study and were attributed to coupling with radial currents in Jupiter's magnetosphere ~0.2 R_J inside Io's orbit, which also caused auroral hiss measured by Voyager and discussed by Morgan et al. (1994). From Figure 5-8, it can be seen that the super-rotational flows measured in this study never fully extend to the Io magnetic footprint and therefore

cannot be attributed to the same source region in the magnetosphere. The differences in the location of the super-rotational flows between this study and the study by Rego et al. (1999) could be due to the spatial detail of the Rego et al. (1999) study. The slit of CSHELL was aligned along the CML in a North-South orientation in the study by Rego et al. (1999), which limited their ability to map the flows of H_3^+ ions. In this study numerous West-East slit positions are used to obtain greater spatial detail, providing a more accurate position of the super-rotational flows in Jupiter ionosphere.

Figure 13 in Stallard et al. (2001) shows super-rotational flows in the M_1 region at a similar location to this study, however, this flow is not discussed in the paper. The orientation of the CSHELL slit was East-West in the Stallard et al. (2001) study, and the orientation of the CRIRES slit in this study was West-East. With different slit orientations, the spatial anisotropy velocities will reverse along with the spatial anisotropies across the slit. However, physical flows will remain the same regardless of slit orientation, although the magnitude will alter depending on the viewing geometry and the accuracy of the measurements will depend on the spectral resolution of the instrument. Therefore, by observing the same flows with three different slit orientations (North-South in Rego et al. (1999); East-West in Stallard et al. (2001); West-East in the present study) and two different instruments (IRTF-CSHELL in Rego et al. (1999) and Stallard et al. (2001), and VLT-CRIRES in this study), this shows that the blue-shift measured in this region is a real flow and not a spatial effect error. This also implies that all other flows observed in Rego et al. (1999), Stallard et al. (2001), and this study are physically real.

Perhaps the origin of the super-rotating ionospheric flows in the M_1 region is a super-rotating flow in the thermosphere, generating ion-drag and causing the H_3^+ ions to rotate faster than corotation. At Earth, more detailed three dimensional models of ion drag during periods of high geomagnetic activity show that the neutrals can move to form vortices in the thermosphere, resulting in regions of super-rotation – notability in the dawn sub-auroral region (Walterscheid and Crowley 2009). The only measurements of thermospheric winds at Jupiter were made by Chaufray et al. (2011). They showed that, typically, neutral H_2 winds were much weaker than their H_3^+ counterparts i.e.: they were closer to corotation. Although Chaufray et al. (2011) did

not identify any super-rotations, the spatial coverage of their data set was limited and hence such a flow in the pre-noon ionosphere cannot be ruled out.

Majeed et al. (2016) showed that neutral flows are easily produced by ionospheric flows, but they provide no longitudinal variability to compare with this study. Models of Jupiter's ionosphere-thermosphere are typically simplified; for example, the JIM model (Achilleos et al. 1998) uses a circular auroral oval and simplistic Dungey cycle midnight flow. This model shows regions of super-rotation equatorward of the main oval, which are very small (tens of m s^{-1}). Smith and Aylward (2009) also show a thermospheric wind which is super-rotational at ~63-73° latitude, in their self-consistent, axisymmetric, thermosphere-magnetosphere coupled global circulation model. A full description of how this super-rotating wind is generated in the thermosphere is given in Section 2.5.2.

The model by Smith and Aylward (2009) shows that a super-rotation of the ionosphere does not imply super-rotation of the magnetosphere (in the region in which they are mapping to). In fact, they suggested that the super-rotating wind will enforce corotation. If the more distant magnetosphere increases in sub-rotation (i.e.: experiences a reduction in velocity), this will in turn increase the super-rotation of the thermosphere (i.e.: increases the velocity) and, since the inner magnetosphere has a relatively low moment of inertia, the inner magnetosphere is brought to near-corotation by the thermospheric super-rotating winds. The sub-rotation of the more distant magnetosphere indirectly supports the corotation of the inner magnetosphere via the super-rotation. However, Smith and Aylward (2009) do not show that the ions in this region are also super-rotating. The H_3^+ wind speeds predicted by Achilleos et al. (1998) are lower than those measured by Stallard et al. (2001) and in this present study, hence the calculated super-rotational flows may fall short of actual measured values.

Another explanation for the super-rotational flows in the M_1 region involves a region of the magnetosphere, but at larger distances of R_J than discussed by Rego et al. (1999). Since the super-rotation appears to be confined to the pre-noon sector, it is possible that the origin of this flow is linked to flux tubes rotating through the dawn sector of the dayside magnetosphere. Cowley et al. (2003) suggested that part of the magnetosphere is coupled to a Dungey cycle like process, confined to the dawn sector

by the Vasyliunas cycle as shown by Figure 2-12 and discussed in Section 2.3. Figure 2-12 shows the extended flux tubes full of iogenic plasma pinch off on the nightside of Jupiter in the region of the Vasyliunas-cycle tail X-line and rotate round into the dawn sector of the dayside magnetosphere. As the field lines rotate through the dawn sector they move radially inwards so that the angular velocity of the plasma increases to conserve angular momentum. Field lines which map further out in the magnetosphere, closer to the magnetopause, and have footprints more poleward in the ionosphere, will have the greatest fractional change in radial distance and hence the greatest fractional increase in angular velocity. However, the actual angular velocity will also depend on the initial angular velocity of the field line before it is compressed. If the field line is severely lagging behind corotation then the compression of the field line may not be sufficient to increase the angular velocity to super-rotation. It could be the case that a field line is near-corotating such that a small change in the radial distance could increase the angular velocity to a point where the field line is super-rotating as observed in Figure 5-8 and Figure 5-9.

Although it is expected that this super-rotation will increase in magnitude towards the pole, the above discussion based on conservation of angular momentum does not apply to the region D as separate processes appear to be driving ionospheric flows there, and these processes will be discussed later in this section. Additionally, the location to which region M_1 maps in the magnetosphere is not known, and very small areas of Jupiter's ionosphere can map to a wide range of distances in the outer magnetosphere, which cannot be resolved with the spatial resolution of CRIRES. Hence it is possible that the M_1 super-rotating region actually maps further out than expected, mapping to regions which are significantly affected by the compression due the shape of the magnetopause. It cannot be said for certain that this super-rotational flow is confined to the pre-noon sector of the ionosphere as our measurements are subject to observational bias: from Earth only the dayside ionosphere can be observed, and currently there have not been any measurements of the LOS velocity of H_3^+ ions in the nightside ionosphere.

The initial distribution of angular velocity of the field lines mapping to region M_1 as the region rotates through the night side into the dawn sector is not known, so it is difficult to be definitive about the details of the resulting angular velocity distribution,

other than that the compression will cause an overall increase as discussed above. Presently, there is no direct evidence of the dawn sector of the dayside magnetosphere super-rotating. Pre-noon Voyager 1 and 2, and Ulysses inbound passes have shown the plasma to be corotational at 10-20 R_J (Belcher 1983, Sands and McNutt 1988, and Kane et al. 1995). Plasma flows derived through forward modelling from Galileo data by Bagenal et al. (2016) has shown that within 5-20 R_J the flow is dominated by azimuthal flow which is between 80 and 100% of corotation. Beyond distances of 20 R_J the flow is expected to fall below corotation and one would expect the region M_1 to map to regions of the magnetosphere which are beginning to lag behind corotation rather than exceed corotation. However, these observations are based on limited data of a very small sample size and it may be the case that the magnetosphere does super-rotate in certain regions as yet unobserved. The more extensive data set of Juno may provide the plasma flow speeds in Jupiter's magnetosphere and potentially determine whether the super-rotational flows in the ionosphere have a magnetospheric origin.

Super-rotational flows in the region M_1 were not expected by models such as Cowley and Bunce (2001). However, Nichols and Cowley (2003) predicted that the peak intensity of the main auroral emission will coincide with the peak in velocity shear assuming a constant conductivity in the ionosphere. This is because a gradient in the velocity in the meridional direction causes gradient in the electric field, as the ions and neutrals are moving at different speeds relative to each other, which sets up a Pedersen current. The model assumes an axisymmetric system, therefore any divergence of this Pedersen current leads to upward field aligned currents which generate the main auroral emission at Jupiter. The orientation of the shear that this study observed between the M_1 and D regions implies an upward field aligned current as shown in Figure 2-18 (the theoretical ionospheric flow schematic from Cowley et al. (2003).

A further model by Nichols and Cowley (2004) includes Pedersen conductance modulated self-consistently by auroral precipitation. This model predicted a local maximum in the angular velocity moving poleward from high latitude sub-auroral regions toward the main auroral emission. Furthermore, the model by Nichols and Cowley (2004) showed that, by taking variable conductivity into account, the peak in

velocity shear will be located poleward of the peak in the Pedersen current. Figure 5-8 and Figure 5-9 show that the peak in the velocity shear is poleward of the peak in average H_3^+ intensity, as predicted by Nichols and Cowley (2004). Although it the peak in H_3^+ intensity is approximately coincident with the peak in UV intensity (Clarke et al. 2004 and Radioti et al. 2013), there will be some small difference in the exact locations owing to the differences in time-scales of H and H_2 excitation and H_3^+ chemical reactions. However, these differences are likely to be small, and since the data are being compared to an axisymmetric model, it can be said that this study in general agrees with the model by Nichols and Cowley (2004).

Since the velocity shear is observed poleward of the peak in average intensity, Nichols and Cowley (2004) suggest that this implies the conductivity is affected by the field aligned currents themselves. This result is not as clear in the M_2 region where the aurora is more diffuse. In the M_2 region, the shear in LOS velocities does not have a constant gradient. There are several localised peaks in the gradient of the shear and also several arcs of diffuse emission, implying more complex processes are present than in the M_1 region.

In the UV dark region (D), this study identifies strong flows of up to ~-2.2 km s^{-1} in the PRF, which imply sub-rotation relative to the rotation of the planet. The same region is being held stationary in the MPRF. Figure 5-9 shows that the region D is always held stationary no matter what the viewing geometry is, and therefore this region is stationary relative to the fast rotation of Jupiter's magnetosphere. Stallard et al. (2003) defined a region of the DPR, which was largely coincident with the UV swirl region (S), as the f-DPR since the ions were being held stationary relative to the magnetic pole. The past observations do not match with those present in this study, which identifies the stationary region in the UV dark region (D) of Jupiter's ionosphere and not coincident with the f-DPR as shown by Figure 5-10. The change in position of the stationary region in Jupiter's ionosphere between the Stallard et al. (2003) study and the present study is likely to be due to the higher spatial resolution of CRIRES and the larger number of slit positions used to scan the aurora. However, since two case studies are being compared, without any information on the solar wind or the internal conditions of Jupiter's magnetosphere, it could be the case that conditions have

changed between the study conducted by Stallard et al. (2001) and this present study causing the stationary region to be observed in a different location.

Stallard et al. (2003) and Cowley et al. (2003) discuss how the f-DPR is coupled to the solar wind through a single cell convection cell as part of a restricted Dungey cycle. They propose that the ions in this region are coupled to open magnetic field lines which are convecting so slowly across the polar aurora that they are stationary relative to the corotational and sub-rotational closed magnetic field lines. However, Delamere and Bagenal (2010) discuss how the results from Stallard et al. (2003) could also be explained by solar-wind viscous drag. The magnetic field lines would be stationary as they are intermittently opened and closed along the dawn flank of the magnetopause. Delamere and Bagenal (2010) suggested that the f-DPR could not be open as it was approximately coincident with the UV swirl region which experiences intense and variable aurora both in the UV and IR. The Kelvin-Helmholtz interaction would be indicative of a boundary layer populated by near-magnetosheath densities of cool plasma, with relatively low energy flux of the sheath plasma (Cowley et al. 2008), which would create weak aurora. Small-scale reconnection may occur due to twisting of field lines in the Kelvin-Helmholtz boundary layer, which could heat the plasma leading to a brighter emission at the footprint. In this this study, the stationary region has been shown to be lacking in IR emission and coincident with the UV dark region (D), which is suggestive of open field lines. However, it should be noted that while the lack emission in the stationary region supports the arguments put forward by Cowley et al. (2003), this data set alone cannot confirm the field lines here are coupled to the solar wind through a Dungey cycle like process.

5.5 Conclusions

This chapter presents a highly detailed case study of Jupiter's auroral H_3^+ ionosphere using projections of the intensity and ionospheric flows in several reference frames (Johnson et al. 2017). In the PRF and MPRF a super-rotational flow is observed in the M_1 region. A thermospheric neutral wind, predicted by the model by Smith and Aylward (2009), could be driving the super-rotational flow through collisional forcing. As the model by Smith and Aylward (2009) is axisymmetric, direct comparison between their results and the observed ionospheric flows is not possible, however, it is

still possible that a thermospheric super-rotational flow exists near to the location of the main auroral emission which is driving super-rotational ionospheric flows. Alternatively, the super-rotational flow could be generated by the flux tubes, which are rotating through the dawn sector of the dayside magnetosphere, being compressed and speeding up. However, current measurements of plasma flow in the dawn sector of the magnetosphere have not revealed any super-rotation. The exact mechanism causing the super-rotational flow remains unknown.

Two of the ionospheric flows reported upon in this study confirm predictions by Nichols and Cowley (2004). An increase in angular velocity was expected by Nichols and Cowley (2004) in the region between the Io magnetic footprint and the M_1 region. An increase in the LOS velocity in this region is observed and suggested that it is related to an increase in conductivity as described by Nichols and Cowley (2004). A strong velocity shear has been observed poleward of the peak in average H_3^+ intensity, implying a major gradient in plasma angular velocity, as predicted by the model of Nichols and Cowley (2004). The poleward position of the velocity shear relative to the peak in intensity means that conductivity in the ionosphere is being affected by the field aligned current itself. Velocity shears are observed in the M_2 region, however, the relation between the peak in the shear, the conductivity and the peak in H_3^+ intensity is clearly more complex in this region of the main auroral emission. Overall it seems clear that conductivity, as well as changes in angular momentum, has a major role in the generation of Jupiter's aurora.

In the PRF, sub-rotational flows are observed in the D region, these flows are near-stationary in the MPRF. The location of this flow has changed since it was first identified by Stallard et al. (2001), which may be due to environmental changes in Jupiter's magnetosphere, the solar wind, or a combination of the two. However, it is more likely that this study reveals a more accurate location of the flow due to the increase of spatial resolution. The H_3^+ ions in this region are stationary when transformed into the MPRF, which suggests an interaction with the solar wind. This study cannot determine the exact mechanisms through which this region of Jupiter's ionosphere is coupled to the solar wind.

This chapter has presented a case study of one night of observations. Future studies which utilise more extensive data sets may be able to determine whether the

super-rotational flow in the M_1 region of the main auroral emission is a permanent ionospheric flow in Jupiter's ionosphere or a transient flow. Additionally, further studies with larger data sets will also confirm the position of the stationary region. Future simultaneous measurements of ionospheric flows determined from H_3^+ emissions with the Juno in-situ data will help determine the characteristics of the magnetic field lines which the ionospheric flows map to. The Juno data may determine whether the source of the super-rotational flow in the M_1 region is driven by the magnetosphere through sampling the flux tubes in-situ. Using simultaneous measurements with ground-based observations and measurements taken by Juno, it may be possible to determine whether the stationary D region is coupled to the solar wind through a Dungey cycle like process or through viscous interaction moderated by Kelvin-Helmholtz instabilities.

Chapter 6 Mapping H_3^+ Temperatures in Jupiter's Northern Auroral Ionosphere

6.1 Introduction

In this chapter the rotational temperature, column density, and total emission were derived from the H_3^+ auroral emission observed on the 31 December 2012 with VLT-CRIRES (the same data set as used in Chapter 5). The entire northern auroral region was observed, providing a highly detailed view of these H_3^+ properties, which were mapped onto polar projections. By comparing all these properties to the LOS velocity from Johnson et al. (2017) (discussed in detail in Chapter 5), we have furthered our understanding of the governing mechanisms in Jupiter's ionosphere.

The temperature of the ionosphere has been measured at semi-regular intervals since H_3^+ was detected at Jupiter. At first, auroral averages were acquired, e.g.: rotational temperature of ~1250 K by Drossart et al. (1989), then studies begin to expand and map the global temperature (e.g. Lam et al. 1997 and Miller et al. 1997). These studies also measured the column density and total emission. Recently, higher spatial and spectral resolution instruments have increased the quality of the mapping of these properties at Jupiter (e.g.: Moore et al. 2017 and Adriani et al. 2017). For a full discussion of the existing literature please refer to Section 2.6.

These properties are key in understanding the mechanisms that cause heating in the auroral regions. Based on knowledge of the Earth system, we know that heating by impact from precipitating particles and Joule heating are likely candidates for the drivers of elevated temperatures measured there. Energy deposited in the auroral regions can be removed from the upper atmosphere through H_3^+ reradiating it into space. By studying all of these properties together, I will investigate the interplay between the heating and cooling mechanisms. Changes in the environment at Jupiter, internal or external to the magnetosphere, may control the temperatures measured. Although past studies have investigated different morphological regions of the aurora, local-time dependencies have not been explored. In this chapter, I study short time scales temperature changes in Jupiter's northern auroral region.

6.2 Data Analysis

This study uses the same data set as Johnson et al. (2017) and Chapter 5, which was taken on 31 December 2012 with VLT-CRIRES and is described in Section 3.4.2. The data was reduced as outlined in Section 3.3. CRIRES is able to simultaneously measure a number of H_3^+ emission lines from the Q-branch, as shown in Figure 5-2. In order to determine the rotational temperature, this study focuses on two H_3^+ emission lines, $Q(1,0^-)$ and $Q(3,0^-)$, which are labelled in Figure 5-2. These emission lines are in the same vibrational manifold and represent transitions from the first excited vibrational energy level to the ground state, $\nu_2 \rightarrow 0$, which is a fundamental transition.

Using the methods outlined in Section 3.5.1, the spectral radiance of the $Q(1,0^-)$ and $Q(3,0^-)$ lines were derived. It is not necessary to perform a LOS intensity correction on the spectral radiance, as only the ratio of the two lines is required for the temperature calculation. Polar projections of the $Q(1,0^-)$ and $Q(3,0^-)$ spectral radiances were made of Jupiter's northern aurora, using methods discussed in Section 3.5.2 and 5.2. To increase signal-to-noise, the average spectral radiance of $Q(1,0^-)$ and $Q(3,0^-)$ was calculated from the six scans taken on 31 December 2012, shown in Figure 6-1.

The rotational temperature of the H_3^+ ions is calculated using the ratio of the spectral radiances of the $Q(1,0^-)$ and $Q(3,0^-)$ fundamental lines, as described in Section 3.5.4. In this study, the ratio was determined by dividing the average spectral radiance of $Q(1,0^-)$ (Figure 6-1a) by that of $Q(3,0^-)$ (Figure 6-1b), and is shown in Figure 6-2. The ratio shows that $Q(3,0^-)$ is generally more intense than $Q(1,0^-)$ in the auroral region, and changes depending on the location within the auroral region. Outside the auroral region, there are some regions where the $Q(1,0^-)$ emission is more intense than $Q(3,0^-)$ emission, however, these coincide with regions of poor signal-to-noise. Once the ratio was determined, the rotational temperature was derived using Equation 3.32 and projected onto a polar map, which is shown Figure 6-3a.

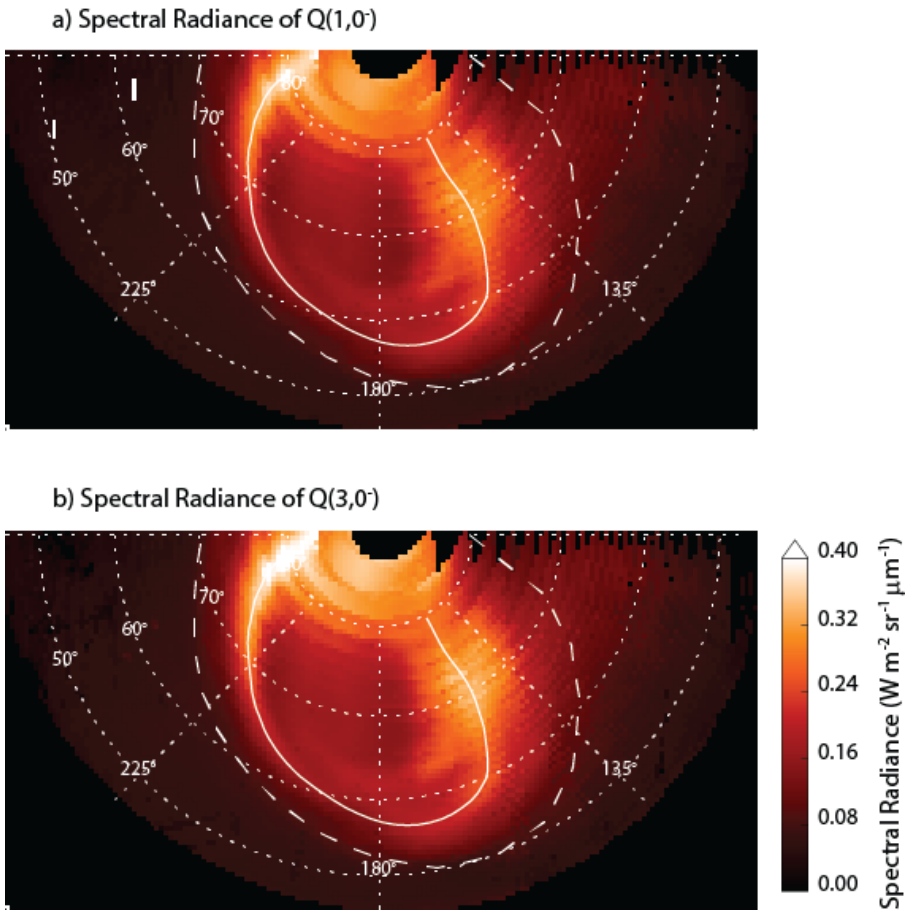

Figure 6-1: Polar projections of the spectral radiances of (a) Q(1,0⁻) and (b) Q(3,0⁻) H_3^+ emission lines. The longitudes are in System III and the latitudes are planetocentric. The white line is the peak in H_3^+ auroral intensity, as measured by Johnson et al. (2017). The white dashed line is the magnetic footprint of Io according to the Grodent et al. (2008) model.

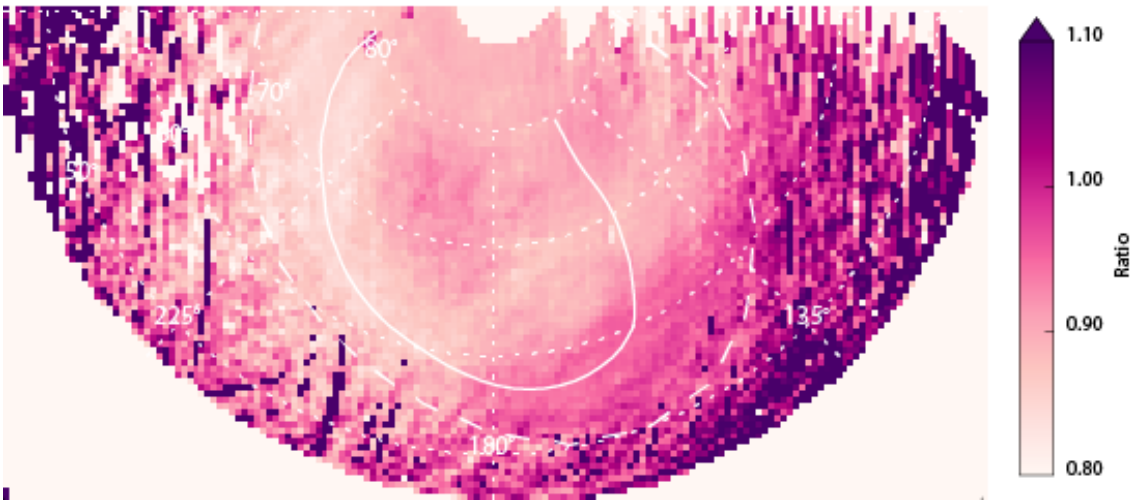

Figure 6-2: The ratio of the spectral radiances of the H_3^+ Q(1,0⁻) and Q(3,0⁻) fundamental lines. Similar format to Figure 6-1.

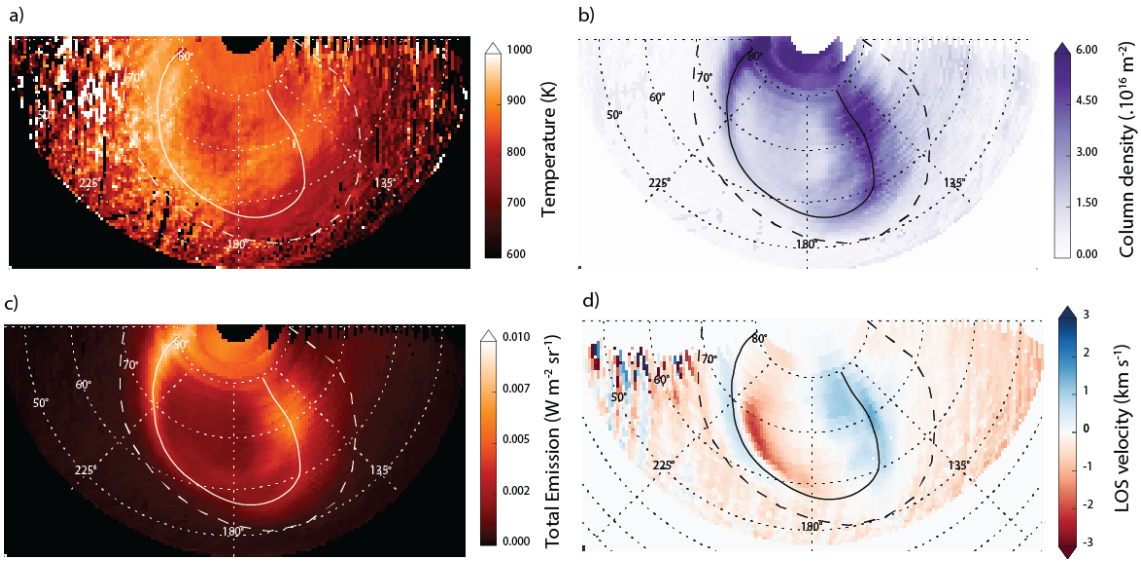

Figure 6-3: Four polar projections of the H_3^+ (a) average rotational temperature, (b) average column density, (c) average total emission, and (d) the line-of-sight velocity in the planetary reference frame derived from IR observations of Jupiter's northern auroral region, taken on 31 December 2012. Similar format to Figure 6-1.

The column density, $N(H_3^+)$, is the density of a column of the planet's atmosphere perpendicular to the planet's surface. It is calculated by dividing the measured intensity from the emission line by the theoretical emission per molecule from that particular line. The total emission, $E(H_3^+)$, is the emission from the H_3^+ population across all possible energy transitions at a given temperature, and is calculated by multiplying the theoretical emission per molecule from all emission lines at a given temperature by the column density. For more information on how the column density and total emission were derived, please refer to Section 3.5.4. Polar projections of these properties are shown in Figure 6-3.

In this study the H_3^+ temperature, column density, and total emission are compared to the LOS velocity of the H_3^+ ions (Figure 6-3d) to investigate the relationship between heating, cooling, and ionospheric flows. For a full discussion on the LOS velocities observed in Figure 6-3d, and how they are derived, please refer to Johnson et al. (2017) and Chapter 5.

In order to investigate short timescale changes in the auroral temperature, I also calculated the temperature for each of the six scans, as shown in Figure 6-4. The temperature calculation is very sensitive to the signal-to-noise: to make sure that any observed temperature differences were not just random fluctuations, averages were taken of the first two (Figure 6-4a and b) and last two (Figure 6-4e and f) polar

projections. These averages are ~80 minutes and ~50° longitude apart and referred to as average 1 and 2 for the start and end of the observations respectively. The temperature difference was then calculated by subtracting the average over the whole observations (Figure 6-3a) from average 1 and 2. The polar projections of average 1 and 2, and the respective temperature differences are shown in Figure 6-5. Note that the above analysis was not performed on the total emission or the column density as no significant variation in these properties was observed over the set of observations.

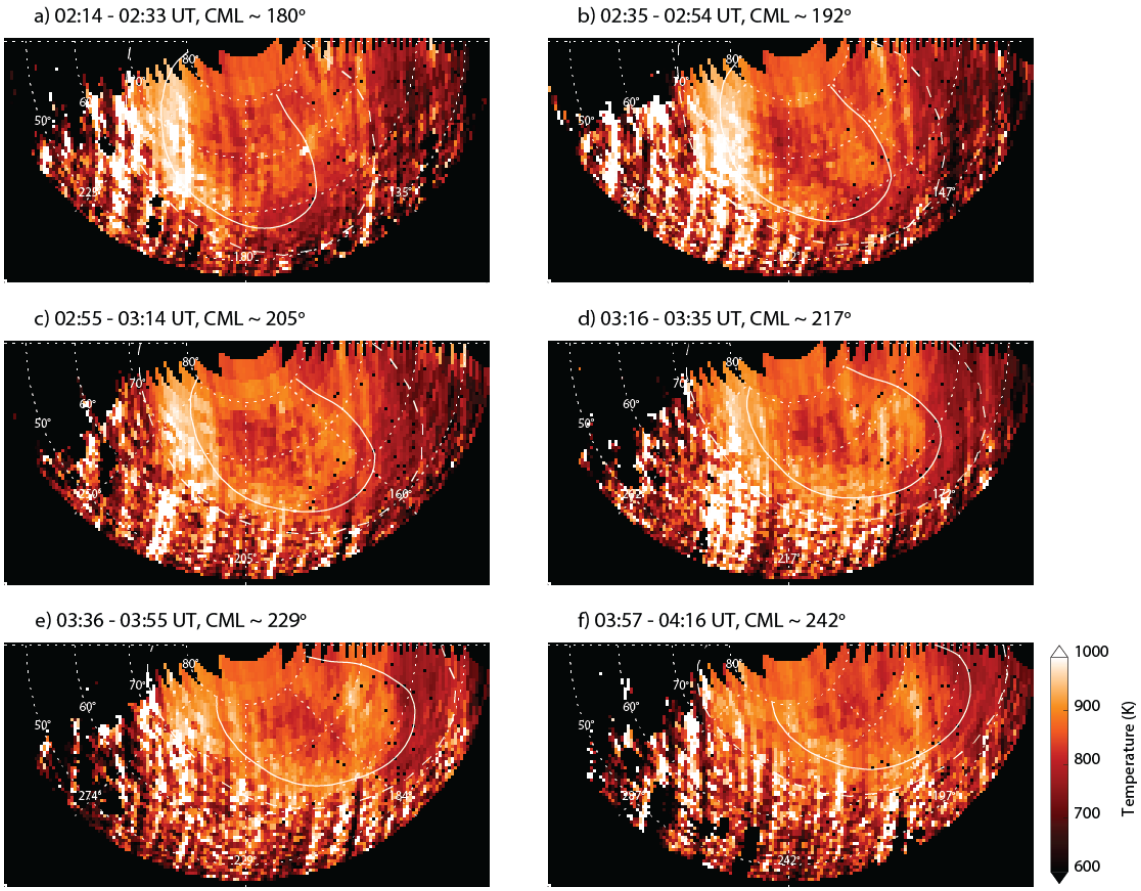

Figure 6-4: (a) – (f) Six polar projections of the temperature derived on the 31 December 2012. Similar format to Figure 6-1.

Since the fundamental emission lines are the least affected by non-LTE effects, as discussed in Section 2.1.3, I will be using the q-LTE assumption in this study. By assuming q-LTE, I acknowledge that non-LTE effects may exist in Jupiter's upper atmosphere but they have a negligible effect on the fundamental emission. Since $Q(1,0^-)$ and $Q(3,0^-)$ are both fundamental lines, they are the least effected by non-LTE effects, any temperatures derived in this study are representative of the ionosphere as well as the thermosphere.

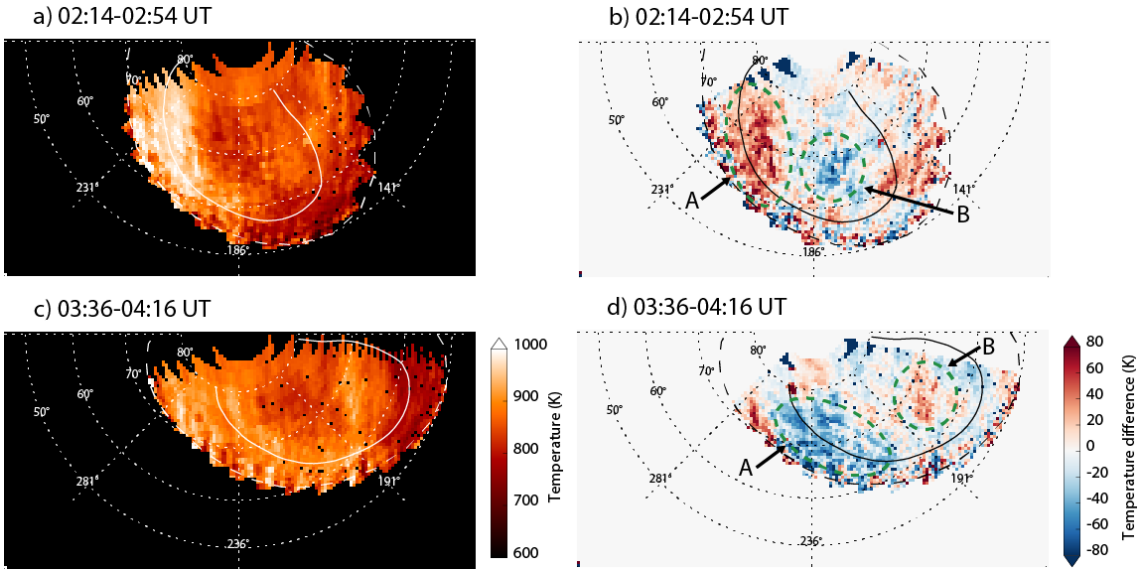

Figure 6-5: The average temperature and temperature differences at the (a and b) start and (c and d) end of the observations. The two broad regions of temperature changes, labelled A and B, are bound by dashed green lines. Similar format to Figure 6-1.

6.2.1 Errors

The errors for the properties calculated in this study are shown in Figure 6-6. The errors mainly result from fitting a Gaussian to the emission lines, and these errors were propagated through the calculations to produce the errors for each property, shown in Figure 6-6a, b, and c. Equatorward of the Io magnetic footprint, the error on all the properties significantly increases as the signal-to-noise decreases. The difference between the Q(1,0$^-$) and Q(3,0$^-$) spectral radiance is very small, and therefore the temperature calculation is very sensitive to noise altering the Q(1,0$^-$):Q(3,0$^-$) ratio. For this reason, in this study the focus will be on the values poleward of the Io footprint where signal-to-noise is good.

The error for the average 1 and 2 are shown in Figure 6-6d and e. The whole auroral region is not shown in Figure 6-6d and e as the error equatorward of the Io magnetic footprint is larger than 35 K. It can be seen that the errors vary across the observations, due to an increase in noise as the air mass increased during the observations. However, in general they remain much lower than 35 K in the auroral region.

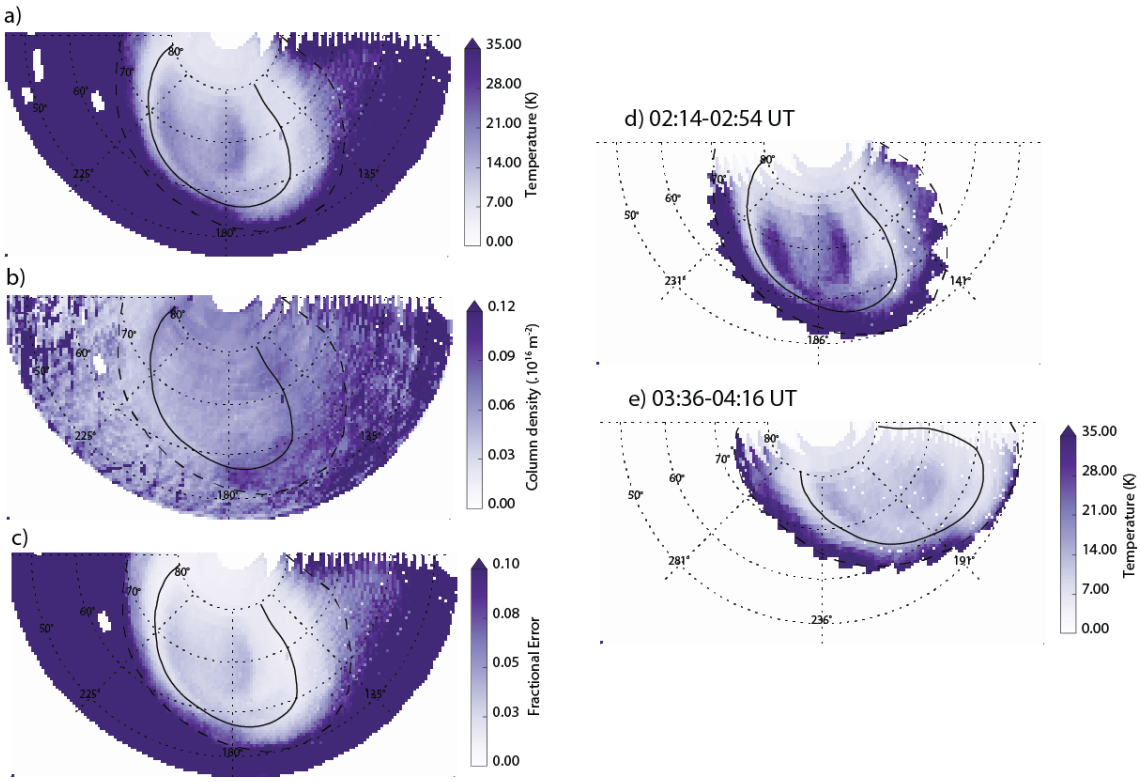

Figure 6-6: The error on the H_3^+ average (a) temperature, (b) column density, and (c) total emission. The temperature error for (a) average 1 and (b) average 2. Similar format to Figure 6-1.

6.3 Results

Figure 6-3 shows the key results for this paper: (a) average rotational temperature, (b) average column density, and (c) average total emission. Figure 6-3d shows the LOS velocity in the planetary reference frame (PRF), taken from Johnson et al. (2017). Since the LOS velocity depends on the viewing geometry, an average of the LOS velocity cannot be taken over the observations as this would lead to unphysical results. Instead the first scan, where there is an excellent view of the northern aurora, is used in Figure 6-3 in order to compare to the other properties. Figure 6-7 shows the properties plotted against each other: (a) total emission versus column density, (b) temperature versus total emission, (c) temperature versus column density, and (d) temperature versus the magnitude of the LOS velocity in the PRF. Only data points poleward of the Io magnetic footprint were used to produce Figure 6-7.

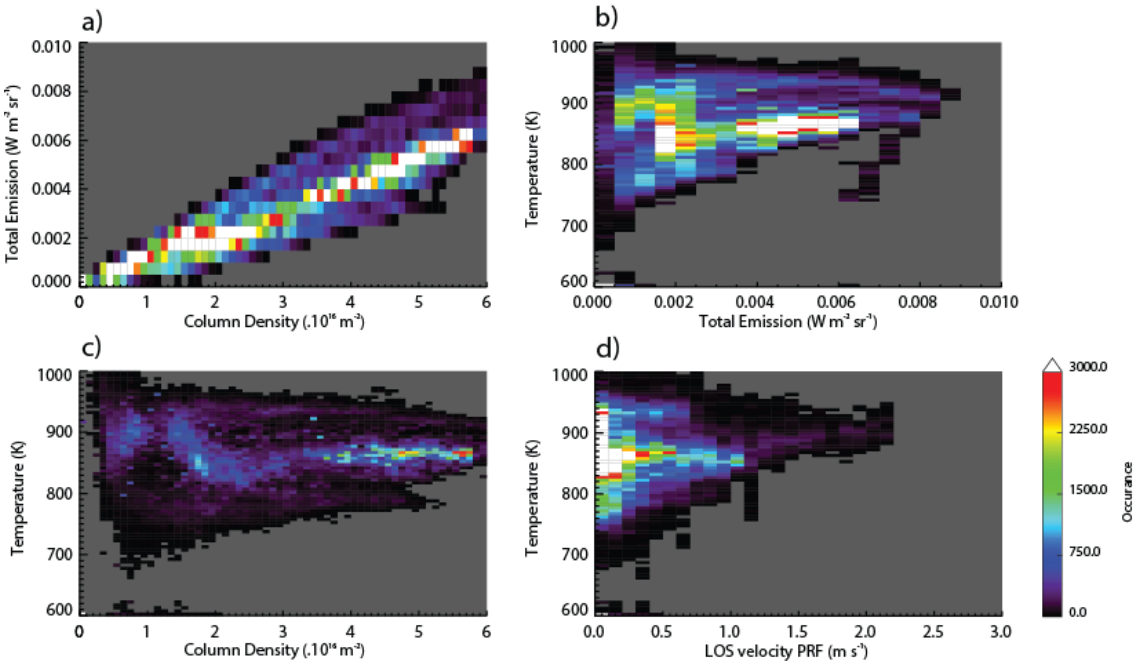

Figure 6-7: The correlation between properties derived from the H_3^+ emission: (a) total emission versus column density, (b) temperature versus total emission, (c) temperature versus column density, and (d) temperature versus the absolute magnitude of the LOS velocity in the PRF. Only data points poleward of the Io magnetic footprint were included in these plots, where the Io magnetic footprint coordinates were taken from the Grodent et al. (2008) model. The grey region indicates the absence of data and the colours show the number of data points present in each bin.

Figure 6-3c shows the average total emission which reaches a maximum of ~10 mW m^{-2} sr^{-1} in the region of the main auroral emission. The range of values which the total emission encompasses is in agreement with past studies. The total emission represents the total energy output from the H_3^+ emission (Lam et al. 1997), and as can be seen from Figure 6-3c, the majority of the energy output is in the region of the main auroral emission and the more active regions of the polar aurora. The column density is shown in Figure 6-3b, with values reaching a maximum of ~6 x 10^{16} m^{-2} in the region of the main auroral emission, driven primarily by impact ionisation by auroral particles. By comparing Figure 6-3c and Figure 6-3b it is possible to see that the column density is large where the total emission is high. This comparison can be seen more qualitatively in Figure 6-7a, where a positive correlation between total emission and column density is shown. The Pearson's correlation coefficient for the total emission and column density is ~0.98, implying a strong positive correlation.

The average temperature is shown in Figure 6-3a, with values in the range ~700-1000 K, which is in agreement with past studies. Using Juno-JIRAM observations,

Adriani et al. (2017) observed elevated temperatures along the main auroral oval. However, in this study the temperature structures appear to be ordered only along the main auroral emission at ~180-270° longitude, and there is no broad region of heating at ~90-180° like that observed by Adriani et al. (2017). Moore et al. (2017) observed higher temperatures at ~180-270° than ~90-180° longitude along the main auroral emission, which is in agreement with the observations in this present study, however, their spatial resolution was relatively modest.

Figure 6-3c (the average total emission) shows a map of where the regions of cooling should be taking place in the auroral region. If H_3^+ was efficiently reradiating the auroral energy into space then where the total emission is large the temperature should be low. By comparing Figure 6-3a and Figure 6-3d, it can be seen that on the main auroral emission at ~180-270° longitude the aurora is bright and also hot, indicating that the rate of heating is larger than the cooling. However, there are some regions where the aurora is bright and the temperature is low, for example within ~140-180° longitude, indicating that the H_3^+ ions are effectively reradiating the auroral energy. Figure 6-7b shows the correlation of the temperature and total emission for this study. There is a high occurrence of temperatures 800-900 K within a total emission range of ~2-6 mW m^{-2} sr^{-1}. At low values of total emission in the range of ~0.5-3 mW m^{-2} sr^{-1} and temperatures in the range of ~800-950 K, there may potentially be an anti-correlation. However, overall the Pearson's correlation coefficient is ~0.71, which implies a modest positive correlation between the temperature and total emission.

In regions where H_3^+ is denser, there is a higher rate of ionisation, therefore, the H_3^+ column density (Figure 6-3b) should show where the ionisation (i.e. particle precipitation) is occurring. If heating by impact from particle precipitation is significant, it would cause elevated temperatures in regions where column density is large. Through comparison of Figure 6-3b and Figure 6-3a, it can be seen that there is some correlation between large column densities and large temperatures along the main auroral emission at 180-270° longitude. However, moving from 270° towards 180° longitude along the main auroral emission, the column density decreases but the temperature remains relatively high. At 90-180° longitude, the structure in the temperatures is very different and some regions present high temperatures and high

column densities. Figure 6-7c shows temperature versus column density. There is a high occurrence of temperatures at ~850 K and column densities at ~4-6 x 10^{16} m^{-2}. There is a potential anti-correlation between the column densities at ~1-3 x 10^{16} m^{-2} for temperatures of ~750-900 K. However, overall there is a modest positive correlation between temperature and column density, with a Pearson's correlation coefficient of ~0.78.

This study has an advantage over past studies as the temperature, column density, and total emission can be directly compared to the LOS velocities derived from the same data set by Johnson et al. (2017). Figure 6-3d shows the LOS velocities in the planetary reference frame (PRF). This reference frame is fixed in System III, and any deviation from zero implies the H_3^+ ions have a velocity greater than or less than the rotation rate of the planet. A super-rotating flow is seen in Figure 6-3d along the main auroral emission at 180-270° longitude, with positive values of LOS velocity of ~1 km s^{-1}. In a dark region of the polar aurora just poleward of the main auroral emission, there is a strongly sub-rotating flow with maximum LOS velocity of ~2.5 km s^{-1}. On the main auroral emission at ~90-180° longitude, there is sub-rotating flow of ~1.5 km s^{-1}. The origins of these ionospheric flows are discussed in greater detail in Johnson et al. (2017).

Joule heating occurs in the auroral regions and its magnitude is governed by the difference in velocity between the charged particles and neutrals. There are very limited measurements of the neutral velocity in the thermosphere, the only two measurements of neutral winds measured in the auroral region were taken by Chaufray et al. (2010; 2011). Therefore, it is often assumed that the neutrals are corotational, which is the assumption used in this paper. In such a scenario, the greatest amount of Joule heating will occur where the largest values of line-of-sight velocities exist. Therefore, Figure 6-3d effectively gives a map of where the Joule heating should be occurring. Stallard et al. (2001) measured an increase in the LOS velocity in the region of the main auroral emission, from 0.5 to 1 km s^{-1}, and Stallard et al. (2002) measured an increase in temperature from 940 to 1065 K, using the same IRTF-CSHELL data set. This positive correlation between the H_3^+ ions velocity and temperature suggests Joule heating increases with velocity, assuming the neutrals are corotating.

The strongest ionospheric flows measured by Johnson et al. (2017) are in a dark region of the polar aurora, with an absolute magnitude of LOS velocity of up to ~2.5 km s^{-1}. Assuming the neutrals are corotating, significant Joule heating should be taking place in this region, however, Figure 6-3a shows that the temperatures here are moderate compared to that of the main auroral emission. Figure 6-7d shows the correlation between the temperature and the absolute magnitude of the LOS velocity in the PRF. There is a high occurrence of LOS velocities at 1 km s^{-1} for the temperature range of 800-950 K. The Pearson's correlation coefficient is ~0.47, implying there is a weak positive correlation which means that there is some increase in Joule heating with velocity, as suggested by Stallard et al. (2001; 2002).

Figure 6-5 shows how the temperature changes over the set of observations. Section 6.2 explains how temperature average 1 and 2 were created, which are ~80 minutes and ~50° apart. Average 1 is shown in Figure 6-5a and average 2 is shown in Figure 6-5c. These averages were then subtracted from the average over the whole set of observations (Figure 6-3d), leading to the temperature differences at the start and end of the observations shown in Figure 6-5b and Figure 6-5d respectively. The observed temperature differences are larger than the calculated errors (Figure 6-6) and so these temperature changes are interpreted as physical.

Figure 6-5b and Figure 6-5d show two broad regions of temperature changes that I will focus on. Part of the main auroral emission at ~230° longitude changes from ~50-70 K hotter than average to ~50-70 K cooler over the ~80 minutes separation of the two averages and is labelled as region A in Figure 6-5. A region in the polar aurora at ~180° longitude changes from ~60 K cooler than average to ~60 K hotter over the observations, labelled region B in Figure 6-5. Although other small-scale variations may exist, the extended spatial coverage of region A and B implies they are not simply random fluctuations. In the following section I will investigate two distinct hypotheses: are the temperature changes caused by the rotation of the aurora through different local times or are they a result of temporal changes of the conditions at Jupiter during the ~80 minutes separation of the two averages?

6.4 Discussion

6.4.1 H_3^+ Rotational Temperature, Column Density, and Total Emission

The energy balance in Jupiter's ionosphere is complex and the H_3^+ properties do not always exhibit simple correlations. Figure 6-7a shows that there is a strong positive correlation between the total emission (Figure 6-3c) and the column density (Figure 6-3b). Other studies, such as Stallard et al. (2002), Moore et al. (2017), and Adriani et al. (2017), also noted this correlation, and it implies that the ionisation rate governs the intensity. However, enhancements in H_3^+ total emission could also be caused by increases in temperature of the ionosphere, but only a modest correlation between the total emission (Figure 6-3c) and the temperature (Figure 6-3a) was observed in Figure 6-7b. Therefore, it appears temperature is a secondary driver of H_3^+ emission brightness to the column density.

Although the correlation between the total emission and column density is clear, past studies have found the correlation between the total emission and temperature harder to quantify. In a study of the northern auroral region using IRTF-CSHELL observations, Stallard et al. (2002) found that the vibrational temperature had no correlation with the Q(1,0$^-$) intensity. Even though they observed high temperatures in the bright region of the main auroral emission at 180-270° longitude, they found that at 90-180° longitude, in the more diffuse region of the main auroral emission, the intensity was at a maximum but the temperature was at a minimum. Lam et al. (1997) and Raynaud et al. (2004) noted an anti-correlation between temperature and column density, but due to the low signal-to-noise in these studies, it was uncertain if the anti-correlation was physical. By comparing synthetic H_3^+ spectra to observations of Saturn analysed by O'Donoghue et al. (2014), Melin et al. (2013) showed that, as long as the uncertainties were small relative to the differences of temperature and column density, then the anti-correlation was physical and not caused by low signal-to-noise. Miller et al. (2010) argued that the H_3^+ thermostat effect could produce the observed anti-correlation, whereby a denser parcel of H_3^+ is subject to more cooling and will end up at a lower temperature.

Overall Figure 6-7b does not show an anti-correlation, which would have implied that temperature was low where cooling by H_3^+ was high. No overall anti-correlation is

seen in Figure 6-7c either, which shows the relationship between the temperature and column density. The recent study of Adriani et al. (2017), which uses Juno-JIRAM data, also shows no evidence of anti-correlation between the temperature and column density, in agreement with the present study. Therefore, H_3^+ is not an efficient thermostat across the entire auroral region.

One mechanism which can drive the heating of Jupiter's auroral regions is impact from particle precipitation. If heating by impact from particle precipitation was driving the elevated temperatures observed in the auroral region, then where the column density is large, the temperature would be high. However, Figure 6-7c shows only a modest positive relationship between temperature (Figure 6-3a) and column density (Figure 6-3b), and therefore it seems that heating by impact from particle precipitation alone cannot be driving the heating in Jupiter's ionosphere and there must be more processes at work.

Another mechanism that drives auroral heating is Joule heating, caused by the divergence of the charged and neutral flows in Jupiter's ionosphere, which are ultimately caused by the magnetosphere-ionosphere coupling currents, as discussed in Sections 1.1.4, 1.1.5, and 2.3. The model by Smith and Aylward (2009) suggested that Joule heating is largest at altitudes where conductivity is highest, which is approximately at the peak emission altitude of the H_3^+ fundamental emission lines (Millward et al. 2002). Stallard et al. (2001; 2002) measured a positive correlation between H_3^+ LOS velocity and temperature; however, only a weak correlation between temperature and LOS velocity was identified in this study and is shown in Figure 6-7d. Therefore, the temperature structure of the aurora is not directly controlled by the Joule heating. The above discussion is for a corotating neutral thermosphere, and the temperature structure will be much more complex if neutral flows deviate from corotation. The neutrals may experience a general sub- or super-rotation, or a more complex regime of flows that differ to the ionospheric flows may exist, however, the dynamics of the neutrals is not known at the time of the observations used in this study. A more rigorous study which takes the relative LOS velocity of the neutrals and ions into account is left for future work.

The strong ionospheric flows observed in the northern auroral region (e.g.: Rego et al. 1999, Stallard et al. 2001, and Johnson et al. 2017) may also be responsible for

redistributing heat. Past studies such as Lam et al. (1997) and Raynaud et al. (2004) have shown a smooth temperature gradient moving from the hot auroral region to the cooler equatorial regions. However, Stallard et al. (2017) showed that the heat transport from the northern auroral region is not uniform, and a region of localised cooling exists at the sub-auroral latitudes. It could be the case that the strong H_3^+ ionospheric flows create regions of increased or decreased temperatures, which are not coincident with the mechanisms which drive the temperatures.

Figure 6-3d shows the ionospheric flows investigated by Johnson et al. (2017). In this study I will focus on the super-rotating flow as it has potential consequences for the temperature structure of the auroral ionosphere. Johnson et al. (2017) discuss how the origin of the super-rotating ionospheric flow could be either magnetospheric or ionospheric forcing. They suggest that this region of the ionosphere maps to a region of magnetosphere where the field lines are being compressed as they rotate through the dawn sector of the magnetosphere. As the field lines are compressed, their rotation rate increases to conserve angular momentum, and the rotation rate of the ionosphere which they map to also increases (Moriguchi et al. 2008). Alternatively, thermospheric neutral winds could be driving the super-rotational flows through collisional forcing. The model by Smith and Aylward (2009) predicts a super-rotating thermospheric flow, just equatorward of the main auroral emission, caused by the zonal Coriolis and advection momentum term dominating the ion-drag term. As the model by Smith and Aylward (2009) is axisymmetric, direct comparison between their results and the observed ionospheric flows is not possible; however, it is still possible that a thermospheric super-rotational flow exists near to the location of the main auroral emission which is driving super-rotational ionospheric flows.

Smith and Aylward (2009) describe how the super-rotating neutral wind produces a cool region just equatorward of the main auroral emission. This cool region is caused by the divergence of a poleward flow at the boundary between the sub-rotating main auroral emission and the corotating lower latitude. The divergence causes an upwelling of gas from lower altitudes that cools adiabatically as it expands, creating a cool, super-rotating region just equatorward of the main auroral emission. As I am assuming q-LTE, I would expect the H_3^+ temperature to be representative of the thermosphere, and hence I would expect to measure low temperatures. However,

the opposite is observed in the data set; the region of the super-rotating ionospheric flow experiences elevated H_3^+ temperatures. It could still be the case that the neutrals and H_3^+ are cooled but at lower altitudes than the peak H_3^+ emission of the fundamental lines (~550 km, Melin et al. 2005), and is therefore not captured by these observations.

It is clear that particle precipitation impact, Joule heating, and the H_3^+ thermostat effect are not working in isolation and it is very likely that the observed temperature are generated by a combination of the above. More detailed studies, which measure the LOS velocities of the H_3^+ ions as well as the temperature, will further our understanding of heat transport in Jupiter's ionosphere. Furthermore, modelling which takes the asymmetries observed in the temperature structure in this study into account may be able to estimate where each mechanism dominates.

6.4.2 H_3^+ Temperature Changes Over a Short Time Period

As discussed in Section 6.3, two broad regions of temperature changes are observed over a period of ~80 minutes. I postulate that these changes could either be caused by the local time dependency of the energy of the precipitating electrons or by the response of the magnetosphere-ionosphere-thermosphere system to a transient enhancement in solar wind dynamic pressure.

First, I will consider the possibility that the temperature changes are caused by a local time dependence in the particle precipitation energy. The altitude of peak production of H_3^+ depends on the energy of the precipitating electrons: when the electron energy is higher the H_3^+ will be produced at lower altitudes, and vice versa. Models such as Grodent et al. (2001) have shown that the thermospheric temperature increases with height, therefore, H_3^+ produced at lower altitudes will be cooler, and vice versa. It could be the case that the electron precipitation is softer in the dawn sector of the ionosphere, becoming harder at noon. Region A in Figure 6-5, begins hotter than average at dawn, where the electrons may be softer creating H_3^+ at higher, hotter altitudes. As it rotates towards noon, where it may now be in a region in which the electron precipitation is harder, penetrating down to lower altitudes, creating H_3^+ where it is cooler. Region B starts off cool around noon, where it may be experiencing

hard electron precipitation. This region becomes hotter as it moves away from noon, suggesting that the dusk sector may be subject to softer electron precipitation.

It could be the case that the aurora as a whole experienced local time differences. As discussed in Section 6.3, the H_3^+ temperature structure measured in this present study are in agreement with those measured by Moore et al. (2017) but not Adriani et al. (2017). Moore et al. (2017) measure the dayside auroral temperatures at local times similar to those presented in this study. However, Adriani et al. (2017) derived the H_3^+ from data taken over a whole Jupiter day, and the polar projections in their study are made up of measurements covering all local times. If local time differences in temperature do exist, then this would explain why the temperature structures observed in the present study agree with Moore et al. (2017) but differ to Adriani et al. (2017). In this present study, I observe cooling in region A and heating in region B, which may imply that the main auroral emission and polar aurora experience different local time behaviour. Different morphology regions of the aurora may experience different local time behaviour. However, the local time coverage of the data set is quite limited and I do not observe regions A and B through the same local times. Therefore, it may be that the local time differences produce the same effect in all regions of the aurora or that they change depending on the morphology region.

The relationship between the energy of the precipitating electrons and the H_3^+ production rate is not linear due to the time-scale in the ion chemistry; however, due to the instantaneous nature of the UV and X-ray emission, observations at these wavelengths are frequently used to probe the energy of precipitating electrons. Branduardi-Raymont et al. (2008) discuss how hard X-rays are produced from main auroral emission and soft X-rays are produced from the polar aurora. This suggests that the precipitating electrons at the main auroral emission are harder and penetrate down to lower altitudes, which would create H_3^+ where the atmosphere is cooler and vice versa for the polar aurora. The H_2 emission at wavelengths of <140 nm is attenuated by hydrocarbon absorption, which occurs at lower altitudes. By taking the ratio of the intensity of this emission to that at longer wavelengths, which is unaffected by hydrocarbon absorption, the colour ratio can be calculated. Gérard et al. (2016) found a positive relationship between intensity and colour ratio in the main

auroral emission. This means that the brightest aurora is produced at lower, cooler altitudes. The relationship was less clear in the polar aurora. Although this study has divided the aurora by morphology, they do not investigate any local-time dependence of energy of the precipitating electrons. Future simultaneous observations at IR, UV and X-ray wavelengths could resolve the local-time dependence of the energy of precipitating electrons.

Now I will consider the hypothesis that the observed H_3^+ temperature changes may be driven by temperature changes at a fixed altitude in the thermosphere. Yates et al. (2014) modelled the velocity and temperature of the neutral thermosphere, and investigated how it responded to a transient response of the magnetosphere. They followed the description of a transient event as given by Cowley et al. (2007) who modelled the response of the magnetosphere to a rapid (2-3 hours) compression and expansion. Yates et al. (2014) triggered the transient event with a pulse of increased solar wind dynamic pressure over 3 hours, reaching 0.213 nPa halfway through the pulse. Figure 6-8 shows the results of their study which describes the behaviour of the neutrals in the thermosphere. The top row shows azimuthal flows, the middle row shows the meridional flows and the bottom row shows the temperature. These parameters are given for before the compression of the magnetosphere begins (first column), while the magnetosphere is fully compressed due to the peak in the pulse of increased solar wind dynamic pressure (second column), and when the magnetosphere is in an expanded state after the pulse has passed Jupiter (third column).

Figure 6-8 shows that during and after the compression the neutral flows and temperatures in the thermosphere become highly dynamic. Focusing on the peak emission altitude of the H_3^+ fundamental lines (~550 km, Melin et al. 2005), the modelled temperature fluctuates by ~50 K, changing from hot to cold and vice versa. In this study, the temperature changes by ~140 K, which is much higher than the temperature changes predicted by the model. Like other models, the model by Yates et al. (2014) generally underestimates the temperatures in the auroral regions. Therefore, it is possible that the fluctuations in temperatures are also underestimated. The model by Yates et al. (2014) is axisymmetric and therefore cannot give an exact location of the temperature changes that could be compared to the observed

temperature changes. However, this model does show that temperature changes of the neutrals in the thermosphere are possible under the right conditions and this could be driving the observed H_3^+ temperature changes.

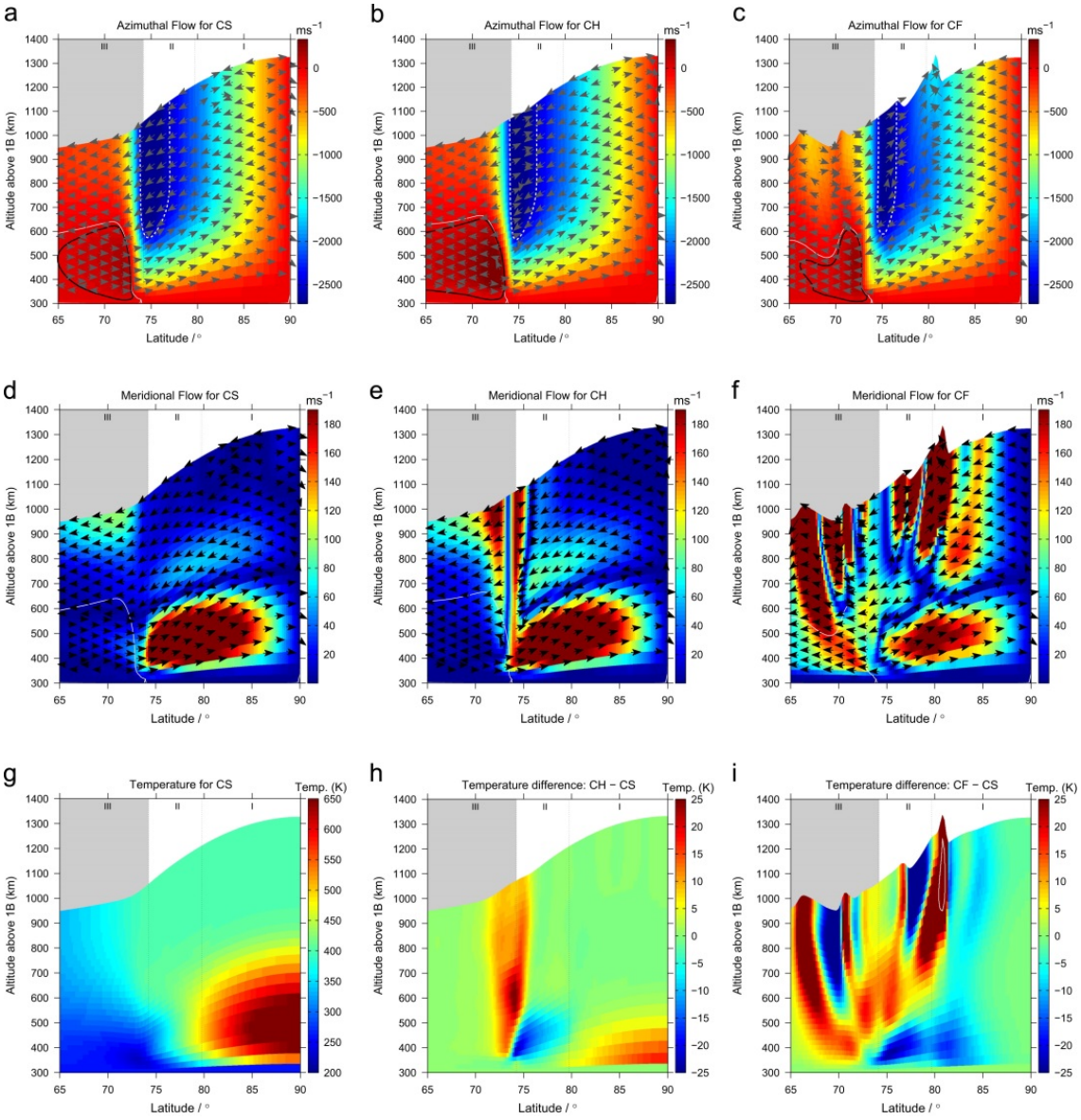

Figure 6-8: The results of the model by Yates et al. (2014): the thermospheric response to a transient event of enhanced solar wind dynamic pressure. The top row shows azimuthal flows, the middle row shows the meridional flows and the bottom row shows the temperature of the thermospheric neutrals. These parameters are given for before the compression of the magnetosphere begins (first column), while the magnetosphere is fully compression due to the peak in the pulse of increased solar wind dynamic pressure (second column), and when the magnetosphere is in an expanded state after the pulse has passed Jupiter (third column).

To test whether this is a likely scenario for our observations, the solar wind dynamic pressure at Jupiter during these observations was investigated using a propagated solar wind model by Tao et al. (2005), shown in Figure 6-9 was generated

using the AMDA online tool[7]. The time of the observations is shown by the vertical red line and a peak in the dynamic pressure of ~0.14 nPa is shown by the horizontal dashed green line. There is a ±20 hour error on the modelled arrival time of the pressure enhancements, which is represented by the green shaded region that is centred on the beginning of the enhancement in dynamic pressure. Considering this error, the initial increase in dynamic pressure could have occurred during our observations. This increase is smaller than that which produced the dynamic response of the thermosphere as modelled by Yates et al. (2014); however the transient response of the magnetosphere to the dynamic pressure enhancement may still be driving significant changes. It is plausible that the response of the magnetosphere and atmosphere to an increase in solar wind dynamic pressure, which triggers the changes in the neutral temperatures, drives the observed changes in the H_3^+ temperature.

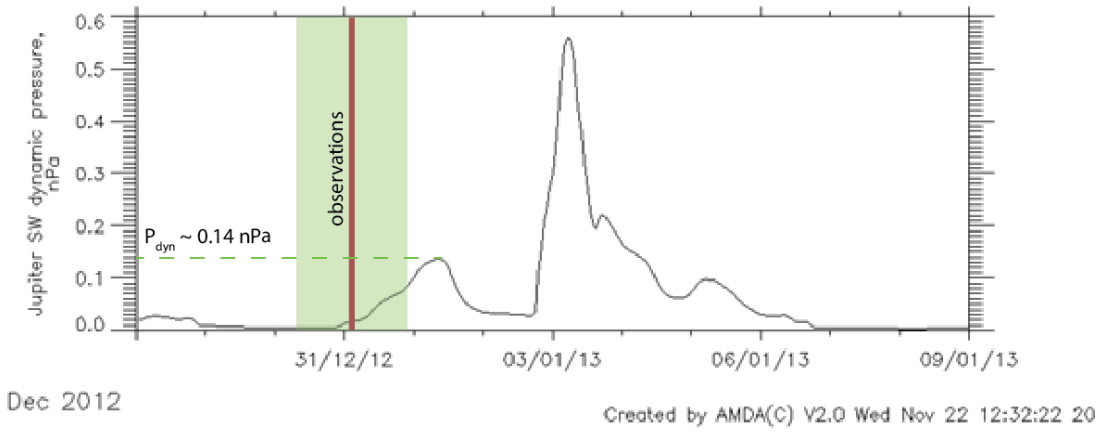

Figure 6-9: The propagated solar wind dynamic pressure calculated from the Tao et al. (2005) model. The plot was generated using the AMDA online tool. The observation is shown by the vertical red line and the peak in dynamic pressure closest to the observations is shown by the horizontal dashed green line. The green shaded region shows the ±20 hour error on the arrival time of the pressure enhancement at Jupiter.

To determine whether the temperature changes are driven by local time dependence in electron precipitation energy or thermospheric dynamics, further observations are required. If local time changes in electron precipitation energy are driving the temperature changes then these patterns should occur every time the aurora rotates into view and will be easily confirmed in future studies. Additionally,

[7] CDPP | Plasma Physics Data Centre. [2018]. *Amda.* [ONLINE] Available at: http://amda.irap.omp.eu/. [Accessed 22 November 2017].

further observations on the night side would allow any local time differences to be investigated there, which may be achieved with Juno measurements. The results from the transient response of the magnetosphere to solar wind dynamic pressure enhancements are likely to vary from one epoch to another. Observations of the aurora while Juno is sampling the solar wind conditions in-situ upstream of Jupiter will be invaluable in identifying pressure enhancements which may drive temperature changes. The possibility remains that both mechanisms could be driving the temperature changes, and the interplay between the two processes could be causing dynamic temperature structures.

A further mechanism that may be responsible for driving the observed temperature changes could be enhanced destruction of H_3^+ at low altitudes. Processes such as upwelling of stratospheric hydrocarbons could cause destruction of H_3^+ at lower altitudes, where the cooler population of H_3^+ exists. This would result in increased temperature being observed as only the hot population at high altitudes would remain to be measured. Future studies, which include simultaneous measurements of hydrocarbons and H_3^+ ions, may be able to determine whether enhanced destruction of H_3^+ at low altitudes drives any temperature changes. Finally, unknown mechanisms yet to be determined may be controlling the temperature changes.

Although this study assumes q-LTE, it is important to note the possibility that this is not a reasonable assumption. The fundamental emission lines are least affected by departures from LTE, and these lines are used in this paper. However, if the q-LTE assumption breaks down this would likely complicate the interpretation of the H_3^+ temperature observations. In order to fully test temperature changes, one would need to measure the kinetic and vibrational temperatures of the H_3^+, in additional to the rotational temperature as measured in this study, to ascertain whether H_3^+ was in LTE. However, these measurements are outside the scope of this study.

6.5 Conclusions

This study has presented high spatial resolution polar projections of the total emission, column density, and temperature of H_3^+ in Jupiter's northern auroral region observed on the 31 December 2012 using VLT-CRIRES. A comparison of these properties, as well

as the previously measured LOS velocity (Johnson et al. 2017), was undertaken and have shown that the heating mechanisms that control the temperature of Jupiter's thermosphere are not simple.

The strong positive correlation between column density and total emission, and the lack of a clear relationship between temperature and total emission, suggests that spatial variations the H_3^+ auroral emission is dominated by ionisation (i.e.: production) rather than H_3^+ brightness enhancements being caused by increased temperatures. Since no significant correlation between temperature and total emission was found, it appears that H_3^+ is not an efficient thermostat across the whole auroral region. This study found no clear relationship between the column density and temperature, suggesting that impact from particle precipitation does not dominate heating in the auroral regions. Although elevated temperatures were found in some regions with strong ionospheric flows, only a weak correlation was found between the LOS velocity and the temperature.

The heating of Jupiter's upper atmosphere appears to be controlled by a combination of energy being reradiating space by H_3^+ and heating by impact from particle precipitation and Joule heating. Since the life time of the H_3^+ ions is not negligible, strong H_3^+ ionospheric flows may be able to transport heat around the auroral region, meaning that the driving mechanism may exist in a different region to the observed temperatures.

This study is the first to present H_3^+ temperature changes over a short period of time, and I proposed two mechanisms to explain the observed temperature changes. Firstly, the temperature changes could be caused by local time changes in particle precipitation energy, which could vary by morphology region in the aurora or affect the auroral regions as a whole. However, due to the limited local time range of the observations I cannot distinguish between either case. Secondly, the temperature changes could be due to the dynamics of the thermospheric neutrals. A model by Yates et al. (2014) has shown that the temperatures and winds of the thermospheric neutrals respond dynamically to the transient response of the magnetosphere caused by a solar wind dynamic pressure enhancement. From propagated solar wind parameters (Tao et al. 2005), it was found that a pressure enhancement could have arrived during the observations inside the ±20 hour error window on arrival time. This

could have caused dynamic temperature structures in the thermosphere, which drive the observed temperature changes in the ionosphere.

I have presented a case study of Jupiter northern ionosphere, and to answer the remaining open questions, further studies are required. If the temperature changes observed here are repeatedly identified at similar local times in future studies, then local time changes in particle precipitation energy will be shown to be causing the changes in temperature. Changes in temperature due to transient dynamic thermospheric behaviour will vary depending on the solar wind conditions and it will be important to observe Jupiter's aurora with space-craft in-situ upstream of Jupiter in the solar wind. In future studies it will also be important to test the validity of the LTE assumption by simultaneously measuring the rotational, vibrational and kinetic temperatures of H_3^+. This will help determine the extent to which H_3^+ is thermalized with the neutrals. Additionally, by observing the temperature and LOS velocity of the neutrals, their effect on the temperature structure of the ionosphere will be determined.

Chapter 7 Summary and Future Work

In this thesis, I have analysed IR observations of Jupiter in order to probe the upper atmosphere using measurements of the properties of the H_3^+ ions. I have used two instruments, both long-slit Echelle spectrometers: IRTF-CSHELL and VLT-CRIRES. These instruments have high spectral resolution which allows the line-of-sight velocity of the H_3^+ ions to be calculated. Additionally, using VLT-CRIRES data, which has broader wavelength coverage, I have measured the rotational temperature, column density, and total emission of Jupiter's auroral ionosphere. By investigating the properties of the H_3^+ ions, important aspects of the dynamics and energy balance of Jupiter's ionosphere were revealed.

The work in Chapter 4 (Johnson et al. 2016) contains the first measurements of the LOS velocity of the H_3^+ ions at mid-to-low latitudes. These measurements showed that the H_3^+ ions in this region are corotating, and I found no evidence of the large flows modelled by Sommeria et al. (1995) in the region of the H Ly-α bulge. It could still be the case that large neutral flows do exist, but at different altitudes to the H_3^+ ions. Alternatively, the velocities of the neutral and charged components of the ionosphere are independent of each other but still exist at the same altitude, as suggested by Uno et al. (2014). However, the magnitude of the flows modelled by Sommeria et al. (1995) are large and therefore it is likely that, through ion-drag, the H_3^+ velocity would be influenced to some degree by the neutral flows. Since the H_3^+ ions were found to be corotating at the mid-to-low latitudes, this validates the assumptions used by auroral models that require this region of the ionosphere to corotating.

A consequence of the fact that the H_3^+ ions are corotating at the mid-to-low latitudes is that any deviations from corotation in the auroral regions are ionospheric flows due to the MIT coupling system. Chapter 5 (Johnson et al. 2017) presents a case study of high spatial resolution mapping of the H_3^+ LOS velocity in Jupiter's northern auroral region. The polar projections revealed several significant ionospheric flows. A super-rotational flow was observed at 180-250° longitude in the main auroral emission and thought to be either driven by the neutral thermosphere or the dawn sector of the magnetosphere. An increase in the LOS velocity between the Io magnetic footprint and

main auroral emission was observed, as predicted by Nichols and Cowley (2004). A strong velocity shear was observed just poleward of the main auroral emission at 180-220° longitude, also predicted by Nichols and Cowley (2004), which suggests that conductivity, as well as changes in momentum of the plasma, plays an important part in generating Jupiter's aurora. When transformed into a reference frame where the LOS component of the magnetic pole is zero, a region of stationary H_3^+ ions was observed coincident with a dark region of the polar aurora. Previously, this stationary region was observed in the same location as the UV swirl region by Stallard et al. (2003). It could be case that changes in local conditions at Jupiter have caused the shift in position; however, it is more likely that the new location is more accurate owing to the high spatial resolution of the data set. Although, the study by Johnson et al. (2017) cannot determine the exact mechanisms, like Stallard et al. (2003) they suggest that this region is coupled to the solar wind in Dungey cycle-like process. Identifying the location for the region of the polar aurora which is coupled to the solar wind is important for constraining models attempting to magnetically map from the ionosphere to the magnetosphere, and vice versa (e.g.: Vogt et al. 2011).

Following the case study presented in Chapter 5 and using the same data set, Chapter 6 investigates the H_3^+ temperature, column density, and total emission of the northern aurora and furthers our understanding of the energy balance in Jupiter's ionosphere. It was found that the energy balance is controlled by a combination of heating by impact from precipitating particles and Joule heating, and cooling by the H_3^+ thermostat effect, which produces a complex temperature structure. The work in Chapter 6 is the first to investigate temperature changes over a short time period (~80 minutes). I propose that the temperature changes could be due to local time dependency of the particle precipitation energy or the MIT systems response to a transient enhancement of the solar wind dynamic pressure at Jupiter. This study is an important first step into investigating the drivers of short term changes in H_3^+ temperatures.

Overall, the work in my thesis has made a significant contribution to the field of study: Chapter 4 presents the first LOS velocity measurements of H_3^+ ions at the mid-to-low latitudes and the case study of Chapters 5 and 6 are the first to measure all of the fundamental H_3^+ properties with a very high spatial resolution, laying the

groundwork for future investigations of the MIT system at Jupiter. Moving forwards, there are a number of ways to enhance the work in this thesis to further our knowledge of the Jovian system.

Throughout the work in this thesis, assumptions have been made about the neutral thermosphere. Instead of assuming that the neutral atmosphere is corotating, rigorous future studies should take simultaneous measurements of the velocity of both the neutral and charged components of the thermosphere. This is possible when observing in the K band atmospheric window at the near-IR wavelengths (2 μm), observing H_2 and H_3^+. If these observations were performed with high spatial resolution instruments then the dynamics of the thermosphere-ionosphere could be mapped globally. As well as observing the neutral and charged components at the IR wavelengths, simultaneous measurements at several wavelengths should be a priority for future studies. To further our understanding of the energy of the precipitating particles, observations at the UV and X-ray wavelengths as well as IR wavelengths should be taken.

The q-LTE assumption has been used in this thesis; however, it is important for future studies to test whether this assumption is strictly valid. The rotational temperature was measured in Chapter 6; however, measurements of the kinetic and vibrational temperatures of H_3^+ were outside the timescale of the study. Using the techniques outlined in this thesis, combined with temperature measurements detailed in Giles et al. (2016), future studies could measure all three temperatures simultaneously. If all three temperatures were mapped globally this would help determine whether the H_3^+ temperature is representative of the thermosphere as well as the ionosphere, and give a very good understanding of under what conditions the LTE assumption breaks down.

In order to interpret the LOS velocities several reference frames are used in this thesis, as well as observing the auroral region as it rotates across the dayside ionosphere; however, the LOS component alone does not give the full picture. By measuring the LOS velocity at several different viewing angles, the true velocity vector could be calculated in a manner similar to that used by SuperDARN on Earth (Ruohoniemi et al. 1989). If it is assumed that the aurora does not changes much over several hours of observations, then the LOS velocity maps, such as in Figure 5-8 and

Figure 5-9, can give the LOS velocity at different viewing angles, from which the true velocity vector could be calculated. However, the aurora is known to change over short periods of time. To overcome this, the average velocity over multiple nights, or more adventurous studies would involve a network of spacecraft, with high spectral resolution IR spectrometers able to measure the LOS velocity of H_3^+ from various viewing angles. At the time of writing there is only one spacecraft in orbit around Jupiter, which has a spectral resolution too low to make these measurements.

During February and March 2016, I led a programme to observe Jupiter's northern aurora with IRTF-CSHELL, while Juno was in its approach phase and collecting in-situ measurements of the solar wind and while JAXA-EXCEED was monitoring the Io torus with UV observations. Future work with these combined data sets, and using the techniques outlined in this thesis, will help determine the external and internal drivers of the aurora and the interplay between the two. Once Juno was in orbit around Jupiter, I performed observations with the new instrument iSHELL at IRTF of the northern and southern aurora. Future work will compared the derived H_3^+ properties to the measurements by the Juno instruments JIRAM, MAG, JADE and JEDI, enabling the ionosphere as well as the magnetosphere to be studied simultaneously.

The combined in-situ data set and ground-based observations have a combined potential greater than the sum of the parts. With Juno-JIRAM, it is possible to measure the auroral temperature on both the day and nightside of Jupiter, allowing local-time dependencies of the ionosphere to be investigate thoroughly. However, Juno-JIRAM does not have sufficient spectral resolution to derive the H_3^+ LOS velocities, and so we will have to wait for future missions with more advanced in-situ instruments in order to explore the dynamics on the nightside. Even in the age of in-situ data from advanced space craft, ground-based observations will still have a role to play in providing the large scale contextual view. Ground-based observations, such as in this thesis, will continue to be critical in furthering our understanding of the Jovian system!

Bibliography

Abel, Bob, and Richard M. Thorne. 2003. “Relativistic Charged Particle Precipitation into Jupiter’s Sub-Auroral Atmosphere.” *Icarus* 166: 311–19. doi:10.1016/j.icarus.2003.08.017.

Achilleos, N., S. Miller, R. Prangé, G. Millward, and M. K. Dougherty. 2001. “A Dynamical Model of Jupiter’s Auroral Electrojet.” *New Journal of Physics* 3 (3): 1–21. doi:10.1088/1367-2630/3/1/001.

Achilleos, N, S Miller, J Tennyson, AD Aylward, I Mueller-Wodarg, and D Rees. 1998. “JIM: A Time-Dependent, Three-Dimensional Model of Jupiter’s Thermosphere and Ionosphere.” *Journal of Geophysical Research* 103 (E9): 20,089-20,112. doi:10.1029/98JE00947.

Adriani, A., A. Mura, M. L. Moriconi, B. M. Dinelli, F. Fabiano, F. Altieri, G. Sindoni, et al. 2017. “Preliminary JIRAM Results from Juno Polar Observations: 2. Analysis of the Jupiter Southern H_3^+ Emissions and Comparison with the North Aurora.” *Geophysical Research Letters*, 1–8. doi:10.1002/2017GL072905.

Adriani, Alberto, Angioletta Coradini, Gianrico Filacchione, Jonathan. I. Lunine, Alessandro Bini, Claudio Pasqui, Luciano Calamai, et al. 2008. “JIRAM, the Image Spectrometer in the near Infrared on Board the Juno Mission to Jupiter.” *Astrobiology* 8 (3): 613–22. doi:10.1089/ast.2007.0167.

Alfven, Hannes. 1976. “On Frozen-In Field Lines and Field-Line Reconnection.” *Journal of Geophysical Research* 81 (22): 16–17. doi:10.1029/JA081i022p04019.

Axford, W. I., and C. O. Hines. 1961. “A Unifying Theory of High-Latitude Geophysical Phenomena and Geomagnetic Storms.” *Canadian Journal of Physics* 39: 1433–64. doi:https://doi.org/10.1139/p61-172.

Bagenal, F., a. Adriani, F. Allegrini, S. J. Bolton, B. Bonfond, E. J. Bunce, J. E P Connerney, et al. 2014. “Magnetospheric Science Objectives of the Juno Mission.” *Space Science Reviews*, 1–69. doi:10.1007/s11214-014-0036-8.

Bagenal, F., F. J. Crary, A. I. F. Stewart, N. M. Schneider, D. A. Gurnett, W. S. Kurth, L. A. Frank, and W. R. Paterson. 1997. “Galileo Measurements of Plasma Density in the Io Torus.” *Geophysical Research Letters* 24 (17): 2119–22. doi:10.1029/97GL01254.

Bagenal, Fran, Robert J. Wilson, Scott Siler, William R. Paterson, and William S. Kurth. 2016. “Survey of Galileo Plasma Observations in Jupiter’s Plasma Sheet.” *Journal of Geophysical Research:Planets* 121: 871–94. doi:10.1002/2016JE005143.

Banwell, Colin N., and Elaine M. McCash. 1994. *Fundamentals of Molecular Spectroscopy*. 4th ed. London, UK: THe McGraw-Hill Companies.

Baron, R. L., T. Owen, J.E. P Connerney, T. Satoh, and J Harrington. 1996. “Solar Wind Control of Jupiter’s H3+ Auroras.” *Icarus* 120: 437–42.

Baumjohnann, Wolfgang, and Rudolf A. Treumann. 1997. *Basic Space Plasma Physics*. London: Imperial College Press.

Belcher, J. W. 1983. "The Low-Energy Plasma in the Jovian Magnetosphere." In *Physics of the Jovian Magnetosphere*, 68–105. Cambridge and New York: Cambridge University Press.

Bhardwaj, Anil, and G Randall Gladstone. 2000. "Auroral Emissions of the Giant Planets." *Reviews of Geophysics* 38 (3): 295–353.

Birkeland, Kristian. 1908. *The Norwegian Aurora Polaris Expedition 1902-1903 Vol. 1*. H. Aschehoug & Co., Christiania. https://archive.org/details/norwegianaurorap01chririch.

Blackwell, D. E., S. K. Leggett, A. D. Petford, C. M. Mountain, and M. J. Selby. 1983. "Absolute Calibration of Infrared Flux from VEGA at 1.24, 2.20, 3.76 and 4.6 Microns by Comparison with a Standard Furnace." *Monthly Notices of the Royal Astronomical Society* 205: 897–905.

Bonfond, B. 2012. "When Moons Create Aurora: The Satellite Footprints on Giant Planets." In *Auroral Phenomenology and Magnetospheric Processes: Earth and Other Planets*, edited by A. Keiling, E. Donovan, F. Bagenal, and T. Karlsson, 133–40. Washington, D. C.: American Geophysical Union. doi:10.1029/2011GM001169.

Bonfond, B., G. R. Gladstone, D. Grodent, T. K. Greathouse, M. H. Versteeg, V. Hue, M. W. Davis, et al. 2017. "Morphology of the UV Aurorae Jupiter during Juno's First Perijove Observations." *Geophysical Research Letters* 44 (10): 4463–71. doi:10.1002/2017GL073114.

Bonfond, B., D. Grodent, J. C. Gérard, T. Stallard, J. T. Clarke, M. Yoneda, A. Radioti, and J. Gustin. 2012. "Auroral Evidence of Io's Control over the Magnetosphere of Jupiter." *Geophysical Research Letters* 39 (L01105): 1–5. doi:10.1029/2011GL050253.

Bonfond, B., M. F. Vogt, J. C. Gérard, D. Grodent, A. Radioti, and V. Coumans. 2011. "Quasi-Periodic Polar Flares at Jupiter: A Signature of Pulsed Dayside Reconnections?" *Geophysical Research Letters* 38 (L02104): 1–5. doi:10.1029/2010GL045981.

Bougher, S. W., J. Hunter Waite, Tariq Majeed, and G. Randy Gladstone. 2005. "Jupiter Thermospheric General Circulation Model (JTGCM): Global Structure and Dynamics Driven by Auroral and Joule Heating." *Journal of Geophysical Research E: Planets* 110 (4): 1–25. doi:10.1029/2003JE002230.

Branduardi-Raymont, G., R. F. Elsner, M. Galand, D. Grodent, T. E. Cravens, P. Ford, G. R. Gladstone, and J. H. Waite. 2008. "Spectral Morphology of the X-Ray Emission from Jupiter's Aurorae." *Journal of Geophysical Research: Space Physics* 113 (A02202): 1–11. doi:10.1029/2007JA012600.

Broadfoot, A. L., M. J. S. Belton, R.Z. Takacs, B. R. Sandel, D. E Shemansky, J. B. Holberg,

J. M. Ajello, et al. 1979. “Extreme Ultraviolet Observations from Voyager 1 Encounter with Jupiter.” *Science* 204 (4396): 979–82.

Broadfoot, A. L., B. R. Sandel, D. E Shemansky, J. C. McConnell, G. R. Smith, J. B. Holberg, S. K. Atreya, T. M. Donahue, D. F. Strobel, and J. L. Bertaux. 1981. “Overview of the Voyager Ultraviolet Spectrometry Results through Jupiter Encounter.” *Journal of Geophysical Research: Space Physics* 86 (A10): 8259–84. doi:10.1029/JA086iA10p08259.

Brown, Michael E. 1994. “Observation of Mass Loading in the Io Plasma Torus.” *Geophysical Research Letters* 21 (10): 847–50. doi:10.1029/94GL00564.

Bunce, E. J., S. W H Cowley, and T. K. Yeoman. 2004. “Jovian Cusp Processes: Implications for the Polar Aurora.” *Journal of Geophysical Research* 109 (A09S13): 1–26. doi:10.1029/2003JA010280.

Caudal, Gérard. 1986. “A Self-Consistent Model of Jupiter’s Magnetodisc Including the Effects of Centrifugal Force and Pressure.” *Journal of Geophysical Research* 91 (A4): 4201–21. doi:10.1029/JA091iA04p04201.

Chaufray, J.-Y., T.K. Greathouse, G.R. Gladstone, J.H. Waite Jr., J.-P. Maillard, T. Majeed, S.W. Bougher, E. Lellouch, and P. Drossart. 2011. “Spectro-Imaging Observations of Jupiter’s 2µm Auroral Emission. II: Thermospheric Winds.” *Icarus* 211 (February): 1233–41. doi:10.1016/j.icarus.2010.11.021.

Chaufray, J. Y., G. R. Gladstone, J. H. Waite, and J. T. Clarke. 2010. “Asymmetry in the Jovian Auroral Lyman-Line Profile due to Thermospheric High-Speed Flow.” *Journal of Geophysical Research E: Planets* 115 (5): 1–12. doi:10.1029/2009JE003439.

Clarke, J. T., G. R. Gladstone, and L. B. Jaffel. 1991. “Jupiter’s Dayglow H Ly Alpha Emission Line Profile.” *Geophysical Research Letters* 18 (11): 1935–38. doi:10.1029/91GL02091.

Clarke, J. T., D. Grodent, S. W. H. Cowley, E. J. Bunce, P. Zarka, J. E. P. Connerney, and T. Satoh. 2004. “Jupiter’s Aurora.” In *Jupiter: The Planet, Satellites and Magnetosphere*, edited by Fran Bagenal, Timothy Dowling, and William B. McKinnon, 639–70. Cambridge, UK: Cambridge University Press: Cambridge Planetary Science.

Clarke, J. T., J. Nichols, J.-C. Gérard, D. Grodent, K. C. Hansen, W. Kurth, G. R. Gladstone, et al. 2009. “Response of Jupiter’s and Saturn’s Auroral Activity to the Solar Wind.” *Journal of Geophysical Research* 114 (A05210): 1–20. doi:10.1029/2008JA013694.

Clarke, J. T., H. A. Weaver, P. D. Feldmen, H. W. Moos, W. G. Fastie, and C. B. Opal. 1980. “Spatial Imaging of Hydrogen Lyman Alpha Emission from Jupiter.” *The Astrophysical Journal* 240: 696–701. doi:10.1086/158277.

Connerney, J E, R Baron, T Satoh, and T Owen. 1993. “Images of Excited H3+ at the Foot of the Lo Flux Tube in Jupiter’s Atmosphere.” *Science (New York, N.Y.)* 262

(5136): 1035–38. doi:10.1126/science.262.5136.1035.

Connerney, John E P, Mario H Acuña, Norman F Ness, and Tsuyoshi Satoh. 1998. “New Models of Jupiter’s Magnetic Field Constrained by the Io Flux Tube Footprint.” *J. Geophys. Res.* 103: 11929–39. doi:10.1029/97JA03726.

Cowley, S. W. H., a. Balogh, M. K. Dougherty, M. W. Dunlop, T. M. Edwards, R. J. Forsyth, R. J. Hynds, N. F. Laxton, and K. Staines. 1996. “Plasma Flow in the Jovian Magnetosphere and Related Magnetic Effects: Ulysses Observations.” *Journal of Geophysical Research* 101 (A7): 15197–210. doi:10.1029/96JA00461.

Cowley, S. W. H., E. J. Bunce, T. S. Stallard, and S. Miller. 2003. “Jupiter’s Polar Ionospheric Flows: Theoretical Interpretation.” *Geophysical Research Letters* 30 (5): 1220. doi:10.1029/2002GL016030.

Cowley, S. W. H., A. J. Deason, and E. J. Bunce. 2008. “Axi-Symmetric Models of Auroral Current Systems in Jupiter’s Magnetosphere with Predictions for the Juno Mission.” *Annales Geophysicae* 26: 4051–74. doi:10.5194/angeo-26-4051-2008.

Cowley, S. W. H., J. D. Nichols, and D. J. Andrews. 2007. “Modulation of Jupiter’s Plasma Flow, Polar Currents, and Auroral Precipitation by Solar Wind-Induced Compressions and Expansions of the Magnetosphere: A Simple Theoretical Model.” *Annales Geophysicae* 25: 1433–63. doi:https://doi.org/10.5194/angeo-25-1433-2007.

Cowley, S. W H, S. V. Badman, S. M. Imber, and S. E. Milan. 2008. “Comment on ‘Jupiter: A Fundamentally Different Magnetospheric Interaction with the Solar Wind’ by D. J. McComas and F. Bagenal.” *Geophysical Research Letters* 35 (10): 1–3. doi:10.1029/2007GL032645.

Cowley, S W H, and E J Bunce. 2001. “Origin of the Main Auroral Oval in Jupiter ’ S Coupled Magnetosphere – Ionosphere System.” *Planetary and Space Science* 49: 1067–88. doi:10.1016/S0032-0633(00)00167-7.

Cravens, T. E., J. H. Waite, T. I. Gombosi, N. Lugaz, G. R. Gladstone, B. H. Mauk, and R. J. MacDowall. 2003. “Implications of Jovian X-Ray Emission for Magnetosphere-Ionosphere Coupling.” *Journal of Geophysical Research: Space Physics* 108 (A12): 1–12. doi:10.1029/2003JA010050.

Delamere, P. a., and F. Bagenal. 2010. “Solar Wind Interaction with Jupiter’s Magnetosphere.” *Journal of Geophysical Research: Space Physics* 115 (10): 1–20. doi:10.1029/2010JA015347.

Delamere, P. A., and F. Bagenal. 2003. “Modeling Variability of Plasma Conditions in the Io Torus.” *Journal of Geophysical Research* 108 (A7): 1276–91. doi:10.1029/2002JA009706.

Dessler, A. J., B. R. Sandel, and S. K. Atreya. 1981. “The Jovian Hydrogen Bulge - Evidence for Co-Rotating Magnetospheric Convection” 29: 215–24. doi:10.1016/0032-0633(81)90035-0.

Dinelli, B. M., F. Fabiano, A. Adriani, F. Altieri, M. L. Moriconi, A. Mura, G. Sindoni, et al. 2017. “Preliminary JIRAM Results from Juno Polar Observations: 1. Methodology and Analysis Applied to the Jovian Northern Polar Region.” *Geophysical Research Letters* 44: 4625–32. doi:10.1002/2017GL072929.

Donoghue, James O. 2014. “The Response Of Gas Giant Ionospheres To Space Environment Forcing Abstract.”

Donoghue, J O, L Moore, T S Stallard, and H Melin. 2016. “Heating of Jupiter’s Upper Atmosphere above the Great Red Spot.” *Nature* 536 (7615). Nature Publishing Group: 1–4. doi:10.1038/nature18940.

Drossart, P., J.-P. Maillard, J. Caldwell, S. J. Kim, J. K. G. Watson, W. a. Majewski, J. Tennyson, et al. 1989. “Detection of H3+ on Jupiter.” *Nature* 340 (6234): 539–41. doi:10.1038/340539a0.

Drossart, Pierre, Bruno Bézard, Sushil K Atreya, James Bishop, J Hunter Waite, and Daniel Boice. 1993. “Thermal Profiles in the Auroral Regions of Jupiter.” *Journal of Geophysical Research* 98 (93): 18,803-818,811. doi:10.1029/93je01801.

Dungey, J. W. 1961. “Interplanetary Magnetic Field and the Auroral Zones.” *Physical Review Letters* 6 (2): 47–48. doi:10.1103/PhysRevLett.6.47.

Dunn, W. R., G. Branduardi-Raymont, L. C. Ray, C. M. Jackman, R. P. Kraft, R. F. Elsner, I. J. Rae, et al. 2017. “The Independent Pulsations of Jupiter’s Northern and Southern X-Ray Auroras.” *Nature Astronomy* 1 (11): 758–64. doi:10.1038/s41550-017-0262-6.

Dunn, William R., Graziella Branduardi-Raymont, Ronald F. Elsner, Marissa F. Vogt, Laurent Lamy, Peter G. Ford, Andrew J. Coates, et al. 2016. “The Impact of an ICME on the Jovian X-Ray Aurora.” *Journal of Geophysical Research A: Space Physics* 121 (3): 2274–2307. doi:10.1002/2015JA021888.

Dunnivant, Frank M., and Jake W. Ginsbach. 2009. “A Review of Optical Physics.” In *Flame Atomic Absorbance and Emission Spectroscopy and Inductively Coupled Spectrometry - Mass Spectrometry*, edited by Mark Beck, William Laxson, Nathan Lien, Kirsten Nicolaysen, Madeline F Polivka, Nicole James, Hannah Main, and Paul DaRosa. Walla Walla, WA 99362: Whitman College, Chemistry Department. http://people.whitman.edu/~dunnivfm/FAASICPMS_Ebook/.

Ebert, Robert, Fran Bagenal, David McComas, and Christopher Fowler. 2014. “A Survey of Solar Wind Conditions at 5 AU: A Tool for Interpreting Solar Wind-Magnetosphere Interactions at Jupiter.” *Frontiers in Astronomy and Space Sciences* 1 (September): 4. doi:10.3389/fspas.2014.00004.

Elsner, R. F., N. Lugaz, J. H. Waite, T. E. Cravens, G. R. Gladstone, P. Ford, D. Grodent, et al. 2005. “Simultaneous Chandra X Ray Hubble Space Telescope Ultraviolet, and Ulysses Radio Observations of Jupiter’s Aurora.” *Journal of Geophysical Research: Space Physics* 110 (A01207): 1–16. doi:10.1029/2004JA010717.

Emerich, C, L B Jaffel, J T Clarke, R Prangé, G R Gladstone, J Sommeria, and G Ballester.

1996. “Evidence for Supersonic Turbulence in the Upper Atmosphere of Jupiter.” *Science (New York, N.Y.)* 273 (5278): 1085–87. doi:10.1126/science.273.5278.1085.

Flasar, F. M., V. G. Kunde, R. K. Achterberg, B. J. Conrath, A. A. Simon-Miller, C. A. Nixon, P. J. Gierasch, et al. 2004. “An Intense Stratospheric Jet on Jupiter.” *Nature* 427: 132–35. doi:10.1038/nature02142.

Förster, M., S. E. Haaland, and E. Doornbos. 2011. “Thermospheric Vorticity at High Geomagnetic Latitudes from CHAMP Data and Its IMF Dependence.” *Annales Geophysicae* 29 (1): 181–86. doi:10.5194/angeo-29-181-2011.

Geballe, T.R., M.-F. Jagod, and T. Oka. 1993. “Detectino of H3+ Infrared Emission Lines in Saturn.” *The Astrophysical Journal* 408: L109–12. doi:10.1086/186843.

Geiner, Walter, Ludwig Neise, and Horst Stocker. 2001. *Thermodynamics and Statistical Mechanics*. *Springer*. doi:10.1017/CBO9780511815836.

Gérard, J.-C., B. Bonfond, D. Grodent, and A. Radioti. 2016. “The Color Ratio-Intensity Relation in the Jovian Aurora: Hubble Observations of Auroral Components.” *Planetary and Space Science* 131. Elsevier: 14–23. doi:10.1016/j.pss.2016.06.004.

Giles, R. S., Leigh N. Fletcher, Patrick G. J. Irwin, Henrik Melin, and Tom S. Stallard. 2016. “Detection of H3+ Auroral Emission in Jupiter’s 5-Micron Window.” *Astronomy & Astrophysics* in press: 3–7. doi:10.1051/0004-6361/201628170.

Gladstone, G. R., J. H. Waite, D. Grodent, W. S. Lewis, F. J. Crary, R. F. Eisner, M. C. Welsskopf, et al. 2002. “A Pulsating Auroral X-Ray Hot Spot on Jupiter.” *Nature* 415 (6875): 1000–1003. doi:10.1038/4151000a.

Greene, T.P., A.T. Tokunaga, D.W. Toomey, and J.S. Carr. 1993. “CSHELL: A High Spectral Resolution Echelle Spectrograph for the IRTF.” *Proc. SPIE* 1946: 313–23. doi:10.1117/12.158684.

Grodent, D., J. T. Clarke, J. Kim, J. H. Waite, and S. W H Cowley. 2003. “Jupiter’s Main Auroral Oval Observed with HST-STIS.” *Journal of Geophysical Research: Space Physics* 108 (A11): 1389. doi:10.1029/2003JA009921.

Grodent, D., J. T. Clarke, J. H. Waite, S. W H Cowley, J. C. Gérard, and J. Kim. 2003. “Jupiter’s Polar Auroral Emissions.” *Journal of Geophysical Research: Space Physics* 108 (A10): 1–9. doi:10.1029/2003JA010017.

Grodent, D., J. C. Gérard, J. T. Clarke, G. R. Gladstone, and J. H. Waite. 2004. “A Possible Auroral Signature of a Magnetotail Reconnection Process on Jupiter.” *Journal of Geophysical Research: Space Physics* 109 (A05201): 1–12. doi:10.1029/2003JA010341.

Grodent, D., J. H. Waite, and J. C. Gerard. 2001. “A Self-Consistent Model of the Jovian Auroral Structure.” *Journal of Geophysical Research* 106 (A7): 12,933-12,952.

Grodent, Denis. 2015. “A Brief Review of Ultraviolet Auroral Emissions on Giant

Planets." *Space Science Reviews* 187 (1–4). Springer Science+Business Media Dordrecht: 23–50. doi:10.1007/s11214-014-0052-8.

Grodent, Denis, Bertrand Bonfond, Jean Claude Gérard, Aikaterini Radioti, Jacques Gustin, John T. Clarke, Jonathan Nichols, and John E P Connerney. 2008. "Auroral Evidence of a Localized Magnetic Anomaly in Jupiter's Northern Hemisphere." *Journal of Geophysical Research: Space Physics* 113 (A09201): 1–10. doi:10.1029/2008JA013185.

Grodent, Denis, J.H. Waite Jr., and Jean-Claude Gerard. 2001. "A Self-Consistent Model of the Jovian Auroral Thermal Structure." *Journal of Geophysical Research* 106 (A7): 12,933-12,952. doi:10.1029/2000JA900129.

Gustin, J., S. W.H. Cowley, J. C. Gérard, G. R. Gladstone, D. Grodent, and J. T. Clarke. 2006. "Characteristics of Jovian Morning Bright FUV Aurora from Hubble Space Telescope/space Telescope Imaging Spectrograph Imaging and Spectral Observations." *Journal of Geophysical Research: Space Physics* 111 (9). doi:10.1029/2006JA011730.

Gustin, J., J. C. Gérard, D. Grodent, S. W H Cowley, J. T. Clarke, and a. Grard. 2004. "Energy-Flux Relationship in the FUV Jovian Aurora Deduced from HST-STIS Spectral Observations." *Journal of Geophysical Research: Space Physics* 109 (A10): 1–17. doi:10.1029/2003JA010365.

Hill, T. W., A. J. Dessler, and C. K. Goertz. 1983. "Magnetospheric Models." In *Physics of the Jovian Magnetosphere*, 353–94. Cambridge and New York: Cambridge University Press. doi:1983phjm.book..353H.

Hill, T W. 1979. "Intertial Limit on Corotation." *Journal of Geophysical Research* 84 (9): 6554–58.

———. 2001. "The Jovian Auroral Oval." *Journal of Geophysical Research* 106 (A5): 8101–7. doi:10.1029/2000JA000302.

Hogness, T. R., and E. G. Lunn. 1925. "The Ionization of Nitrogen by Electron Impact as Interpreted by Positive Ray Analysis." *Physical Review* 26: 44–55. doi:10.1103/PhysRev.26.786.

Huang, T S, and T W Hill. 1989. "Corotation Lag of the Jovian Atmosphere, Ionosphere and Magnetosphere." *Journal of Geophysical Research* 94 (A4): 3761–65. doi:10.1029/JA094iA04p03761.

Iijima, T., and T. A. Potemra. 1976. "Field-Aligned Currents in the Dayside Cusp Observed by Triad." *Journal of Geophysical Research* 81 (34): 5971–79. doi:10.1029/JA081i034p05971.

Ingersoll, A. P., T. E. Dowling, P. J. Gierasch, P. L. Read, A. Sanchez-Lavega, A P Showman, A. A. Simon-Miller, and A. R. Vasavada. 2004. "Dynamics of Jupiter's Atmosphere." In *Jupiter: The Planet, Satellites and Magnetosphere*, edited by F. Bagenal, T. E. Dowling, and B McKinnon, W, 105–28. Cambridge, UK: Cambridge University Press.

Ip, W-H, D. J. Williams, R. W. McEntire, and B. H. Mauk. 1998. “Ion Sputtering and Surface Erosion at Europa Ion Production Rate Is on the Order.” *Geophysical Research Letters* 25 (6): 829–32.

Jaffel, L. B., Y. J. Kim, and J. Clarke. 2007. “The H Lyman-α Emission Line from the Upper Atmosphere of Jupiter: Parametric Radiative Transfer Study and Comparison with Data.” *Icarus* 190 (2): 504–27. doi:10.1016/j.icarus.2007.03.013.

Johnsen, Rainer, and Steven L. Guberman. 2010. “Dissociative Recombination of H3+ Ions with Electrons. Theory and Experiment.” In *Advances in Atomic, Molecular and Optical Physics*, edited by E. Arimondo, P.R. Berman, and C.C. Lin, 59thed., 59:75–128. Elsevier Inc. doi:10.1016/S1049-250X(10)59003-7.

Johnson, Rosie E., Tom S. Stallard, Henrik Melin, Steve Miller, and Jonathan D. Nichols. 2016. “Measurements of the Rotation Rate of the Jovian Mid-to-Low Latitude Ionosphere.” *Icarus* 280. Elsevier Inc.: 249–54. doi:10.1016/j.icarus.2016.06.026.

Johnson, Rosie E., Tom S. Stallard, Henrik Melin, Jonathan D. Nichols, and Stan W.H. Cowley. 2017. “Jupiter’s Polar Ionospheric Flows: High Resolution Mapping of Spectral Intensity and Line-of-Sight Velocity of H3+ions.” *Journal of Geophysical Research: Space Physics* 122 (7): 7599–7618. doi:10.1002/2017JA024176.

Kane, M., B. H. Mauk, E. P. Keath, and S. M. Krimigis. 1995. “Hot Ions in Jupiter’s Magnetodisc: A Model for Voyager 2 Low-Energy Charged Particle Measurements.” *Journal of Geophysical Research* 100 (A10): 19,473-19,486. doi:10.1029/95JA00793.

Kaufl, Hans Ulrich, Pascal Ballester, Peter Biereichel, Bernhard Delabre, Rob Donaldson, Reinhold Dorn, Enrico Fedrigo, et al. 2004. “CRIRES : A High Resolution Infrared Spectrograph for ESO’s VLT.” *SPIE* 5492: 1218–27. doi:10.1117/12.551480.

Khurana, K. K., M. G. Kivelson, V. M. Vasyliunas, N. Krupp, J. Woch, A. Lagg, B. H. Mauk, and W. S. Kurth. 2004. “The Configuration of Jupiter’s Magnetosphere.” In *Jupiter: The Planet, Satellites and Magnetosphere*, edited by Fran Bagenal, Timothy Dowling, and William B. McKinnon.

Kim, Y. H., and J. L. Fox. 1994. “The Chemistry of Hydrocarbon Ions in the Jovian Ionosphere.” *Icarus* 112: 310–25. doi:10.1006/icar.1994.1186.

Kim, YH, JL Fox, and HS Porter. 1992. “Densities and Vibrational Distribution of H3+ in the Jovian Auroral Ionosphere.” *Journal of Geophysical Research* 97 (E4): 6093–6101. http://www.agu.org/pubs/crossref/1992.../92JE00454.shtml.

Kimura, T., S. V. Badman, C. Tao, K. Yoshioka, G. Murakami, A. Yamazaki, F. Tsuchiya, et al. 2015. “Transient Internally Driven Aurora at Jupiter Discovered by Hisaki and the Hubble Space Telescope.” *Geophysical Research Letters* 42: 1662–68. doi:10.1002/2015GL063272.

Kita, Hajime, Tomoki Kimura, Chihiro Tao, Fuminori Tsuchiya, Hiroaki Misawa, Takeshi Sakanoi, Yasumasa Kasaba, et al. 2016. “Characteristics of Solar Wind Control on

Jovian UV Auroral Activity Deciphered by Long-Term Hisaki EXCEED Observations: Evidence of Preconditioning of the Magnetosphere?" *Geophysical Research Letters* 43 (13): 6790–98. doi:10.1002/2016GL069481.

Kivelson, M. G., F. Bagenal, W. S. Kurth, Fritz M. Neubauer, Chris Paranicas, and Joachim Saur. 2004. "Magnetospheric Interactions with Satellites." In *Jupiter: The Planet, Satellites and Magnetosphere*, edited by F. Bagenal, T. E. Dowling, and W. B. McKinnon, 513–36. Cambridge and New York: Cambridge University Press. http://www.igpp.ucla.edu/public/mkivelso/Publications/277-Ch21.pdf.

Kliore, A, D L Cain, G Fjeldbo, B L Seidel, and S I Rasool. 1974. "Preliminary Results on the Atmospheres of Io and Jupiter from the Pioneer 10 S-Band Occultation Experiment." *Science (New York, N.Y.)* 183 (4122): 323–24. doi:10.1126/science.183.4122.323.

Knight, Stephen. 1973. "Parallel Electric Fields." *Planetary and Space Science* 21 (5): 741–50. doi:10.1016/0032-0633(73)90093-7.

Krupp, N., J. Woch, A. Lagg, E. G. Roelof, D. J. Williams, S. Livi, and B. Wilken. 2001. "Local Time Asymmetry of Energetic Ion Anisotropies in the Jovian Magnetosphere." *Planetary and Space Science* 49: 283–89. doi:10.1016/S0032-0633(00)00149-5.

Lam, Hoanh An, Nicholas Achilleos, Steven Miller, Jonathan Tennyson, Laurence M Trafton, Thomas R Geballe, and Gilda E Ballester. 1997. "A Baseline Spectroscopic Study of the Infrared Auroras of Jupiter" 393: 379–93.

Lanzerotti, L. J., C. G. Maclennan, and D. M. Feldmen. 1993. "Ulysses Measurements of Energetic H3 Molecules in Jupiter's Magnetosphere." *Journal of Geo* 98 (A12): 21145–49. doi:10.1029/93JA02589.

Lindal, G. F., D. N. Sweetnam, and V. R. Eshleman. 1985. "The Atmosphere of Saturn - an Analysis of the Voyager Radio Occultation Measurements." *The Astronomical Journal* 90: 1136. doi:10.1029/JA086iA10p08721.

Lord, Steven D. 1992. "A New Software Tool for Computing Earth's Atmospheric Transmission of Near- and Far-Infrared Radiation." *NASA Technical Memorandum 103957*. doi:1992nstc.rept.....L.

Lystrup, M. B., S. Miller, N. Dello Russo, R. J. Vervack, Jr., and T. Stallard. 2008. "First Vertical Ion Density Profile in Jupiter's Auroral Atmosphere: Direct Observations Using the Keck II Telescope." *The Astrophysical Journal* 677 (1): 790–97. doi:10.1086/529509.

Lystrup, M. B., S. Miller, T. Stallard, C. G. A. Smith, and A. Aylward. 2007. "Variability of Jovian Ion Winds : An Upper Limit for Enhanced Joule Heating." *Annales …* 25: 847–53. http://hal.archives-ouvertes.fr/hal-00318303/.

Maillard, Jean-Pierre, Pierre Drossart, J. K. G. Watson, S. J. Kim, and J. Caldwell. 1990. "H3+ Fundamental Band in Jupiter's Auroral Zones at High Resolution from 2400 to 2900 Inverse Centimeters." *The Astrophysical Journal* 363: L37–41.

doi:10.1086/185859.

Majeed, T., S. W. Bougher, A. J. Ridley, J. H. Waite, G. R. GLadstone, and J. M. Bell. 2016. “Global Response of the Upper Thermospheric Winds to Large Ion Drifts in the Jovian Ovals.” *Journal of Geophysical Research : Space Physics* 121: 4647–67. doi:10.1002/ 2015JA021328.

Majeed, T., J. H. Waite, S. W. Bougher, and G. R. Gladstone. 2009. “Processes of Auroral Thermal Structure at Jupiter: Analysis of Multispectral Temperature Observations with the Jupiter Thermosphere General Circulation Model.” *Journal of Geophysical Research E: Planets* 114 (7): 1–22. doi:10.1029/2008JE003194.

Majeed, T., J. Hunter Waite, S. W. Bougher, and G. Randy Gladstone. 2005. “Processes of Equatorial Thermal Structure at Jupiter: An Analysis of the Galileo Temperature Profile with a Three-Dimensional Model.” *Journal of Geophysical Research E: Planets* 110 (12): 1–10. doi:10.1029/2004JE002351.

Mauk, B. H., D. K. Haggerty, S. E. Jaskulek, C. E. Schlemm, L. E. Brown, S. A. Cooper, R. S. Gurnee, et al. 2017. “The Jupiter Energetic Particle Detector Instrument (JEDI) Investigation for the Juno Mission.” *Space Science Reviews* 213: 289–346. doi:10.1007/s11214-013-0025-3.

Mauk, B. H., D. K. Haggerty, C. Paranicas, G. Clark, P. Kollmann, A. M. Rymer, S. J. Bolton, et al. 2017. “Discrete and Broadband Electron Acceleration in Jupiter’s Powerful Aurora.” *Nature* 549 (7670). Nature Publishing Group: 66–69. doi:10.1038/nature23648.

Mauk, B H, J T Clarke, D Grodent, J H Waite, C P Paranicas, and D J Williams. 2002. “Transient Aurora on Jupiter from Injections of Magnetospheric Electrons.” *Nature* 415: 1003–5. doi:10.1038/4151003a.

Mauk, B H, S A Gary, M Kane, E P Keath, S M Krimigis, and T P Armstrong. 1996. “Hot Plasma Parameters of Jupiter’s Inner Magnetosphere.” *Journal of Geophysical Research* 101 (A4): 7685–95.

Mauk, B H, D J Williams, R W McEntire, K Khurana, and J G Roederer. 1999. “Storm-like Dynamics of Jupiter’s Inner and Middle Magnetosphere.” *Journal of Geophysical Research* 104 (A10): 22759–78. doi:10.1029/1999JA900097.

McCall, Benjamin John. 2001. “Spectroscopy of H3+ in Laboratory and Astrophysical Plasmas.” University of Chicago. doi:2001PhDT.....2M.

McComas, D. J., F. Allegrini, F. Bagenal, F. Crary, R. W. Ebert, H. Elliott, A. Stern, and P. Valek. 2007. “Diverse Plasma Populations and Structures in Jupiter’s Magnetotail.” *Science* 318 (5848): 217–21. doi:10.1126/science.1147393.

McComas, D. J., and F Bagenal. 2007. “Jupiter: A Fundamentally Different Magnetospheric Interaction with the Solar Wind.” *Geophysical Research Letters* 34 (L20106): 1–5. doi:10.1029/2007GL031078.

McComas, D. J., and F. Bagenal. 2008. “Reply to Comment by S. W. H. Cowley et Al. on

'Jupiter: A Fundamentally Different Magnetospheric Interaction with the Solar Wind.'" *Geophysical Research Letters* 35 (10): 2–4. doi:10.1029/2008GL034351.

McConnell, J. C., B. R. Sandel, and A. L. Broadfoot. 1980. "Airglow from Jupiter's Nightside and Crescent: Ultraviolet Spectrometer Observations from Voyager 2" 42: 128–42. doi:10.1016/0019-1035(80)90113-X.

McElroy, Michael B. 1973. "The Ionospheres of the Major Planets." *Space Science Reviews* 14: 460–73.

Melin, H., L. N. Fletcher, T. S. Stallard, R. E. Johnson, J. O'Donoghue, L. Moore, and P. T. Donnelly. 2018. "The Quest for H3+ at Neptune: Deep Burn Observations with NASA IRTF iSHELL." *Monthly Notices of the Royal Astronomical Society* 474: 3714–19. doi:10.1093/mnras/stx3029.

Melin, H., T. S. Stallard, J. O'Donoghue, S. V. Badman, S. Miller, and J. S. D. Blake. 2013. "On the Anticorrelation between H3+ Temperature and Density in Giant Planet Ionospheres." *Monthly Notices of the Royal Astronomical Society* 438 (2): 1611–17. doi:10.1093/mnras/stt2299.

Melin, Henrik, Steve Miller, Tom Stallard, and Denis Grodent. 2005. "Non-LTE Effects on H3+ Emission in the Jovian Upper Atmosphere." *Icarus* 178 (1): 97–103. doi:10.1016/j.icarus.2005.04.016.

Melin, Henrik, Steve Miller, Tom Stallard, Chris Smith, and Denis Grodent. 2006. "Estimated Energy Balance in the Jovian Upper Atmosphere during an Auroral Heating Event." *Icarus* 181 (1): 256–65. doi:10.1016/j.icarus.2005.11.004.

Melin, Henrik, and T.S. Stallard. 2016. "Jupiter's Hydrogen Bulge: A Cassini Perspective." *Icarus* 278. Elsevier Inc.: 238–47. doi:10.1016/j.icarus.2016.06.023.

Miller, S, N Achilleos, G E Ballester, H A Lam, J Tennyson, T R Geballe, and L M Trafton. 1997. "Mid-to-Low Latitude H3+ Emission from Jupiter." *Icarus* 130: 57–67. doi:10.1006/icar.1997.5813.

Miller, S, RD Joseph, and J Tennyson. 1990. "Infrared Emissions of H3 (+) in the Atmosphere of Jupiter in the 2.1 and 4.0 Micron Region." *The Astrophysical Journal* 360: L55–58. http://adsabs.harvard.edu/full/1990ApJ...360L..55M.

Miller, Steve, Tom Stallard, Henrik Melin, and Jonathan Tennyson. 2010. "H3+ Cooling in Planetary Atmospheres." *Faraday Discussions* 147: 283-291-403. doi:10.1039/c004152c.

Miller, Steve, Tom Stallard, Chris Smith, George Millward, Henrik Melin, Makenzie Lystrup, and Alan Aylward. 2006. "H3+: The Driver of Giant Planet Atmospheres." *Philosophical Transactions. Series A, Mathematical, Physical, and Engineering Sciences* 364 (1848): 3121-35-7. doi:10.1098/rsta.2006.1877.

Miller, Steve, Tom Stallard, Jonathan Tennyson, and Henrik Melin. 2013. "Cooling by H3+ Emission." *The Journal of Physical Chemistry A* 117: 9770–77. doi:10.1021/jp312468b.

Millward, G, S Miller, T Stallard, A.~D. Aylward, and N Achilleos. 2002. “On the Dynamics of the Jovian Ionosphere and ThermosphereIII. The Modelling of Auroral Conductivity.” *Icarus* 160 (February 1992): 95–107. doi:10.1006/icar.2002.6951.

Millward, George, Steve Miller, Tom Stallard, Nick Achilleos, and Alan D. Aylward. 2005. “On the Dynamics of the Jovian Ionosphere and Thermosphere. IV. Ion-Neutral Coupling.” *Icarus* 173 (1): 200–211. doi:10.1016/j.icarus.2004.07.027.

Moore, L, H Melin, T Stallard, C Tao, B Zieger, J Clarke, M F Vogt, et al. 2017. “Variability of Jupiter’s IR H3+ Aurorae during Juno Approach.” *Geophysical Research Letters*, submitted. doi:10.1002/2017GL073156.

Morgan, D D, D a Gurnett, W S Kurth, and F Bagenal. 1994. “The Source of Jovian Auroral Hiss Observed by Voyager 1.” *Journal of Geophysical Research* 99 (A11): 21213–24.

Moriguchi, Tadanori, Aoi Nakamizo, Takashi Tanaka, Takahiro Obara, and Hironori Shimazu. 2008. “Current Systems in the Jovian Magnetosphere.” *Journal of Geophysical Research: Space Physics* 113 (5): 1–10. doi:10.1029/2007JA012751.

Morioka, A., S. Yaegashi, H. Nozawa, H. Misawa, Y. S. Miyoshi, F. Tsuchiya, and S. Okano. 2004. “H3+ Emissions in the Jovian Sub-Auroral Region and Auroral Activity.” *Geophysical Research Letters* 31 (L16806): 1–7. doi:10.1029/2004GL020390.

Moses, J. I., T. Fouchet, R.V Yelle, A J Freidson, G. S. Orton, B. Bezard, P. Drossart, G.R. Gladstone, T. Kostiuk, and T. A. Livengood. 2004. “The Stratosphere of Jupiter.” In *Jupiter: The Planet, Satellites and Magnetosphere*, edited by Fran Bagenal, Timothy Dowling, and William B. McKinnon, 129–58. Cambridge, UK: Cambridge University Press.

Neale, L., S. Miller, and J. Tennyson. 1996. “Spectroscopic Properties of the H3+ Molecule: A New Calculated Line List.” *The Astrophysical Journal* 464: 516–20. doi:10.1086/177341.

Nichols, J. D. 2011. “Magnetosphere-Ionosphere Coupling in Jupiter’s Middle Magnetosphere: Computations Including a Self-Consistent Current Sheet Magnetic Field Model.” *Journal of Geophysical Research: Space Physics* 116 (10): 1–18. doi:10.1029/2011JA016922.

Nichols, J. D., S. V. Badman, F. Bagenal, S. J. Bolton, B. Bonfond, E. J. Bunce, J. T. Clarke, et al. 2017. “Response of Jupiter’s Auroras to Conditions in the Interplanetary Medium as Measured by the Hubble Space Telescope and Juno.” *Geophysical Research Letters*. doi:10.1002/2017GL073029.

Nichols, J. D., E. J. Bunce, J. T. Clarke, S. W H Cowley, J. C. G??rard, D. Grodent, and W. R. Pryor. 2007. “Response of Jupiter’s UV Auroras to Interplanetary Conditions as Observed by the Hubble Space Telescope during the Cassini Flyby Campaign.” *Journal of Geophysical Research: Space Physics* 112 (2): 1–18.

doi:10.1029/2006JA012005.

Nichols, J D, J T Clarke, J C Gerard, D Grodent, and K C Hansen. 2009. “Variation of Different Components of Jupiter ’s Auroral Emission.” *Journal of Geophysical Research* 114 (A06210): 1–18. doi:10.1029/2009JA014051.

Nichols, J D, and S W H Cowley. 2003. “Magnetosphere-Ionosphere Coupling Currents in Jupiter’s Middle Magnetosphere: Dependence on the Effective Ionospheric Pedersen Conductivity and Iogenic Plasma Mass Outflow Rate.” *Annales Geophysicae* 21 (7): 1419–41. doi:10.5194/angeo-21-1419-2003.

———. 2004. “Magnetosphere-Ionosphere Coupling Currents in Jupiter’s Middle Magnetosphere: Effect of Precipitation-Induced Enhancement of the Ionospheric Pedersen Conductivity.” *Annales Geophysicae* 22: 1799–1827. doi:10.5194/angeo-22-1799-2004.

O’Donoghue, James, Tom S. Stallard, Henrik Melin, Stan W H Cowley, Sarah V. Badman, Luke Moore, Steve Miller, Chihiro Tao, Kevin H. Baines, and James S D Blake. 2014. “Conjugate Observations of Saturn’s Northern and Southern H3+ Aurorae.” *Icarus* 229. Elsevier Inc.: 214–20. doi:10.1016/j.icarus.2013.11.009.

Oka, T, and T R Geballe. 1990. “Observations of the 4 Micron Fundamental Band of H3+ in Jupiter.” *The Astrophysical Journal* 351: L53–56. doi:10.1086/185678.

Oka, Takeshi. 1980. “Observation of the Infrared Spectrum of H3+.” *Physical Review Letters* 45 (7): 531–34. doi:10.1103/PhysRevLett.45.531.

Oliva, E, A Tozzi, D Ferruzzi, L Origlia, A Hatzes, R Follert, T Loewinger, et al. 2014. “Concept and Optical Design of the Cross-Disperser Module for CRIRES+.” *Proc. SPIE* 9147 (Ground-based and Airborne Instrumentation for Astronomy V): 14. doi:10.1117/12.2054381.

Pallier, L, and R Prangé. 2004. “Detection of the Southern Counterpart of the Jovian Northern Polar Cusp: Shared Properties.” *Geophys. Res. Lett.* 31 (L06701): 1–4. doi:10.1029/2003GL018041.

Pallier, Laurent, and Renée Prangé. 2001. “More about the Structure of the High Latitude Jovian Aurorae.” *Planetary and Space Science* 49: 1159–73. doi:10.1016/S0032-0633(01)00023-X.

Parker, E. N. 1958. “Dynamics of the Interplanetary Gas and Magnetic Fields.” *The Astrophysical Journal* 128: 664. doi:10.1086/146579.

Pontius, Duane H, and T. W. Hill. 1982. “Departure from Corotation of the Io Plasma Torus: Local Plasm Production.” *Geophysical Research Letters* 9 (12): 1321–24. doi:10.1103/PhysRevB.89.104420.

Prangé, Renée, Daniel Rego, Laurent Pallier, John E P Connerney, Philippe Zarka, and Julien Queinnec. 1998. “Detailed Study of FUV Jovian Auroral Features with the Post-COSTAR HST Faint Object Camera.” *Journal of Geophysical Research* 103 (E9): 20195. doi:10.1029/98JE01128.

Pryor, Wayne R., A. Ian F. Stewart, Larry W. Esposito, William E. McClintock, Joshua E. Colwell, Alain J. Jouchoux, Andrew J. Steffl, et al. 2005. “Cassini UVIS Observations of Jupiter’s Auroral Variability.” *Icarus* 178 (2): 312–26. doi:10.1016/j.icarus.2005.05.021.

Radioti, A., D. Grodent, J.-C. Gérard, and B. Bonfond. 2010. “Auroral Signatures of Flow Bursts Released during Magnetotail Reconnection at Jupiter.” *Journal of Geophysical Research* 115 (A07214): 1–8. doi:10.1029/2009JA014844.

Radioti, A., D. Grodent, J. C. Gérard, B. Bonfond, and J. T. Clarke. 2008. “Auroral Polar Dawn Spots: Signatures of Internally Driven Reconnection Processes at Jupiter’s Magnetotail.” *Geophysical Research Letters* 35 (L03104): 1–5. doi:10.1029/2007GL032460.

Radioti, A., D. Grodent, J. C. Gérard, M. F. Vogt, M. Lystrup, and B. Bonfond. 2011. “Nightside Reconnection at Jupiter: Auroral and Magnetic Field Observations from 26 July 1998.” *Journal of Geophysical Research: Space Physics* 116 (A03221): 1–8. doi:10.1029/2010JA016200.

Radioti, A., M. Lystrup, B. Bonfond, D. Grodent, and J. C. Gérard. 2013. “Jupiter’s Aurora in Ultraviolet and Infrared: Simultaneous Observations with the Hubble Space Telescope and the NASA Infrared Telescope Facility.” *Journal of Geophysical Research: Space Physics* 118: 2286–95. doi:10.1002/jgra.50245.

Ray, L C, N A Achilleos, M F Vogt, and J N Yates. 2014. “Local Time Variations in Jupiter’s Magnetosphere-Ionosphere Coupling System.” *Journal of Geophysical Research: Space Physics* 119: 4740–51. doi:10.1002/2014JA019941.Received.

Raynaud, E., Emmanuel Lellouch, J. P. Maillard, G. R. Gladstone, J. H. Waite, B. B??zard, P. Drossart, and T. Fouchet. 2004. “Spectro-Imaging Observations of Jupiter’s 2 Micron Auroral Emission. I. H3+ Distribution and Temperature.” *Icarus* 171 (1): 133–52. doi:10.1016/j.icarus.2004.04.020.

Rego, D., S. Miller, and N. Achilleos. 2000. “Latitudinal Profiles of the Jovian IR Emissions of H3+ at 4 Mm with the NASA Infrared Telescope Facility: Energy Inputs and Thermal Balance.” *Icarus* 147 (2): 366–85. doi:10.1006/icar.2000.6444.

Rego, Daniel, Nicholas Achilleos, Tom Stallard, Steve Miller, R Prange, Michele Dougherty, and RD Joseph. 1999. “Supersonic Winds in Jupiter’s Aurorae.” *Nature* 399: 121–24. doi:10.1038/20121.

Rishbeth, H. 1988. “Basic Physics of the Ionosphere: A Tutorial Review.” *Journal of the Institution of Electronic and Radio Engineers* 58 (6S): S207–23. doi:10.1049/jiere.1988.0060.

Ruohoniemi, J. M., R. a. Greenwald, K. B. Baker, J.-P. Villain, C. Hanuise, and J. Kelly. 1989. “Mapping High-Latitude Plasma Convection With Coherent HF Radars.” *Journal of Geophysical Research* 94 (A10): 13,463-13,477.

Sandel, B. R., A. L. Broadfoot, and D. F. Strobel. 1980. “Discovery of a Longitudinal Asymmetry in the H Lyman-Aplha Brightness of Jupiter.” *Geophysical Research*

Letters 7 (1): 5–8. doi:DOI:10.1029/GL007i001p00005.

Sands, Mark R, and Ralph L. McNutt. 1988. “Plasma Bulk Flow in Jupiter’s Dayside Middle Magnetosphere.” *Journal of Geophysical Research* 93 (A8): 8502–18.

Santos-Costa, D., I de Pater, R J Sault, M A Janssen, S M Levin, and S J Bolton. 2014. “Multifrequency Analysis of the Jovian Electron-Belt Radiation during the Cassini Flyby of Jupiter.” *Astronomy & Astrophysics* 568 (A61): 1–11. doi:10.1051/0004-6361/201423896.

Schreier, Ron, Aharon Eviatar, and Vytenis M. Vasyliūnas. 1998. “A Two-Dimensional Model of Plasma Transport and Chemistry in the Jovian Magnetosphere.” *Journal of Geophysical Research: Planets* 103 (E9): 19901–13. doi:10.1029/98JE00697.

Schunk, Robert W., and Andrew F. Nagy. 2000. *Ionospheres: Physics, Plasma Physics, and Chemistry*. Cambridge University Press.

Seidelmann, P. K., and Neil Divine. 1977. “Evaluation of Jupiter Longitudes in System III(1965).” *Geophysical Research Letters* 4 (2): 65–68.

Seiff, Alvin, Donn B. Kirk, Tony C. D. Knight, Richard E. Young, John D. Mihalov, Leslie A. Young, Frank S. Milos, Gerald Schubert, Robert C. Blanchard, and David Atkinson. 1998. “Thermal Structure of Jupiter’s Atmosphere near the Edge of a 5-Mm Hot Spot in the North Equatorial Belt.” *Journal of Geophysical Research: Planets* 103 (E10): 22857–89. doi:10.1029/98JE01766.

Shemansky, D. E, J. M. Ajello, and D. T. Hall. 1985. “Electron Impact Excitation of H2: Rydberg Band Systems and the Benchmark Dissociative Cross Section for H Lyman-Alpha.” *The Astronomical Journal* 296: 765–73. doi:10.1086/163493.

Skinner, T. E., M. T. Deland, G. E. Ballester, K. A. Coplin, P. D. Feldman, and H. W. Moos. 1988. “Temporal Variation of the Jovian H I Lyman Alpha Emission (1979-1986).” *Journal of Geophysical Research* 93 (A1): 29–34. doi:10.1029/JA093iA01p00029.

Smith, C G A, and A D Aylward. 2009. “Coupled Rotational Dynamics of Jupiter’s Thermosphere and Magnetosphere.” *Ann. Geophys.* 27: 199–230.

Sommeria, J., Jaffel, B. L., Prange, R. 1995. “On the Existence of Supersonic Jets in the Upper Atmosphere of Jupiter.” *Icarus* 119: 2–24. doi:10.1006/icar.1995.1174.

Southwood, D J, and M G Kivelson. 2001. “A New Perspective Concerning the Influence of the Solar Wind on the Jovian Magnetosphere.” *Journal of Geophysical Research* 106 (A3): 6123–30.

Speiser, T. W. 1965a. “Particle Trajectories in a Model Current Sheet, Based on the Open Model of the Magnetosphere, with Applications to Auroral Particles.” *Journal of Geophysical Research* 70 (7): 1717. doi:10.1029/JZ070i007p01717.

———. 1965b. “Particle Trajectories in Model Current Sheets: 1. Analytical Solutions.” *Journal of Geophysical Research* 70 (17): 4219–26. doi:10.1029/JZ070i017p04219.

———. 1967. “Particle Trajectories in Model Current Sheets: 2. Applications to Auroras

Using a Geomagnetic Tail Model." *Journal of Geophysical Research* 72 (15): 3919–32. doi:10.1029/JZ072i015p03919.

Stallard, T., S. Miller, G. Millward, and R. D. Joseph. 2002. "On the Dynamics of the Jovian Ionosphere and Thermosphere II. The Measurement of H3+ Vibrational Temperature, Column Density, and Total Emission." *Icarus* 156 (2): 498–514. doi:10.1006/icar.2001.6793.

Stallard, T. S., H. Melin, S. Miller, J. O'Donoghue, S. W. H. Cowley, S. V. Badman, A. Adriani, R. H. Brown, and K. H. Baines. 2012. "Temperature Changes and Energy Inputs in Giant Planet Atmospheres: What We Are Learning from HFormula." *Philosophical Transactions of the Royal Society A: Mathematical, Physical and Engineering Sciences* 370 (1978): 5213–24. doi:10.1098/rsta.2012.0028.

Stallard, T. S., S. Miller, S. W. H. Cowley, and E. J. Bunce. 2003. "Jupiter's Polar Ionospheric Flows: Measured Intensity and Velocity Variations Poleward of the Main Auroral Oval." *Geophysical Research Letters* 30 (5): 1221. doi:10.1029/2002GL016031.

Stallard, T, S Miller, G Millward, and R D Joseph. 2001. "On the Dynamics of the Jovian Ionosphere and Thermosphere I. The Measurement of Ion Winds." *Icarus* 154 (2): 475–91. doi:10.1006/icar.2001.6681.

Stallard, Thomas S. 2001. "Dynamical Studies of the Jovian Ionosphere." University of London.

Stallard, Tom, Steve Miller, George Millward, and Robert D Joseph. 2001. "On the Dynamics of the Jovian Ionosphere and Thermosphere I : The Measurement of Ion Winds" 44 (0): 475–91.

Stallard, Tom S., John T. Clarke, Henrik Melin, Steve Miller, Jon D. Nichols, James O'Donoghue, Rosie E. Johnson, John E P Connerney, Takehiko Satoh, and Michael Perry. 2016. "Stability within Jupiter's Polar Auroral 'Swirl Region' over Moderate Timescales." *Icarus* 268: 145–55. doi:10.1016/j.icarus.2015.12.044.

Stallard, Tom S., Henrik Melin, Steve Miller, Luke Moore, James O'Donoghue, John E. P. Connerney, Takehiko Satoh, et al. 2017a. "The Great Cold Spot in Jupiter's Upper Atmosphere." *Geophysical Research Letters*, 3000–3008. doi:10.1002/2016GL071956.

Stallard, Tom S., Henrik Melin, Steve Miller, Luke Moore, James O'Donoghue, John E.P. Connerney, Takehiko Satoh, et al. 2017b. "The Great Cold Spot in Jupiter's Upper Atmosphere." *Geophysical Research Letters* 44 (7): 3000–3008. doi:10.1002/2016GL071956.

Stallard, Tom S, Henrik Melin, Steve Miller, Sarah V Badman, Kevin H Baines, Robert H Brown, James S.D. Blake, et al. 2015. "Cassini VIMS Observations of H3+ Emission on the Nightside of Jupiter." *Journal of Geophysical Research A: Space Physics* 120 (8): 6948–73. doi:10.1002/2015JA021097.

Tao, Chihiro, Sarah V. Badman, and Masaki Fujimoto. 2011. "UV and IR Auroral

Emission Model for the Outer Planets: Jupiter and Saturn Comparison." *Icarus* 213 (2). Elsevier Inc.: 581–92. doi:10.1016/j.icarus.2011.04.001.

Tao, Chihiro, Hitoshi Fujiwara, and Yasumasa Kasaba. 2009. "Neutral Wind Control of the Jovian Magnetosphere-Ionosphere Current System." *Journal of Geophysical Research: Space Physics* 114 (8): 1–17. doi:10.1029/2008JA013966.

Tao, Chihiro, Ryuho Kataoka, Hiroshi Fukunishi, Yukihiro Takahashi, and Takaaki Yokoyama. 2005. "Magnetic Field Variations in the Jovian Magnetotail Induced by Solar Wind Dynamic Pressure Enhancements." *Journal of Geophysical Research: Space Physics* 110 (A11): 1–9. doi:10.1029/2004JA010959.

Tao, Chihiro, Yoshizumi Miyoshi, Nick Achilleos, and Kita Hajime. 2014. "Response of the Jovian Thermosphere to Variations in Solar FUV Flux." *Journal of Geophysical Research: Space Physics* 119: 3664–82. doi:10.1002/2013JA019411.

Taylor, F. W., S. K. Atreya, T. Encrenaz, D. M. Hunten, P.G. J. Irwin, and T.C. Owen. 2004. "The Composition of the Atomsphere of Jupiter." In *Jupiter: The Planet, Satellites and Magnetosphere*, edited by Fran Bagenal, Timothy Dowling, and William B. McKinnon, 59–78. Cambridge, UK: Cambridge University Press.

Thomson, J. J. 1911. "Rays of Positive Electricity." *Philosophical Magazine* 21 (112): 225–49. doi:https://doi.org/10.1080/14786440208637024.

Tokunaga, A. T., D. W. Toomey, J. Carr, D. N. B. Hall, and H. W. Epps. 1990. "Design for a 1-5-Micron Cryogenic Echelle Spectrograph for the NASA IRTF." In *Instrumentation in Astronomy VII*, 131–43. doi:10.1117/12.19082.

Trafton, L. M., D. F. Lester, and K. L. Thompson. 1989. "Unidentified Emission Lines in Jupiter's Nothern and Southern 2 Micron Aurorae." *The Astrophysical Journal* 343: L73–76. doi:10.1086/185514.

Trafton, L.M., T.R. Geballe, S. Miller, J. Tennyson, and G.E. Ballester. 1993. "Detection of H3+ from Uranus." *Astrophysical Journal* 405 (2): 761–66. doi:10.1086/172404.

Uno, T, Y Kasaba, C Tao, T Sakanoi, M Kagitani, S Fujisawa, H Kita, and S V Badman. 2014. "Vertical Emissivity Profiles of Jupiter's Northern H3+ and H2 Infrared Auroras Observed by Subaru/IRCS." *Journal of Geophysical Research: Space Physics* 119: 10219–41. doi:10.1002/2014JA020454.

Vasyliunas, Vytenis M. 1983. "Plasma Distribution and FLow." In *Physics of the Jovian Magnetosphere*, edited by A. J. Dessler, 1st ed., 395–453. Cambridge University Press.

Vogt, Marissa F., Margaret G. Kivelson, Krishan K. Khurana, Raymond J. Walker, Bertrand Bonfond, Denis Grodent, and Aikaterini Radioti. 2011. "Improved Mapping of Jupiter's Auroral Features to Magnetospheric Sources." *Journal of Geophysical Research: Space Physics* 116 (3). doi:10.1029/2010JA016148.

Waite, J.H, D Grodent, B.M Mauk, T Majeed, G.R Gladstone, S.J Bolton, J.T Clarke, et al. 2000. "Multispectral Observations of Jupiter's Aurora." *Advances in Space*

Research 26 (10): 1453–75. doi:10.1016/S0273-1177(00)00089-2.

Waite, J Hunter, G Randall Gladstone, William S Lewis, Raymond Goldstein, David J McComas, Pete Riley, Raymond J Walker, et al. 2001. "An Auroral Flare at Jupiter." *Nature* 410 (6830): 787–89. doi:10.1038/35071018.

Walterscheid, R. L., and G. Crowley. 2009. "Large-Scale Instabilities of the Lower Thermosphere during an Active Period." *Journal of Geophysical Research: Space Physics* 114 (A07306): 1–10. doi:10.1029/2008JA013892.

West, Robert A., Kevin H Baines, A J Freidson, D Banfield, D Ragent, and F W Taylor. 2004. "Jovian Clouds and Haze." In *Jupiter: The Planet, Satellites and Magnetosphere*, edited by Fran Bagenal, Timothy Dowling, and William B. McKinnon, 79–104. Cambridge, UK: Cambridge University Press.

Woch, J., N. Krupp, A. Lagg, B. Wilken, S. Livi, and D. J. Williams. 1998. "Quasi-Periodic Modulations of the Jovian Magnetotail." *Geophysical Research Letters* 25 (8): 1253–56. doi:10.1029/98GL00861.

Woch, Joachim, Norbert Krupp, and Andreas Lagg. 2002. "Particle Bursts in the Jovian Magnetosphere: Evidence for a near-Jupiter Neutral Line." *Geophysical Research Letters* 29 (7): 1138–41. doi:10.1029/2001GL014080.

Yates, J. N., N. Achilleos, and P. Guio. 2012. "Influence of Upstream Solar Wind on Thermospheric Flows at Jupiter." *Planetary and Space Science* 61 (1). Elsevier: 15–31. doi:10.1016/j.pss.2011.08.007.

———. 2014. "Response of the Jovian Thermosphere to a Transient 'Pulse' in Solar Wind Pressure." *Planetary and Space Science* 91. Elsevier: 27–44. doi:10.1016/j.pss.2013.11.009.

Yelle, Roger V, and S Miller. 2004. "Jupiter 's Thermosphere and Ionosphere." In *Jupiter: The Planet, Satellites and Magnetosphere*, edited by Fran Bagenal, Thimothy Dowling, and William McKinnon, 1sted., 185--218. Cambridge, UK: Cambridge University Press: Cambridge Planetary Science. http://www.cambridge.org/us/academic/subjects/astronomy/planetary-science/jupiter-planet-satellites-and-magnetosphere.

Yoneda, M., H. Nozawa, H. Misawa, M. Kagitani, and S. Okano. 2010. "Jupiter's Magnetospheric Change by Io's Volcanoes." *Geophysical Research Letters* 37 (L11202): 1–5. doi:10.1029/2010GL043656.

Zieger, B., G. Tóth, M. Opher, and T. Gombosi. 2015. "Solar Wind Prediction at Pluto during the New Horizons Flyby: Results from a Two-Dimensional Multifluid MHD Model of the Outer Heliosphere." *Abstract SM31D-2539 Presented at 2015 Fall Meeting*.